

DESIGN OF TOOL AND BACKING/CLAMPING  
SYSTEM FOR DISSIMILAR FRICTION  
STIR WELDING OF HIGH STRENGTH  
AA7075-T6 AND AA2024-T351  
ALUMINUM ALLOYS

MOHAMMED MIDHAT HASAN

UMP

Doctor of Philosophy

UNIVERSITI MALAYSIA PAHANG

## UNIVERSITI MALAYSIA PAHANG

### DECLARATION OF THESIS AND COPYRIGHT

Author's Full Name : Mohammed Midhat Hasan

Date of Birth : 17-04-1975

Title : Design of tool and backing/clamping system for dissimilar  
friction stir welding of high strength AA7075-T6 and  
AA2024-T351 aluminum alloys

Academic Session : 2016/2017

I declare that this thesis is classified as:

- CONFIDENTIAL (Contains confidential information under the Official Secret Act 1997)\*
- RESTRICTED (Contains restricted information as specified by the organization where research was done)\*
- OPEN ACCESS I agree that my thesis to be published as online open access (Full Text)

I acknowledge that Universiti Malaysia Pahang reserves the following rights:

1. The Thesis is the Property of Universiti Malaysia Pahang
2. The Library of Universiti Malaysia Pahang has the right to make copies of the thesis for the purpose of research only.
3. The Library has the right to make copies of the thesis for academic exchange.

Certified by:

\_\_\_\_\_  
(Student's Signature)

A9267612

\_\_\_\_\_  
Passport Number

Date: / / November/ 2017

\_\_\_\_\_  
(Supervisor's Signature)

Associate Professor  
Dr. Mahadzir bin Ishak

\_\_\_\_\_  
Name of Supervisor

Date: / / November/ 2017

NOTE: \* If the thesis is CONFIDENTIAL or RESTRICTED, please attach a thesis declaration letter.

### SUPERVISOR'S DECLARATION

We hereby declare that we have checked this thesis and in our opinion, this thesis is adequate in terms of scope and quality for the award of the degree of Doctor of Philosophy of Mechanical Engineering.

---

(Supervisor's Signature)

Full Name : Dr. Mahadzir bin Ishak

Position : Associate Professor

Date : / November/ 2017

---

(Co-supervisor's Signature)

Full Name : Dr. Mhod Ruzaimi bin Mat Rejab

Position : Senior lecturer

Date : / November/ 2017

### STUDENT'S DECLARATION

I hereby declare that the work in this thesis is based on my original work except for quotations and citations which have been duly acknowledged. I also declare that it has not been previously or concurrently submitted for any other degree at Universiti Malaysia Pahang or any other institutions.

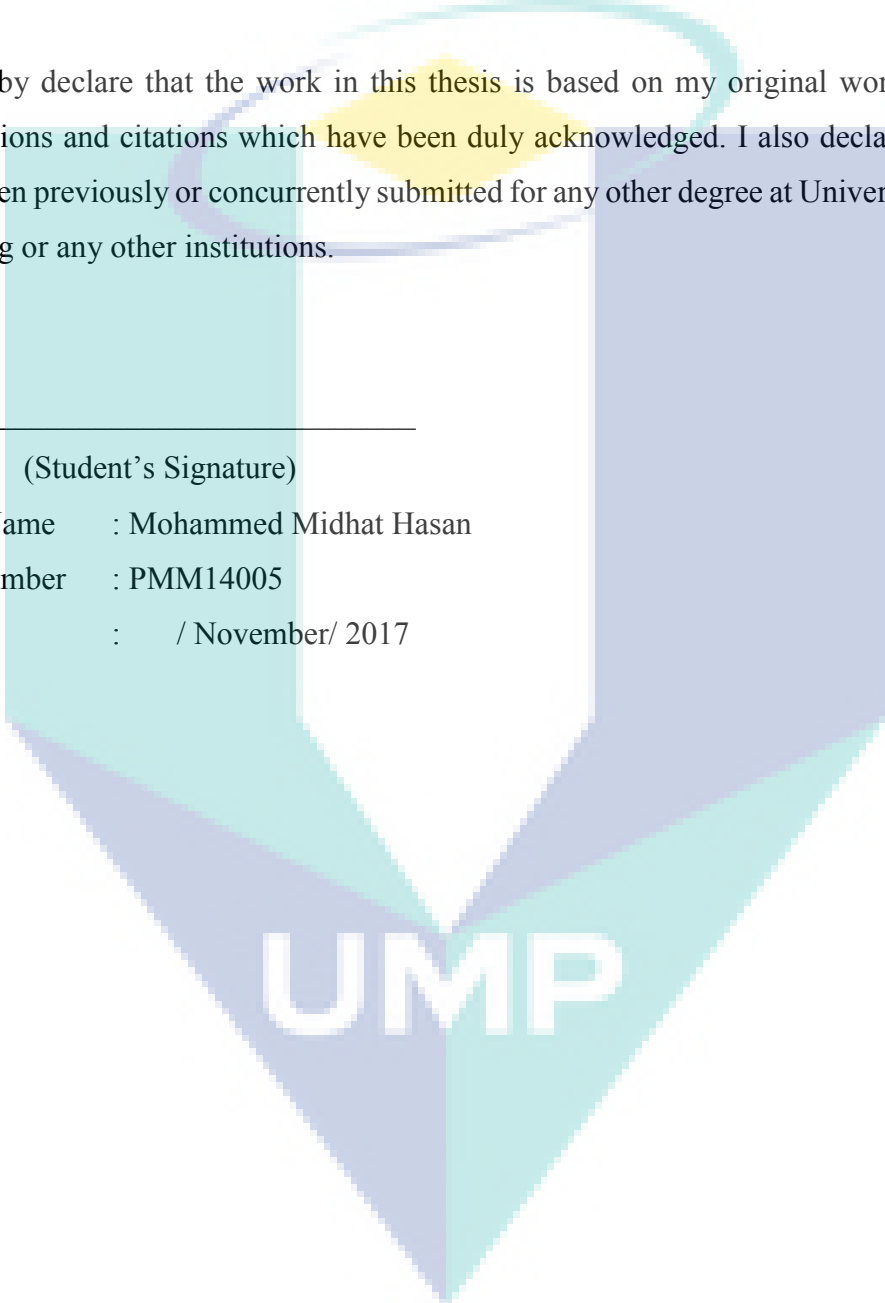
---

(Student's Signature)

Full Name : Mohammed Midhat Hasan

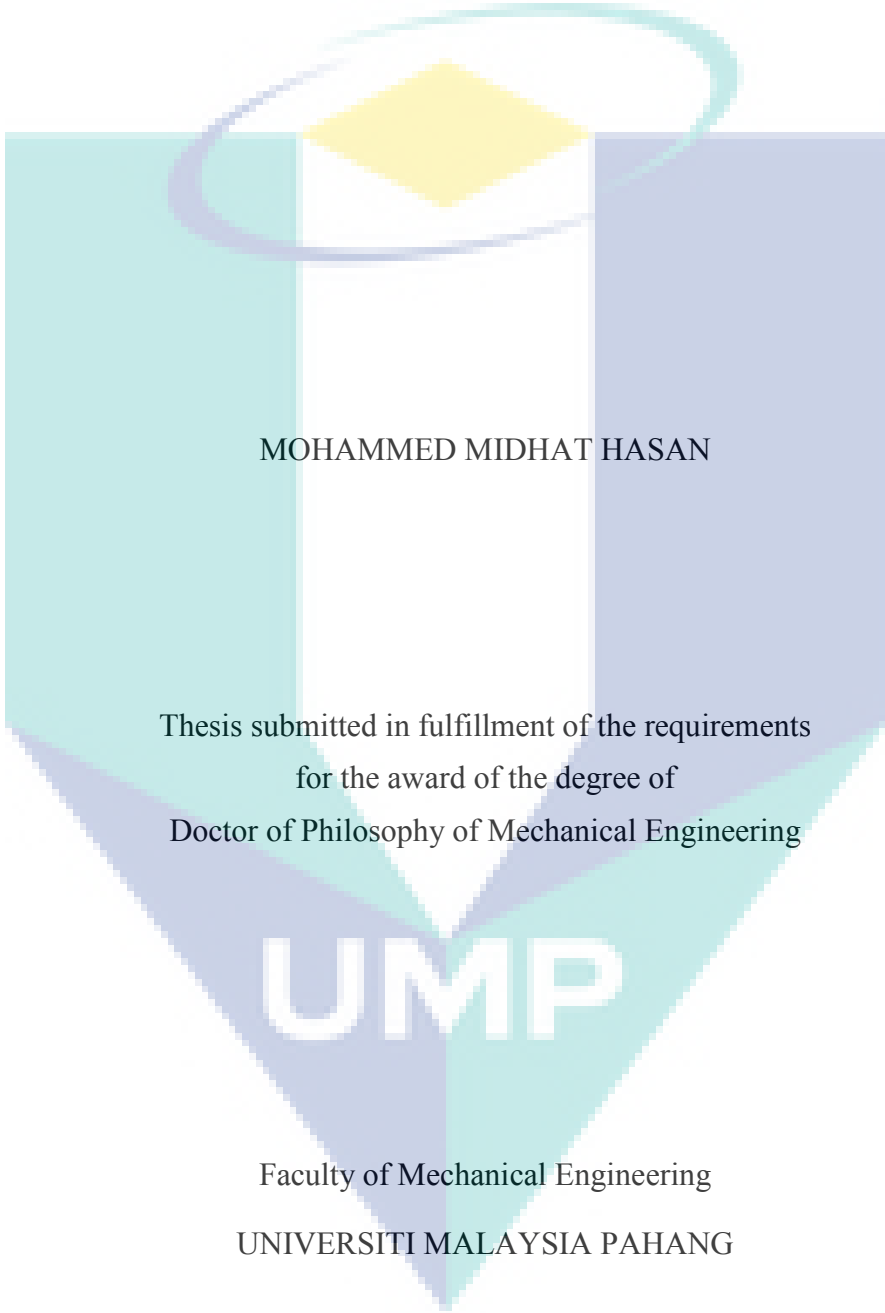
ID Number : PMM14005

Date : / November/ 2017



UMP

DESIGN OF TOOL AND BACKING/CLAMPING SYSTEM  
FOR DISSIMILAR FRICTION STIR WELDING OF HIGH STRENGTH  
AA7075-T6 AND AA2024-T351 ALUMINUM ALLOYS



MOHAMMED MIDHAT HASAN

Thesis submitted in fulfillment of the requirements  
for the award of the degree of  
Doctor of Philosophy of Mechanical Engineering

UMP

Faculty of Mechanical Engineering  
UNIVERSITI MALAYSIA PAHANG

NOVEMBER 2017

## ACKNOWLEDGEMENTS

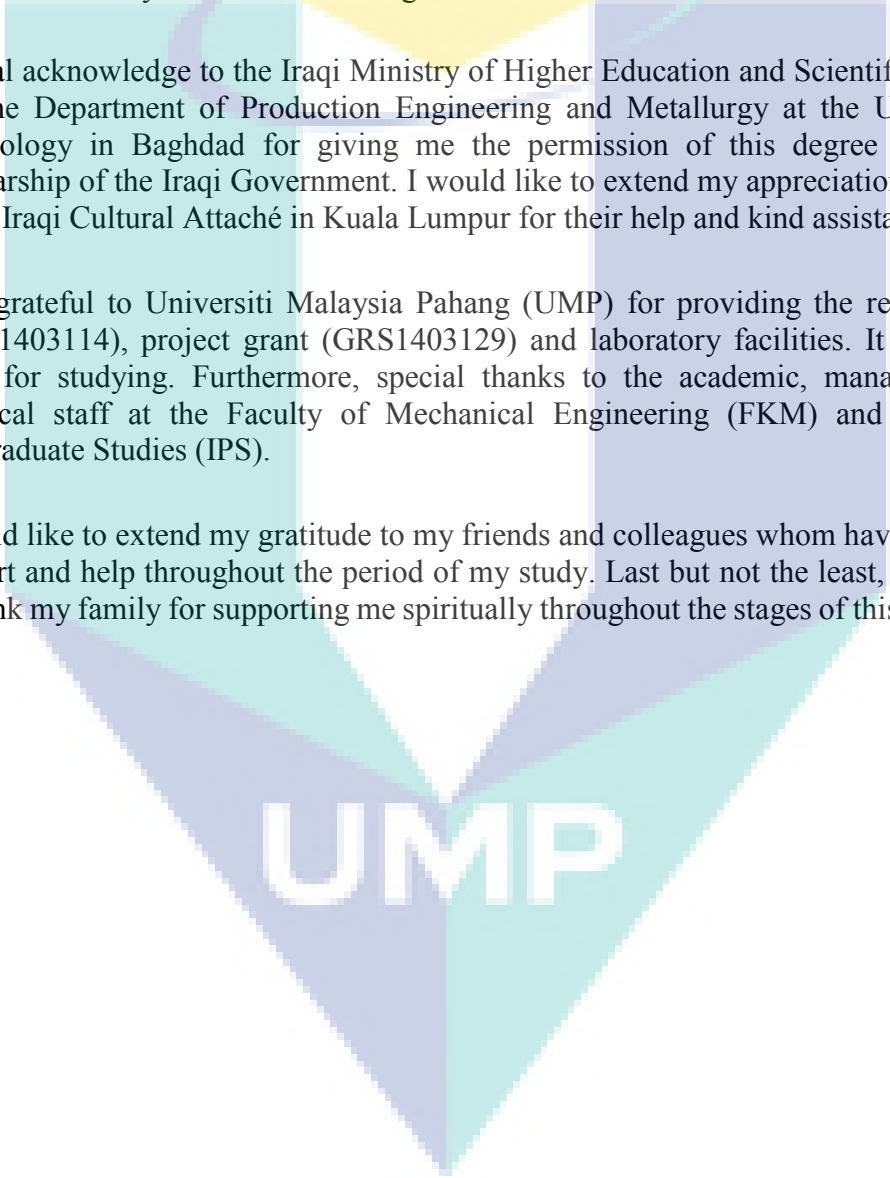
All thanks and praises to the Great Allah, the most Gracious and most Merciful for giving me the opportunity, strength and patience to complete my dissertation after all challenges and difficulties.

I would like to express my sincere gratitude to my supervisors: Associate Professor Dr. Mahadzir bin Ishak and Dr. Mohd Ruzaimi bin Mat Rejab for their continuous support, motivation and immense knowledge during my doctoral study and related researches. Thanks for all of your honest encouragement.

Special acknowledge to the Iraqi Ministry of Higher Education and Scientific Research, and the Department of Production Engineering and Metallurgy at the University of Technology in Baghdad for giving me the permission of this degree through the Scholarship of the Iraqi Government. I would like to extend my appreciation to the staff of the Iraqi Cultural Attaché in Kuala Lumpur for their help and kind assistance.

I am grateful to Universiti Malaysia Pahang (UMP) for providing the research grant (RDU1403114), project grant (GRS1403129) and laboratory facilities. It was a good place for studying. Furthermore, special thanks to the academic, management and technical staff at the Faculty of Mechanical Engineering (FKM) and Institute of Postgraduate Studies (IPS).

I would like to extend my gratitude to my friends and colleagues whom have given their support and help throughout the period of my study. Last but not the least, I would like to thank my family for supporting me spiritually throughout the stages of this PhD thesis.



UMP

## ABSTRAK

Kajian ini dilakukan pada pelbagai logam yang digunakan bagi menyambung bahagian aloi aluminium yang sukar dikimpal tetapi kini menjadi aplikasi penting dalam industri moden. Kajian ini bertujuan untuk menghasilkan kimpalan bebas-kecacatan yang mempunyai kekuatan AA7075-T6 dan aloi aluminium AA2024-T351 yang berkuasa. Tinggi dengan menggunakan cara geseran kacau kimpalan (FSW) yang telah dicadangkan sebagai kaedah kimpalan alternatif. Prosedur percubaan telah dibangunkan dengan memperkenalkan reka bentuk alat kimpalan dan sistem sokongan/penjepit yang betul dengan menggunakan pemboleh ubah proses (kelajuan kimpalan, sudut kecondongan alat, daya pengapit, urutan dan kedudukan bahan relatif dan orientasi). Ciri-Ciri alat pin yang berbeza (silinder dan tirus, licin dan diulirkan, rata dan tidak rata) disiasat bersama dengan pelbagai peringkat pembolehubah mesin melalui kaedah reka bentuk komposit berpusat. Untuk mengurangkan jumlah kos, bahan-bahan yang diperlukan bagi kajian ini disediakan dari AA6061 yang digunakan secara meluas dan aloi aluminium AA7075 yang mempunyai daya kekuatan yang tinggi. Selanjutnya, reka bentuk alat dikaji dengan menyiasat pengaruh jejari serpihan alat pin pada aliran bahan dan sifat tegangan pada kimpalan yang berbeza. Kaedah baru dua peringkat kimpalan tanpa menggunakan fasa terjun diperkenalkan untuk mengelakkan kehausan alat pin longitudinal. Untuk mengendalikan haba keseluruhan proses kimpalan, tiga sistem sokongan dan pengoperasian yang terdiri daripada bahan kekonduksian haba yang tinggi dan rendah digunakan. Selain itu, pembinaan suatu sistem sokongan asimetrik dan pengoperasian diperkenalkan untuk menilai pengedaran suhu semasa proses kimpalan yang dinilai dengan menggunakan wayar termokopel imbedded. Pemeriksaan visual, analisis metalografi, pengagihan kekerasan dan sifat tegangan telah dijalankan untuk memeriksa kualiti kimpalan yang telah dilakukan. Keputusan menunjukkan bahawa kekuatan bersama boleh ditingkatkan sehingga 31% apabila alat pin silinder lurus dipotong, diulirkan dan dimesin dengan rata tunggal. Ia juga menggambarkan bahawa kualiti kimpalan boleh ditingkatkan lagi apabila rataan tambahan diubahsuai kepada seruling tunggal dengan radius yang sama dengan radius alat pin. Kekuatan kimpalan AA7075-AA2024 kira-kira 400 MPa yang mewakili kecekapan sebanyak 89% dicatatkan apabila aloi AA2024 yang lebih lembut telah ditetapkan pada bahagian hadapan dengan kelajuan gelendong 900 rpm, 100 mm / min kadar traverse, 3° sudut miring dan tekanan pengapit sederhana 3 kN. Kecekapan telah ditingkatkan kepada 91.6% apabila kadar melintas dinaikkan kepada 150 mm/min di bawah pemboleh ubah proses yang sama. Kimpalan bebas cecair dihasilkan selepas 12 saat masa kelewatan pegun. Kimpalan yang paling stabil dicapai dengan menggunakan kaedah kimpalan dua peringkat, yang dengan ketara mengurangkan bentuk alat bilah pin yang disebabkan oleh kitaran penyusutan. Hasilnya menjelaskan bahawa kesan sokongan dan bahan penjepit pada kekuatan kimpal berubah dengan kelajuan kimpalan yang digunakan. Lebih-lebih lagi, perbezaan dalam suhu proses telah diperhatikan antara sisi pemanjangan dan pengembalian kimpalan. Suhu lebih tinggi pada bahagian yang maju ke hadapan berbanding dengan yang berundur di sisi. Sistem sokongan/penjepit asimetri mengeluarkan lebih banyak haba kimpalan dari bahagian yang maju dan mengurangkan asimetri suhu. Ini seterusnya meningkatkan kekuatan kimpalan sehingga 426 MPa, yang mewakili kecekapan kira-kira 95%. Sebagai tambahan kepada pemboleh ubah proses FSW yang lain, reka bentuk alat kimpalan dan sistem sokongan/penjepit menjejaskan corak aliran bahan, pengedaran suhu, profil kekerasan dan dengan itu kualiti kimpalan. Hasil kajian ini mengandungi pengetahuan terkini yang boleh digunakan dalam kajian masa depan dengan menggunakan gabungan logam yang berbeza.

## ABSTRACT

This work was carried out on dissimilar metal joining of the hard-to-weld aluminum alloys, which has become an important application in the modern industries. The study aims on producing defects-free welds of high strength AA7075-T6 and AA2024-T351 aluminum alloys by the friction stir welding (FSW), which has been proposed as an alternative welding method. The experimental setup was developed through introducing proper design of welding tool and backing/clamping system, considering the process variables (welding speeds, tool tilt angle, clamping force, dwell sequence and relative materials position and orientation). Different pin tool profiles (cylindrical and tapered, smooth and threaded, flatted and non-flatted) were investigated in conjunction with varying levels of machine variables through the central composite design method. To reduce the total cost, the workpieces in this level of the study were prepared from the widely used AA6061 and high strength AA7075 aluminum alloys. Tool design was further studied by considering the influence of pin tool flute radius on the material flow and tensile properties of the dissimilar weld. A new method of two-stage welding without applying the ordinary plunge phase was introduced to avoid the longitudinal pin tool wear. To control the total heat of welding process, three backing and cover systems consisted of high and low thermal conductivity materials were used. In addition, a new construction of asymmetric backing and cover system was introduced to access the temperature distribution during the welding process, which was observed using imbedded thermocouple wires. Visual inspection, metallographic analysis, hardness distribution and tensile properties were conducted to detect the weld quality. The results showed that the joint strength can be enhanced up to 31% when a straight cylindrical pin tool is truncated, threaded and machined with single flat. It was also noticed that the weld quality can be further improved when the additional flat is modified to a single flute with a radius equal to that of the pin tool radius. The dissimilar AA7075-AA2024 weld strength of about 400 MPa, which represents an efficiency of 89% was recorded when the softer AA2024 alloy was fixed on the advancing side at 900 rpm of spindle speed, 100 mm/min of traverse rate, 3° of tilting angle and moderate clamping pressure of 3 kN. The efficiency was increased to 91.6% when the traverse rate was raised to 150 mm/min under the same process variables. Defect-free weld was produced after 12 seconds of stationary delay time. The most stable weld was attained by using the two-stage welding method, which significantly reduced the longitudinal deformation of the pin tool caused from the plunging cycle. The results clarified that the effect of backing and clamping materials on the weld strength is changed related to the applied welding speed. Moreover, a considerable difference in process temperature was noticed between the advancing and retreating sides of the weld. The temperatures were higher on the advancing side compared to those measured on the retreating side. The asymmetric backing/clamping system extracted more amount of the welding heat from the advancing side and reduced the temperature asymmetry. This in turn enhanced the weld strength up to 426 MPa, which represents the maximum joint efficiency of about 95%. In addition to the other FSW process variables, design of the welding tool and backing/clamping system affect the pattern of material flow, temperature distribution, hardness profile and hence weld quality. The outcomes of the present study provided advanced knowledge for the future work in dissimilar metal joining.

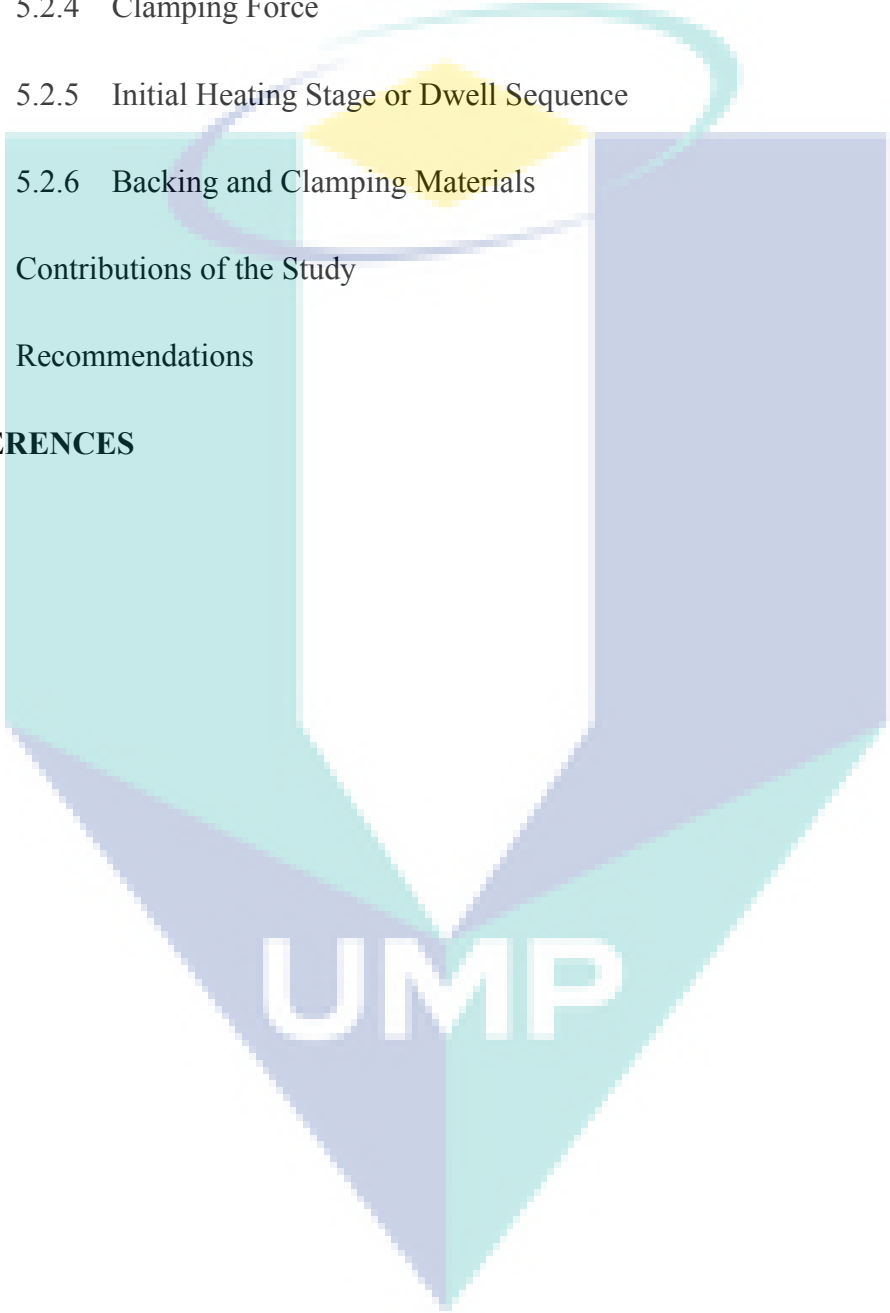
# TABLE OF CONTENT

<b>DECLARATION</b>	
<b>TITLE PAGE</b>	
<b>ACKNOWLEDGEMENTS</b>	<b>ii</b>
<b>ABSTRAK</b>	<b>iii</b>
<b>ABSTRACT</b>	<b>iv</b>
<b>TABLE OF CONTENT</b>	<b>v</b>
<b>LIST OF TABLES</b>	<b>ix</b>
<b>LIST OF FIGURES</b>	<b>xi</b>
<b>LIST OF SYMBOLS AND ABBREVIATIONS</b>	<b>xix</b>
<b>CHAPTER 1 INTRODUCTION</b>	<b>1</b>
1.1 Background	1
1.2 Problem Statement	5
1.3 Objectives of the Study	7
1.4 Scope of the Study	7
1.5 Thesis Organization	8
<b>CHAPTER 2 LITERATURE REVIEW</b>	<b>9</b>
2.1 Introduction	9
2.2 Friction Stir Welding Technology	9
2.3 Process Parameters	11
2.3.1 Tool Design	13

2.3.2	Machine Variables	28
2.4	Backing Materials and Clamping Equipment	39
2.5	Temperature Distribution and Measuring Procedures	51
2.6	Summary	52
<b>CHAPTER 3 METHODOLOGY</b>		<b>54</b>
3.1	Introduction	54
3.2	Main Frame of the Study	54
3.3	Material Characterization	54
3.4	Preparation of the Welding Coupons	57
3.5	Design of the Welding Tools	58
3.5.1	Geometry and Dimensions	59
3.5.2	Tool Material and Heat Treatments	61
3.6	Backing/Clamping Systems	63
3.6.1	Fixtures Design	63
3.6.2	Construction of the Developed Design	65
3.7	Temperature Measurement	67
3.8	Welding Procedures	70
3.8.1	Workpieces Clamping	70
3.8.2	Design of Experiments and Process Parameters	71
3.9	Tensile Testing and Metallographic Analysis	80
3.10	Summary	84

<b>CHAPTER 4 RESULTS AND DISCUSSION</b>	<b>85</b>
4.1 Introduction	85
4.2 Properties of the Welding Base Materials	85
4.2.1 Mechanical Properties	86
4.2.2 Metallographic Inspections	86
4.3 Tool Design and Process Parameters	89
4.3.1 Design of Experiments and Statistical Analysis	89
4.3.2 Validation Tests	92
4.3.3 Sensitivity Analysis	93
4.3.4 Microstructure and Tensile Properties	96
4.3.5 Effect of Materials Direction and Position	101
4.4 FSW of Dissimilar AA7075-T6 and AA2024-T351 Aluminum Alloys	108
4.4.1 Effect of Clamping Force	110
4.4.2 Effect of Tool Rotation Speed	112
4.4.3 Initial Plunge Phase and Dwell Sequence	124
4.4.4 Effect of Backing and Clamping Material	132
4.4.5 Characterization of the Pin Tool Design	153
4.5 Summary	161
<b>CHAPTER 5 CONCLUSIONS AND RECOMMENDATIONS</b>	<b>162</b>
5.1 Introduction	162
5.2 Summary of the Findings	162

5.2.1	Tool Design	162
5.2.2	Mathematical Modeling	163
5.2.3	Materials Direction and Position	164
5.2.4	Clamping Force	164
5.2.5	Initial Heating Stage or Dwell Sequence	165
5.2.6	Backing and Clamping Materials	166
5.3	Contributions of the Study	167
5.4	Recommendations	167
<b>REFERENCES</b>		<b>169</b>

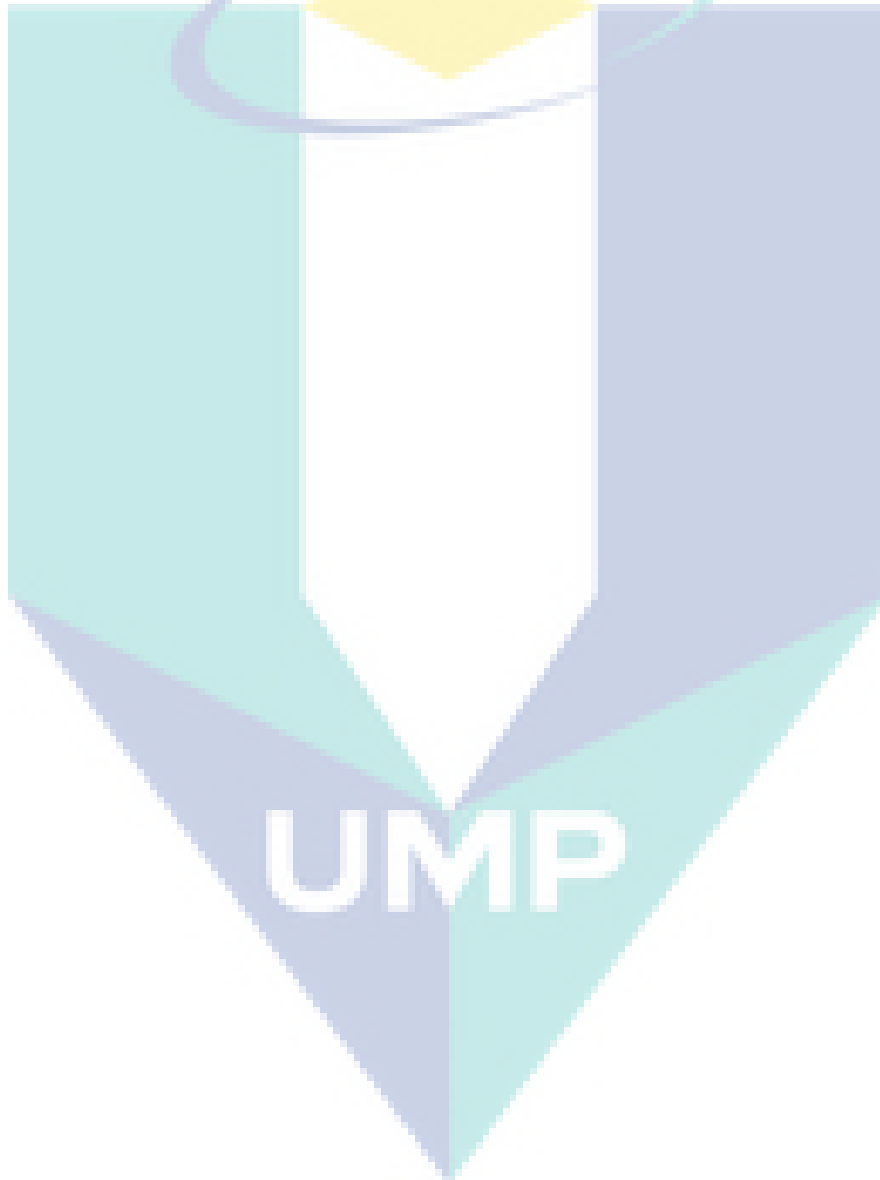
The logo for UWP (Universiti Wawasan) is a large, downward-pointing arrow shape. It is composed of several overlapping geometric shapes in shades of teal, light blue, and yellow. The letters 'UWP' are printed in a bold, white, sans-serif font across the bottom of the arrow.

**UWP**

## LIST OF TABLES

Table 2.1	Summary of the machine variables used previously to join aluminums 6061 and 2024 to the high-strength AA7075 alloy	38
Table 3.1	The standard and supplier mechanical properties of the welding base materials	56
Table 3.2	The standard and supplier chemical composition (wt.%) of the welding base materials	57
Table 3.3	Description of the fluted/flatted pin tools shown in Figure 3.4-(c)	61
Table 3.4	Chemical composition (wt.%) with thermal, physical and mechanical properties of the welding tool material (AISI H13 tool steel) according to the supplier	61
Table 3.5	Description of the clamping system and fixtures used to join the 3-mm-thick AA7075-AA6061 aluminum sheets	64
Table 3.6	Description of the developed backing/clamping system	67
Table 3.7	Levels of the selected parameters used to investigate the influence of pin tool design on the tensile strength of dissimilar AA7075-AA6061 friction stir welds	72
Table 3.8	The CCD matrix of the response surface methodology	76
Table 3.9	Configuration of the weld related to the location and rolling direction of AA7075 and AA6061 aluminum alloys	77
Table 3.10	The calibrated values of the applied torques related to the clamping forces	78
Table 3.11	Values of the notations presented in Figure 3.12-(b)	82
Table 4.1	Results of the tensile tests for the welding base materials	86
Table 4.2	Estimated regression coefficients for UTS	90
Table 4.3	Regression coefficients of the developed model	91
Table 4.4	ANOVA of UTS for the developed model	91
Table 4.5	The verification table	93
Table 4.6	The acquired chemical composition (wt.%) of the weld related to the spectrums shown in Figure 4.13	103
Table 4.7	The acquired chemical composition (wt.%) of the weld related to the spectrums shown in Figure 4.15	104

Table 4.8	The chemical composition (wt.%) of the weld HAZ, TMAZ and the regions shown in Figure 4.26 at 900 rpm	117
Table 4.9	The chemical composition (wt.%) of the weld related to the regions shown in Figure 4.28 at 1800 rpm	119
Table 4.10	The chemical composition (wt.%) of the weld related to the regions shown in Figure 4.62	149
Table 4.11	The chemical composition (wt.%) of the weld related to the regions shown in Figure 4.68, Figure 4.70 and Figure 4.72	158



## LIST OF FIGURES

Figure 1.1	Schematic drawing of the FSW process. (a) plunge and dwell sequences, (b) stirring or the main welding phase and (c) tool withdrawal at the end of weld	3
Figure 1.2	Interaction between the physical effects and FSW process variables	4
Figure 2.1	Main advantages of the friction stir welding technology	10
Figure 2.2	Friction stir welding machines	11
Figure 2.3	Conventional friction stir welding tool and machine variables	12
Figure 2.4	Commonly used tool designs in the friction stir welding	13
Figure 2.5	Tool materials used in dissimilar FSW	14
Figure 2.6	The cylindrical (T1), tapered (T2) and cylindrical-tapered (T3) pin tool profiles	18
Figure 2.7	Shapes of the pin tool. (CG): tapered cylinder with grooves, (TS): Tapered square, (TH): Tapered hexagon, (PS): Paddle shape, (SC): Straight cylinder	19
Figure 2.8	Straight and tapered probes	20
Figure 2.9	Threaded and unthreaded pin tools	21
Figure 2.10	Triangular and cylindrical probes	21
Figure 2.11	featured and featureless pin tool designs	22
Figure 2.12	The threaded pin tools with different number of flats and their corresponding joint strengths	23
Figure 2.13	Schematic drawing of the square frustum and conical probes	24
Figure 2.14	The five pin tool designs. (a) threaded tapered, (b) triangular, (c) square, (d) four-flute square, and (e) four-flute cylindrical	25
Figure 2.15	Shoulder profiles of the pinless tool design	26
Figure 2.16	The pin and pinless tools with different shoulder diameters	27
Figure 2.17	Schematic drawings of the raised, recessed and ramp shoulder designs	27
Figure 2.18	Effect of tool rotation speed and materials placement on the dissimilar AA7075-AA6061 weld	28

Figure 2.19	Hardness distribution of the dissimilar AA6061-AA7075 weld at different traverse speeds. Aluminium 6061 placed on the RS in D2 and D3, while it fixed on the AS in D4 and D5	29
Figure 2.20	Distribution of the tensile strain of the friction stir weld	30
Figure 2.21	Stress distribution of the dissimilar friction stir weld	31
Figure 2.22	Effect of the post-weld heat treatment on the dissimilar weld hardness	31
Figure 2.23	Fracture location of the dissimilar weld at various spindle speeds	33
Figure 2.24	Hardness profile of the dissimilar AA7075-AA2024 joint when the harder AA7075 alloy placed on the AS	35
Figure 2.25	Hardness distribution of the dissimilar AA7075-AA2024 weld at various tool rotation and traverse speeds	36
Figure 2.26	The dissimilar AA7075-AA2024 weld macrograph and hardness distribution at 1000 rpm of tool rotation rate and 254 mm/min of traverse speed	37
Figure 2.27	Interaction diagram between the process variables and thermal boundary conditions of the workpieces	39
Figure 2.28	Macrographs of the friction stir weld zones	40
Figure 2.29	Schematic drawing of the heat flow (HF) during the FSW process	42
Figure 2.30	Schematic drawings of the backing/cover systems and the resulted hardness profiles at 100 mm/min traverse speed. (a) denotes System 1, (b) represents Systems 2 (without the steel sheet) and (c) Systems 3 (with 0.5 mm steel sheet below the base material)	43
Figure 2.31	The transverse macrographs, and the hardness, strength and elongation of the weld at different materials of backing plate (BP)	44
Figure 2.32	Mechanical properties and macrographs of the weld related to the selected backing materials	46
Figure 2.33	Maximum weld temperature for different backing materials: asbestos (ASB), stainless steel (SS), and mild steel (MS) at various tool rotation rate and traverse speed	47
Figure 2.34	Single and dual compliant rollers with conventional clamping claws and pressure bars	49

Figure 2.35	Measuring instruments of the clamping force, and the resulted gap and gap-free welds	50
Figure 2.36	Different sensing techniques used to measure the friction stir weld temperature. (a) thermocouples spot welded inside the pin tool (the black dots indicate the locations of thermocouples). (b) thermocouple placement in the backing plate and (c) the image of IR camera with the corresponding thermal profiles	52
Figure 3.1	The flow-chart of research methodology	55
Figure 3.2	The experimental setup	56
Figure 3.3	The preparation steps of the welding coupons	57
Figure 3.4	Design and dimensions in millimeters of the welding tools	60
Figure 3.5	Heat treatment stages of the welding tool	62
Figure 3.6	Photo of the clamping system and fixtures used to join the 3-mm-thick AA7075-AA6061 aluminum sheets	64
Figure 3.7	Schematic drawing and photographs of the developed backing/clamping systems	66
Figure 3.8	Preparation steps of the transient temperature observation during the welding route	68
Figure 3.9	Aligning and clamping of the composite backing plate and workpieces using the specially fabricated sharpened edge tool	70
Figure 3.10	The load sensor and torque wrench used to control the applied clamping forces on the welding specimens	71
Figure 3.11	Schematic drawing of the eight case studies of relative materials direction and position	77
Figure 3.12	Sample, locations and dimensions in millimeters of the tension test specimens cut from the welding joints	81
Figure 3.13	The automatic mounting press and the encapsulated metallographic specimens	83
Figure 3.14	(a) The LED light-microscope, (b) The micro-hardness tester and (c) The SEM/EDS tabletop microscope	84
Figure 4.1	Microstructures of the welding base materials	87
Figure 4.2	The SEM images and EDS spectrums with the acquired chemical compositions of base materials	88
Figure 4.3	Micro-hardness of the base materials	89

Figure 4.4	Dissimilar AA6061-AA7075 friction stir welds	90
Figure 4.5	Scatter plot of the observed and predicted results of UTS	92
Figure 4.6	Response 3D contour plots. In each plot, the two other factors were fixed at their intermediate levels	94
Figure 4.7	Results of the sensitivity analysis	95
Figure 4.8	Stress–strain curves of the base materials and welding joints using the five tools at the central levels of the other three variables	96
Figure 4.9	Macrographs of the weld nuggets related to the five welding tools with the observed ultimate tensile strength (UTS). The AA6061 alloy is placed on the left-hand side (AS) of each photo	97
Figure 4.10	Macrographs of the weld nuggets related to the tools T <sub>2</sub> , T <sub>3</sub> and T <sub>4</sub> showing the onion rings. The AA6061 alloy is placed on the left-hand side (AS) of each photo	98
Figure 4.11	The weld micro-hardness distribution related to the five tools at the central levels of the other three variables	100
Figure 4.12	Photo of specimen A3 after welding showing the relative materials position and direction	102
Figure 4.13	The weld microstructure of specimen A3	103
Figure 4.14	The SEM image of zone A shown in Figure 4.13 with the corresponding EDS spectrums	103
Figure 4.15	The weld microstructure of specimen A4	104
Figure 4.16	The weld tensile strength and percent elongation related to the materials position and rolling direction	106
Figure 4.17	The weld micro-hardness distribution related to the materials position and rolling direction	107
Figure 4.18	The initial welding trials of the 6-mm-thick AA7075-T6 and AA2024-T351 aluminum alloys	108
Figure 4.19	A photograph captured during the joining of dissimilar AA7075-AA2024 aluminum alloys using the developed backing/clamping system, and selected group of the produced welding joints	109
Figure 4.20	Joint tensile strength and percentage elongation related to the applied clamping forces	110

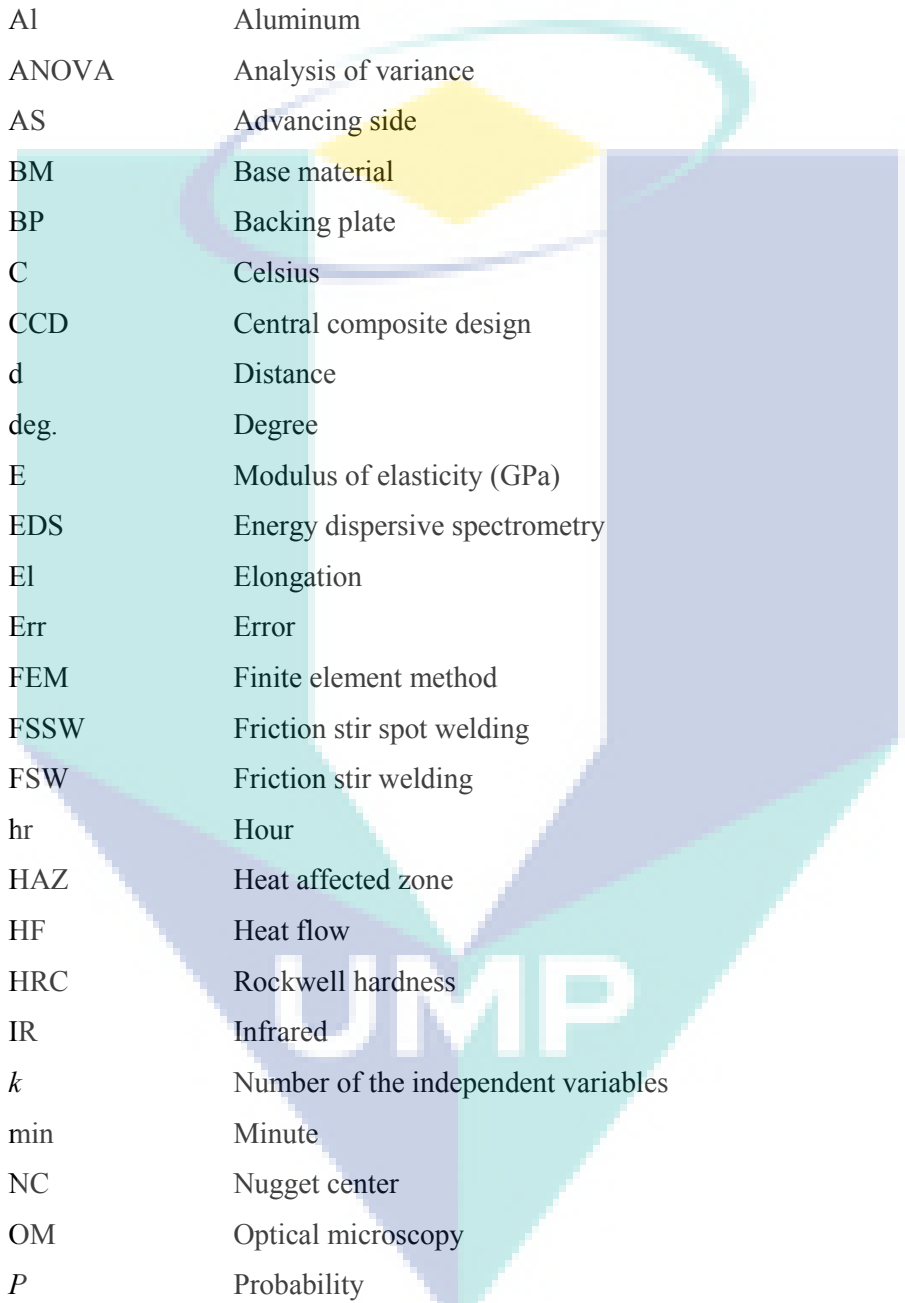
Figure 4.21	The weld profile under 6 kN of clamping force	111
Figure 4.22	Surface finish of the resulting welds at different tool rotation speeds and materials position	113
Figure 4.23	Macrographs of the weld at different tool rotation speeds	114
Figure 4.24	Micrographs of the weld nugget at 600- and 900 rpm of spindle speed. (a) AA7075-T6 placed on AS and (b) AA2024-T351 placed on AS	115
Figure 4.25	Micrographs of the weld nugget-TMAZ-HAZ at 900 rpm. AA7075-T6 placed on RS	116
Figure 4.26	Variation of the onion rings from the edge of weld nugget close to the AS towards the nugget center (NC) at 900 rpm. AA2024-T351 placed on AS	117
Figure 4.27	Micrographs of the weld nugget at 1200- and 1500 rpm of spindle speed. (a) AA7075-T6 placed on AS and (b) AA2024-T351 placed on AS	118
Figure 4.28	Micrographs of the weld nugget at 1800 rpm. (a) AA7075-T6 placed on AS and (b) AA2024-T351 placed on AS	119
Figure 4.29	The weld micro-hardness distribution related to the tool rotation rate	121
Figure 4.30	Fracture locations of the tension test specimens at different tool rotation rates	122
Figure 4.31	The weld ultimate tensile strength and percentage elongation at different spindle speeds and materials position	123
Figure 4.32	Difference in the weld ultimate tensile strength ( $\Delta$ UTS) related to the materials position under various spindle speeds	123
Figure 4.33	The weld surface finish at at the first welding quarter under different stationary dwell sequences. (a) 3 sec, (b) 6 sec, (c) 12 sec and (d) 24 sec	125
Figure 4.34	Macrographs of the weld and their corresponding nugget micrographs related to the applied dwell sequences	126
Figure 4.35	Higher magnification of the upper left-hand side of the weld nugget after (a) 3 sec and (b) 6 sec of stationary dwell time	127
Figure 4.36	An illustration of the TSW. $v_o = 30$ mm/min along 6 mm of the welding line and $v = 100$ mm/min (welding traverse speed)	128

Figure 4.37	Macrograph of the weld and the corresponding nugget microstructure with a photo of the welding joint resulted from using the TSW method	128
Figure 4.38	The weld tensile strength and its variation along the welding seam related to the stationary dwell sequences and TSW method	129
Figure 4.39	Variation of the tensile strength along the welding seam related to the stationary dwell sequences and TSW method	130
Figure 4.40	Hardness distribution at the start quarter of welding seam related to the dwell sequences and TSW method	131
Figure 4.41	Profile of the pin tool (a) before welding, (b) after 14 plunge cycles and one complete weld (without pilot hole) and (c) after 15 weldments (with pilot hole)	132
Figure 4.42	Surface finish of the resulting welds related to the backing/clamping systems at 900 rpm spindle speed and 100 mm/min traverse rate	133
Figure 4.43	Surface finish of the resulting welds related to the backing/clamping systems at 900 rpm spindle speed and 50 mm/min traverse rate	134
Figure 4.44	Surface finish of the resulting welds related to the backing/clamping systems at 900 rpm spindle speed and 150 mm/min traverse rate	134
Figure 4.45	Surface finish of the resulting welds related to the backing/clamping systems at 900 rpm spindle speed and 200 mm/min traverse rate	135
Figure 4.46	Surface finish of the resulting welds related to the backing/clamping systems at 900 rpm spindle speed and 250 mm/min traverse rate	135
Figure 4.47	Surface finish of the unsuccessful welding trial at 900 rpm spindle speed and 300 mm/min traverse rate	136
Figure 4.48	Joint strength and percentage elongation related to the three backing/clamping systems at different traverse speeds and materials position	136
Figure 4.49	The fracture locations related to the backing/clamping systems at 900 rpm spindle speed and 100 mm/min traverse rate	137
Figure 4.50	The fracture locations related to the backing/clamping systems at 900 rpm spindle speed and 50 mm/min traverse rate	138

Figure 4.51	The fracture locations related to the backing/clamping systems at 900 rpm spindle speed and 150 mm/min traverse rate	138
Figure 4.52	The fracture locations related to the backing/clamping systems at 900 rpm spindle speed and 200 mm/min traverse rate	139
Figure 4.53	The fracture locations related to the backing/clamping systems at 900 rpm spindle speed and 250 mm/min traverse rate	139
Figure 4.54	Macrographs of the weld and their corresponding nugget microstructures related to the backing/clamping systems at 900 rpm and 100 mm/min. AA2024-T351 placed on AS	141
Figure 4.55	Temperature distributions in the AS at 900 rpm and 100 mm/min related to the materials position and backing/clamping systems. AA2024-T351 placed on AS	142
Figure 4.56	Temperature distributions in the RS at 900 rpm and 100 mm/min related to the materials position and backing/clamping systems. AA7075-T6 placed on RS	143
Figure 4.57	Peak temperatures from the eight thermocouples at 900 rpm and 100 mm/min related to the backing/clamping systems	144
Figure 4.58	Macrographs of the weld and their corresponding nugget microstructures related to the backing/clamping systems at 900 rpm and 150 mm/min. AA2024-T351 placed on AS	145
Figure 4.59	Temperature distributions in the AS at 900 rpm and 150 mm/min related to the materials position and backing/clamping systems. AA2024-T351 placed on AS	146
Figure 4.60	Temperature distributions in the RS at 900 rpm and 150 mm/min related to the materials position and backing/clamping systems. AA7075-T6 placed on RS	147
Figure 4.61	Photographs of the surface finish (on the left) and bottom profile (on the right) of the weld produced using the novel asymmetric backing/clamping system (System 4) at 900 rpm and 150 mm/min	148
Figure 4.62	Macrograph of the weld and the corresponding nugget microstructure resulted from using the asymmetric backing/clamping system (System 4) at 900 rpm and 150 mm/min. AA2024-T351 placed on AS	149
Figure 4.63	Temperature distributions in the advancing and retreating sides of the weld produced using the asymmetric backing/clamping system (System 4) at 900 rpm and 150 mm/min. AA2024-T351 placed on AS	150

Figure 4.64	Peak temperatures from the eight thermocouples at 900 rpm and 150 mm/min for all backing/clamping systems	151
Figure 4.65	The weld micro-hardness distribution at 900 rpm and 150 mm/min for all backing/clamping systems	152
Figure 4.66	Stress-strain curves of the base materials and welding joints for all backing/clamping systems at 900 rpm and 150 mm/min. AA2024-T351 placed on AS	152
Figure 4.67	Macrographs of the dissimilar welding joints related to the pin tool profile and materials position	153
Figure 4.68	Micrographs of the weld nugget produced by the pin tool R0. (a) AA7075-T6 placed on AS and (b) AA2024-T351 placed on AS	154
Figure 4.69	Micrographs of the weld nugget produced by the pin tool R2. (a) AA7075-T6 placed on AS and (b) AA2024-T351 placed on AS	155
Figure 4.70	Micrographs of the weld nugget produced by the pin tool R3. (a) AA7075-T6 placed on AS and (b) AA2024-T351 placed on AS	156
Figure 4.71	Micrographs of the weld nugget produced by the pin tool R6. (a) AA7075-T6 placed on AS and (b) AA2024-T351 placed on AS	156
Figure 4.72	Micrographs of the weld nugget produced by the pin tool R $\infty$ . (a) AA7075-T6 placed on AS and (b) AA2024-T351 placed on AS	157
Figure 4.73	The EDS spectrums as per the regions numbered in Figure 4.68	158
Figure 4.74	Joint strength and percentage elongation related to the pin tool design	159
Figure 4.75	The weld micro-hardness distribution related to the pin tool design and materials position	160

## LIST OF SYMBOLS AND ABBREVIATIONS



3D	Three dimensional
AA	Aluminum alloy
AGI	Average grain intercept
Al	Aluminum
ANOVA	Analysis of variance
AS	Advancing side
BM	Base material
BP	Backing plate
C	Celsius
CCD	Central composite design
d	Distance
deg.	Degree
E	Modulus of elasticity (GPa)
EDS	Energy dispersive spectrometry
El	Elongation
Err	Error
FEM	Finite element method
FSSW	Friction stir spot welding
FSW	Friction stir welding
hr	Hour
HAZ	Heat affected zone
HF	Heat flow
HRC	Rockwell hardness
IR	Infrared
$k$	Number of the independent variables
min	Minute
NC	Nugget center
OM	Optical microscopy
$P$	Probability
Q	Thermal energy (W)
$R^2$	Coefficient of determination
RD	Rolling direction
RS	Retreating side
RSM	Response surface methodology

sec	Second
SD	Standard deviation
SE	Standard error
SEM	Scanning electron microscope
SiC	Silicon carbide
SS	Stainless steel
SZ	Stir zone
THK	Thickness (mm)
<i>T</i>	Tool
TD	Transverse direction
TMAZ	Thermal mechanical affected zone
TSW	Two stage welding
TWI	The welding institute
UNC	Unified National Coarse
UTS	Ultimate tensile strength (MPa)
VHN	Vickers hardness number
wt.	Weight (N)
WD	Welding direction
$x_i$	The coded value of the $i$ -factor
$X_i$	The actual value of the $i$ -factor
$\bar{X}_i$	The average of the high and low actual values of the $i$ -factor
$Y$	The predicted response
$\beta_i$	The linear effect term
$\beta_{ii}$	The squared effect term
$\beta_{ij}$	The interactive effect term
$\beta_o$	The intercept constant term
$\varepsilon_t$	Tensile strain (mm/mm)
$\theta$	Tilt angle (deg.)
$v$	Traverse speed (mm/min)
$\sigma_t$	Tensile stress
$\omega$	Tool rotation or spindle speed (rpm)
$\Delta X_i$	The step change value

## CHAPTER 1

### INTRODUCTION

#### 1.1 Background

Dissimilar metal welding is the joining of two separate metals which would not ordinarily weld together as they have differing chemical and mechanical qualities, and are from different alloy systems. If the core properties of two metals are different but they share the same name, they are still dissimilar in nature (Fuchs et al., 2010). Joining dissimilar metals has benefits for many different industries, such as the construction, automotive and electronics industry, whereby there is often a necessity to weld together different parts and components to save on material costs or to use the best possible metals always for the perfect product (Kumar et al., 2015).

Although a number of welding techniques, such as laser and gas metal arc plug welding have been developed so far to deal with different types of materials (Islam et al., 2016), friction stir welding (FSW), the green technology, has become one of the most operative and economic joining techniques due to its ability to connect a wide range of ferrous and even nonferrous materials such as steel (El-Batahgy et al., 2016), titanium (Fu et al., 2016), aluminum (Salih et al., 2015), magnesium (Pasha et al., 2016) and some of polymers and plastics (Eslami et al., 2016). Dissimilar welding of the heat-treatable and hard-to-weld 7xxx, 6xxx and 2xxx aluminum alloys has become more efficient by using this joining process (Kumar et al., 2015). These alloys are widely used in the automotive, aerospace, aircraft, pipelines, storage tanks, marine frames, and transportation industries due to their high strength-to-weight ratio, good machinability and high resistance to corrosion (Ishak et al., 2015; Moghadam et al., 2016). However, these materials cannot be welded by the traditional fusion methods, since they are highly affected by the elevated temperature required for material melting (Bertoncello et al.,

2015). For this reason, mechanical fastener assembly was the traditional technique used in the fabrication of the aircraft stiffened panels, which are produced from the aluminum highly alloyed series (A. Murphy et al., 2014). Among aluminum alloys, AA7075-T6 represents the strongest alloy whose tensile strength is about double of the widely used AA6061-T6 alloy. The advanced AA2024-T351 aircraft aluminum alloy is different from AA2024-T3 due to the unlike processing procedure. It has a lower tensile and yield strength and more pronounced plasticity than AA2024-T3 and deforms more homogeneously than the AA7075-T6 alloy (Đurđević et al., 2015; Wang et al., 2016). FSW of this developed alloy results in an average static strength of about 85% of the base material and a very high fatigue strength (Dursun & Soutis, 2014). Consequently, joining this developed alloy to the higher strength AA7075-T6 alloy could enhance the mechanical properties of the produced construction.

The melting points of materials would not be exceeded during the FSW process, and the welding occurs in a solid-state due to the relatively lower heat energy input (Caseiro et al., 2013). Accordingly, this advanced technology has been introduced as an alternative joining method to riveting in the automotive and transportation industries. It has become a very impressive way to reduce the manufacturing cost and time by eliminating the requisite for expensive non-standard materials (A Murphy et al., 2014). The static strength and fatigue properties of joints produced by this novel technology are higher in comparison with the mechanical fastening and traditional fusion welding methods (Shao et al., 2014). Materials of thickness ranging from less than 1 mm to about 75 mm could be joined by the FSW (Thomas & Nicholas, 1997) in various configurations including square butt, edge butt, T-butt, lap, multiple lap, T-lap and fillet joints (Mishra & Mahoney, 2007).

Since 1991, when this novel technique was invented by Wayne Thomas and his colleagues at The Welding Institute (TWI) in the UK (Thomas et al., 1991), researchers started to understand the effect of process parameters on the properties of welding joint. Tool design, machine and other variables have been investigated in numerous research studies to improve the outcome of this technique. High quality joints were obtained between dissimilar materials, and the trials have even been extended to join some metallic to non-metallic materials (Khodabakhshi et al., 2016; Kumar et al., 2015). However, much remains to be learned about the process, and the opportunities for advance research

studies and improvements are still promising. The friction stir process consists of three simple phases, as illustrated in Figure 1.1. A non-consumable rotating tool consists of a probe (or pin) and shoulder is inserted between the workpieces until the shoulder be slightly penetrated inside the materials. During this initial plunge phase of the process, the friction between the pin tool surface and welding coupons generates some of the heat required for softening the abutting materials around the probe. After a suitable dwell sequence, the tool is stirred with an appropriate traverse speed to produce the weldment in the main welding phase.

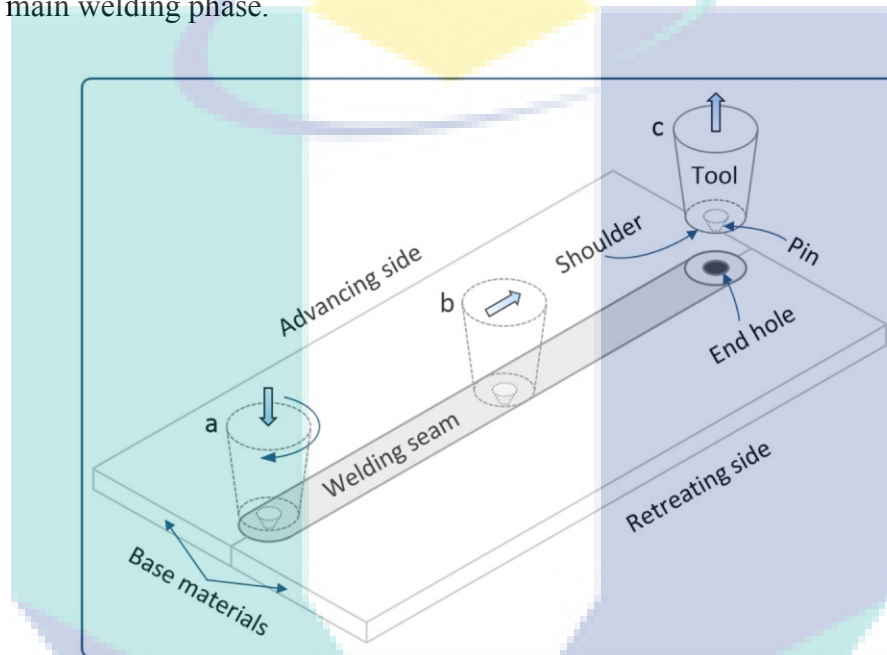


Figure 1.1 Schematic drawing of the FSW process. (a) plunge and dwell sequences, (b) stirring or the main welding phase and (c) tool withdrawal at the end of weld

Adapted from: Jain et al. (2016)

The welding side in which the direction of the tool rotation is parallel to the welding direction is called advancing side (AS), whereas the other is called retreating side (RS). Materials placement on these sides represents an additional factor upsetting the friction stir processing and must be considered when dissimilar materials are to be joined. Most of the total heat in this thermomechanical process is generated by the friction between the shoulder and materials surface in the dwell and stir stages (Sevvel & Jaiganesh, 2015; Trueba Jr et al., 2015). The stationary dwell sequence is important for initial heating, so the materials of the workpieces be soft enough and ready for mixing. Finally, the tool is withdrawn leaving an exit hole comparable to the pin profile. Mechanical properties of the weldment are sensitive to the generation and distribution of

the welding heat, which in turn depends on the process variables and physical effects (Colligan & Mishra, 2008).

Tool design represents the central parameter in FSW, since it is the key source of the generated heat and mixing of the coupled materials in the weld zone. Many of the advances made in FSW have been enabled by the development of new tools with different profiles and added features. However, there is no accepted optimum tool design in use nowadays (Colligan, 2010), since a particular tool may produce different responses when the same set of input parameters are used on different materials or with different plate thicknesses (Blignault et al., 2011). Figure 1.2 shows the interaction between the FSW process variables and physical effects. This interaction represents the complexity of the friction stir process, which appears to be a simple method when one sees a rotating tool plunged then stirred between two abutting materials. For that reason, careful procedures must be followed to achieve stable and sound weld.

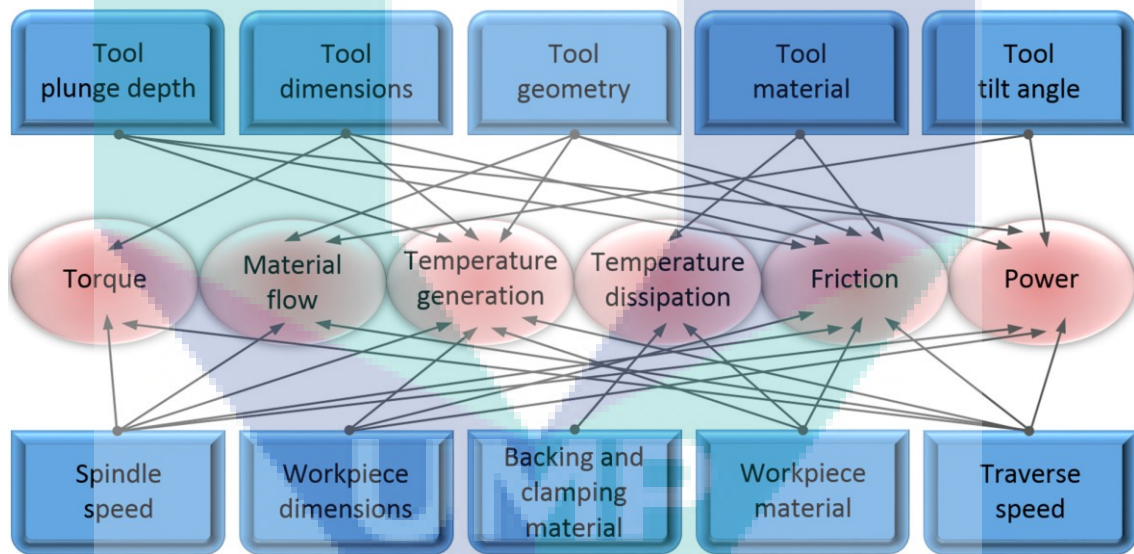


Figure 1.2 Interaction between the physical effects and FSW process variables  
Adapted from: Colligan & Mishra (2008)

Temperature distribution is highly affected by the backing materials and clamping system, which are quite significant factors (Imam et al., 2014; Parida et al., 2015; Upadhyay & Reynolds, 2012). Temperature dissipation is dependent on the thermal diffusivity of workpieces and their surrounding materials. Furthermore, it is important that the workpieces should not be spread or lifted during the process; therefore, welding fixtures must be designed with features permit to achieve this objective. The quality of

weld depends on the manufacturing precision of the clamping system and welding table (Colligan, 2010). The impact of clamping method on the joint performance should be recognized so that the essential stable quality could be ensured. Appropriate clamping forces, which should be applied by specially designed fixtures are required in FSW. This result in a significant rise of the total process cost. Thus, a comprehensive knowledge regarding the required forces would assist to optimize the clamping system with respect to cost and efficiency (Smith et al., 2003). At the time of designing new optimized clamping systems for particular applications, there is a need for essential information about the actual forces required so that the parts to be joined are fixed correctly in place.

## **1.2 Problem Statement**

The heat treatable aluminum 2xxx, 6xxx, and 7xxx series are crack sensitive and categorized as unweldable or difficult to weld by the conventional fusion welding method (Dursun & Soutis, 2014). The relatively new FSW technique permits to join such these materials in a solid state and produce high-integrity joints. However, the assembly of dissimilar aluminum alloys differing in mechanical, thermal and chemical properties still a challenge (Kumar et al., 2015). Furthermore, there is limited studies regarding the joining of highest strength AA7075 alloy with aluminum AA6061 and AA2024 by the FSW. These advanced lightweight aluminum alloys are widely used in transportation industries to improve fuel economy while maintaining and improving safety and performance (Mishra et al., 2014).

Joint formulation by the FSW is considered as a complex procedure due to the interaction between the processing parameters, and the difficulty increases when the connected materials are dissimilar. The success of weld depends on the thermal conditions under which the process is carried out (Schmidt, 2010). Unlike other hot working technologies, the heat flux in the FSW is primarily generated during the process by the friction (at the interface between the welding tool and the workpieces) and the deformation process, so it is very hard to control its amount. This heat must keep the maximum temperature in the workpieces high enough to sufficiently soft the abutting materials for the pin to stir, but low enough to prevent the melting of these materials (Tang et al., 1998). Too cold welding results in a non-bonding and volumetric or void formation and too hot welding results in an excessive material flow, which lead to material expulsion such as flash formation, collapse of the nugget within the mixing stir

zone (SZ), reduction of the weld hardness, especially at the heat affected zone (HAZ) and hence degradation of the mechanical properties of the joint (Zettler et al., 2010). A successful weld with high strength and smooth surface finish could be then achieved by a careful selection of the welding parameters such as tool design, spindle speed, traverse rate and tool tilt angle. The tool should be designed to give the desired material flow and heat generation based on the workpiece materials and dimensions, welding speeds, joint configuration and user's own experiences and preferences (Mishra et al., 2015). Periodic use of the welding tool results in a permanent deformation in its profile and dimensions due to the mechanical and other types of wear, especially in the initial heating stage during the plunge and dwell periods of the process (Miles et al., 2013). This change in tool design affects the way of material mixing at the nugget zone and results in a weak and unstable joint.

The clamping force and construction can impact the weld quality and process variables. The use of improper clamping system causes in a non-uniform temperature distribution in addition to the ability of spreading or lifting of the workpieces (Richter-Trummer et al., 2012). Thermal boundary conditions that are present at the workpieces are also affect the temperature distribution and hence the strength of the joint for a given set of welding parameters. The rate of heat flux through the top, sides and bottom of workpieces mostly depends on the thermal diffusivity of backing plate and fixtures, as was pointed out in literature (Upadhyay & Reynolds, 2014). Furthermore, it was reported that the temperature are higher on the advancing side when welding similar materials (Nandan et al., 2008). Consequently, location of the welding materials in dissimilar FSW leads to severe temperature asymmetry. This asymmetry in temperature between the advancing and retreating sides could significantly affect the joint quality and mechanical properties, which mainly depends on the properties of base materials and welding parameters (Guo et al., 2014). It is hence thought necessary to understand the influence of process variables in conjunction with varying levels of the thermal conductivity of backing/clamping materials and materials position. In the previous studies, the effect of thermal boundary conditions has not received as much attention as the other process parameters, especially in case of welding dissimilar materials. Accordingly, the present work aims on providing an effective design of welding tool and backing clamping/system to produce quality joints of dissimilar aluminum alloys using the friction stir welding.

### **1.3 Objectives of the Study**

The objectives of the present work could be summarized as follows:

- i. To design a welding tool for efficient joining of dissimilar aluminum alloys by the FSW.
- ii. To identify the optimal spindle speed, traverse rate, clamping force and initial heating stage or dwell sequence for the FSW of high-strength AA7075-T6 and AA2024-T351 aluminum alloys.
- iii. To access the temperature distribution during the FSW of dissimilar aluminum alloys by developing a new design of composite backing/clamping system.
- iv. To investigate the influence of pin tool flute radius on the material flow of dissimilar aluminum alloys.

### **1.4 Scope of the Study**

This work aims to produce high quality weld of dissimilar aluminum alloys. Accordingly, the tests are experimentally conducted to identify the optimal tool design, process parameters (tool rotation speed; tool traverse rate; tool tilt angle; relative materials position; clamping force; dwell sequence) and thermal boundary conditions. In this regard, the following points are noted down to clarify the scope of the study:

- i. FSW technique is used to join the welding coupons with butt configuration.
- ii. The welding joints were prepared from dissimilar aluminum alloys of the same metal family (AA7075-T6, AA2024-T351 and AA6061-T6). The latter alloy, which is relatively inexpensive material was joined to the AA7075-T6 alloy during the identification of the optimal tool design using the design of experiment and statistical analysis in order to reduce the total cost.
- iii. Pin tool profile is considered with concave shoulder design, and all tools were made of AISI H13 steel.
- iv. The weldments are naturally aged before the mechanical and metallurgical tests without any post-weld heat treatment.

- v. The workpieces are subjected to equal vertical and lateral clamping forces.
- vi. AISI 304 stainless steel and aluminum 6061-T6 are used to fabricate the backing/clamping systems.
- vii. Temperature distributions during the welding process are measured experimentally at the mid-plane of the workpieces along the transverse centerline using high quality thermocouple wires.

## **1.5 Thesis Organization**

This thesis is arranged in a way that provides details on the facts, observations, arguments and procedures to achieve the objectives. It comprises five chapters organized as follows: Chapter 1 represents an introduction to the research work and its problem statement, main objectives and scope. A comprehensive literature survey related to the research area, which covers the state of the art on the friction stir welding of aluminum alloys is presented in Chapter 2. Recent advances in tool design, process parameters and thermal boundary conditions were reviewed and discussed. Chapter 3 deals with the research methodology. Materials characterization, joint preparation, design and fabrication of the welding tool and backing/clamping systems with the geometry and dimensions of test specimen are described. The design of experiments and metallographic analysis were also explained in this chapter. The results and discussion are presented in Chapter 4. Finally, conclusions and recommendations for future work are provided in Chapter 5.

## CHAPTER 2

### LITERATURE REVIEW

#### 2.1 Introduction

This chapter comprehends a literature survey of the friction stir processing related to the topic of research. The importance and effectiveness of this relatively new welding technique in comparison with the other traditional joining methods are addressed. The ability of this method to connect similar and dissimilar materials in different configurations are reviewed. According to the target of the study, particular emphasis is given to the recent development in the FSW of dissimilar aluminum alloys. The major factors affecting the material flow and weld strength, such as tool design, machine variables and thermal boundary conditions are reviewed and discussed in detail. The process outcomes and methods used to improve the mechanical properties of the produced joints are surveyed. The procedures used to measure and estimate the temperature distribution during the welding process are also illustrated in this chapter. Finally, the main concluding remarks are noted down to draw a future map and to give an indication and starting point of the present work.

#### 2.2 Friction Stir Welding Technology

In the late of the eighteenth century, welding started to enroll in the manufacturing technologies. Since then, different methods have been discovered and developed, such as gas and arc welding. Materials to be joined by these fusion welding processes must be locally molten together and then harden to produce the weldment. By this way, large weld area and wide heat affected zones are generated, which degrade the mechanical properties of the base material (BM) and result in hazardous defects and high distortions. These methods were then developed to reduce the undesirable effects, as in the plasma arc welding. After that, laser beam welding was invented and become one of the most

energetic joining technologies used in the modern industries nowadays. Higher quality and thicker welds could be produced by this method with a significantly small nugget and heat affected zones (Lohwasser & Chen, 2010). However, heat treatable aluminum alloys are very sensitive to the elevated temperature, which makes the traditional fusion welding techniques incompetent to produce efficient joints (A. Murphy et al., 2014). This was the main problem that led to originate non-fusion welding approaches, such as friction welding which was used in limited industrial applications. In this process, a frictional heat is generated by a relative rotational or linear motion between the compressed materials to be welded. This heat softens the workpieces at the contact region and assist to produce the weldment by increasing the applied pressure.

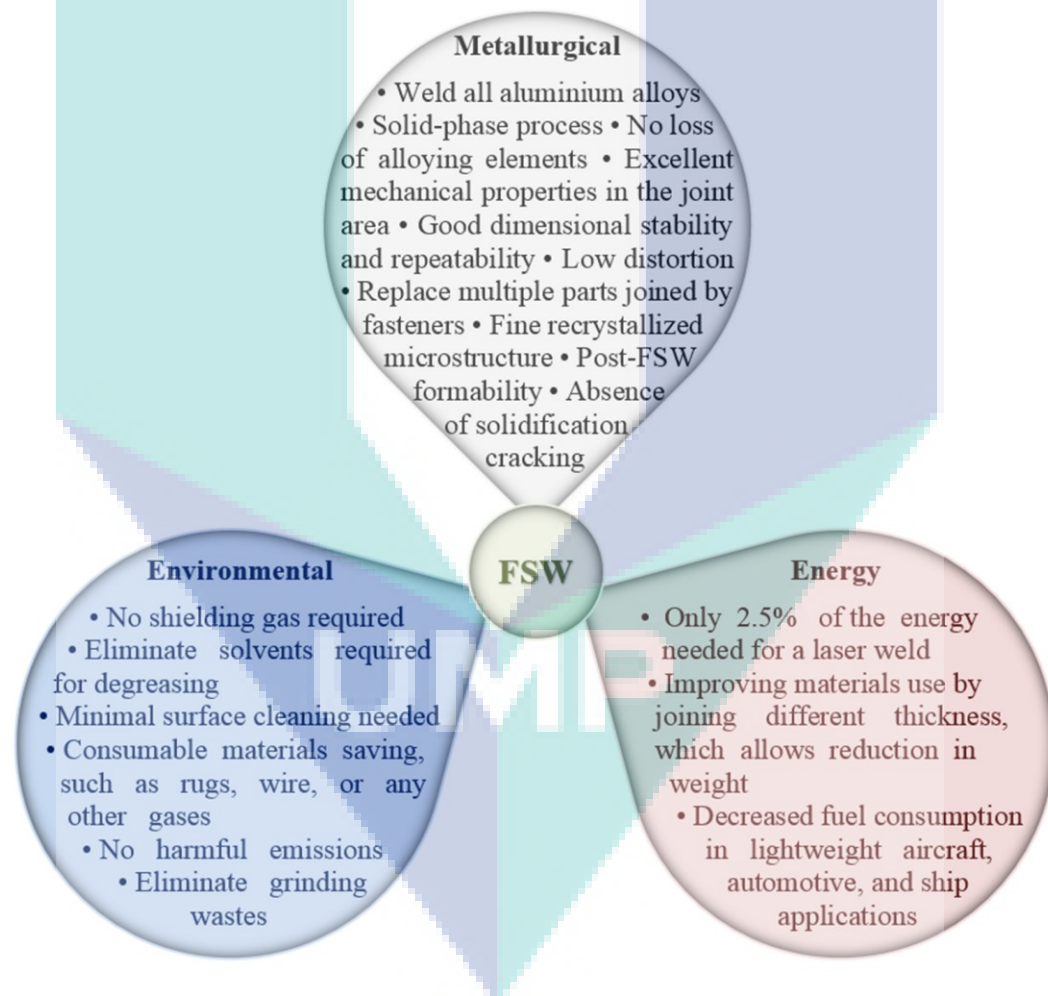


Figure 2.1 Main advantages of the friction stir welding technology

Adapted from: Kumar et al. (2015)

The principal basis of the traditional friction welding method generated a strong knowledge and create a new idea to invent the solid-state friction stir welding technique,

which represents the greatest development of metal joining nowadays. The main challenge of welding the heat treatable aluminum alloys and hard-to-weld materials has been efficiently implemented by this novel technology with distinctive metallurgical, environmental and power benefits, as illustrated in Figure 2.1. Accordingly, some of the welding methods have been replaced by this green and economic process in the modern industries (Salih et al., 2015).

### 2.3 Process Parameters

Friction stir welding is a continuous hot shear welding process. The essentials of this technology are plunging and stirring a hard tool generally consisting of a shoulder and a pin or probe into the workpieces to be welded (Ma et al., 2002; Thomas & Dolby, 2003). The workpieces are joined together through heating, material movement, and forging dominated by the welding tool. The generated heat, material flow and formation of the weld seam are mainly depending on the design of tool and machine variables.



Figure 2.2 Friction stir welding machines

Traditional milling and developed or custom-built machines were primarily used for conventional friction stir welding of butt and lap configurations. Subsequently, different CNC and robotic FSW machines have been industrialized to produce complex linear and non-linear friction stir welds (Mendes et al., 2016). Examples of dedicated and robotic FSW machines are shown in Figure 2.2. In all machine types, the welding tool is held in the spindle and the workpieces are fixed on the machine table. The specially designed tool is rotated, tilted and plunged between the abutting workpieces. After that, the weld seam is created by conducting a relative motion between the tool and base materials. In the traditional machines, the workpieces are joined by moving the machine table while the tool is stationary rotating, whereas the tool is stirring in the robotic machines and the weldments are fixed on a secure table. According to the vocabulary–ISO25239-1 standard (Threadgill, 2007) that contains the FSW terms and their definitions, the relative velocity between the tool and base materials represents the welding speed, which also known as traverse speed; the rate by which the welding tool is rotating represents the rotation or spindle speed; the angle between the normal line through the start point of welding and tool axis is named the tilt angle; and the heel penetration of the tool shoulder is called the plunge depth. These parameters denote the key variables of welding machine, which are illustrated in Figure 2.3.

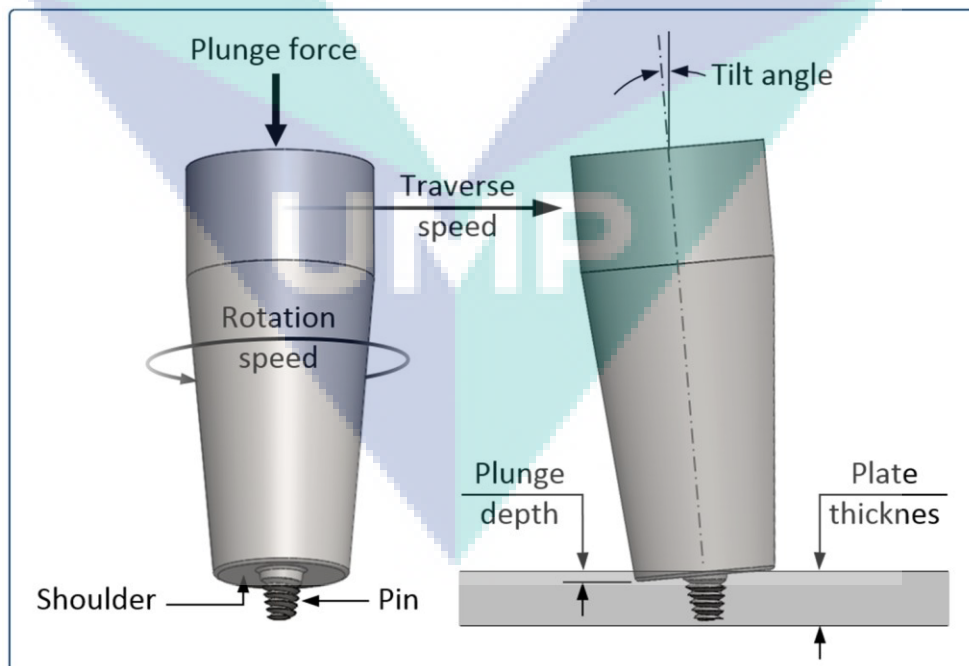


Figure 2.3 Conventional friction stir welding tool and machine variables  
Adapted from: Colligan (2010)

The friction between the rotating tool (pin at initial plunge stage and mainly shoulder during the run) and workpieces generates most of the process heat. The remaining amount of the welding heat is created during the process by the severe plastic deformation of the base materials. The base materials around the pin are softened by the localized heating and then translated from the front of the pin to the back by the tool rotation, thus filling the hole in the tool wake as the tool moves forward. The tool shoulder restricts metal from flowing out and applies forging pressure to consolidate the material right behind the moving pin.

### 2.3.1 Tool Design

Tool design is the most developmental aspect in the FSW process. It mainly focuses on the shoulder geometry, pin profile and their additional features, which influence the material flow and mixing and hence, the mechanical properties of the welding joint. Selection of tool material, geometry and features (flats, flutes, steps, and threads) depends on the welding configuration (butt or lap), type of welding (similar or dissimilar) and material and thickness of the workpiece (Salih et al., 2015).



Figure 2.4 Commonly used tool designs in the friction stir welding  
Adapted from: Mishra & Mahoney (2007)

Design of the tools used in the friction stir welding has been comprehensively reviewed in considerable research articles and review papers (Çam, 2011; Kumar et al., 2015; Mishra & Ma, 2005; Mishra & Mahoney, 2007; Nandan et al., 2008; Rai et al., 2011; Thomas, Johnson, et al., 2003; Zhang et al., 2012). Many of the advances made in

FSW have been empowered by the development of new welding tools with different profiles and added features. However, there is no accepted optimum tool design in use nowadays (Colligan, 2010), since a particular tool may produce different responses when the same set of input parameters are used on different materials or with different plate thicknesses (Blignault et al., 2011). The conventional and self-reacting or bobbin tools are the main types of FSW tools (Zappia et al., 2010). Tapered threaded probe with an odd number of equally spaced flats or flutes; concave, convex scroll and flat shoulders are commonly designs used in the fabrication of the friction stir welding tools (García-Bernal et al., 2016; Mishra & Mahoney, 2007). However, these tools are used to weld metallic materials and may not be suitable for the friction stir welding of non-metallic materials (Banjare et al., 2017; Scialpi et al., 2009). Different tool designs used in the friction stir welding are presented in Figure 2.4.

Weld quality, tool wear and cost are the most significant considerations in the selection of tool material. The selection is primarily depending on the materials and thickness of the workpieces to be welded. In dissimilar FSW, higher attention was made to the selection of tool material. As shown in Figure 2.5, tool steel, polycrystalline cubic boron nitride and tungsten-based materials are commonly used to fabricate the FSW tools Relating to the workpiece material (Kumar et al., 2015).

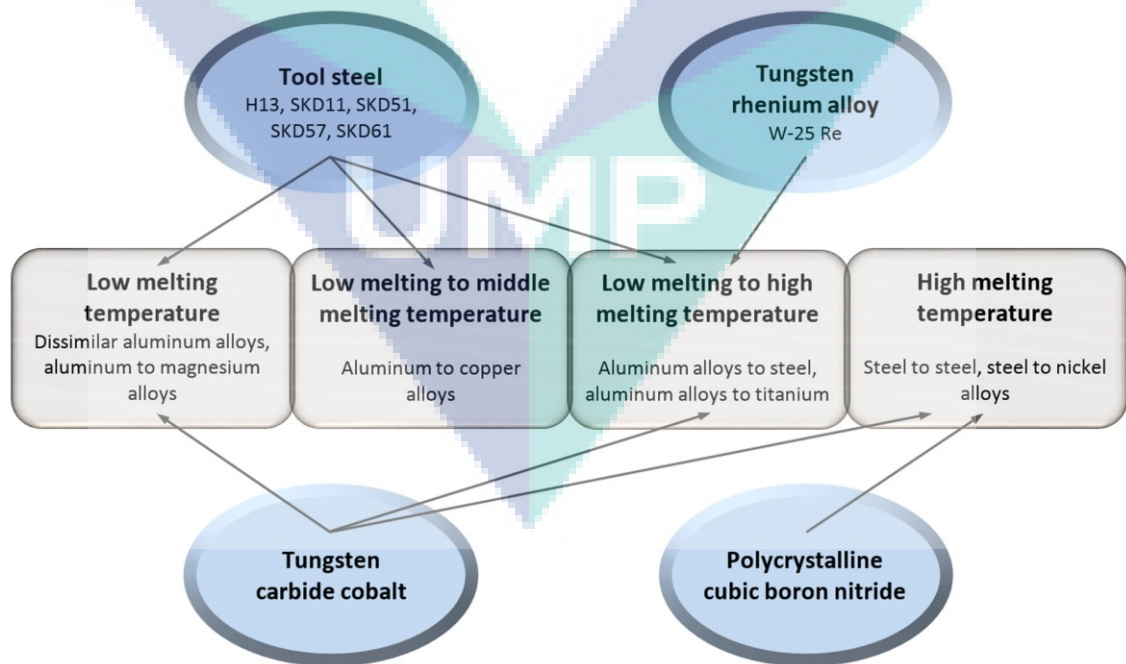


Figure 2.5 Tool materials used in dissimilar FSW

Among the types of tool steel, AISI H13 is found to be the optimal material that could be used for producing the tools used for friction stir welding of aluminum and magnesium alloys with a thickness up to 12 mm (Aliha et al., 2016; Doley & Kore, 2016; Zhao et al., 2016). This type of steel has a relatively high toughness, good machinability and wear resistance. In addition, the manufacturing cost of the tool would be relatively low compared to the polycrystalline cubic boron nitride and tungsten-based materials. Four tools were made of mild steel, stainless steel, armor steel and high speed steel materials were examined by Padmanaban and Balasubramanian (2009) to show the effect of tool material on the joint strength of AZ31B magnesium alloy friction stir weld. It has been noted that the tool material affects the tensile strength of the welding joint, since it controls the generated and dissipated heat during the welding process. The generation and dissipation of the welding heat depend on the thermal conductivity of tool's material and coefficient of friction between the tool and workpieces, which in turn depends on the hardness of the tool. It was then reported that the higher the hardness and the lower the thermal conductivity of tool material, the higher the joint strength. The authors did not address the range of tensile strength resulted from the use of these materials. However, they reported that the lowest joint strength was resulted from using the mild steel tool, which has about 30 HRC (Rockwell hardness) and low co-efficient of friction.

FSW tool of at least 48 HRC is required for joining aluminum and magnesium alloys, and this level of hardness can be found in the H13 tool steel (Mishra et al., 2015). Nevertheless, proper heat treatments are usually conducted to increase this number to about 52-60 HRC in order to improve the wear resistance of welding tool (Rai et al., 2011). Tool wear is a key issue in the FSW, since it may changes the profile and dimensions of the tool and hence, results in a weak joint (Miles et al., 2013). The physical erosion and chemical corrosion endured during the cyclic FSW processing result in a severe deformation in the main tool parts. The initial plunge phase of process is the main cause of the early wear of pin tool due to the high compressive stress and temperature endured by the probe (Park et al., 2009; Salih et al., 2015). Further wear could also be occurred in the shoulder due to the stationary dwell time prior to the main welding phase. High-strength and wear-resistant polycrystalline cubic boron nitride and tungsten based tools can be used to extend the lifetime of the probe. In addition to the fabrication cost, high ductile to brittle transition temperature of these materials results in substantial problems in the pin tool during the plunge cycle (Mishra & Mahoney, 2007).

Accordingly, auxiliary preheat and inter-pass heating of the workpieces are commonly used in the hybrid FSW techniques. These methods increase the total cost of the process and their applications are limited to certain types of materials (Bang et al., 2016). Drilling pilot hole at the weld start point is another way used to minimize the compressive stresses on the tool pin (Farias et al., 2013). In this case, sufficient dwell sequence must be allowed to compensate the heat generated by the friction between the probe and the workpieces in the normal plunge cycle. As per the available open access articles, dwell time has not been previously considered when a hole is to be created at the weld start point, especially in the FSW of aluminum alloys. There is no information about the optimal delay period that must be considered to produce stable joints.

Most of the generated heat is occurred at the interface between the tool shoulder and the workpiece. The majority of the frictional and deformational heat is produced by this part of the welding tool, especially in thin sheets and also by the bobbin tools which consist of two shoulders at the upper and bottom surfaces of the workpiece (Zhang et al., 2015). The required shoulder area is a function of the workpiece dimensions and material. For aluminum and magnesium alloys, the required shoulder area typically lies between three to five times of the workpiece thickness (Malarvizhi & Balasubramanian, 2012; Sevel & Jaiganesh, 2015; Zhang et al., 2012). Smaller shoulder diameter is needed for the FSW of steel and titanium, since the thermal conductivities of these materials are relatively low (Colligan, 2010). The shoulder produces the downward forging action necessary for the weld consolidation, and the increase of its diameter results in the upsurge of peak temperature, spindle power, and torque requirements regardless of the tool rotational speed (Mehta et al., 2011). With respect to the size of welding tool, shoulder diameter used for the FSW of similar and dissimilar aluminum alloys commonly lies between 2 and 3.3 times of the pin diameter (Mishra et al., 2015). The first and often used shoulder design is the concave shoulder, which produces quality friction stir welds (Trimble et al., 2015). This design requires  $6^\circ$  to  $10^\circ$  of concavity and  $2^\circ$  to  $4^\circ$  of tool tilt angle to maintain the material reservoir and enable the trailing edge of the shoulder tool for producing a compressive forging force on the weld. Tapered or curved convex shoulder is another design that permits larger flexibility in the contact area between the shoulder and workpiece, improves the joint mismatch tolerance, increases the ease of joining different workpiece thicknesses and improves the ability of welding complex structures. Furthermore, scoops, concentric circles, and scrolls are the features that can

be added to the shoulder surface to improve the material mixing and joint properties (Scialpi et al., 2007; Trueba Jr et al., 2015).

The pin tool is designed to disrupt the faying or contacting surfaces of the workpieces, shear material in front of the tool and move materials behind the tool. At the initial plunge stage, heating is created by the friction between the rotating pin and workpieces. A majority of the heating in thick workpieces is produced by the pin (Mishra & Mahoney, 2007). In addition, the depth of deformation and tool travel speed are governed by the pin design. Suitable pin size must be selected to resist the traverse loads and to ensure a complete consolidation of the workpiece material behind the tool before the material cools. The probe length, in general, is almost the workpiece thickness in butt welding and equal to, or slightly longer than, the upper material in lap configuration (Cao & Jahazi, 2011). The pin tools used in butt configuration were modified to produce quality lap joints. MX Triflute, Flared-Triflute, Trivex pins and skew-stir tools are examples of the frequently FSW tools used to produce lap-joints (Thomas, Staines, et al., 2003). Exhaustive studies have recently provided by a number of researchers regarding the design of pin tool (size, geometry and features) and their impacts on the output of the process.

To minimize the transverse loads and to maintain an approximately uniform stress distribution arising from torsion and the forward thrust, the tool pin is usually fabricated in tapered shape (Thomas & Dolby, 2003). Inspection of the taper angle is one of the important parameters that influence the FSW process. A fully coupled thermomechanical three-dimensional (3D) FEM analysis was performed by Buffa et al. (2006) to study the effect of pin taper angle on the FSW process. Joints of AA7075 aluminum alloy in butt configuration was simulated. It was concluded that the use of conical pin in FSW produces a helical movement in the weld zone and causes material flow down in the leading edge and flow up in the trailing edge. This increases the material circulation and leads to more uniform distribution of parameters such as strain, strain rate and temperature thorough weld thickness. The results showed that the bigger taper angle, the wider welding zones and a higher and uniform temperature distribution along the work piece thickness. It is clear from the output of this work and the research study of Querin et al. (2009) that the optimum pin taper angle is dependent on the welding and tool rotation speeds. Better quality AA2198-T4 lap-joints have been also gained by Buffa et

al. (2009) using cylindrical-conical tool. Comparison has been attained, through experimental and numerical investigations, with conical and cylindrical tools, as seen in Figure 2.6. Smooth or non-threaded pins were used in these three articles.

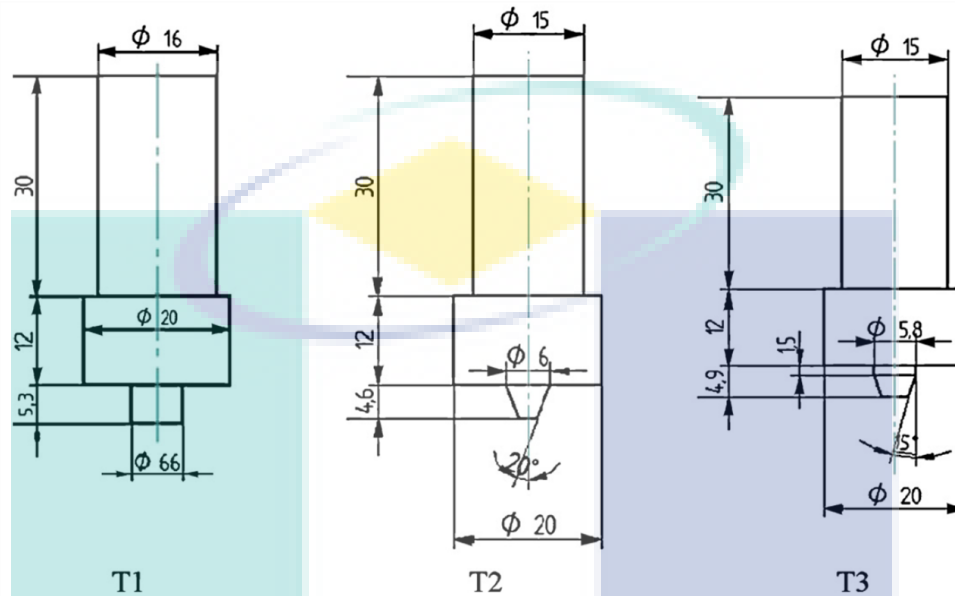


Figure 2.6 The cylindrical (T1), tapered (T2) and cylindrical-tapered (T3) pin tool profiles

Source: Buffa et al. (2009)

Zhao et al. (2006) studied the impact of tool pin design on the mechanical properties and material flow in friction stir butt welded AA2014 aluminum alloy. Asymmetrical flow of material during the welding process and significant differences in the flow patterns on the advancing and retreating sides were observed. It was reported that the use of smooth cylindrical or tapered pins results in poor material mixing and hence lower weld strength. On the contrary, defects-free welds were gained when threads were added to the conical pin, which improved the vertical material flow. Same observation is found in the works of Elangovan et al. (2008) and Ilangovan et al. (2015), when similar AA6061 and dissimilar AA6061-AA5086 aluminum alloys were friction stir welded, respectively. Other studies have also confirmed that tools with screw threads generate more heat and improve the flow of the softer material by exerting a downward force (Nandan et al., 2008). Coarse threads are usually used in a direction opposite to that of the tool rotation, in order to transport material from the shoulder down to the bottom of the pin (Mishra & Mahoney, 2007; Peel et al., 2003; Thomas & Dolby, 2003). However, threaded pins are not suitable for high-strength and temperature materials, such

as steels and Ti-alloys. In such specific FSW applications, severe wear and fracture could not be resisted by the welding tool. Same problem occurs when very thin sheets are friction stir welded due to small pin size (Threadgill, 2010). For these cases, featureless probes, conical pins with flats, stepped spiral pins, and even pinless tools have been used (Costa et al., 2015; Li et al., 2014; Tozaki et al., 2010).

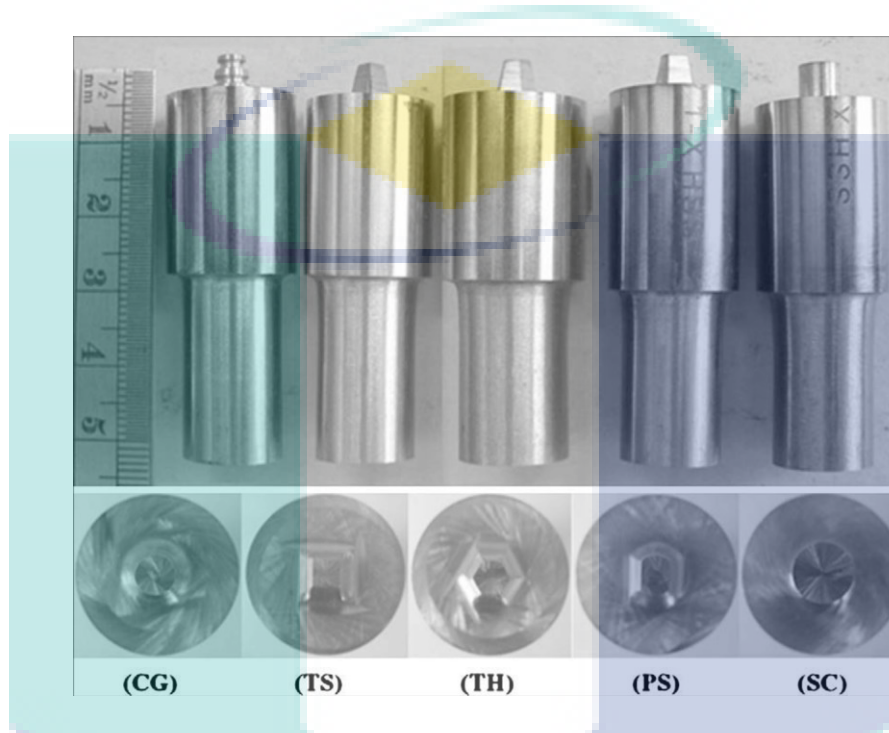


Figure 2.7 Shapes of the pin tool. (CG): tapered cylinder with grooves, (TS): Tapered square, (TH): Tapered hexagon, (PS): Paddle shape, (SC): Straight cylinder

Source: Shanmuga Sundaram & Murugan (2010)

Flat and round or chamfered edges are common pin bottom profiles used in tool design. Appropriate forging load and suitable tool parameters enable to eliminate the disadvantages of these shapes. The round ended pin was the first achieved geometry, while flattened one is the most commonly used in tool design (Zhang et al., 2012). The forge force, stress concentration and tool wear could be eliminated by using round pin with a dome radius up to 75% of the pin diameter. On the other hand, surface velocity at the bottom of the pin could be increased significantly by reducing this radius up to flat-ended pin (Mishra & Mahoney, 2007).

Pin features are much more complex compared to those of the shoulder. Adding flats to a tapered pin tool results in good material mixing and higher mechanical properties for similar and dissimilar FSW (Thomas & Dolby, 2003; Thomas et al., 2010).

Sundaram and Murugan (2010) have made dissimilar AA2024-T6 and 5083-H321 friction stir welds using tapered square, tapered hexagon, paddle shape and straight cylinder pin tools, as presented in Figure 2.7. The experiments were conducted at different machine variables. Regardless of the process variables used in this work, maximum and minimum joint strength and tensile elongation were measured using the tapered hexagon and straight cylinder probes, respectively.

Another pin tool designs were examined by Palanivel et al. (2012) in different spindle speeds. Figure 2.8 shows the straight square, straight hexagon, straight octagon, tapered square and tapered octagon, which are the pin tool profiles used by the researchers in their experimental work to weld dissimilar AA5083-H111 and AA6351-T6 aluminum alloys. Irrespective the applied rotation speeds, the straight square pin shape resulted in the highest tensile strength of the dissimilar welds.



Figure 2.8 Straight and tapered probes

Source: Palanivel et al. (2012)

Pin tool design was also studied in conjunction with the spindle rotation rate by Elangovan and Balasubramanian (2007, 2008). Five different pin tool profiles (straight cylindrical, tapered cylindrical, threaded cylindrical, triangular and square) have been used in these two works to connect 6 mm-thick AA2219 aluminum plates in butt configuration, as seen in Figure 2.9. The results showed that superior mechanical properties and defects free welds can be achieved by using the square tool pin profile. Different results were found in the paper of Padmanaban and Balasubramanian (2009) when the same five pin shapes have been used to join 6-mm-thick AZ31B magnesium alloy in butt configuration. It was reported that the joint fabricated using threaded pin tool

produced mechanically sound and metallurgically defect-free welds with higher tensile strength than the square probe.

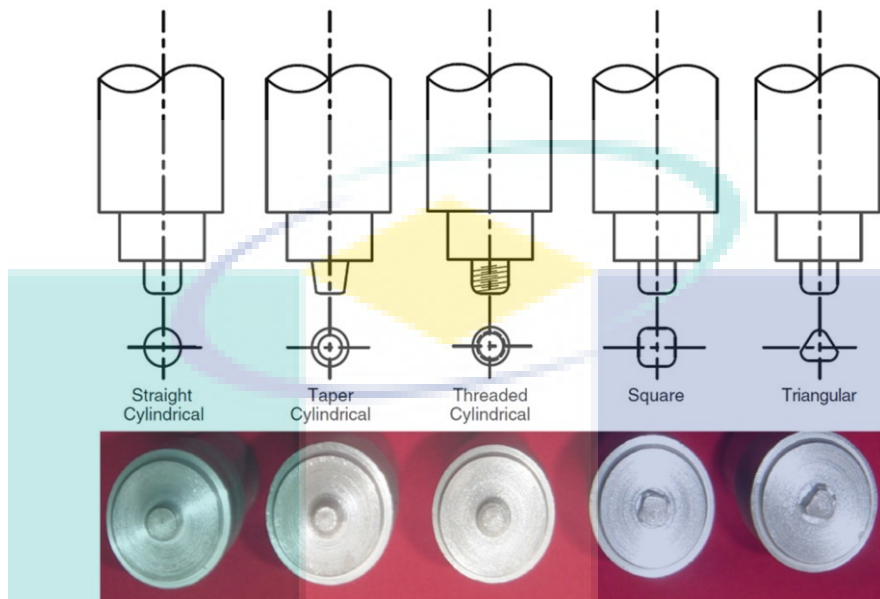


Figure 2.9 Threaded and unthreaded pin tools  
Source: Elangovan and Balasubramanian (2007, 2008)

It can be concluded then, that the optimal tool pin design is dependent on the workpiece materials. This conclusion is supported by the results of Fujii et al. (2006). They made their experiments on three aluminum alloys (AA1050-H24, AA6061-T6 and AA5083-O) using various spindle speeds and three pin tool shapes shown in Figure 2.10.

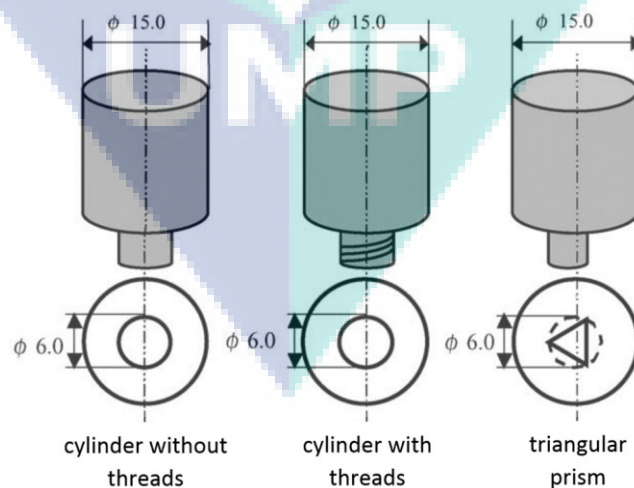


Figure 2.10 Triangular and cylindrical probes  
Source: Fujii et al. (2006)

It has been observed that the microstructure and mechanical properties of the weld is sensitive to the pin tool design and the rotation speed in different response manner for each material. The authors attributed the variation in weldability of the adjoined plates to the deformation resistance of materials, which is varied according to the selected alloys. In the conclusion, they recommended using the smooth probe to improve the mechanical properties of the weld.

Three welding tools with threaded cylindrical, triflute and unthreaded cylindrical probes, shown in Figure 2.11, were used by Krasnowski et al. (2015) to connect AA6082-T6 plates in butt configuration.



Figure 2.11 featured and featureless pin tool designs  
Source: Krasnowski et al. (2015)

It was noted that a slight increase in joint strength could be achieved by using the triflute pin tool in comparison with the threaded cylindrical probe. These two designs resulted in the highest tensile performance without any defects or imperfections, whereas a considerable degradation in weld strength occurred when the cylindrical unthreaded pin tool was used. These results are completely conflicting the outcomes of Fujii et al. (2006), whom outlined that a smooth pin tool is preferable for producing sound 6xxx aluminum alloy weld, and the probe geometry does not affect the microstructure and tensile properties of the joints made of this low resistance to deformation material.

Triflute pin tool was found by Trimble et al. (2015) to be the best choice in high speed FSW compared to the square and cylindrical probes due to its unique three flute helical ridge shape. Plastic deformation and material mixing of the workpieces could be improved using this profile at elevated welding speeds, as was attributed by the authors. This resulted in a considerable increase in joint strength, tensile elongation and nugget

hardness. The manufacturing cost of this pin tool design is relatively high due to its complex helical ridge flutes.

Reza-E-Rabby et al. (2015) studied the effect of pin features (flats/flutes) and material position related to the advancing and retreating sides of the welding tool on the FSW of dissimilar AA2050-AA6061 aluminum alloys. Threaded pin with 2.12 mm pitch thread and three flats/flutes were used. Butt welding joints were performed with three sets of rotational and welding speeds. It was observed that threaded pin with three flats produces quality welds regardless of the location of base materials on the advancing or retreating sides of the tool.

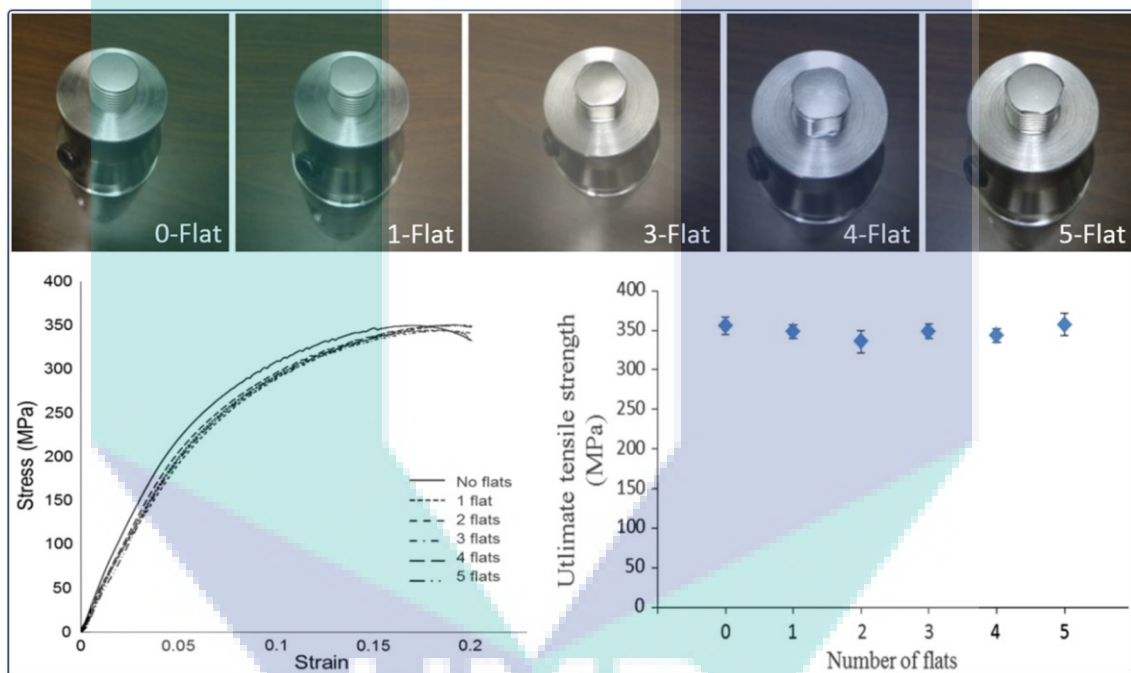


Figure 2.12 The threaded pin tools with different number of flats and their corresponding joint strengths

Source: Schneider et al. (2016)

Schneider et al. (2016) made an investigation to examine the effect of the number of probe flats on the weldability of 8.306-mm-thick of AA2219-T87 aluminum alloys. Threaded cylindrical pin tools with 0, 1, 2, 3, 4 and 5 flats were used in this study, as shown in Figure 2.12. However, the pin tool with 2-Flat was not presented in the published article. Shoulder diameter, pin diameter, pin length and thread pitch were set to 30.5 mm, 12.7 mm, 8.1 mm and 20 UNC, respectively. Flat depth was 0.98 mm for all tools except of the last one, which was set to 0.76 mm. No information regarding the

reason behind the flat depth selection was stated. Considerable difference in the weld microstructure was observed, but modest variation in the measured strength and insignificant change in the applied force and torque were noted. Moreover, adding any number of flats to the probe cylinder did not noticeably change the weld hardness compared to the base threaded pin tool without flat.

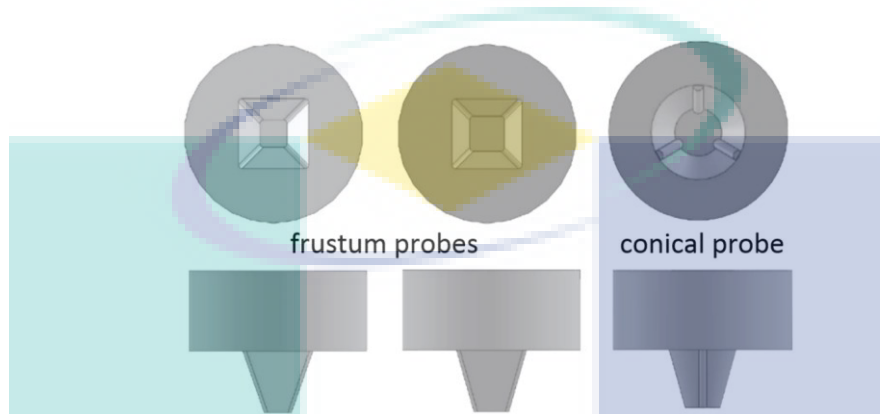


Figure 2.13 Schematic drawing of the square frustum and conical probes  
Source: Jamshidi Aval (2015)

Aval (2015) have made a comparison between two square frustum probes (tapered square) in two different taper angles and a conical probe containing three grooves, as shown in Figure 2.13. Dissimilar friction stir welded AA6082–AA7075 aluminum alloys in butt configuration were produced using the presented tools. The results showed that the conical probe tool containing three grooves produces higher temperatures than those with a square frustum probe, while the mixture of materials in the weld nugget was more uniform when the tools with square frustum probe were used. Slight change in joint strength could be noted related to the pin tool shapes used in this paper.

Bahrami et al. (2014), made a comparison between threaded tapered, triangular, square, four-flute square, and four-flute cylindrical pin tools presented in Figure 2.14 during the FSW of a 6-mm-thick AA7075-O aluminum plate in butt configuration. The authors stated that the threaded tapered pin tool resulted in the most uniform particle distribution within the mixing SZ. However, the maximum and minimum weld strength were achieved using the triangular and four-flute cylindrical probe, respectively. Unfortunately, these outputs cross the previously discussed results of Elangovan and Balasubramanian (2008) and Aval (2015).



Figure 2.14 The five pin tool designs. (a) threaded tapered, (b) triangular, (c) square, (d) four-flute square, and (e) four-flute cylindrical

Source: Bahrami et al. (2014)

Adding grooves to the pin tool was also considered in the work of Mustafa et al. (2015). Tapered probes (without groove, with right-angled groove, with left-angled groove) were used in nine tools to make T-joint AA6061-T6 aluminum alloy friction stir weldments. Various pin taper angles with different shoulder and probe diameters were tested in this optimization study. The results showed that the pin tool with right-angled groove produces the most efficient joint. The authors attributed this trend to the increase in the facility of the tool for mixing materials and reduce traverse and thrust forces during welding. This can also be attributed to the improvement of the vertical flow due to the inclined groove, which is identical to the effect of the threaded probes.

Hattingh et al. (2008) studied the effect of tool pin geometry on the ultimate strength of friction stir welded 5083-H321 aluminum alloy. Temperature, applied torque and welding forces were examined throughout the joining process. Four variations of six geometric factors were investigated in this work including flute design (number, depth and taper angle), pin diameter with its taper angle and the pitch of threads. A noticeable fluctuation in joint strength was observed among the selected set of weld conditions. Maximum joint strength was recorded when a cylindrical threaded pin tool including one and three tapered flutes were used for butt welding of 6-mm-thick plates. The tool performance was evaluated under constant tool rotation speed, traverse rate and flute radius.

A trial has been made by Lammlein et al. (2009) to investigate a welding tool consisted of a smooth conical probe without shoulder. The results showed that only (50–60%) percentage of the aluminum 6061 base material's strength could be achieved using this type of tool. On the other side, weldments produced by using tools without pin were

examined in several research studies. These trials were made due to the difficulties of fabricating pin tools to join materials of thicknesses less than 2 mm by the FSW. In addition, pinless tools enables to eliminate the keyhole that forms in the friction stir spot welding (FSSW) and after the tool withdrawal at the end of the friction stir process (Xu et al., 2016). In this regard, three tools without probes were used in the research of Zhang et al. (2011) to weld thin plate (1.6-mm-thick) of AA2024-T3 aluminum alloy. Shoulder designs contained inner concave, concentric circular and three-spiral flutes. The results showed inconsiderable effect of the shoulder profile on the grain size within the nugget zone. However, maximum joint strength was obtained by using the tool with three-spiral flutes shoulder, which enabled large displacement of material flow during the weld. In a similar way, various shoulder designs were used in four pinless tools by Ji et al. (2016) to weld 1.2-mm-thick AA6061-O aluminum alloy. Same shoulder tool profiles shown in Figure 2.15 were then used by Liu et al. (2016) to join 0.78-mm-thick alcauld 2A12-T4 aluminum alloy by the FSW. In both articles, the pinless tool with the six-grooves shoulder resulted in the highest joint strength and tensile elongation. In addition, material flow and mixing were improved by the use of this shoulder tool. This design has been also resulted in the best weld finish compared to other pinless tools.

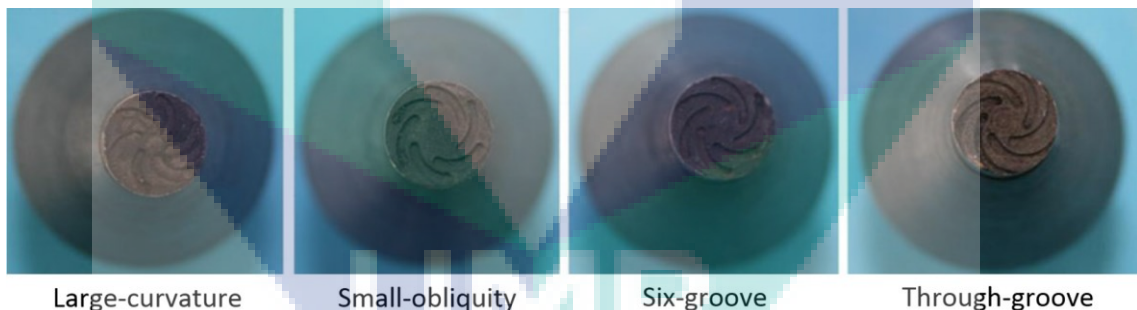


Figure 2.15 Shoulder profiles of the pinless tool design

Source: Ji et al. (2016) and Liu et al. (2016)

Forcellese et al. (2012) made a comparison between the pin and pinless tools shown in Figure 2.16. Two shoulder diameters were selected in the fabrication of the welding tools, which were used to join 1.5-mm-thick AZ31 magnesium alloy. The experiments were conducted under various rotation and traverse speeds, and the pin tools used were consisting of smooth truncated cones. It was noted that the pinless tools resulted in lower joint strength than the normal pin tools. Nonetheless, more

homogeneous microstructure was seen when the weld has been made using the tool of the pinless design.



Figure 2.16 The pin and pinless tools with different shoulder diameters  
Source: Forcellese et al. (2012)

For the conventional FSW tools, shoulder design was also considered in a few research studies. Six tools with different shoulder profiles presented in Figure 2.17 were tested in the work of Trueba Jr et al. (2015). The raised and recessed features were 0.5 mm inside and above the shoulder surface, respectively. The tools, which were consisting of smooth cylindrical probes with flat bottoms, have been manufactured from Ti-6Al-4V and used to weld 6.35-mm-thick AA6061-T6 aluminum coupons. The results showed that high-quality welds can be produced by using the raised spiral features. These complex shoulder designs required special metallic additive manufacturing methods, such as the electron beam melting that has been used in this work. In addition, high wear-resistance materials should be selected for such these geometries, which in turn increase the total fabrication cost. In contrast, the simple concave shoulder profile has been found, as mentioned previously, to be the most effective design that can be used to produce sound welds with smooth surface finish in the FSW of aluminum alloys.

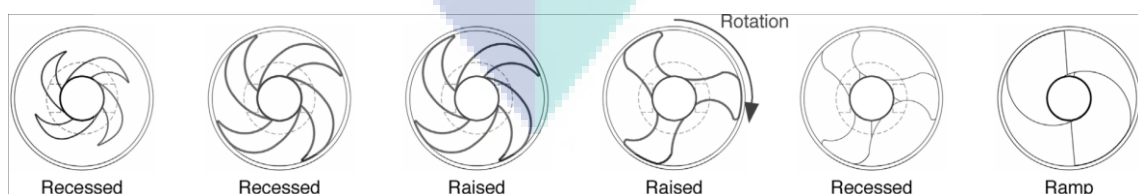


Figure 2.17 Schematic drawings of the raised, recessed and ramp shoulder designs  
Source: Trueba Jr et al. (2015)

### 2.3.2 Machine Variables

Ultimate strength is a measure of the joint quality, which is mainly dependent on machine variables. Improper selection of these effective parameters results in poor or excessive material flow and mixing within the stir zone and lead to form undesirable internal and external defects such as voids, cracks and surface imperfections or lack of fill. The amount of heat generated during the process is varied according to the rotation rate of the spindle and tool traverse speed, which are the most influencing variables. Plunge depth and tilt angle are also affecting the applied force and torque throughout the welding route. There exist no standard parameters that can be applied in the friction stir welding of aluminum alloys to obtain optimum joint strength. This fact arises from the fluctuated variables used by the researchers in the previous published works. The main reason behind that is the change in boundary conditions and properties of the welded materials. In addition, the use of different clamping system, backing materials and tool designs is also change the level of the optimized welding speeds and other process parameters.

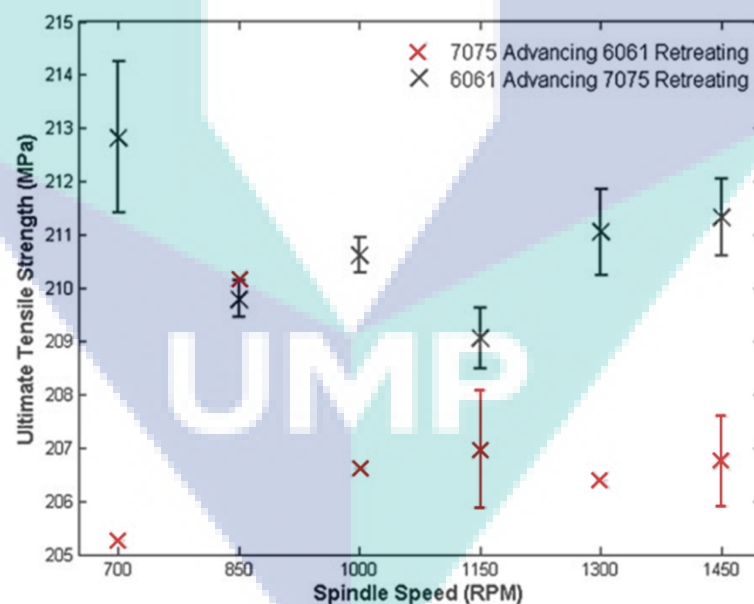


Figure 2.18 Effect of tool rotation speed and materials placement on the dissimilar AA7075-AA6061 weld

Source: Cole et al. (2013)

Several articles were found during the survey of the machine variables used previously to join aluminum 6xxx and 2xxx series to the higher strength 7xxx alloy. Cole

et al. (2013) made an investigation to find the optimal welding speeds that can be applied to join AA6061-T6 and AA7075-T6 by the FSW. Five rotation rates between 700- and 1450-rpm with a fixed traverse speed of 100 mm/min were examined in this work. Rolled sheets of 4.76-mm-thick were connected in butt configuration using mild steel backing and clamping materials. A triflat threaded pin tool of 4.7-mm-length and truncated from 7- to 5.2-mm were used. This tool was made of AISI H13 steel with a 15-mm-diameter concave shoulder of 4.4° concavity. No information about the tool tilt angle and welding direction (WD) were found. The authors mentioned that both 700- and 1450-rpm of the spindle speeds could be used to produce high quality welds, when the AA7075 base material was placed on the RS. The authors attributed this to the wide range of the processing window of the AA6061-T6 aluminum alloy. However, the presented results drawn in Figure 2.18 shows slight variation in the ultimate tensile strength (UTS) of the welded joints.

Five welds were prepared by Guo et al. (2014) to study the influence of machine variables on the dissimilar FSW of 6.3-mm-thick AA6061-T6 and AA7075-T6 aluminum alloys. The welding seam was produced normal to the rolling direction (RD) of the base materials using threaded triflat tapered pin tool of 5 mm base diameter and 15-mm-diameter shoulder. The authors did not mention anything about the backing materials and fixtures used in their experiments.

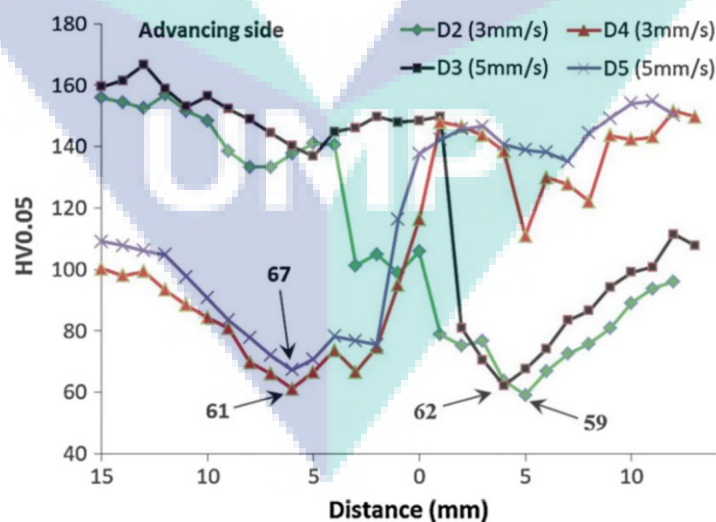


Figure 2.19 Hardness distribution of the dissimilar AA6061-AA7075 weld at different traverse speeds. Aluminium 6061 placed on the RS in D2 and D3, while it fixed on the AS in D4 and D5

Source: Guo et al. (2014)

Three welding travers speeds from 2-3 mm/sec were used at constant spindle rotation rate of 1200 rpm and 2.5° tilt angle. Temperature distribution were measured during the process normal to the weld line. Maximum weld strength was observed in this work when the softer AA6061 alloy was located on the AS and the highest travel rate of 5 mm/sec (300 mm/min) was applied. The lowest heat input was recorded at these conditions, which in turn decreased the hardness drop in the HAZ of the base materials, as shown in Figure 2.19. Fracture started at the heat affected zone of the softer alloy in all tension test specimens regardless of the base materials location. Accordingly, this area represented the weakest zone in the dissimilar friction stir welds.

Mahoney et al. (1998), in their work made on the similar FSW of AA7075 T651 aluminum alloy, clarified that the reason behind the initiation of the fracture from the HAZ in the tensile test is due to the strain concentration at this welding zone, as seen in Figure 2.20. The presented results also showed that the highest strain was concentrated in the AS, where the fracture occurred.

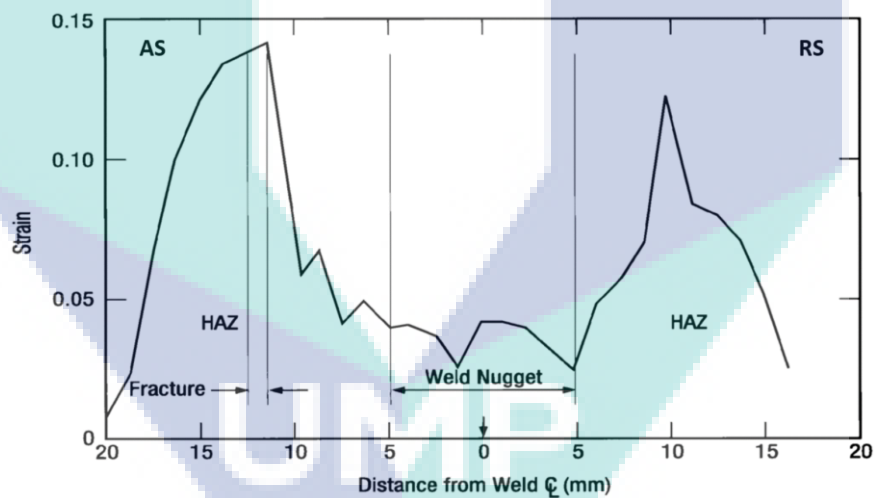


Figure 2.20 Distribution of the tensile strain of the friction stir weld

Source: Mahoney et al. (1998)

Same behavior was noticed by Prime et al. (2006) during the FSW of dissimilar 25.4-mm-thick AA7050 and AA2024 aluminum alloys. They found that the residual stresses concentrated at the heat affected zones of both welding materials along the joint thickness, as shown in Figure 2.21. The stress value was higher in the side of the softer AA2024 material, where the fracture occurred.

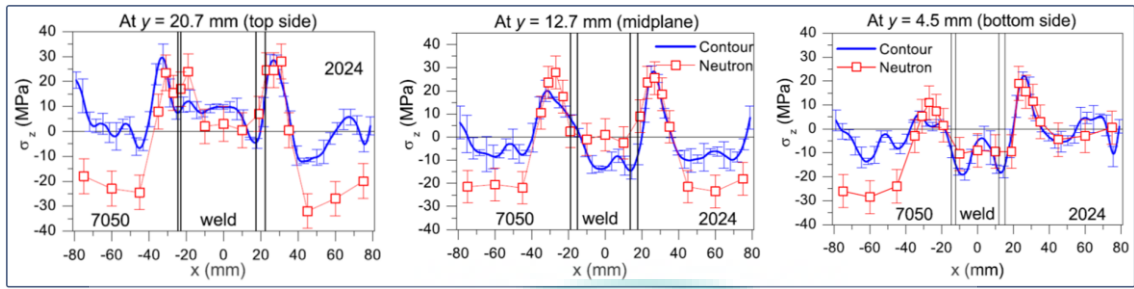


Figure 2.21 Stress distribution of the dissimilar friction stir weld

Source: Prime et al. (2006)

In the work of İpekoğlu and Çam (2014), aluminum 7075 in the O and T6 temper conditions were joined with aluminum 6061 of the identical initial temper conditions. The experiments have been conducted using vertical CNC machine, where the welding tool cannot be tilted.

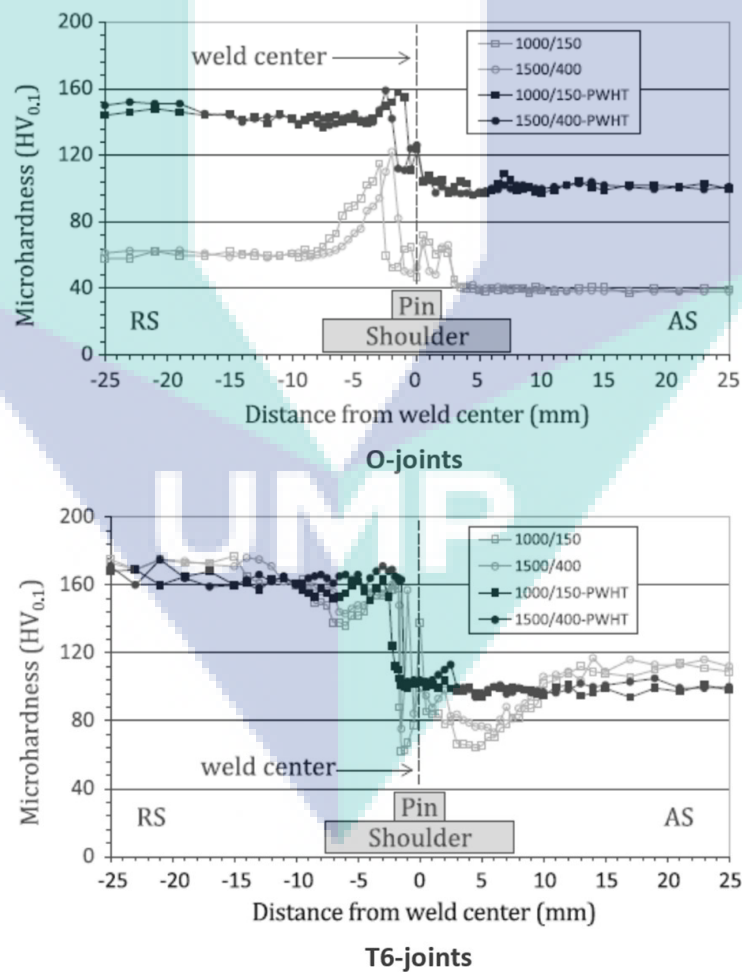


Figure 2.22 Effect of the post-weld heat treatment on the dissimilar weld hardness

Source: İpekoğlu & Çam (2014)

The workpieces of 3.17-mm-thick were clamped to the machine table by means of conventional fixtures and steel backing material, and the aluminum 6061 was placed on the AS. The welding seam was produced, in an unknown welding direction, by stirring H13 steel tool consisted of M4 threaded cylindrical pin tool with 3-mm-length and a concave shoulder of 15-mm-diameter. The probe radius and concave angle of the shoulder were not included in the text of this article. Two spindle speeds of 1000- and 1500-rpm with 150- and 400-mm/min were selected to make eight welds, which were then examined with and without post-weld heat treatment (PWHT). The results showed that the maximum tensile yield strength and elongation of the T6 joints were achieved using the 1500 rpm and 400 mm/min speeds in both as-weld and heat-treated conditions. The dissimilar joints of the O tempered alloys were not affected by the welding speeds for the as-weld tests, while the tensile strength has been increased in the heat-treated specimens. The authors stated that the weld hardness was improved in the O tempered materials, while it decreased in the post-weld heat treated joints, as shown in Figure 2.22. It is worth noting herein that the PWHT approach is alternatively used to recover some of the lost hardness in the weld zone. However, this method reduces the level of the yield strength and is used in limited industrial FSW applications according to the additional cost and time required (Williams & Steuwer, 2010).

Three levels of welding speed and tilt angle were used by Shah et al. (2014) to find the optimal machine variables that can be applied to realize sound friction stir welds of dissimilar AA7075-T6 and AA6061-T6 aluminum alloys. The welding coupons of 2-mm-thick were butt joined by using a flat shoulder of 18-mm-diameter and straight cylindrical probe of 1.7-mm-length and 6-mm-diameter in a tool made of AISI H13 steel. The AA7075 was placed on the RS using mild-steel backing plate. The tensile strength was measured in this work when the tool was rotated, traversed and tilted with 1000 rpm, 110 mm/min and 3°, respectively. Welding direction was also not clarified in this study.

Another three levels of spindle and traverse speeds were examined by Bayazid et al. (2015) with different materials placements on the advancing and retreating sides of weld. Rotation rates were selected between 800- and 1600-rpm, and the travel speed was increased from 80-160 mm/min. Dissimilar 5-mm-thick specimens of AA6063-T6 and AA7075-T6 aluminum alloys were joined in this work using a tool made of AISI H13 steel with 18- and 5-mm shoulder and probe diameters, respectively. Further description

of the tool design, tilting angle and welding direction were not presented. The results showed that maximum joint strength could be obtained by placing the AA7075 alloy on the AS and stirring the tool with 120 mm/min while it rotates through 1600 rpm.

Aluminum 6061-T6 was friction stir butt welded to aluminum 7050-T7451 by Rodriguez et al. (2015) using 270-, 340-, and 410-rpm of tool rotation rates and constant traverse speed of 114 mm/min. Welding was made normal to the 5-mm-thick plate rolling direction when the AA7050 alloy was fixed on the advancing side. Shoulder and pin of 18- and 10-mm diameters, respectively in a threaded cylindrical tool was used. Tool material, pin length, tilt angle and clamping/backing design were not explained in this paper.

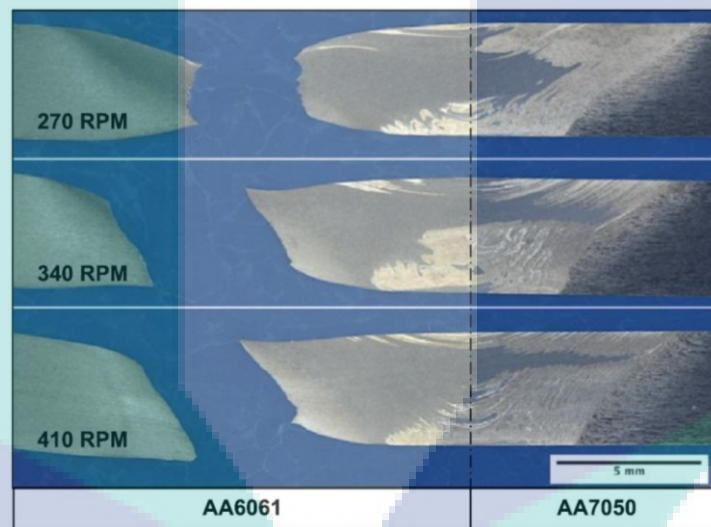


Figure 2.23 Fracture location of the dissimilar weld at various spindle speeds  
Source: Rodriguez et al. (2015)

Joint yield and ultimate strength were increased with increase of the spindle speed in which the maximum records were noted down at 410 rpm. At this speed level, fracture of the tension test specimen occurred at the HAZ of the AA6061 alloy. On the other hand, tensile elongation showed opposite behavior as the maximum percent value was measured at 270 rpm. The fracture at this lower rotation rate was arisen from the SZ, and this was attributed to the incomplete material mixing. The increase in joint yield and tensile strengths at the higher rotation speed is a reasonable effect due to the improve in material flow and mixing, as was stated by the authors and presented in Figure 2.23.

Nonetheless, the growth in weld elongation at the lower spindle speed dose not coincide with the resulted poor material mixing.

Dissimilar friction stir welds of 2-mm-thick aluminum 7075-6061 were made by Sathari et al. (2015) using a tool made of AISI H13 steel containing flat shoulder of 18-mm-diameter and cylindrical probe of 6-mm-diameter and 1.7-mm-length. The welded coupons were prepared through various material locations and spindle speeds, which ranged from 800-1400 rpm. Constant traverse speed and tilt angle of 100 mm/min and 3°, respectively were used. Further details regarding the clamping procedures and stirring direction were not expressed in the methodology of this work. The results showed that defect-free weld with the highest tensile strength has been obtained when the AA7075 alloy was fixed on the RS using 1000 rpm of tool rotation rate.

The AA6061 and AA7075 in T6 temper condition were also joined by the FSW in the work of Saravanan et al. (2016). Wide range of machine variables and tool shoulder to pin diameter ratios were investigated. Conflicting the previously discussed article, the authors declared that low feed rate of 26 mm/min was the optimal welding speed that resulted in the strongest joint at 1100 rpm. Further studies on dissimilar FSW of the 6xxx to 7xxx have been made by Shrivastava et al. (2015), Aliha et al. (2016), Daniolos et al. (2016) and others, which can be found elsewhere.

Limited number of articles are found in the literature considering the dissimilar friction stir welding of the high-resistant to deformation AA7075 and AA2024 aluminum alloys. The first trials were made by Cavaliere et al. (2005; 2006) to investigate the mechanical and microstructural response of a dissimilar AA7075-T6 and AA2024-T3 joint. Sheets of 2.5-mm-thick were friction stir welded using 700 rpm of tool rotation rate, 160 mm/min of traverse speed and 3° of tilt angle. In these two works, aluminum 7075 was fixed on the AS of the weld. A steel tool of 20-mm-diameter shoulder was used. The probe length and diameter were 6- and 2.5-mm, respectively. More details regarding the tool design and other processing steps were not cited. The optical microscopy (OM) examination showed defect-free weld, and the tensile test represented higher longitudinal strength compared to the transverse result. The AA2024 exhibited higher fatigue life than the second alloy, but with the lowest hardness level. As seen in Figure 2.24, minimum Vickers hardness number (VHN) was measured at the HAZ of the softer alloy, where the fracture has occurred in the tensile specimen. In another work, fatigue properties of 4-

mm-thick butt joints made of AA7075-T6 and AA2024-T3 plates were inspected by Cavaliere and Panella (2008) under different tool positions. This time, AA2024 alloy was located on the AS, and 1600 rpm rotation rate with 120 mm/min traverse speeds were selected. The weld seam was normal to the rolling direction of the abutting materials. Welding tool design and clamping description were not included in the experimental procedure of this work. The results disclosed that the mechanical properties of the weld were improved when the pin tool has been moved toward the softer alloy.

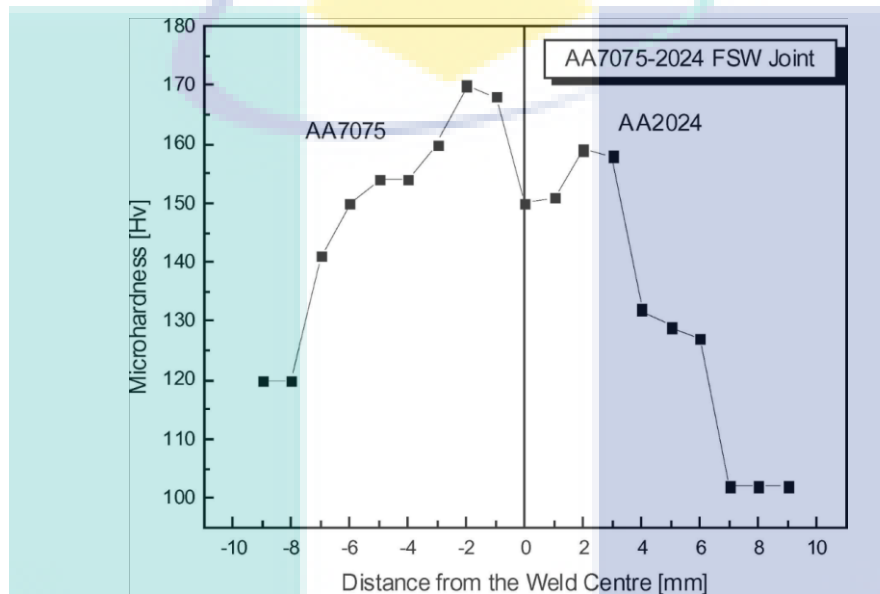


Figure 2.24 Hardness profile of the dissimilar AA7075-AA2024 joint when the harder AA7075 alloy placed on the AS

Source: Cavaliere et al. (2005; 2006)

Several welding rotation and traverse speeds were examined by Khodir and Shibayanagi (2007, 2008) in different material locations. The spindle speed was ranged between 400- and 1200 rpm and the welding traverse rate was varied from 0.7-3.3 mm/sec. It was reported that defect-free welds with maximum tensile strength could be obtained by applying 1200 rpm of rotation speed with 1.7 mm/sec (about 100 mm/min) of feed rate to join 3-mm-thick sheets of AA7075-T6 and AA2024-T3 aluminum alloys. At these conditions, aluminum 7075 was placed on the RS of the welding tool. The tool was made of SKD61 steel consisting of 4-mm-diameter threaded pin and 12-mm-diameter shoulder. Fixtures used, pin tool length and tilt angle were not found in the text of these papers. Comparable with the previously published data, minimum weld hardness level was observed at the HAZ of the softer alloy regardless of the process parameters

used, as seen in Figure 2.25. It was also reported that the fracture of the tensile specimens was initiated from the weakest zone, where the hardness dropped or the defects formed.

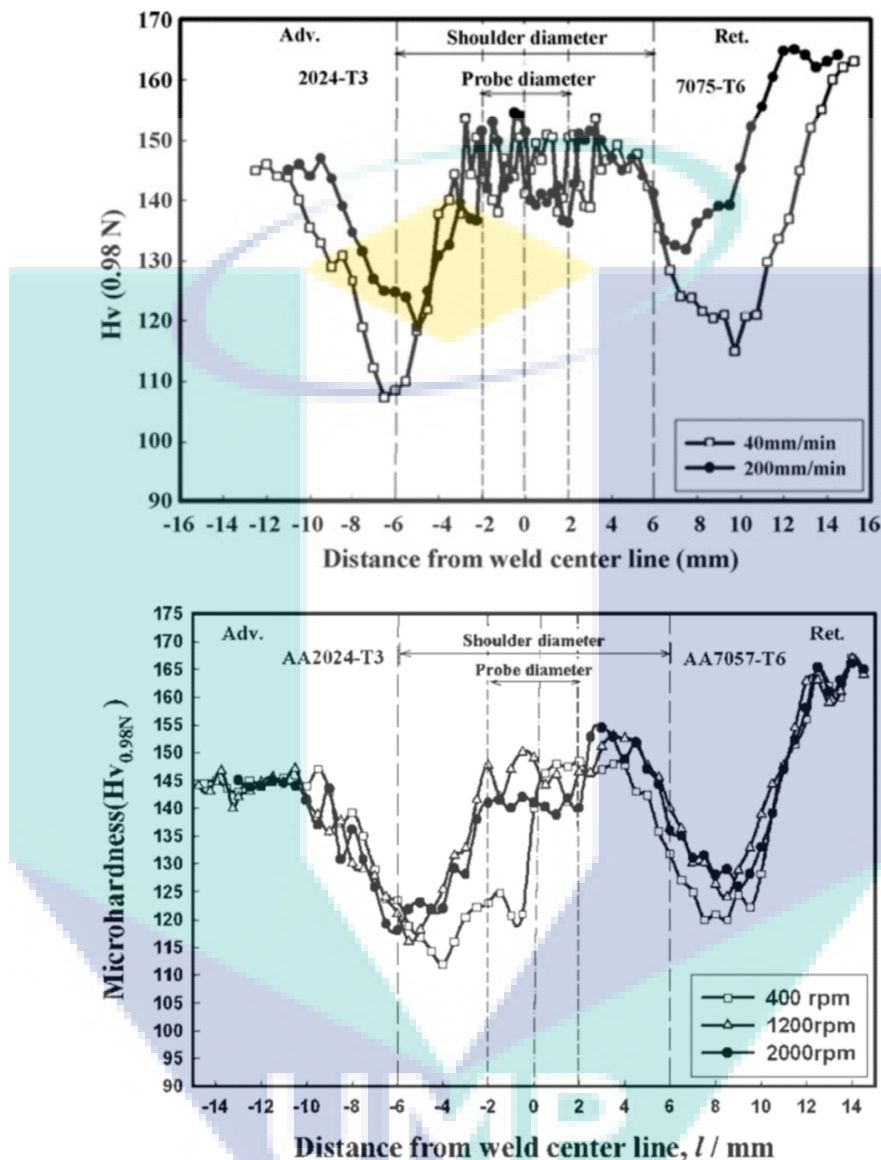


Figure 2.25 Hardness distribution of the dissimilar AA7075-AA2024 weld at various tool rotation and traverse speeds

Source: Khodir and Shibayanagi (2007, 2008)

Mechanical properties and material flow of three welded butt joints prepared from 3-mm-thick sheets of AA7075-T6 and AA2024-T3 aluminum alloys were evaluated in the work of da Silva et al. (2011). The spindle speed has been varied between 400- and 2000 rpm while keeping the other variables constant. The authors outlined that the higher joint strength resulted through using 1000 rpm of tool rotation rate and 254 mm/min of traverse speed. The AA7075 alloy was placed on the AS and the tilt angle were fixed at

3°. The tool used was fabricated with flat shoulder of 12-mm-diameter and threaded cylindrical pin tool of 4-mm-diameter and 2.85-mm-length. The macrograph and hardness distribution presented in this work for the best weld is shown in Figure 2.26.

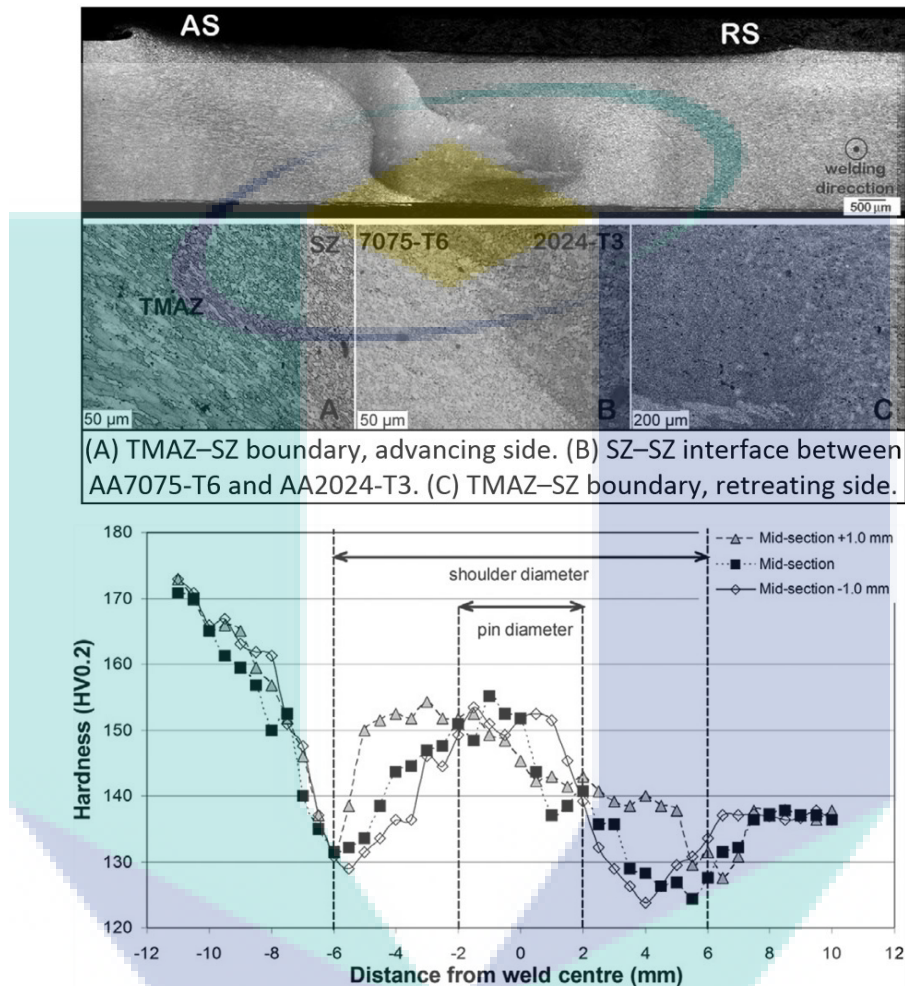


Figure 2.26 The dissimilar AA7075-AA2024 weld macrograph and hardness distribution at 1000 rpm of tool rotation rate and 254 mm/min of traverse speed

Source: da Silva et al. (2011)

The OM examination showed absence material mixing at the SZ, but the perceived weld efficiency was so high. Micro-hardness profile was drawn upper and lower the weld transverse centerline as well the mid-plane. The variation in the weld hardness throughout the joint thickness was attributed by the authors to the inadequate material mixing at the stir zone. The fracture location of the tensile specimen was also observed at the HAZ of the softer alloy, which represented the weakest region that exhibited the lowest hardness number. In contrast, low traverse speed of 12 mm/min with 1200 rpm of tool rotation rate was used by Saravanan et al. (2016) to join 5-mm-thick

plates of AA7075-T6 and AA2024-T3 aluminum alloys in the butt configuration. The AA2024 alloy was kept in this work on the AS, and the welding seam was made along the transverse direction (TD) of the base materials. The welding tool was made of high-carbon steel containing flat shoulder and straight cylindrical probe in various diameter ratios. High-strength AA7075-T6 and AA2024-T3 was also friction stir welded by other researchers in lap and butt configurations with different thickness ratios (Avinash et al., 2014; Dubourg et al., 2010; Song et al., 2014).

Table 2.1 Summary of the machine variables used previously to join aluminums 6061 and 2024 to the high-strength AA7075 alloy

Reference	Material placed on the AS	THK (mm)	$\omega$ (rpm)	$v$ (mm/min)	$\theta$ (deg.)
<b>Dissimilar FSW between AA6061 and AA7075 aluminum alloys</b>					
(Cole et al., 2013)	AA7075-T6	4.76	1450	100	---
(Guo et al., 2014)	AA6061-T6	6.3	1200	300	2.5°
(İpekoğlu & Çam, 2014)	AA6061-T6	3.17	1500	400	0°
(Shah et al., 2014)	AA6061-T6	2	1000	110	3°
(Bayazid et al., 2015)	AA7075-T6	5	1600	120	---
(Rodriguez et al., 2015)	AA7050-T7	5	410	114	---
(Sathari et al., 2015)	AA6061-T6	2	1000	100	3°
(Saravanan, Rajakumar, & Muruganandam, 2016)	---	---	1100	26	---
<b>Dissimilar FSW between AA2024 and AA7075 aluminum alloys</b>					
(Cavaliere et al., 2005; Cavaliere et al., 2006)	AA7075-T6	2.5	700	160	3°
(Khodir & Shibayanagi, 2007, 2008)	AA2024-T3	3	1200	100	---
(Cavaliere & Panella, 2008)	AA2024-T3	4	1600	120	---
(da Silva et al., 2011)	AA7075-T6	3	1000	254	3°
(Saravanan, Rajakumar, Banerjee, et al., 2016)	AA2024-T3	5	1200	12	---

(**THK**): joint thickness; ( $\omega$ ): tool rotation speed, ( $v$ ): travers speed; ( $\theta$ ) tool tilt angle

According to these literature findings, optimal welding speeds and other process variables could not be assigned due to the fluctuation in the previously applied parameters, as summarized in Table 2.1. On the other side, joining of AA2024-T351 to AA7075-T6 by the FSW has not been studied before. This advanced aircraft aluminum alloy is different from the aluminum 2024-T3 due to the unlike processing procedure. It has lower tensile and yield strength and more pronounced plasticity than the AA2024-T3 alloy (Đurđević et al., 2015; Wang et al., 2016). FSW of this developed material resulted in an average static properties of about 85 % of the base material and very high fatigue strength (Dursun & Soutis, 2014).

## 2.4 Backing Materials and Clamping Equipment

Friction stir welding is considered as a thermal-mechanical joining method, in which material mixing or plastic deformation is highly dependent on the heat flow during the process. The amount of heat generated is based upon the design of the welding tool and machine variables. Moreover, the workpieces materials and thermal boundary conditions of the backing/clamping components and welding tool govern the heat dissipation or loss. Consequently, the interaction between the process variables and thermal boundary conditions of the workpieces determine the weld strength, as illustrated in Figure 2.27.

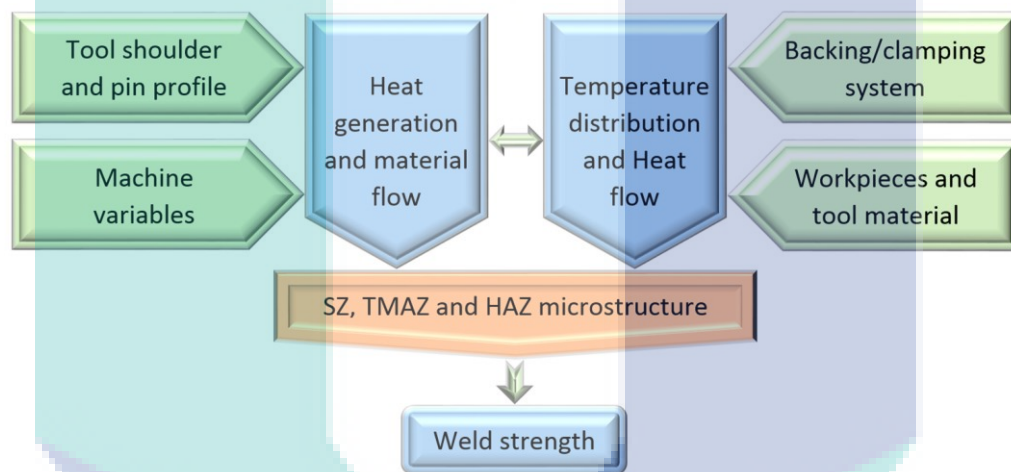


Figure 2.27 Interaction diagram between the process variables and thermal boundary conditions of the workpieces

Adapted from: Lohwasser & Chen (2009)

As the welding tool rotated, plunged and stirred between the abutting materials to be welded, the process heat is generated and the materials around the pin tool plasticized forming the weld nugget. Materials in this nugget, or the widely recognized nowadays as the stir zone, are recrystallized to form the solid-state joint with fine grains. As shown in Figure 2.28-(a), the recrystallized SZ is surrounded by a thermally-mechanically affected zone (TMAZ). Without recrystallization, the grains in this area are stretched and re-oriented due to the severe plastic deformation and material flow. The TMAZ is occasionally divided into recrystallized TMAZ or nugget and non-recrystallized TMAZ, as seen in Figure 2.28-(b). In this classification, the nugget area is considered as a part of the TMAZ, which incorporates the deformed materials (Kallee et al., 2010). The hardness

of this part of the weld is found to be lower than the adjoined materials in all similar and dissimilar friction stir welds. The maximum drop in hardness occurs in the HAZ, which is laid between the TMAZ and non-affected zone or base material. The hardness reduction in this critical zone has been attributed to the increase of the heat input, as mentioned before. In aluminum alloys, recovery of the cold work due to the elevated temperature at the HAZ results in a significant change of the base material properties.

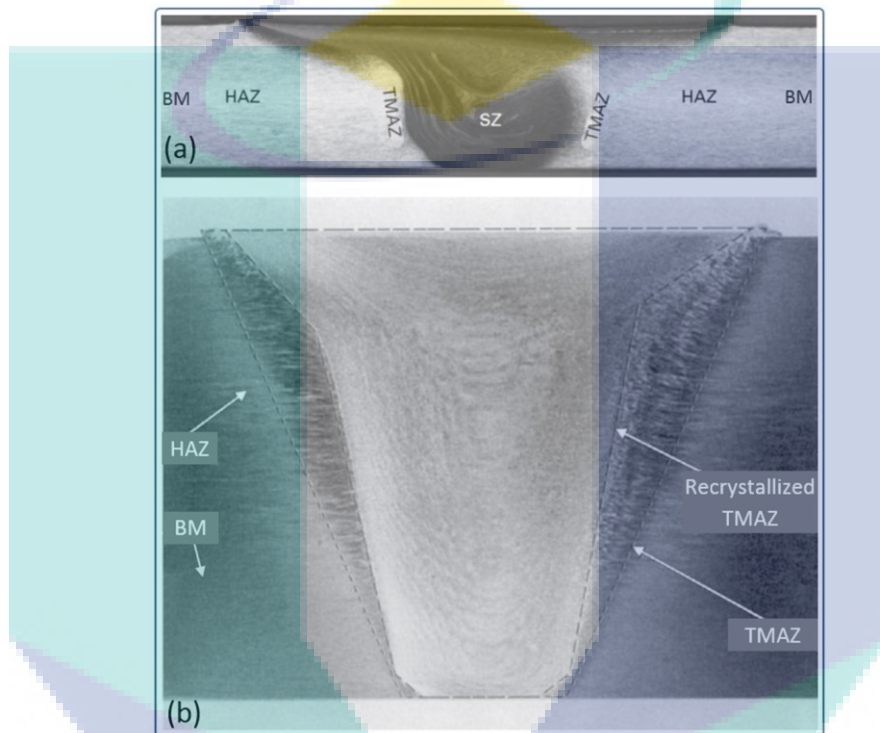


Figure 2.28 Macrographs of the friction stir weld zones

Source: (Kallee et al., 2010)

Since the process heat could not be directly controlled during the FSW, the researchers tried to reduce its amount by decreasing the tool rotation rate and/or increasing the traverse speed as one of the methodologies used for increasing the joint strength (Threadgill et al., 2009). For the reason that the temperature must be kept high enough to soften the materials around the welding pin tool to stir, this way requires inspecting the optimal welding speeds which are varied according to the joint configuration, materials type and materials dimensions (Salih et al., 2015). For this reason, there is a very limited range of spindle rotation rate and travel speeds that could be used. Cooling of the welding tool and the backing plate should offer another way of reducing the elevated temperature. Water or gas cooling and welding under water can be

effectively used for joining high-temperature materials, such as steel and titanium (Fratini et al., 2010). For aluminum alloys, ambient air is found to be enough for cooling the welding tool and anvil, while the coolant-cooling is not required for such low-temperature materials (Mishra & Mahoney, 2007). The use of a proper and effective tool design with additional shoulder and pin features is an active way to improve the material flow with minimum energy input throughout the plunging and stirring sequences (Rai et al., 2011). In the FSW of dissimilar materials, tool offset is another method used to decrease the process temperature and hence increase the mechanical properties of the welding joint (Cavaliere & Panella, 2008). Controlling the tool position between the abutting materials has to be conducted by selecting an appropriate position of the workpieces on the advancing and retreating sides of weld (Cole et al., 2013). It was reported that the temperatures are higher on the AS when similar materials are welded (Abbasi et al., 2015; Casavola et al., 2015; Nandan et al., 2008). This asymmetry in temperature distribution might be increased in dissimilar FSW and affect the quality of the joint (Guo et al., 2014). Zettler et al. (2006) noticed that in case of dissimilar friction stir welding, the alloy with the lower resistance to deformation always produces the higher processing temperature regardless of the relative materials location on the advancing and retreating sides of the weld. They stated that one of the reasons for higher process temperatures in what can be termed the softer low solute content alloys can be seen to be related to an increasing deformation volume, i.e. stir zone. Hence an increased stir zone gives rise to an increased potential for adiabatic shear and heat generation to occur. Subsequently, it can be assumed for such alloys that viscous heat dissipation dominates over the friction induced heating. On the other side, thermal boundary conditions present at the workpieces are also affecting the temperature distribution and hence the strength of the joint for a given set of welding parameters. The rates of heat flux through the top, sides and bottom of the workpieces mostly depend on the thermal diffusivity of the backing plate and fixtures (Zappia et al., 2010). Some of the frictional and deformational or adiabatic shear process heating in the FSW is transferred through the base materials to the atmosphere, tool, and the backing/clamping parts by conduction, convection and radiation, as schematically presented in Figure 2.29. Consequently, the total thermal energy (Q) could be presented in the following equation:

$$Q_{\text{total}} = Q_{\text{SZ}} + Q_{\text{tool}} + Q_{\text{BM}} + Q_{\text{air}} + Q_{\text{backing plate}} + Q_{\text{clamps}} \quad (2.1)$$

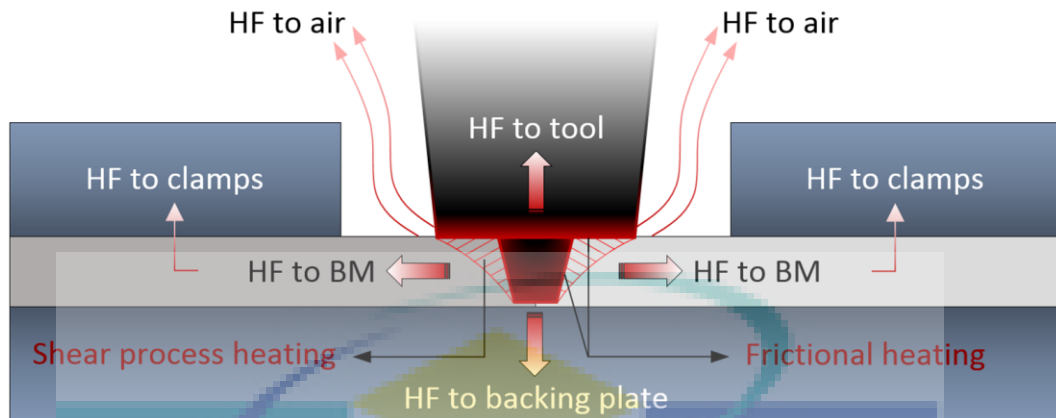


Figure 2.29 Schematic drawing of the heat flow (HF) during the FSW process  
Adapted from: Zettler (2010)

The heat transferred to the atmosphere represents the lowest amount of the lost energy. Chao et al. (2003) studied the heat transfer during the friction stir butt welding of 8.1-mm-thick AA2195-T8 aluminum alloy. Experimental and numerical modeling were conducted using 2.36- and 3.32-mm/sec (about 140- and 200-mm/min) of traverse speed with a fixed rate of spindle rotation of 240 rpm. The research considered the heat loss to the welding tool, which was made of M2 steel with shoulder and probe diameters of 25.4- and 10-mm, respectively. The heat flow to the backing anvil and clamps were not included in this work, and the heat lost by radiation was neglected. The results showed that only 5% of the process heat was transferred to the welding tool.

Future research will continue to advance the science of FSW and deepen the understanding of the complex physical interactions, which underlie a process that emerged first as a technology. One area of much interest recently is thermal management, which is being attempted with both thermal boundary condition modification and closed-loop temperature control (Gibson et al., 2014). With the objective of creating very high strength welds, researchers just started to investigate the effect of thermal properties of the backing/clamping system on the friction stir process outcomes. Limited number of studies was found in this regard, and the base materials joined in all of these researches were aluminum alloys. Khodir et al. (2006) investigated the effect of backing material and cover plate on the hardness distribution during the friction stir butt welding of 3-mm-thick AA2024 aluminum alloy. Three systems of backing and cover materials were used in this work, as shown in the schematic drawings of Figure 2.30.

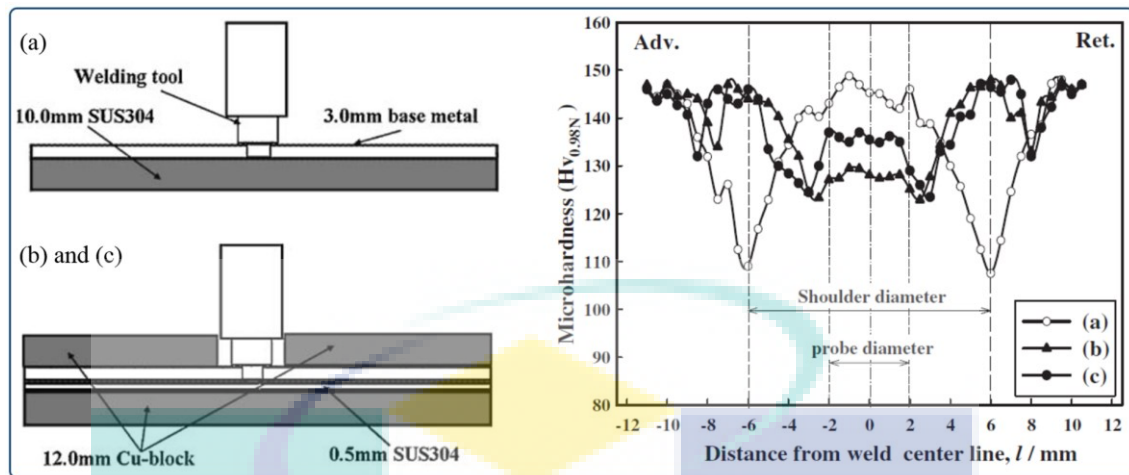


Figure 2.30 Schematic drawings of the backing/cover systems and the resulted hardness profiles at 100 mm/min traverse speed. (a) denotes System 1, (b) represents Systems 2 (without the steel sheet) and (c) Systems 3 (with 0.5 mm steel sheet below the base material)

Source: Khodir et al. (2006)

In system (a), the workpiece was fixed on 10-mm-thick steel backing plate without cover material. System (b) consisted of 12-mm-thick copper backing and cover plates, while the third system or system (c) was a combination of steel-copper materials, which was identical to system (b) but with 0.5-mm-thick steel sheet. The authors mentioned that the cover plate was used to extract more amount of frictional heat throughout the joining process. The welding tool was fabricated from SKD61-steel with threaded pin. Diameter of the shoulder and pin tool were 12- and 4-mm, respectively. Two welding speeds of 50- and 100-mm/min and fixed tool rotation and tilt angle of 1250 rpm and  $3^\circ$ , respectively were used to prepare the weldments. Defect-free welds were observed for all backing/cover systems. The hardness profiles presented in the previous figure showed a growth in the VHN at the SZ using system (a) with a noticeable drop at the HAZ. This was attributed to the highest temperature measured in this case. On the other hand, the lowest hardness level was observed in the nugget area by using the copper backing and cover plate of system (b). The higher thermal conductivity of the copper material resulted in the maximum dissipation of the thermal energy. This heat lost decreased the SZ temperature, but minimized the drop in the HAZ compared to the first system. System (c) resulted in a medium SZ hardness level and the apex joint strength. These behaviors were identical in both of the selected welding speeds. The outputs of this work indicated that the hardness of the nugget increased when the heat loss decreased,

while the drop of hardness in the HAZ could be minimized by improving the heat sink regardless of the weld traverse speed.

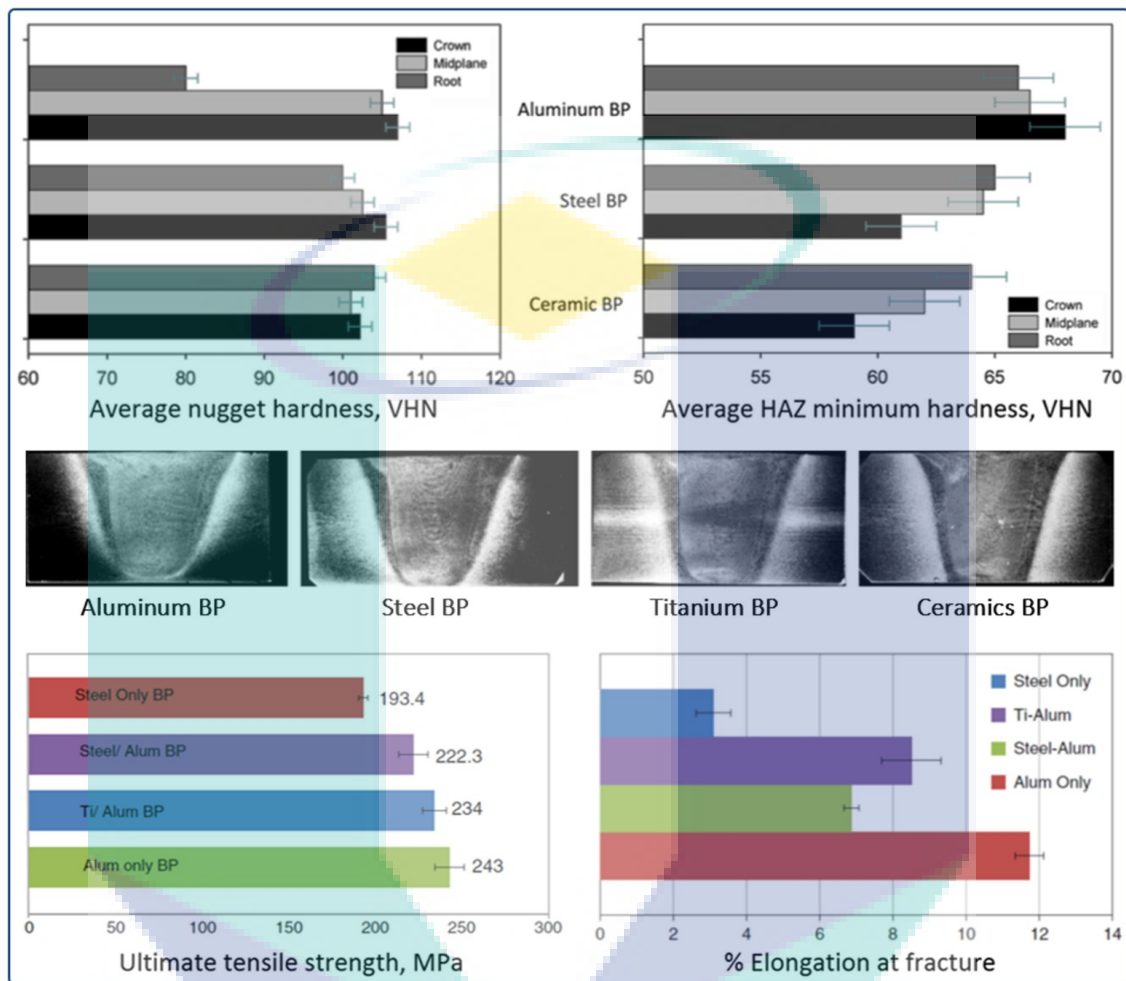


Figure 2.31 The transverse macrographs, and the hardness, strength and elongation of the weld at different materials of backing plate (BP)

Source: Upadhyay & Reynolds (2014)

Upadhyay and Reynolds (2012) reported that the peak process temperature can be controlled by changing the backing plate material without any variation in the spindle and travel speeds. Aluminum, ceramic, steel, and titanium backing plates were used to join 4.2-mm-thick AA6056-T451 aluminum alloy in butt configuration. The authors in another work (Upadhyay & Reynolds, 2014) used the same backing materials to weld 25.4-mm-thick of AA6061-T4 aluminum alloy. Thickness of the backing plates was 25 mm, and joints were also produced using composite backing materials of aluminum and steel or titanium. A threaded pin tool made of MP159 was used with a single scrolled AISI H13 steel shoulder. Diameters of the probe and shoulder were 19 mm (at the base)

and 35 mm, respectively. The pin tool length was tapered with  $8^\circ$  along its length of 25.2 mm containing three flats. The welds were prepared using 480 rpm tool rotation and 6.8 mm/sec traverse speeds without remarking the tool tilt angle. The probe temperature was measured at the mid-plane and near the backing plate. There was no significant gap in the peak temperature at the mid-plane, while about  $45^\circ\text{C}$  was the difference between the aluminum and ceramic backing materials. Figure 2.31 shows the weld macrographs and results of the joint hardness, strength and elongation presented in this paper. The nugget size and profile were alike for all backing materials. The VHN was measured transversely at the crown (below the shoulder), mid-plane, and the root (above the backing plate). Compared to the results of Khodir et al. (2006), same behavior was noticed at the HAZ but contrary records were observed at the SZ. The hardness decreased at the HAZ, and the minimum levels were measured when the lower thermal conductivity ceramic backing material was used. This action was also detected at the nugget area, in which the average hardness numbers were presented. The graphs of the tensile strength and elongation indicated that the aluminum and composite backing systems resulted in stronger joints with respect to the traditional steel plate.

The influence of backing material diffusivity on the mechanical properties and material mixing of the friction stir welds was also considered in the work of Zhang et al. (2013). The welding seam was made parallel to the rolling direction of 3.175-mm-thick aluminum 2024-T3 plates. The workpieces were fixed on wider backing blocks of copper, steel and granite with a fixed thickness of 9.4 mm. Concave shoulder of 10-mm-diameter and threaded probe were used in the welding tool, which was fabricated from unidentified material. The pin tool length and diameter were 2.9- and 3.4-mm, respectively. The spindle and traverse speeds were fixed at 600 rpm and 200 mm/min, respectively and the tool was slanted with  $2.5^\circ$ . The temperature history was recorded by a single thermocouple wire at a point located at 12 mm from the weld centerline on the AS. Figure 2.32 shows the transverse macrographs and mechanical properties of the welding joints related to the selected backing materials. Defect-free welds were resulted from using the granite and steel backing materials, while root defects were observed in the SZ of the third weldment, in which the copper backing plate was used. Generation of the defects was not discussed by the authors.

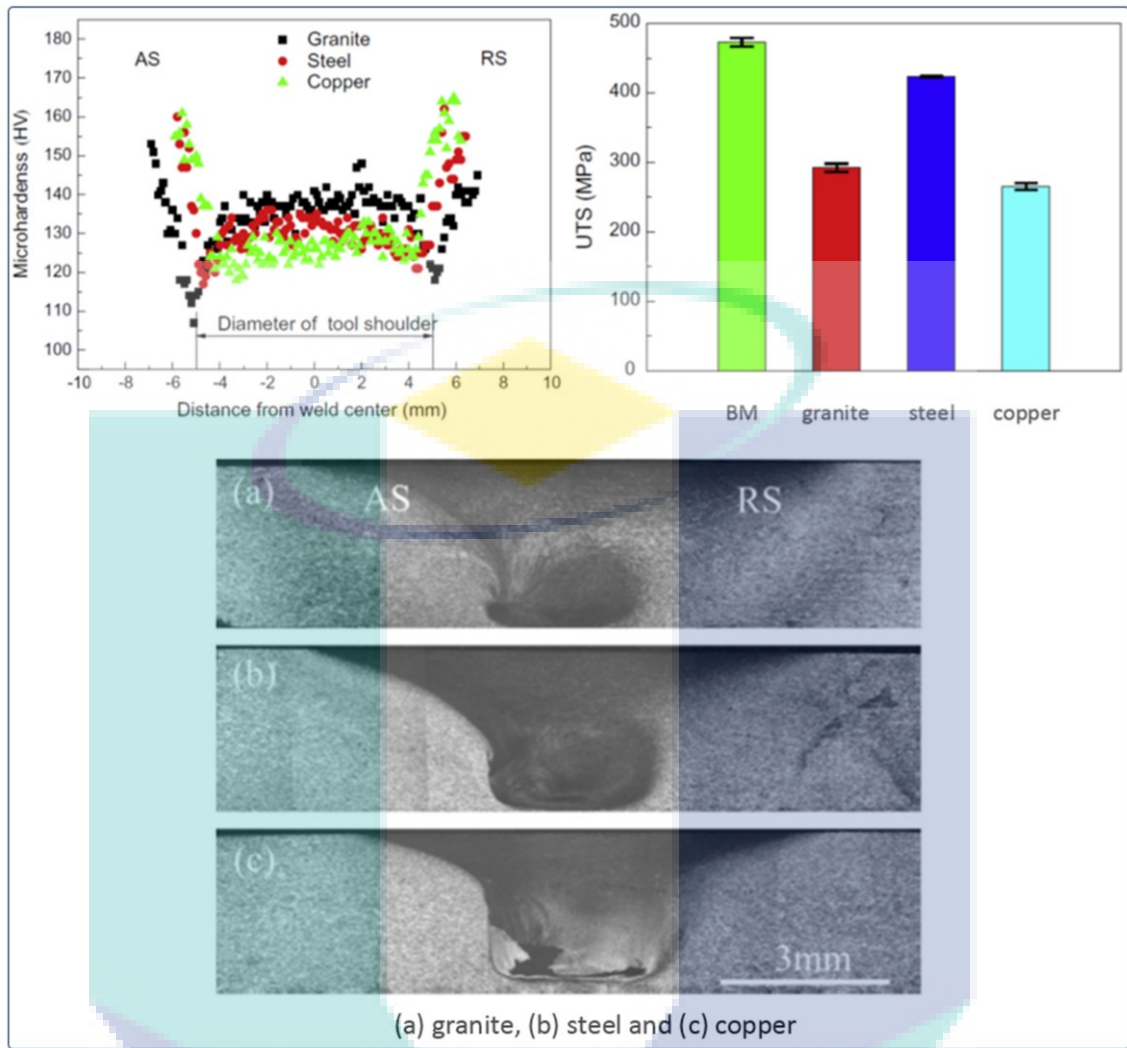


Figure 2.32 Mechanical properties and macrographs of the weld related to the selected backing materials

Source: Zhang et al. (2013)

It is worth noting herein that this type of defects commonly results from using short pin tool. The change in nugget width shown in the OM macrograph of the SZ made by using the copper backing material endorses this conclusion. Longitudinal or compressive wear might have occurred in the pin tool at the plunge stages of the welding routes, which resulted in a probe length reduction and an increase in its diameter. The higher thermal conductivity backing material resulted in the maximum and minimum reduction of hardness in the SZ and HAZ, respectively. On the other hand, using the granite backing plate, which has the lowest thermal diffusivity among the three selected materials improved the nugget hardness and resulted in a noticeably degradation in the VHN at the HAZ. The presented distributions illustrated that the maximum drop occurred

in the HAZ of the AS. This behavior indicates that the temperature was higher on the advancing side of the weld. The growth of the process temperature on the AS was also observed elsewhere (Guo et al., 2014; Mishra et al., 2015; Nandan et al., 2008); hence, there is no doubt that this asymmetry of the generated heat would be higher in the FSW of dissimilar materials. The weld hardness profile produced over the steel backing plate laid between the other two schemes. This backing system resulted in the highest joint strength, as seen in the column graph of the UTS. The weld temperature measured in this case was in between the copper and granite backing materials. It could be concluded then that the enhancement of joint strength could be gained by improving the hardness level in both SZ and HAZ, and this could be achieved through a proper control of the input thermal energy as was stated by Trimble et al. (2015). Consequently, temperature distribution during the FSW process plays an important role in the resulting properties of the welding joint.

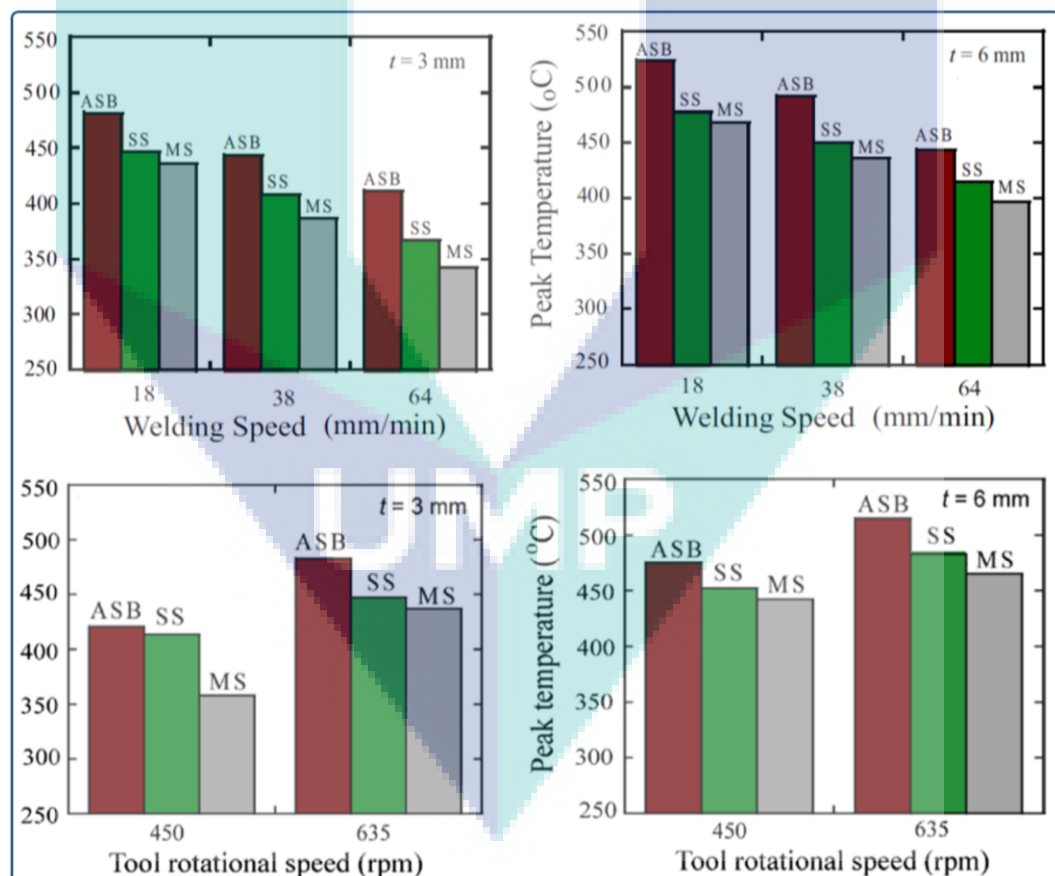


Figure 2.33 Maximum weld temperature for different backing materials: asbestos (ASB), stainless steel (SS), and mild steel (MS) at various tool rotation rate and traverse speed

Source: Imam et al. (2014)

Butt and lap joining of 3- and 6-mm-thick AA6063-T4 aluminum alloy were inspected by Imam et al. (2014) using mild steel, stainless steel and asbestos backing plate plates. Thermal conductivities of these materials were 54-, 16.2- and 2.5-W/m K, respectively. The experiments were made using two spindle speeds of 450- and 635-rpm with low rates of traverse speeds (18-64 mm/min). A tool made of SS316 steel with a 24-mm-diameter shoulder and square probe was stirred with 0° tilt angle. Dimensions of the backing plates were not found in the text of the published paper. As shown in Figure 2.33, maximum weld temperature was resulted from the use of the lowest thermal conductivity asbestos backing material, regardless of the tool rotation and travel speeds. Nevertheless, it was concluded that defect-free welds in both the butt and lap arrangements were obtained by using the asbestos backing plate. This conclusion is different from the previously stated recommendations of the other researchers. However, the temperature graphs showed that the input thermal energy has grown with the slowing of the traverse rate, rising the spindle speed and increasing the workpiece thickness.

It is clear that the previous investigations have been conducted on the FSW of similar aluminum alloys through limited ranges of welding rotation and traverse speeds. It is hence thought necessary to understand the influence of backing plate and cover materials in conjunction with varying levels of welding speeds in case of dissimilar joining. Placing the materials to be weld on the advancing and retreating sides of the tool is another factor that should be considered when dissimilar materials are friction stir welded.

In addition to the backing and cover materials, clamping system and fixtures are quite significant factors in the FSW (Papahn et al., 2015). It is important that the workpieces should not spread or lifted during the process; therefore, the welding fixtures must be designed with features enable to achieve this objective. The quality of weld depends on the manufacturing precision of the clamping system and welding table (Colligan, 2010). The impact of the design and setting of the fixtures and clamping force on the joint performance should be recognized so that the required constant quality could be ensured. Various mechanical clamping structures were used in the industry for the FSW based on the weld size, workpiece materials, joint type and the production request. The materials to be joined are conventionally fixed on the backing plates and machine table using the easy and less costly clamping claws. However, this method leads to

fluctuate the temperature distribution throughout the welding route due to the variation in the heat sinking, which could be reduced through the use of pressure bars close to the weld seam (Zappia et al., 2010). Advanced studies indicated that continuous clamping approaches could lead to a more consistent FSW quality along the weld seam (Mishra & Mahoney, 2007). Single or dual pre-loaded rollers were used to affix the workpiece on the backing plate, as seen in Figure 2.34. These compliant rollers are pressed in advance, beside or just behind the welding pin tool using special surface sensors. Alternative high-cost pneumatic, hydraulic and vacuum clamping systems and fixtures are used for specific applications and sequential production.

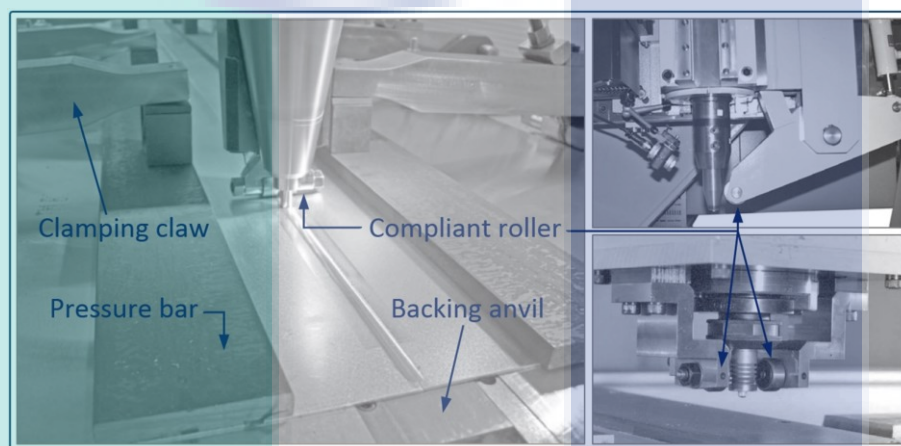


Figure 2.34 Single and dual compliant rollers with conventional clamping claws and pressure bars

Source: Kallee et al. (2010)

Essential clamping forces are required and should be supported by the fixtures during the welding period, which significantly increase the total process cost. Consequently, a key knowledge regarding the required forces would result in the chance of developing the clamping system with respect to the manufacturing cost and weld efficiency (Smith et al., 2003). Designing new optimized clamping system for a particular application necessitates crucial information regarding the actual forces required to hold the parts to be joined fittingly in place. Compressive forces through basic clamping conditions for fusion and laser welding were studied by several researchers (Liu & Zhang, 2009; Liu et al., 2009; Zain-ul-abdein et al., 2010; Zain-Ul-Abdein et al., 2008). It was observed in these investigations that an increase of the restraining forces would lead to enhance the weld quality. For the FSW, Christner and Sylva (1996) recorded that the formation of gap between specimens up to 36% of the plate thickness does not affect the

joint strength. In a comparable work, Leonard and Lockyer (2003) noted that a gap presence up to 33% of the workpiece thickness could be tolerated without the existence of weld flaws. These results conflict the fact that the oxides, impurities, voids and such weld defects are generated in the SZ if there is any creation of gaps between the workpieces (Kallee et al., 2010). This fact was supported by the outcomes of the work of Richter et al. (2012) in which the effect of clamping force on the FSW of 3.18-mm-thick plates of AA2198-T851 aluminum alloys was investigated. The experiments were conducted by applying several ranges of vertical and lateral clamping forces, which were controlled using eight vertical and horizontal load cells, as shown in Figure 2.35-(a). The welding tool was fabricated with triflats threaded probe of 4-mm-diameter and scrolled shoulder of 17-mm-diameter. Spindle rotation and traverse speeds were fixed at 600 rpm and 250 mm/min, respectively.

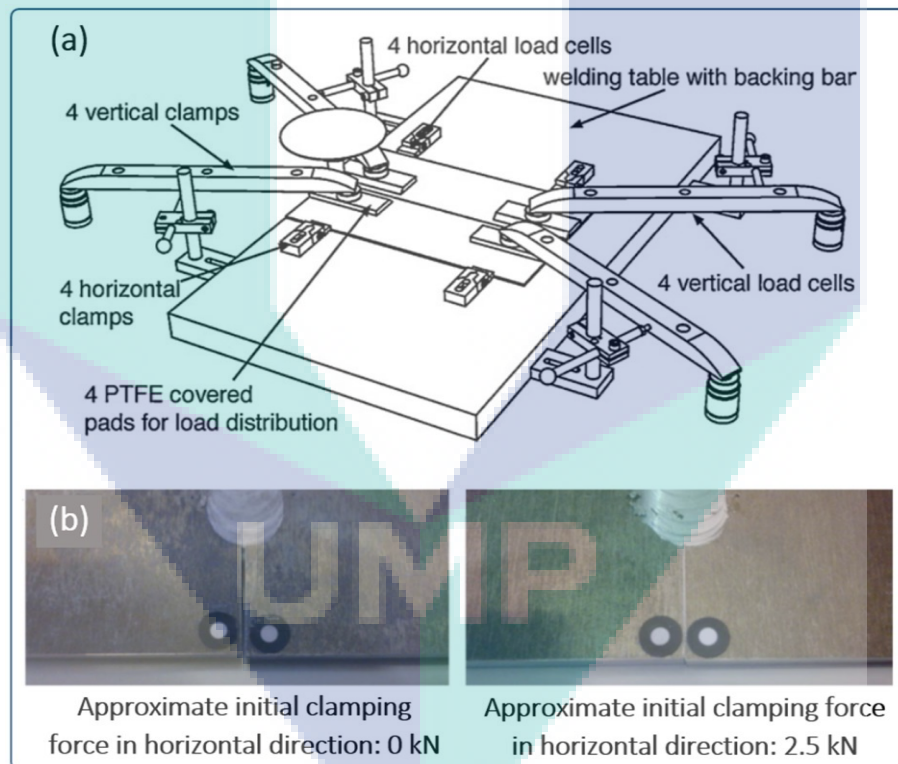


Figure 2.35 Measuring instruments of the clamping force, and the resulted gap and gap-free welds

Source: Richter-Trummer et al. (2012)

The results showed that higher joint properties with lesser distortion and more consistent distribution of the residual stresses through the thickness can be achieved by applying equal and moderate but higher clamping forces. It was demonstrated that the

possibility of defects could also be minimized by preventing any creation of gaps between the abutting plates, as shown in Figure 2.35-(b). Based on the outcomes of this work, Parida et al. (2015) developed a measuring system of the applied clamping force using strain gauges. The clamping area was also studied through a 3D finite element analysis by Farajkhah and Liu (2016). The numerical study was accomplished using the same process parameters of the work of Guo et al. (2014) but through similar FSW of 6-mm-thick AA6061-T6 aluminum alloy. The results showed that the use of wider clamping area reduces the residual stresses to about 40% in comparison with narrower areas.

## **2.5 Temperature Distribution and Measuring Procedures**

A brief description of the methods used to estimate the temperature distribution during the FSW is involved in this section, which also presents the principal consideration of the process heat throughout the joining of aluminum alloys. Weld temperature can be an indication of the amount of energy that is being created and can be used as a signal to monitor the weld quality. The heat flow in the weld zone directly correlated to the final mechanical properties of the produced joint (Guo et al., 2014). Precisely measuring the weld temperature is challenging, as it can be difficult to place probes directly at the mixing stir zone and FSW pin tool. As shown in Figure 2.36, different sensing techniques included placing a temperature probe or thermocouples spot welded inside the FSW pin tool (Iliopoulos et al., 2015; Upadhyay & Reynolds, 2014), thermocouple placement along the anvil backing plate (Chao et al., 2003; Mironov et al., 2015; Tang et al., 1998; Zappia, 2010) and infrared radiation thermometry, such as pyrometer and infrared (IR) camera (Serio et al., 2016) are used to measure the friction stir weld temperature. These techniques have their advantages and disadvantages, but all can be used to monitor the heat being imparted to the welding regions. Most evaluations of the thermal field use thermocouples, although thermal cameras and pyrometers have been used to indicate the surface temperatures around the shoulder (Mishra et al., 2015). It was stated that the existence of the thermocouples and holes used to contain them would not influence the welding temperature field, and with care, an accuracy on the order of 10 °C can be achieved (McClure et al., 1998). This accuracy can be considerably increased by using the new high-quality GG-K36 thermocouple grade wire together with the high temperature and thermal conductivity epoxy adhesive from Omega. It is well established that the peak temperature gradient along the thickness direction of the aluminum alloys

friction stir welds is not large and nearly constant through the transverse center plane of the joint (Mishra et al., 2014; Tang et al., 1998).

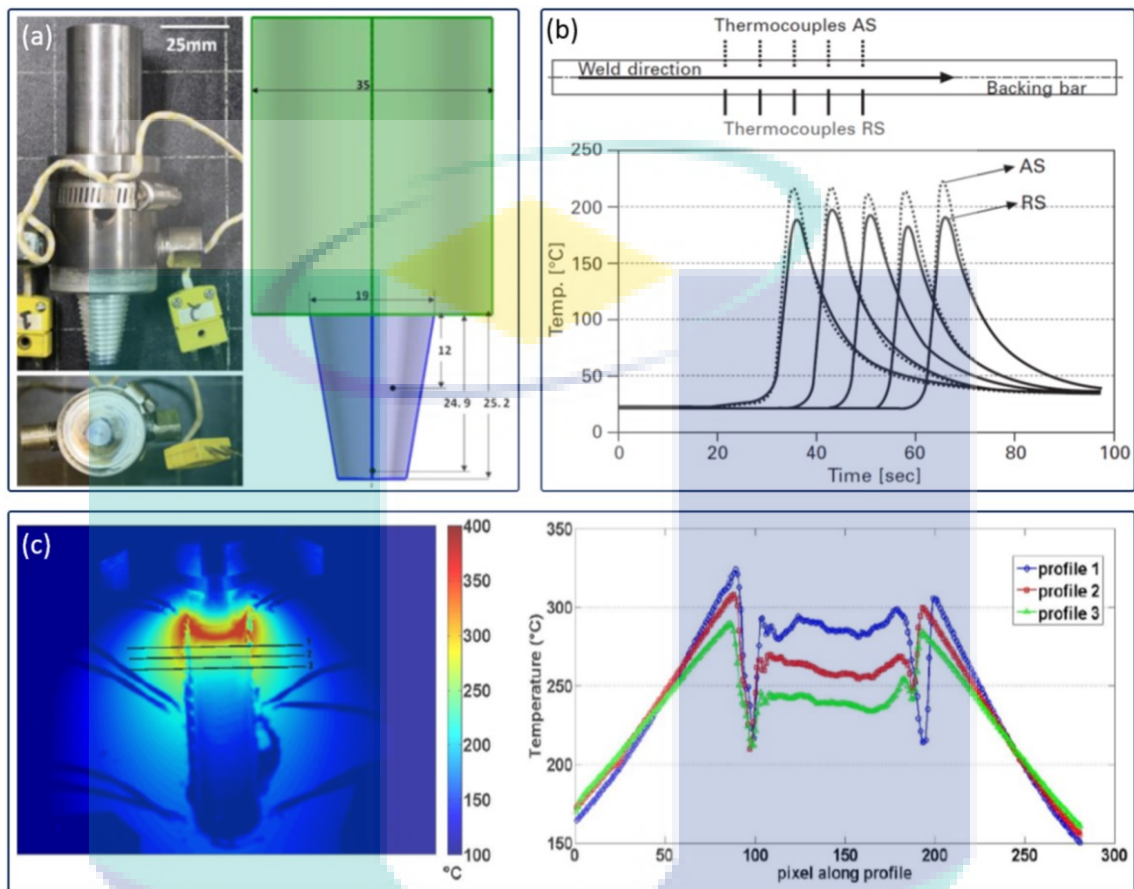


Figure 2.36 Different sensing techniques used to measure the friction stir weld temperature. (a) thermocouples spot welded inside the pin tool (the black dots indicate the locations of thermocouples). (b) thermocouple placement in the backing plate and (c) the image of IR camera with the corresponding thermal profiles

Source: Serio et al. (2016), Upadhyay & Reynolds (2014) and Zappia (2010)

Accordingly, the temperature history in the FSW of aluminum alloys is commonly measured using K-type thermocouples embedded at the mid-plate thickness for one or both sides of the weld (Kallee et al., 2010).

## 2.6 Summary

The performance of the FSW method is predominantly quantified by the tool design, machine variables and thermal boundary conditions of the coupled materials. Welding tool is the main source of the process heat and mainly depends on the shoulder and probe design. Concave shoulder is found to be an active shape for the FSW of

aluminum alloys, but the probe design is much more intricate and depends on the type of materials to be welded and joint dimensions and configurations. There was no optimal pin tool geometry as well machine variables that could be allocated for general use. Furthermore, pin tools with single flat/flute features were not extensively considered compared to other profiles. Consequently, the analysis of these geometries should continue, and the user's own experiences and preferences through a series of welding trials are required to tailor a proper pin tool design for a specific application. The longitudinal pin tool wear during the plunge and dwell sequence may reduce its effectiveness. This issue was not taken into account in the FSW of aluminum alloys.

It was stated that the fracture arises in tension test from the weakest zone, which suffers from a drop in the weld hardness or an existence of the unacceptable defects. In sound weld, the minimum hardness level was noticed in the HAZ of the advancing side in similar joining, or the HAZ of the softer material in dissimilar FSW. Improving the weld efficiency by reducing the temperature at the HAZ was usually made by controlling the applied process variables, post-weld heat treatment and cooling the workpieces. Recently, few trials were accomplished to control the weld temperature and hardness distribution by changing the backing material in similar FSW. Nevertheless, effect of backing material was not studied during the FSW of dissimilar materials in which the asymmetry in temperature distribution may affect the weld quality. In addition, there was no comprehensive fixture design previously invented considering both backing material and clamping system.

The next chapter presents the research methodology and test procedures of the present work, which was attained to produce quality weld of dissimilar aluminum alloys by the FSW through the design of welding tool and backing/clamping system.

## CHAPTER 3

### METHODOLOGY

#### 3.1 Introduction

The developed experimental setup and strategy used for producing quality friction stir welds of dissimilar aluminum alloys is presented and clarified in this chapter. Characterization of the welding base materials and workpiece preparation are described. It also presents the material, design and dimensions of the welding tools with their fabrication stages and heat treatments. The developed design of backing/clamping system and welding fixtures are explained in detail. The design of experiments, process parameters and welding procedures are clarified. Observation of the temperature distribution during the joining process is elucidated. Finally, the procedures and standards of tensile testing and metallographic analysis are outlined.

#### 3.2 Main Frame of the Study

The strategy frame of the present research methodology is presented by the flow-chart in Figure 3.1. The main stages of the work are shown with their relative key implements. The successive procedures of the experiments are logically arranged to clarify the obtained results. The work was implemented in this study by joining dissimilar aluminum alloys by the FSW using a proper design of welding tool and backing/clamping system. Figure 3.2 shows the experimental setup, and the detail description is provided in the following sections.

#### 3.3 Material Characterization

In this work, three materials were used to prepare the welding coupons, two for the construction of the backing/clamping systems and one to fabricate the welding tools.

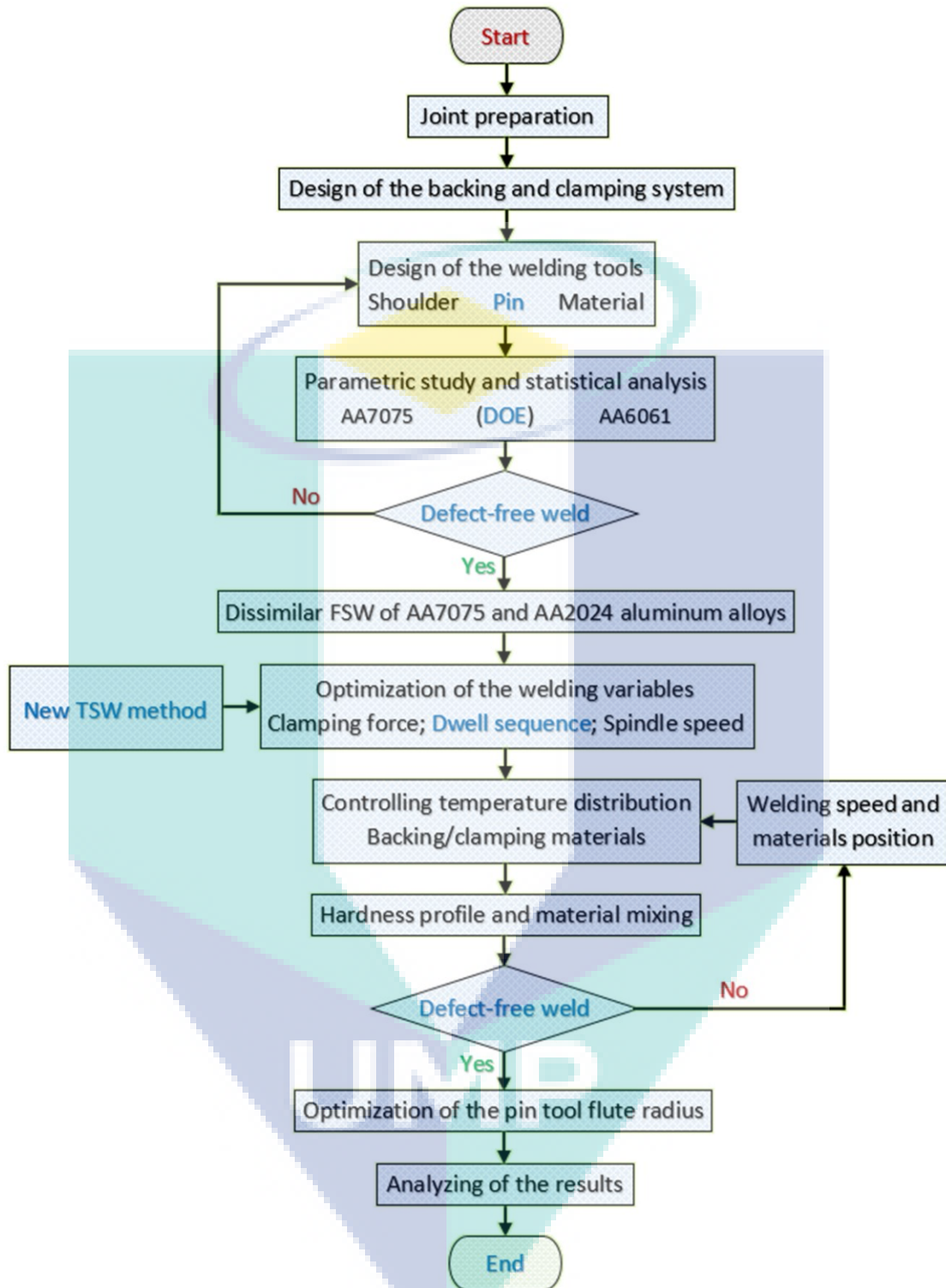


Figure 3.1 The flow-chart of research methodology

High strength and resistance to deformation AA7075-T6 and AA2024-T351 with the lower resistance and widely used AA6061-T6 aluminum alloys were selected as the welding base materials. The AA6061-T6 aluminum alloy was used in the level of the investigation of welding tool design. The standard and supplier mechanical and chemical

properties of these materials are listed in Table 3.1 and Table 3.2, respectively. The 3-mm-thick AA7075-T6 and AA6061-T6 aluminum sheets were imported from USA, while the 6-mm-thick AA7075-T6 and AA2024-T351 aluminum plates were Swiss made. The first pair of materials were used to inspect the proper pin tool profile for the FSW of dissimilar aluminum alloys. This is to clarify the effect of workpiece thickness on the applied process parameters, and reduce the effort and total experimental cost since the thicker materials of the second pair are hard to weld and relatively expensive.

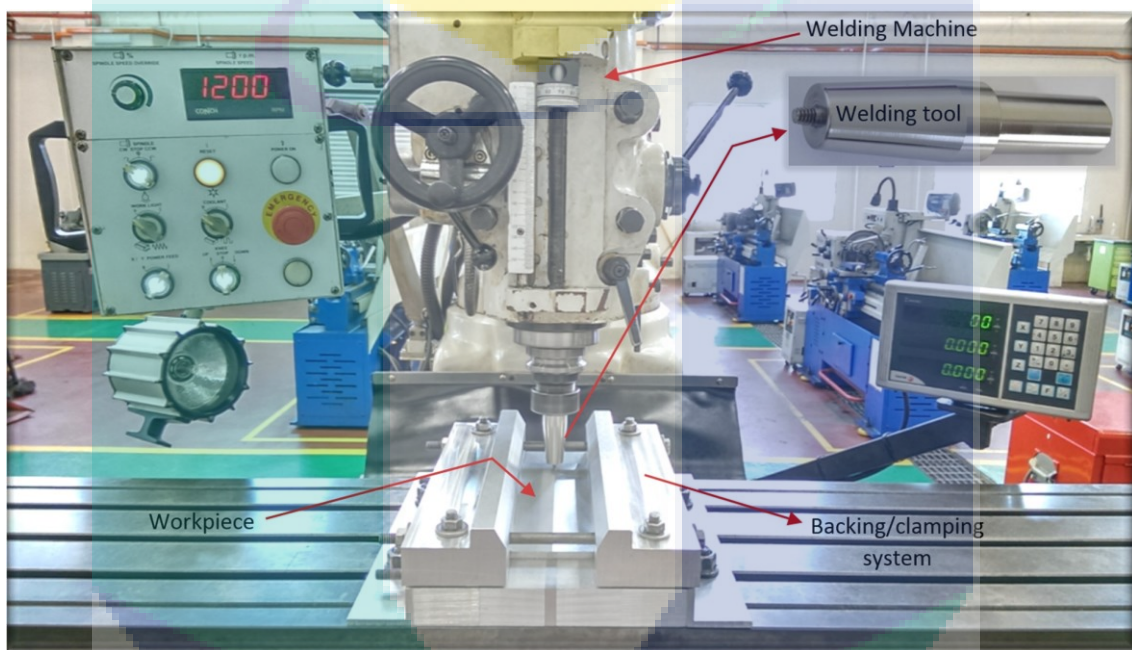


Figure 3.2 The experimental setup

Table 3.1 The standard and supplier mechanical properties of the welding base materials

Aluminum	Source	UTS	El (%)	VHN	Source
AA6061-T6	Standard	310	12	107	(Mondolfo, 2013)
	Supplier	308	12	---	
AA7075-T6	Standard	572	11	175	(Mondolfo, 2013)
	Supplier	562	12.25	---	
AA2024-T351	Standard	469	19	137	(Mondolfo, 2013)
	Supplier	444	18	---	

(UTS): ultimate tensile strength; (El): elongation at break; (VHN): Vickers hardness number.

The materials used in the clamping/backing designs are AA6061-T6 aluminum alloy and AISI 304 stainless steel. The specifications and detailed description of these materials will be explained later.

Table 3.2 The standard and supplier chemical composition (wt.%) of the welding base materials

Aluminum alloy	Source	Si	Fe	Cu	Mn	Mg	Cr	Zn	Ti	Al
AA6061-T6	Standard*	0.40-0.80	Max 0.70	0.15-0.40	Max 0.15	0.80-1.20	0.04-0.35	Max 0.25	Max 0.15	Balance
	Supplier	0.67	0.32	0.23	0.014	1.06	0.21	0.01	0.02	Balance
AA7075-T6	Standard*	Max 0.40	Max 0.50	1.20-2.00	Max 0.30	2.10-2.90	0.18-0.28	5.10-6.10	Max 0.20	Balance
	Supplier	0.04	0.12	1.30	0.02	2.40	0.19	5.80	0.07	Balance
AA2024-T351	Standard*	Max 0.50	Max 0.50	3.80-4.90	0.30-0.90	1.20-1.80	Max 0.10	Max 0.25	Max 0.15	Balance
	Supplier	0.06	0.15	4.37	0.50	1.47	0.01	0.02	0.06	Balance

\* Source: (Mondolfo, 2013).

### 3.4 Preparation of the Welding Coupons

Joining aluminum alloys without grinding and proper cleaning of the contact surfaces with the welding tool generates aluminum oxide and other impurities in the SZ (Colligan, 2010).

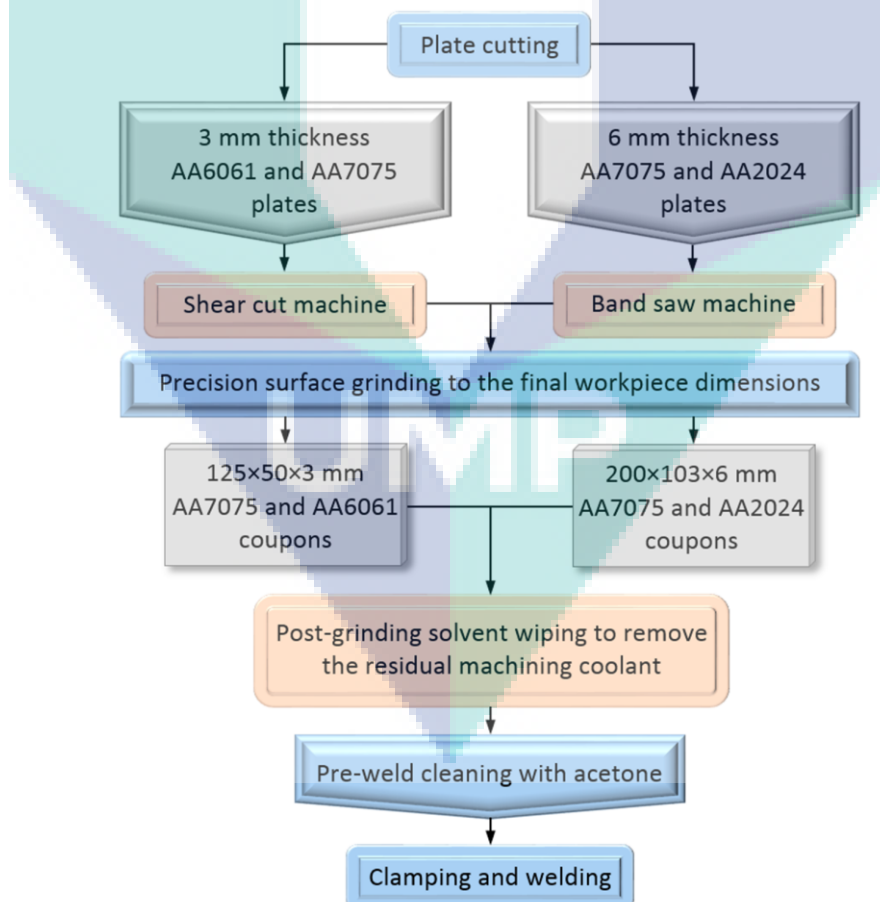


Figure 3.3 The preparation steps of the welding coupons

In addition, internal voids and such weld defects could also form within the mixing zone based on the degree of roughness of the abutting edges. Possibility of the creation of gaps between the workpieces grows in rougher edges. This in turn increases the expanse of weld imperfections and hence degrade the mechanical properties and stability of the weldments. In the FSW of rolled, extruded and heat treatable aluminum plated, careful grinding and cleaning of the stirred surfaces followed by natural aging of the weld can be effectively assisted to avoid these undesirable results. The preparation steps followed in the current work are shown in the block diagram presented in Figure 3.3. The efficient LVD MVS-C hydraulic shearing machine was used to cut the 3-mm-thick AA6061 and AA7075 aluminum rolled sheets. The thicker AA7075 and AA2024 aluminum plates of 6 mm thickness was cut by the EVERISING S-300HB fully automatic band saw machine. The cut pieces were then machined to the final dimensions of the welding coupons. The precision surface grinding machine Okamoto GRIND-X ACC65DX was used for this purpose. Smooth edges and high accurate dimensions were conducted using this automatic machine.

Dimensions of the thinner aluminum 7075 and 6061 workpieces were  $125 \times 50 \times 3$  mm, in which the width was normal to the rolling direction of the base materials in some coupons and parallel in the others, as will be explained later in Section 3.8.2. The final dimensions of the thicker AA7075 and AA2024 aluminum workpieces were  $200 \times 103 \times 6$  mm, and the plate rolling direction was always along the length. The workpiece sizes were selected to be suitable for the dimensions of the tensile test and metallographic specimens (see Section 3.9). During the grinding processing, coolant liquid is normally used to prevent the temperature rise. For that reason, the machined pieces were gently wiped with solvent to remove the residual cooling fluid. Then, the prepared coupons were enclosed with thin plastic wrap and stored on a flat table. Prior to the clamping and welding, the workpieces were properly cleaned with acetone to prevent any generation of external oxides or internal impurities during the joining process.

### **3.5 Design of the Welding Tools**

This part presents the material, geometries and dimensions of the welding tools used in this study. Fabrication stages and heat treatments are also explained in the following sections.

### 3.5.1 Geometry and Dimensions

Design of the welding tools was focused in this work on the probe geometry. The most common used concave shoulder profile, which produces quality friction stir welds was encompassed in all tools. Various pin tool designs were tested through a range of machine variables and process parameters. Based on the dimensions of the welding coupons, two groups of tools were prepared. The first set were used to investigate the optimal pin tool profile that can be used to produce high-efficient dissimilar weld. Five different probes were fabricated and tested through joining the 3-mm-thick AA7075 and AA6061 aluminum alloys. The primary dimensions of the welding tool and the five probe designs used in this stage of the study are presented in Figure 3.4-(a). The overall length of the tool was about 100 mm with 25-mm-base diameter. The blue-colored shaded part of 44-mm-length and 20-mm-diameter was used to secure the tool inside the holder. After 10 mm beyond the holder, the body of the tool was tapered along a length of 43 mm toward the 12-mm-diameter shoulder, which was concaved with  $8^\circ$ . The sharp edges were slightly chamfered, and the tip of the probe was flattened. The base diameter and length of the pin tool were fixed at 4- and 2.7-mm, respectively. As shown in the previous figure, the first probe design was the straight cylindrical probe (Figure 3.4-a-1). The other four pin tools were tapered with  $10^\circ$  toward the probe tip. Consequently, the second profile was the truncated pin tool (Figure 3.4-a-2). Parallel to the cone of the probe, single flat with a depth equal to about third of the base pin tool diameter was added in the third design (Figure 3.4-a-3). Left-hand M4 $\times$ 1 threads were formed on the truncated pin tool in the fourth design (Figure 3.4-a-4). The latter threaded probe was modified by adding single flat identical to that used in the third profile, and the resulted pin tool geometry represents the fifth design used in this level of the study (Figure 3.4-a-5). The tools were fabricated using semi-automatic lathe and milling machines. The second group of welding tools were used to join the 6-mm-thick dissimilar AA7075-T6 and AA2024-T351 aluminum alloys. The tools were provided by the Malaysian CNC machining company (Highturn Engineering SDN BHD) with concave shoulders and conical threaded probes. Figure 3.4-(b) shows a sample of the fabricated tools with the complete dimensions and tool holder. Each tool has a shoulder of 18-mm-diameter with an  $8^\circ$  of concave angle. The base diameter of the pin tool is 6 mm, and the length is 5.7 mm, which represents 97 % of the workpiece thickness. The probe was tapered with  $10^\circ$  and threaded with a left hand M6 $\times$ 1 standard threads.

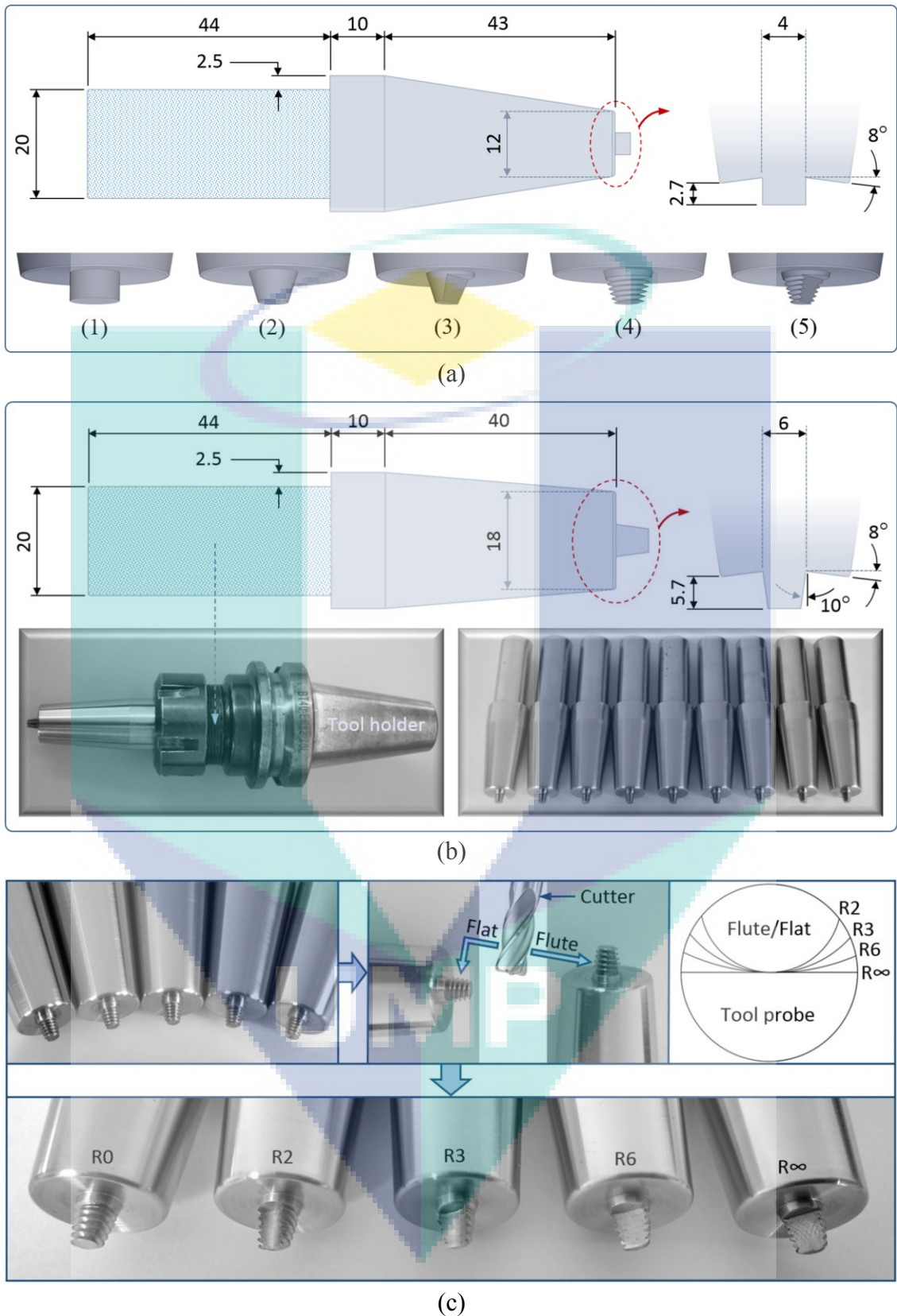


Figure 3.4 Design and dimensions in millimeters of the welding tools

Four of the provided welding tools were self-machined to add flute/flat to the truncated threaded probes. Milling cutters with radius of (2-, 3-, and 6-mm) were used to

add 10° tapered flutes with various bows to three pin tools. To do so, each probe was machined with a position in which the centerline of the cutter was parallel to their cone, while it was perpendicular to the tapered cone in the last tool to generate the flatted probe, as illustrated in Figure 3.4-(c) and described in Table 3.3. According to the results presented in the work of Hattingh et al. (2008), the depth of each flute/flat was 3 mm which is equal to the base radius of the probe.

Table 3.3 Description of the fluted/flatted pin tools shown in Figure 3.4-(c)

Tool number	Notation	Description
1	R0	Flute radius = 0 (pin tool without additional flute)
2	R2	Flute radius = 2 mm
3	R3	Flute radius = 3 mm
4	R6	Flute radius = 6 mm
5	R∞	Flute radius = ∞ (pin tool with single flat)

### 3.5.2 Tool Material and Heat Treatments

All tools were made of AISI H13 tool steel, whose chemical composition with thermal, physical and mechanical properties are listed in Table 3.4.

Table 3.4 Chemical composition (wt.%) with thermal, physical and mechanical properties of the welding tool material (AISI H13 tool steel) according to the supplier

Chemical properties								
C	Si	Mn	P	S	Cr	Mo	V	Fe
0.35	1.00	0.34	0.018	0.001	5.50	1.30	0.933	Balance
Thermal conductivity (W/m K)								
27 °C			204 °C		427 °C		649 °C	
17.6			23.4		25.1		26.8	
Physical and mechanical properties								
Density (kg/m <sup>3</sup> )	Melting point (°C)	Hardness (HRC)		YS (MPa)	UTS (MPa)	E (GPa)		
7750	1427	48		1250	1470	215		

(HRC): Rockwell hardness; (YS): yield strength; (UTS): ultimate tensile strength; (E): modulus of elasticity

This material has a relatively low thermal conductivity at elevated temperatures. Moreover, the hardness of this tooling material is higher enough than those of the aluminum alloys to be weld. However, further heat treatments were proceeded to increase the toughness and wear resistance of the welding tools (Bahrami et al., 2005).

To improve the hardness of welding tools, a proper heat treatment was followed. As schematically presented in Figure 3.5, annealing stage was conducted to reduce the residual stresses followed by tempering progression using high-temperature controlled furnace. To ensure a uniform temperature, the tools were gradually heated from the room temperature through 200, 400, 600 to 850 °C and left for two hours under this apex heating level. They were then slowly cooled inside the turned-off furnace until the temperature have reached 480 °C. The tools were subsequently exposed to air cooling toward the room temperature (Thelning, 2013). After these annealing periods, the set of tools was heat treated through single tempering sequence. To achieve the maximum hardness of the tool steel material, stepwise heating from the room temperature through 200, 400, 600, 800 to the austenitizing temperature (1050 °C) was accomplished. The tool pieces were then hold inside the furnace for about 30 minutes under constant temperature. After this soaking period, the steel tools were exited from the furnace and cooled in the ambient air until the temperature reached about 50 °C and then returned directly to the furnace, which was stabilized at 550 °C. The metals were left inside the closed furnace at this tempering temperature for two hours. Finally, the welding tools were cooled in the atmosphere to the room temperature.

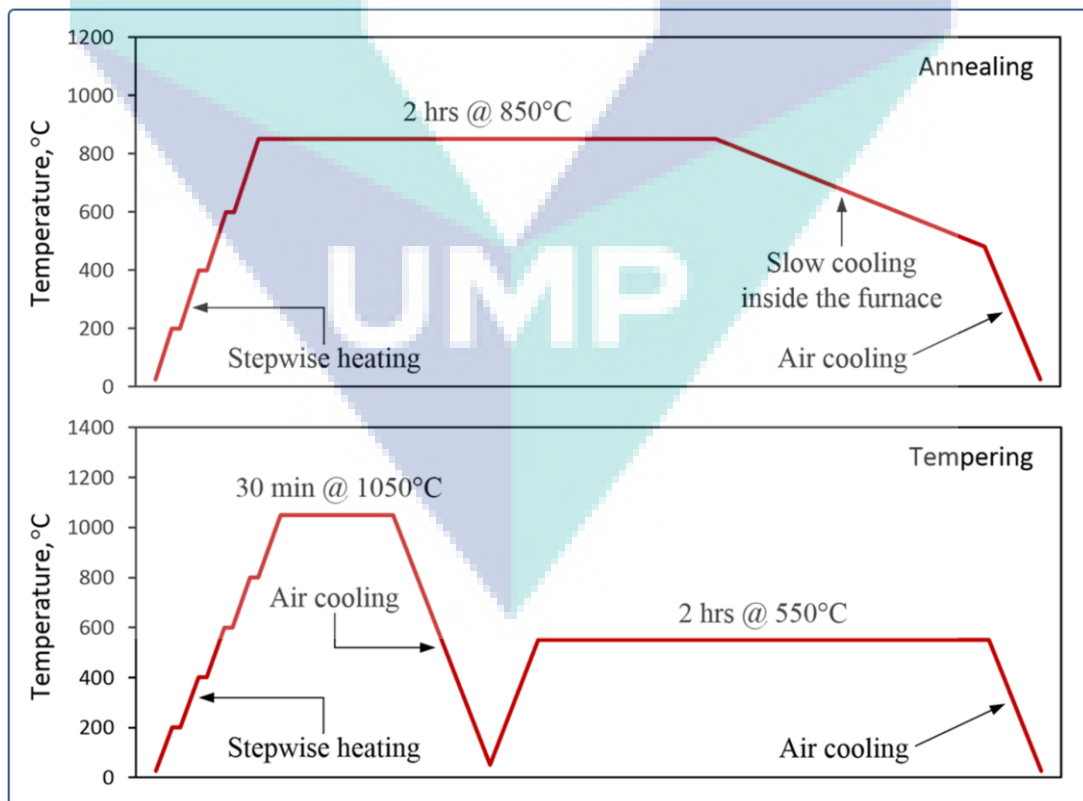


Figure 3.5 Heat treatment stages of the welding tool

Chemical anti-scale cleaning compound were successively used after the heat-treating periods to remove the oxide layers or any induced scale. In addition, the heat-treated tools were then carefully ground by silicon carbide (SiC) papers.

### **3.6 Backing/Clamping Systems**

After the preparation of the workpieces and the fabrication of the welding tools, a need for proper clamping way of the workpieces on the machine table has become vital. A simplified design of clamping system and fixtures was fabricated and verified throughout the joining of 3-mm-thick AA7075 and AA6061 aluminum alloys. After that, an advanced clamping/backing system was constructed and developed to investigate the effect of backing materials and cover plates on the mechanical properties of the dissimilar AA7075-AA2024 friction stir welds. Following are detailed characterizing of the initial and developed friction stir welding jigs.

#### **3.6.1 Fixtures Design**

The most common problems occurred during the FSW process are the separation and slipping of the abutting plates when the conventional clamping claws are used. Accordingly, an active design of clamping fixtures was presented and verified during the investigation of the optimal pin tool design made by joining the 3-mm-thick AA7075 and AA6061 aluminum alloys. The clamping construction is presented in Figure 3.6 and described in Table 3.5. The workpieces are secured on the machine table through this design by an easy and economical way using a set of vertical and horizontal bolts and nuts. Lateral restraints consist of two L-shaped aluminum plates with two long bolts. These fixtures permit to apply uniform side pressure on the abutting plates and increase the heat sinking. The vertical clamping forces were applied by means of bolt/nut fastening and composite stainless steel and aluminum (SS/Al) pressure bars to ensure uniform pressure and temperature distribution throughout the weldments (Zappia et al., 2010). Composite Al/SS backing plate was used to increase the cooling rate and hence improve the joint strength (Khodir et al., 2006; Upadhyay & Reynolds, 2014). The horizontal plane containing the workpieces was free of bolts and their holes. This is to avoid any change in the heat sink during the process. In addition to the use of the four vertical bolts (B<sub>1</sub>-B<sub>4</sub>) to fix the workpieces on the backing anvils, bolts B<sub>3</sub> and B<sub>4</sub> were also used to prevent sliding of the workpieces during the welding route and lock the position of the

backing plates on the machine table. The length of the backing plates and fixtures were selected to be suitable for the size of the welding coupons.

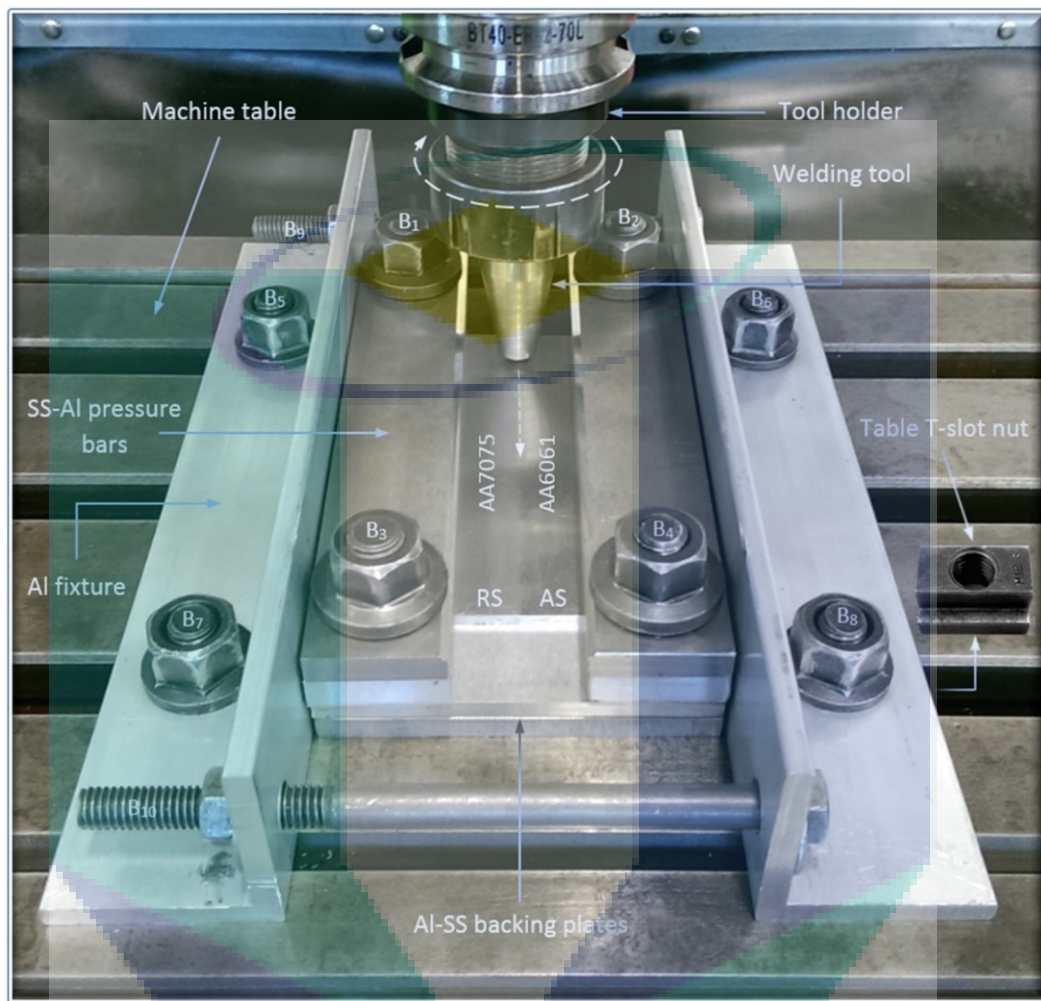


Figure 3.6 Photo of the clamping system and fixtures used to join the 3-mm-thick AA7075-AA6061 aluminum sheets

Table 3.5 Description of the clamping system and fixtures used to join the 3-mm-thick AA7075-AA6061 aluminum sheets

Part	Description
Pressure bars	Composite AISI 304 SS on AA6061-T6 Al bars of 150×30×6 mm close to the lateral restrains.
Lateral restrains	Two L-shaped AA6061-T6 Al fixtures of 250×50×50×6 mm.
Backing plates	Composite AA6061-T6 Al on AISI 304 SS plates of 150×96×6 mm each.
Bolts and nuts	Eight M12 bolts and two 150-mm-long M9 bolts with their nuts: B <sub>1</sub> -B <sub>4</sub> to fix the workpieces on the backing anvils, B <sub>5</sub> -B <sub>8</sub> to secure the lateral restrains on the machine table and B <sub>9</sub> -B <sub>10</sub> to subject the side pressure on the welding coupons.
Table T-slot nuts	Eight table T-slot nuts to secure the M12 bolts inside the grooves of the machine table.

To apply the lateral pressure directly on the workpiece by means of the two L-shaped side plates, the width of the backing plates was slightly shorter than the total width of the abutting base materials. Finding the center position of the welding tool between the abutting coupons can be simply achieved through this design, and the system parts can be easily assembled, detached and handled.

### 3.6.2 Construction of the Developed Design

After the verification of the fixture design, a developed backing/clamping system was invented in this work to investigate the FSW of dissimilar AA7075-T6 and AA2024-T351 aluminum alloys. Composite backing plate was fabricated from AA6061-T6 aluminum bars and AISI 304 stainless steel strip. These materials have relatively high and low thermal conductivities at elevated temperatures. For the aluminum alloy, thermal conductivity increases from 167 W/m K at 25 °C to 230 W/m K at 450 °C, while it remains below 19 W/m K up to 450 °C for the stainless steel (Maisonnette et al., 2011). As shown in Figure 3.7-(a) and described in Table 3.6, four 300×50×30 mm Al bars and central 300×45×30 mm SS strip were assembled using two lateral fixtures of 300×50×30×6 mm L-shaped AA6061-T6 aluminum plates and two 250-mm-long M9 bolts. The lateral fixtures were also used to increase the heat sink and fix the whole system to the machine table using four sets of M12 bolts and machine T-slot nuts. The heads of vertical bolts used to apply the vertical clamping forces were inserted inside the Al backing bars. Aluminum 6061-T6 blocks were used to fabricate the pressure bars. These two bars were machined to a length of 300 mm and width of 80 mm, while the thickness was 60 mm near the welding tool and 30 mm below the fastening M9 bolts. The bottom face of each bar was ground to a depth of 5 mm and width of 70 mm to apply the side pressure on the workpieces using two 250-mm-long M9 bolts. Uniform pressure and temperature distribution throughout the welding plates could be achieved using this clamping design. All parts were ground by the surface grinding machine to ensure precise dimensions. To avoid any change in the heat sink during the welding process, the horizontal plane containing the workpieces was free of bolts and their holes. The invented backing/clamping system was then modified to insert different backing and cover materials. The upper face of the Al backing blocks and the bottom surfaces of the pressure bars were machined and ground to a depth of 2 mm. Thin backing and cover changeable sheets were cut from 2-mm-thick AA6061-T6 and AISI 304 plates.

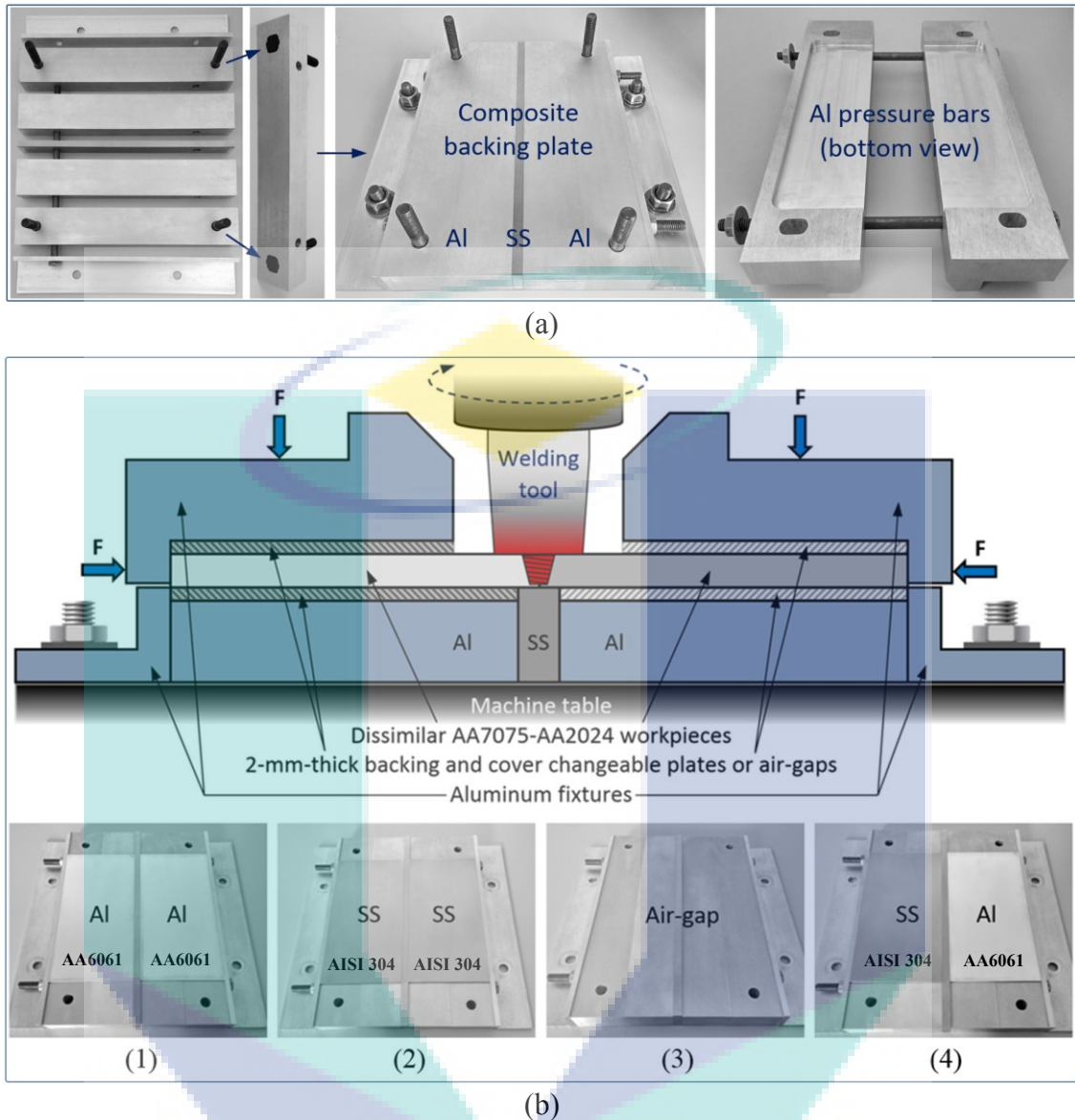


Figure 3.7 Schematic drawing and photographs of the developed backing/clamping systems

Dimensions of the backing sheet were identical to the workpiece size, while the length and width of the cover plate were 200- and 70-mm, respectively. Consequently, four symmetric and asymmetric backing and cover systems were used, as illustrated in the schematic drawing and seen in the photographs of Figure 3.7-(b). The photos of the covering systems were not presented in this figure since they were identical to the backing arrangements. System 1 shown in Figure 3.7-b-(1) was accomplished by inserting the aluminum sheets below and above the welding coupons. Hence, there was no difference between this system and the original developed one, and the change was only made in the other three systems. Figure 3.7-b-(2) shows that the steel backing and cover sheets

were used in System 2. The workpieces in System 3, which presented in Figure 3.7-b-(3) were placed on the central steel strip without inserting any backing or cover materials.

Table 3.6 Description of the developed backing/clamping system

Part	Description
Backing plates	Composite Al-SS-Al backing system consist of four 300×50×30 mm AA6061-T6 Al bars and central 300×45×30 mm AISI 304 SS strip.
Backing fixtures	Two L-shaped AA6061-T6 Al plates of 300×50×30×6 mm.
Pressure bars	Two AA6061-T6 Al bars of 300×80×30 mm with increased thickness at the upper face close to the welding tool. The bottom face is ground to a depth of 5 mm and width of 70 mm to apply the side pressure on the workpieces.
Bolts and nuts	Twelve bolts with their nuts: four 250-mm-long M9 bolts to assemble the parts of the composite backing plate and subject the lateral pressure on the workpieces, four M9 bolts to compress the workpieces on the backing plate by the pressure bars and four M12 bolts to fix the whole system to the machine table.
Table T-slot nuts	Four table T-slot nuts to secure the M12 bolts inside the grooves of the machine table.

To support the welding coupons in this situation, small 2-mm-thick steel pieces were located below and above the free edges. In this system, the welding plane of the workpieces was insulated by the air-gaps from the backing and cover aluminum bars. Asymmetric backing materials were used in System 4, as shown in Figure 3.7-b-(4). This system was used based on the obtained results of the previous systems, as will be discussed in the next chapter.

### 3.7 Temperature Measurement

Further modification was made to the invented jigs for the measuring of the welding temperatures. As seen in Figure 3.8-(a) three thru-holes were drilled on each side of the SS strip at the transverse centerline of the composite backing plate and the inserted sheets. Centers of the holes were located at 10-, 20- and 30-mm from the longitudinal centerline of the SS strip (welding centerline). Another two holes were also made on the bottom side edges of the pressure bars. Diameter of the drilled holes, which were used to insert the thermocouple wires to the welding coupons, was 3 mm. Temperature distribution during the welding process were recorded using high temperature and high thermal conductivity GG-K-36 thermocouple wires from Omega. The transient temperatures were inspected on the advancing and retreating sides of the welding seam. Accordingly, eight wire segments were cut and passed through the center T-slot of the

machine table towards the prepared holes of the backing/clamping systems. The wires were numbered related to their corresponding locations. The A1-A4 wires were used to record the temperature history on the advancing side, while the R1-R4 were used to measure the temperatures on the retreating side. The length of each wire segment was less than 1 m (about 0.75 m), as recommended by the manufacturing company.



Figure 3.8 Preparation steps of the transient temperature observation during the welding route

According to Mahoney et al. (Mahoney et al., 1998), Tang et al. (Tang et al., 1998) and Chao et al. (Chao et al., 2003), three small holes (1-mm-diameter) were drilled from the bottom surface of each workpiece to a depth of 3 mm to imbed the thermocouple wires, as shown in Figure 3.8-(b). These holes were created at a suitable distance from the weld start point (on the transverse centerline of the workpiece) to ensure thermal stability (Tang et al., 1998). The holes were located at 10.5-, 20.5- and 30.5-mm from the weld centerline on each side. Another two holes were drilled at the centers of the workpieces side-edges. Diameter and depth of these side holes were also 1- and 3-mm, respectively. It is worth noting herein that drilled holes does not affect the temperature field during the joining process (McClure et al., 1998).

High temperature and thermal conductivity epoxy adhesive (Omegabond<sup>®</sup>200) was used to secure the beaded wire thermocouples inside the workpiece holes, as shown in Figure 3.8-c-(1). This type of epoxy is recommended by Omega for fast and accurate temperature measurement. It is a two-part black epoxy system able to bond temperature sensors to several types of materials, such as metals, ceramics, glass and most of plastics. The paste has excellent strength and cures at elevated temperatures with freedom of sag. Because of its high temperature rating and for proper formulating, the epoxy system is supplied in twin packs containing 100 parts of OB-200 Resin (the black color) and 10 parts of special OB-200 Catalyst (the white color) by weight, as seen in Figure 3.8-c-(2). As per the direction for use, the pouch was heated to approximately 65° C in warm water by a controlled water heater. By this way, the solid catalyst became a liquid and ready to be mixed with the resin. After that, the divider was removed and the two components were mixed inside the pouch and became ready for use, as shown in Figure 3.8-c-(3). The corner of the pouch was sniped off to dispense the bond and locked again by the divider after each use, as seen in Figure 3.8-c-(4). As advised by the manufacturer, the pouch was kept in a dry environment under refrigeration to extend the shelf life to about one year.

The other free ends of the thermocouple wires were connected to a national instruments multichannel PC-based data logger. The heat sensors were fastened to twin 4-channel (NI 9211) thermocouple input, and the temperature-time history were recorded using DASyLab software at 2 Hz.

### 3.8 Welding Procedures

This part describes how the welding process was carried out in the present work, and highlights the procedures that were followed to achieve successful joints. Method of clamping and machine variables are presented and clarified in the following sections.

#### 3.8.1 Workpieces Clamping

The first stage in each set of welding trials is the cleaning up of the machine table with degreasing, lubricating and testing its sliding parts. After that, the workpieces are clamped by the invented fixtures. The developed backing/clamping system is considered in this explanation. A special conical tool with sharp edge was fabricated and used to align the composite backing plate on the machine table and to precisely place the workpieces on this backing system, as shown in Figure 3.9. This method is used to ensure that the pin tool is travelling along the contact line of the abutting workpieces during the welding route, and to keep this stir path over the longitudinal centerline of the steel anvil (red dash-dot line). The sharpened-edge tool was also used to locate the weld start point between the welding coupons. Furthermore, welding traverse speed was also calibrated by this multi-purpose tool.

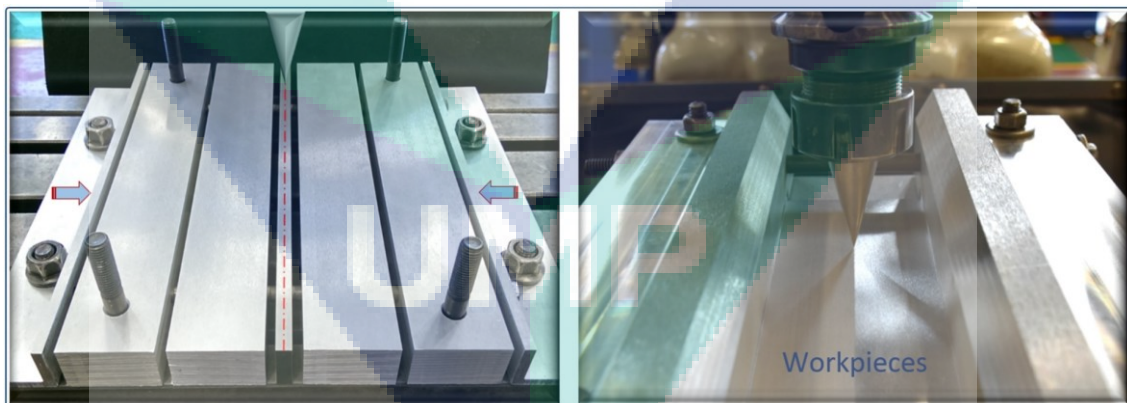


Figure 3.9 Aligning and clamping of the composite backing plate and workpieces using the specially fabricated sharpened edge tool

Based on the results of Richter-Trummer et al. (Richter-Trummer et al., 2012), the workpieces were then subjected to a constant moderate vertical and lateral clamping forces. These forces were controlled by means of digital mini torque wrench (Eclatorque-DM2-20), which was calibrated by a single thru-hole load washer (LCMWD) from

Omega, as shown in Figure 3.10. This load cell is a high-accurate force sensor especially designed for bolt-fastening measurement.

In the developed backing/clamping system, there are four vertical and two horizontal clamping bolts. Six load cells are then required to control the applied forces. The present method facilitated to diminish the error of the torque wrench and reduce the number of load sensors from six to just one, hence the cost was reduced to about 75%. The load cell wires were linked to the DASyLab software to adjust the compressive forces and the corresponding torques.

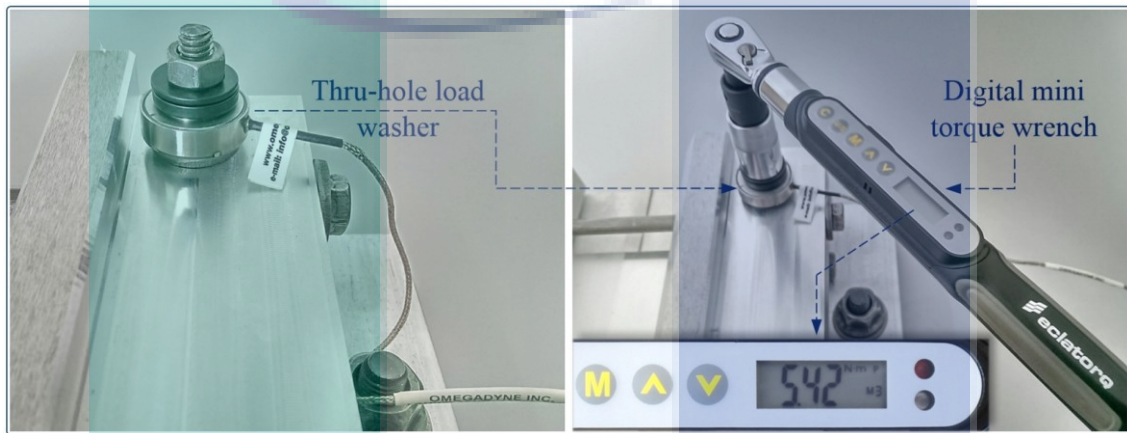


Figure 3.10 The load sensor and torque wrench used to control the applied clamping forces on the welding specimens

### 3.8.2 Design of Experiments and Process Parameters

Before starting of the welding trials, tool rotation and traverse speeds were examined and identified. Machine spindle speed was calibrated using a portable laser light tachometer (MONARCH PLT200). The difference in gauge between the machine and this optical tachometer did not exceed 3 rpm within a range of 500-2500 rpm. Therefore, the machine meter was considered to regulate the tool rotation speeds. The traverse speed was determined by moving the sharpened-edge tool close to the welding centerline between two points located on the workpieces (close to the weld start and end points). The tool travel between these lines was repeated several times with different table speeds, and the travel time was inspected using a stop-watch timer. The operational traverse speed was then equal to the ratio of the travel distance in meter to the measured travel time in second.

Extensive use of experimentation with varying levels of influencing factors are required to be inspected for producing sound or high efficient friction stir welds. The welding variables were selected in this work as per the literature findings and preliminary investigations. In addition, design of experiment and statistical methods can be significantly used to reduce the number of the required experiments (Montgomery, 2013). Consequently, the influence of pin tool profile on the tensile strength of dissimilar AA7075-AA6061 friction stir welds was presented by the response surface methodology (RSM) through different machine variables. This method is a collection of mathematical and statistical approaches to evaluate relationships between a group of quantitative independent variables and one or more responses. It enables to evaluate operation variables that may or may not have significant effect in the main response (Steinberg & Kenett, 2014). Central composite design (CCD), the most important and common experimental design used in this methodology, was used to build a second order experimental model and performed to investigate the significance of the independent variables.

Table 3.7 Levels of the selected parameters used to investigate the influence of pin tool design on the tensile strength of dissimilar AA7075-AA6061 friction stir welds

Coded level	Parameter			
	Tool, $T$	Rotation speed, $\omega$ (rpm)	Traverse speed, $v$ (mm/min)	Tilt angle, $\theta$ (deg.)
-2		900	200	2.0
-1		1000	250	2.5
0		1100	300	3.0
+1		1200	350	3.5
+2		1300	400	4.0

The five tools shown previously in Figure 3.4-(a) were tested through five levels of tool rotation and traverse speeds. Location of the softer AA6061 aluminum alloy was kept on the AS. The tool tilt angle was varied between 2° and 4° due to the concavity of the tool shoulder (Mishra & Mahoney, 2007). The working range of parameters was

examined by varying one factor while keeping the others constant (Heidarzadeh & Saeid, 2013; Karthikeyan & Balasubramanian, 2013). Visual inspection and microstructure were observed for appropriate arrangement of the selected variables, which were coded according to the following form:

$$x_i = \frac{X_i - \bar{X}_i}{\Delta X_i} \quad (3.1)$$

where  $x_i$  and  $X_i$  are the coded and actual values of the  $i$ -factor, respectively;  $\bar{X}_i$  represents the average of the high and low actual values of the  $i$ -factor; and  $\Delta X_i$  is the step change value. With this form, the upper and lower levels of each factor were coded as +2 and -2, respectively, as presented in Table 3.7 which shows the levels of the selected parameters ( $T$ ,  $\omega$ ,  $v$  and  $\theta$ ).

The experiments were carried out randomly with a complete design matrix of 31 experimental points, as will be shown in the results and discussion part. Second-order polynomial regression was developed to fit the experimental data and expressed by using the following response surface equation (Mason et al., 2003):

$$Y = \beta_o + \sum_{i=1}^k \beta_i X_i + \sum_{i=1}^k \beta_{ii} X_i^2 + \sum_{i=1}^{k-1} \sum_{j=2}^k \beta_{ij} X_i X_j \quad (3.2)$$

In this general form,  $Y$  is the predicted response which is a function of the independent variables ( $X$ ) in coded representation. The regression coefficients  $\beta_o$ ,  $\beta_i$ ,  $\beta_{ii}$  and  $\beta_{ij}$  are the intercept constant, linear effect, squared effect and interactive effect terms, respectively.

The success of RSM depends on an estimation of the predicted response at different locations in the response surface. Therefore, the analysis of the response surface started with investigation of the selected variables. The CCD method enables estimation of the regression parameters to fit the second-order polynomial regression model to the given response. It requires three types of trials, i.e.,  $2^k$  factorial trials,  $2k$  axial trials and center point trials, where  $k$  is the number of factors studied in the experiment. Values at the center point are used to detect curvature in the response, i.e., they contribute to the estimation of the coefficients of quadratic terms. The axial points are also used to estimate

the coefficients of quadratic terms, while the factorial points are used mainly to estimate the coefficients of linear terms and two-way interactions. Since there are four different variables in the present study, the number of independent factors in Equation (3.2) will be ( $k = 4$ ). The ultimate tensile strength, which represents the predicted response could be then expressed as follows:

$$\begin{aligned}
 UTS = & \beta_0 + \beta_1(T) + \beta_2(\omega) + \beta_3(v) + \beta_4(\theta) + \beta_{11}(T^2) + \beta_{22}(\omega^2) \\
 & + \beta_{33}(v^2) + \beta_{44}(\theta^2) + \beta_{12}(T\omega) + \beta_{13}(Tv) + \beta_{14}(T\theta) \\
 & + \beta_{23}(\omega v) + \beta_{14}(\omega\theta) + \beta_{34}(v\theta)
 \end{aligned} \tag{3.3}$$

In order to obtain an efficient experiment, unimportant independent variables need to be separated from important ones. One should never start an analysis of the surface until significant factors are identified. In practice, no model can be fit perfectly to measured values because of measurement errors or relationships between factors and response that cannot be described by a second-order polynomial. This results in residual values at the design points, i.e., deviations from the measured values. The quality of the model is assessed by the coefficients of determination:  $R^2$ , adjusted  $R^2$  and predicted  $R^2$  (Dutka et al., 2015).

$R^2$  represents a pure correlation between measured and predicted values and is indicative of the response variation explained by a model. However, every term added to the model equation will improve the model fit to the measured data. Therefore, adjusted  $R^2$  is used to compare the explanatory power of models, and its value increases only when an added term improves the model more than by chance. Both these coefficients are calculated using data that were themselves used for model development. A model's predictive capability for new observations is assessed using predicted  $R^2$ . This coefficient is calculated by systematically removing each observation from the data set, estimating the regression equation and determining the model's capability in predicting the removed observations. Predicted residual sums of squares statistic is used to calculate the value of predicted  $R^2$ .

The statistical significance of the terms of the model defined by Equation (3.3) can be evaluated using the analysis of variance (ANOVA), which is based on partitioning the variation in the data into components (Kass et al., 2014). For all the terms of the model equation, values of a so-called ANOVA table are calculated individually. The *adjusted*

*sum of squares* (Adj SS) for a specific term calculates reduction in the residual sum of squares resulting from the inclusion of this term to the model. *Adjusted mean squares* (Adj MS) are calculated by dividing Adj SS by the number of degrees of freedom (DF) for the respective term. Variation in the data unexplained by the model is represented by the *Residual Error* (RE), for which Adj SS is calculated as the residual sum of squares and Adj MS value of the RE is calculated as explained above. Ratios of the Adj MS for all terms of the model equation and Adj MS of the RE are calculated.

Because the ratios of variances follow an *F*-distribution, a statistical *F*-test is employed to identify statistically significant terms of the model. One can obtain *P*-values from this test for each term of the model, which are a measure of the probability of obtaining data at least as extreme as the data from the model, assuming that the null hypothesis is true, i.e., in this case, a particular term does not provide an effect on the results from the model. Therefore, the lower the *P*-values for the analyzed terms, the greater effect these terms have on the response predicted by the model.

Pure error lack-of-fit test is used to assess whether the model is adequate to describe the functional relationships between the experimental factors and the response. The test is based on partitioning the RE sum of squares into two components: lack-of-fit sum of squares, which is associated with variation due to factors other than measurement error, and pure error sum of squares, resulting from random variation caused by measurement error. The ratio of mean squares for lack-of-fit and pure error follows *F*-statistic, and similar to the aforementioned description, low *P*-value for lack-of-fit in ANOVA table means that the analyzed model does not fit to the experimental data.

Consequently, the statistical significance of the regression model and its coefficients were analyzed using ANOVA. The accuracy and general ability of the preferred polynomial model were evaluated by the coefficient of determination ( $R^2$ ) with a 95% confidence level. Therefore, the probability *P*-value of less than 0.05 was considered to be statistically significant. Design of experiments and statistical analysis were carried out by means of the Minitab software (Mathews, 2010).

The experimental procedures were followed to assess the ultimate tensile strength of the welds and the collected data are presented in Table 3.8, which represents the complete CCD matrix of the response surface methodology. This matrix consists of 16

factorial points ( $2^k$ ), 8 axial points ( $2k$ ) and 7 central points. The effective clamping system and the careful joint preparation enabled to obtain stable results with lower standard deviation. To validate the accuracy of the developed model, additional workpieces were friction stir welded with selected levels of variables (other than those used in the design matrix).

Table 3.8 The CCD matrix of the response surface methodology

Run No.	The actual levels of parameters				Ultimate tensile strength, UTS (MPa)				
	T	$\omega$	$\nu$	$\theta$	Test 1	Test 2	Test 3	Mean	SD
Factorial points									
1	T <sub>2</sub>	1000	250	2.5	222.23	225.46	226.44	224.7	2.20
2	T <sub>4</sub>	1000	250	2.5	213.87	218.27	219.13	217.1	2.82
3	T <sub>2</sub>	1200	250	2.5	226.02	228.36	227.01	227.1	1.18
4	T <sub>4</sub>	1200	250	2.5	219.82	221.73	225.83	222.5	3.07
5	T <sub>2</sub>	1000	350	2.5	217.06	219.30	218.45	218.3	1.13
6	T <sub>4</sub>	1000	350	2.5	210.76	215.48	212.82	213.0	2.37
7	T <sub>2</sub>	1200	350	2.5	216.83	219.02	223.31	219.7	3.30
8	T <sub>4</sub>	1200	350	2.5	212.10	214.35	214.29	213.6	1.28
9	T <sub>2</sub>	1000	250	3.5	219.74	223.07	222.62	221.8	1.81
10	T <sub>4</sub>	1000	250	3.5	216.18	215.89	217.31	216.3	0.75
11	T <sub>2</sub>	1200	250	3.5	223.41	227.75	226.60	225.9	2.25
12	T <sub>4</sub>	1200	250	3.5	216.67	220.20	220.79	219.2	2.23
13	T <sub>2</sub>	1000	350	3.5	212.03	217.54	220.71	216.8	4.40
14	T <sub>4</sub>	1000	350	3.5	207.24	206.71	208.94	207.6	1.17
15	T <sub>2</sub>	1200	350	3.5	215.90	217.11	216.10	216.4	0.65
16	T <sub>4</sub>	1200	350	3.5	212.36	210.01	208.59	210.3	1.90
Axial points									
17	T <sub>1</sub>	1100	300	3.0	199.08	201.62	202.84	201.2	1.92
18	T <sub>5</sub>	1100	300	3.0	188.54	193.21	194.61	192.1	3.19
19	T <sub>3</sub>	900	300	3.0	229.81	227.94	227.39	228.4	1.27
20	T <sub>3</sub>	1300	300	3.0	229.70	234.01	236.01	233.2	3.23
21	T <sub>3</sub>	1100	200	3.0	232.07	231.84	234.70	232.9	1.59
22	T <sub>3</sub>	1100	400	3.0	213.91	219.11	221.19	218.1	3.75
23	T <sub>3</sub>	1100	300	2.0	239.46	240.30	239.67	239.8	0.44
24	T <sub>3</sub>	1100	300	4.0	229.02	234.63	233.34	232.3	2.94
Central points									
25	T <sub>3</sub>	1100	300	3.0	248.03	252.55	251.19	250.6	2.32
26	T <sub>3</sub>	1100	300	3.0	250.48	251.20	248.05	249.9	1.65
27	T <sub>3</sub>	1100	300	3.0	252.91	254.76	253.61	253.8	0.93
28	T <sub>3</sub>	1100	300	3.0	248.82	253.57	255.83	252.7	3.58
29	T <sub>3</sub>	1100	300	3.0	247.73	254.81	251.90	251.5	3.56
30	T <sub>3</sub>	1100	300	3.0	251.50	253.28	255.18	253.3	1.84
31	T <sub>3</sub>	1100	300	3.0	250.47	253.73	254.08	252.8	1.99

The effect of materials direction and position on the tensile strength of the welding joint were then investigated through eight further case studies in two groups, which are schematically represented in Figure 3.11 and described in Table 3.9.

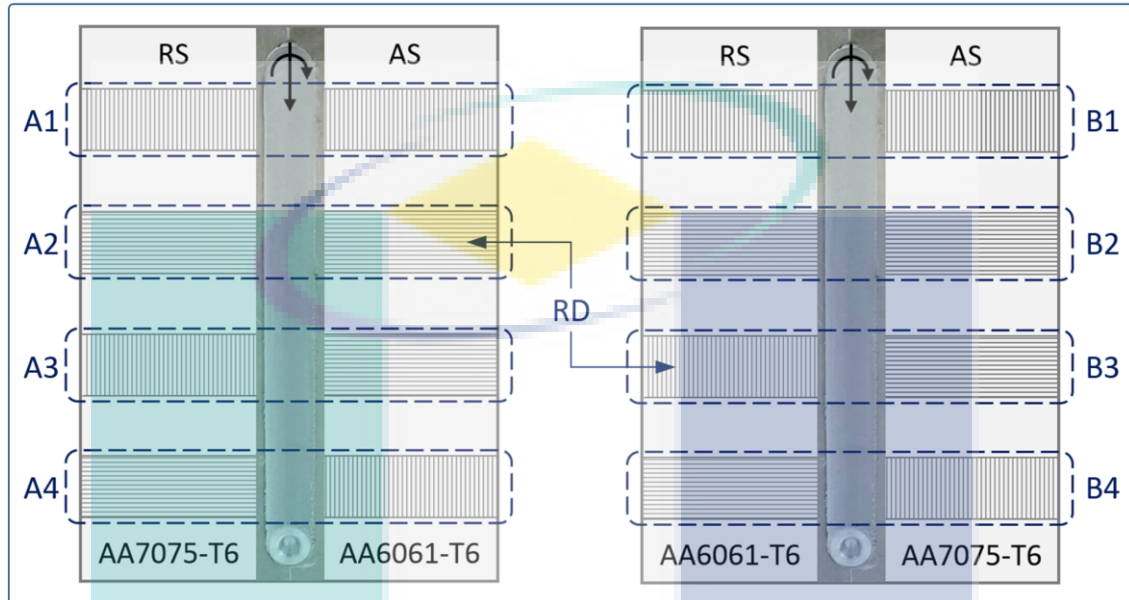


Figure 3.11 Schematic drawing of the eight case studies of relative materials direction and position

Table 3.9 Configuration of the weld related to the location and rolling direction of AA7075 and AA6061 aluminum alloys

Case studies	Material on the AS	Direction of welding
A1	AA6061	Parallel to the RD of both alloys
A2	AA6061	Normal to the RD of both alloys
A3	AA6061	Parallel to the RD of AA7075 and normal to the RD of AA6061
A4	AA6061	Parallel to the RD of AA6061 and normal to the RD of AA7075
B1	AA7075	Parallel to the RD of both alloys
B2	AA7075	Normal to the RD of both alloys
B3	AA7075	Parallel to the RD of AA6061 and normal to the RD of AA7075
B4	AA7075	Parallel to the RD of AA7075 and normal to the RD of AA6061

Different configurations related to the RD of the base materials were considered considering the location of the workpieces on the advancing and retreating sides of the welding tool. The softer AA6061-T6 aluminum alloy was placed on the AS in group A, while the harder AA7075-T6 aluminum alloy was fixed on the AS in group B. The

machine variables and tool design were selected as per the previous optimization results of the present work. The welding seam in all other trials were made in a direction parallel to the RD of the base alloys.

Friction stir welding of the 6-mm-thick AA7075-T6 and AA2024-T351 aluminum alloys was started through inspecting the optimal clamping force, tool rotation speed and initial dwell sequence for maximum and stable joint strength. The developed backing/clamping system shown in Figure 3.7-(a) was used during these investigations. Six levels of equal clamping forces ranged between 1-6 kN were firstly tested. This range was selected according to the results of Richter-Trummer et al. (Richter-Trummer et al., 2012). Table 3.10 presents the calibrated values of the applied torques related to the clamping forces. The AA2024 aluminum alloy was fixed on the AS during the tests, and the welding speeds used by Khodir and Shibayanagi (Khodir & Shibayanagi, 2007, 2008) which have presented previously in Table 2.1 were applied. The welding tool illustrated in Figure 3.4-(b) were used in this stage of the study and during the next investigation.

Table 3.10 The calibrated values of the applied torques related to the clamping forces

<b>Force (kN)</b>	<b>Torque (N.m)</b>	<b>Torque wrench memory</b>
1	1.81	M1
2	3.64	M2
3	5.42	M3
4	7.35	M4
5	9.24	M5
6	10.37	M6

Normal plunging phase was applied to insert the pin tool between the abutting materials. Equal penetration of the tool shoulder inside the workpieces with 3° of tilt angle were applied. The tilted rotating tool was slowly pressed until the shoulder heel penetrated to about 0.2 mm inside the workpieces. The stirring was then started after about 3 seconds of stationary dwell time. This method was also used during the joining of the 3-mm-thick plates. The welding tool was successively replaced after each two joining trials to avoid any change in the probe design. To inspect the best rotation rate, five spindle speeds ranged between 600- and 1800 rpm were examined with different material locations. These parameters were selected according to the background information outlined in the literature review. The tests were conducted through fixed

travel rate of 100 mm/min and the same tilting angle used before. The optimal clamping force and spindle speed were fixed during the next levels of the study.

The welding tool was successively replaced during the previous stages of this research to ensure that the dimensions and geometry of the probe does not change during the initial plunge stage. An active methodology for welding without applying the conventional plunge cycle was then conducted to avoid the primary deformation of the pin tool. In this method, a pilot hole slightly smaller than the probe diameter was created at the weld start point using an end mill of 5.8-mm-diameter. The depth of this hole was slightly less than the thickness of the welded plates. The end mill was slanted with the same tilt angle of the welding tool. The rotating probe was inserted inside the hole until the shoulder heel penetrated to about 0.2 mm inside the workpieces. This method was intended to reduce the longitudinal wear of the pin tool during the initial plunge sequence and hence, extend the welding tool life. An estimation of the appropriate stationary dwell time is then indispensable to generate the sufficient heat required to soften the welded materials before the main welding phase. Consequently, four stationary dwell periods (3-, 6-, 12- and 24-seconds) were examined. After the dwell sequence, stirring was conducted at 900 rpm spindle speed, 100 mm/min feed rate and 3° of tilt angle along the centerline between the dissimilar materials. These parameters were selected as per the previous investigation of the optimal spindle speed. To minimize the shoulder wear that may result from the stationary delay time, a new method of using two-stage welding (TSW) was introduced. This method, which will be explained later in Section 4.4.3, was applied during the next stages of the study. The revealed microstructure and measured ultimate strength of the welding joints were considered, and four transverse tensile specimens normal to the welding seam were tested to inspect the efficiency of each weldment during this level of the work.

The influence of backing and clamping materials on the tensile strength of dissimilar AA7075-AA2024 friction stir welded aluminum alloys were studied. The modified backing/clamping systems that discussed previously were examined through various welding travers speeds and materials placement. Five speeds rated between 50-250 mm/min, and the truncated threaded pin tool were used. Temperature distribution throughout the welding route was considered in this stage of the study. The idea of the

fourth novel asymmetric backing/clamping system was then applied as per the results of the weld tensile strength.

Finally, a new experimental study was attended to investigate the influence of pin tool flute radius on the material flow and tensile strength of AA7075-AA2024 friction stir welds. Considering the relative materials position, the welding tools shown in Figure 3.4-(c) and described in Table 3.3 were stirred through 900 rpm of spindle speed and 150 mm/min of traverse speed using the Al/SS composite backing/clamping system, as per the previous obtained results.

### **3.9 Tensile Testing and Metallographic Analysis**

For the age-hardenable alloys, the mechanical properties of the as welded joints are considerably decreased due to the partial dissolution and coarsening of the hardening particles (Aval & Serajzadeh, 2014; Koohbor et al., 2010). To recover the hardness and strength of the welds, the metallographic and transverse tensile specimens were prepared after a suitable period of natural aging. The tests were conducted after about one month for the AA7075-AA6061 friction stir welds and two months for the AA7075-AA2024 dissimilar joints (Mishra & Mahoney, 2007). The specimens were prepared using EDM wire cut and sectioning cut-off machines.

The tensile properties of each base material were inspected parallel and normal to their rolling direction. Three uniaxial tensile specimens were cut from each welding joint, as shown in Figure 3.12-(a). This number of specimens were also prepared and tested for each direction of the welding base materials. The specimens were prepared as per the American society for testing of materials standard (ASTM:E8/E8M-11, 2011). Locations and dimensions of the metallographic and tensile specimens for the 3- and 6-mm-thick friction stir welds are presented in Figure 3.12-(b) and described in Table 3.11. Since the plate thickness of the AA7075-AA6061 joints was less than 6 mm, the tensile specimens were cut with sub-size dimensions (Guillo & Dubourg, 2016). On the other side, standard dimensions were used to prepare the tension test specimens for the 6-mm-thick AA7075-AA2024 friction stir welds (Abdullah et al., 2001). Location of the holes made to embed the thermocouple wires are also shown in this figure. The metallographic specimen was cut after a suitable distance from the weld start point to ensure stable weld. However, it was located close to the start point for the cases used to inspect the optimal dwell

sequence. Four tensile specimens at an equal span ( $a = b = c = d = 40$  mm) were cut from the welding joints for this investigation.

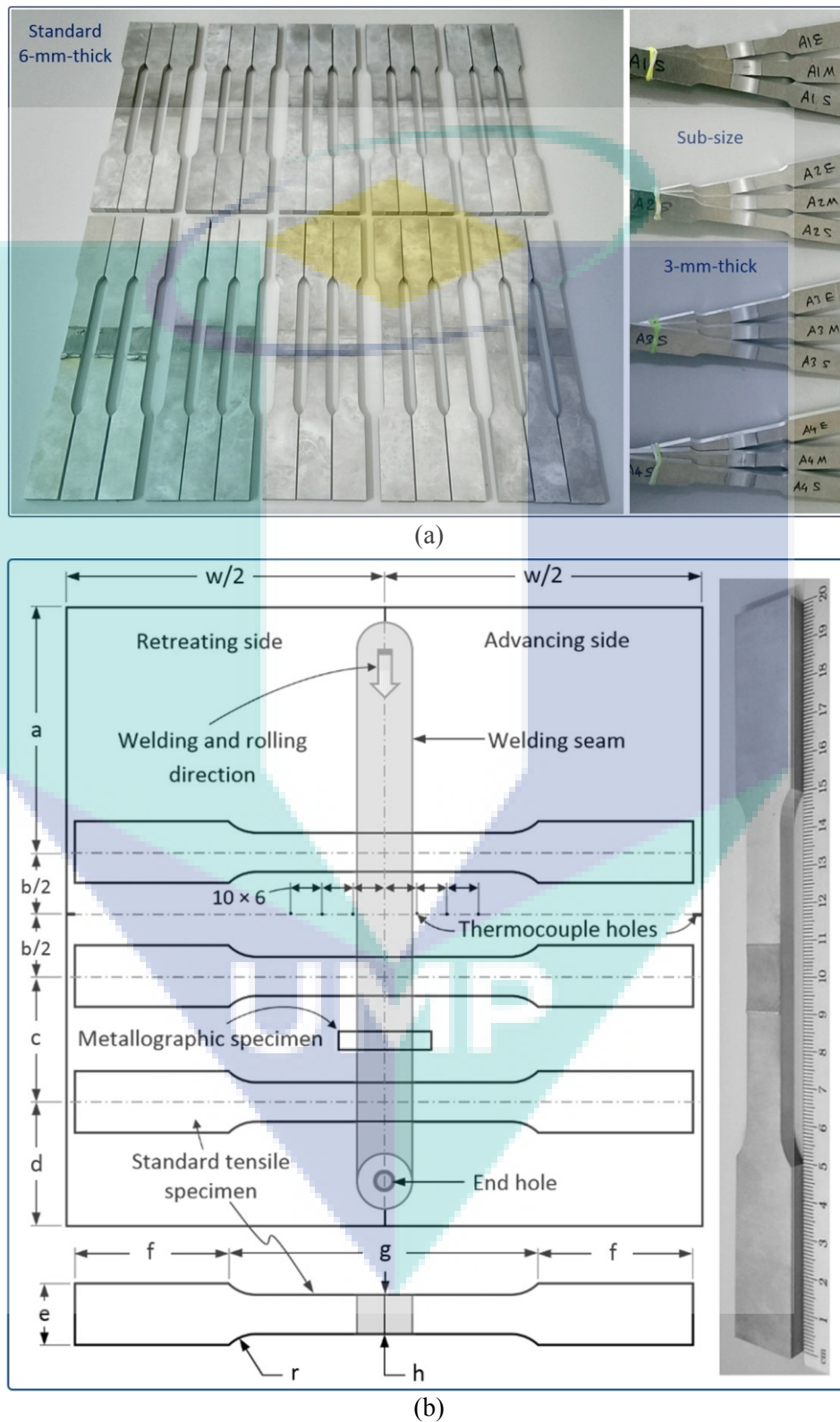


Figure 3.12 Sample, locations and dimensions in millimeters of the tension test specimens cut from the welding joints

Table 3.11 Values of the notations presented in Figure 3.12-(b)

Case study	Distance and dimension (mm)									
	a	b	c	d	e	f	g	h	r	w
3-mm-thick AA7075-AA6061 joints	45	25	25	30	10	30	40	6	6	100
6-mm-thick AA7075-AA2024 joints	80	40	40	40	20	50	100	12.5	12.5	206

The tensile tests were performed at room temperature through a speed of 1 mm/min using a 50 kN universal testing machine (INSTRON 3369) with the Bluehill 3 software. For accurate results, careful procedures were followed during the test set-up. The test specimens were properly aligned, centered and secured inside the grips before applying the load to avoid the potential problems such as specimen misalignment and worn grips (Davis, 2004). The mean value of the recorded results was considered for each case and the indicated standard error (SE) was calculated based on the standard deviation (SD). The weld efficiency was calculated with respect to the strength of the softer material (Giraud et al., 2016).

The standard guide of preparing the metallographic specimens (ASTM:E3-11, 2011) was followed to prepare the metallographic specimens, which were firstly encapsulated into a compression mounting compound using the automatic mounting press (SimpliMet<sup>®</sup>1000) shown in Figure 3.13-(a). The main purpose of this initial step is to improve handling of the specimen and protect their edges. The automatic grinding/polishing machines and roll grinder presented in Figure 3.13-(b) were used to grind and polish the mounted specimens.

Typical abrasive grinding procedure consist of 240, 320, 400, 600 and 800 grit silicon carbide papers were accomplished to remove the saw marks levels and clean the specimens' surfaces. After the finest grinding step, the specimens were polished through free 6-, 3- and 1- $\mu$ m abrasives on cloths to remove the artefacts of the grinding. After each grinding/polishing stage, the specimens were cleaned with distilled water, dried using a hand dryer and examined under an optical microscope. Finally, the prepared specimens were etched with a modified Keller's reagent so that the grain structure of the weld zone could be clearly observed.



(a)



(b)

Figure 3.13 The automatic mounting press and the encapsulated metallographic specimens

The macro and microstructural characterization were performed under the LED light-microscope and the micro-hardness tester (TUKON 1202) shown in Figure 3.14-(a and b). The latter device was used to measure the hardness across the weld centerline in a direction normal to the weld seam. The HV0.5 test method was applied with an indent time of 10 seconds. The TM303Plus scanning electron microscope (SEM) equipped with an energy dispersive spectrometry (EDS) was used to examine the construction of the base and joined materials, as shown in Figure 3.14-(c). The average grain intercept (AGI) method was used to measure the grain size by drawing a set of randomly positioned line segments on the micrograph, counting the number of times each line segment intersects a grain boundary and finding the ratio of intercepts to line length (Prakash & Regener, 2008). The mean AGI value calculated from the microstructure was then considered as the average grain size.



Figure 3.14 (a) The LED light-microscope, (b) The micro-hardness tester and (c) The SEM/EDS tabletop microscope

### 3.10 Summary

This chapter presented a detailed description of the developed experimental setup and research methodology. The development involved the design of welding tool and backing/clamping system for the FSW of dissimilar aluminum alloys. Welding stages, process parameters and design of experiments were clarified. The preparation steps of the workpieces were explained, and the tools used for joining the prepared welding coupons with their design, fabrication steps and post heat treatments were presented. Method of clamping the workpieces to the machine table was illustrated by introducing the construction of the developed backing/clamping systems. A new strategy of two-stage welding without applying the ordinary plunge phase was introduced. All measuring instruments and testing equipment were included with their classification and descriptions. The research methodology was followed to collect the data of the present work, and the acquired results with their discussions are presented in the next chapter.

## CHAPTER 4

### RESULTS AND DISCUSSION

#### 4.1 Introduction

The acquired results of the current research study are presented and discussed in this chapter. Mechanical properties and metallographic inspection of the welding base materials were firstly performed and verified. Results of the experimental work and statistical analysis of the pin tool design in conjunction with machine variables and materials direction are presented. The outcomes of joining the high-strength AA7075-T6 and AA2024-T351 aluminum alloy are provided. Influence of the clamping pressure, spindle speed, dwell sequence and backing/clamping materials on the dissimilar friction stir welds are presented and discussed. In addition, a new design study of the welding pin tool is presented by investigating the effect of flute radius on the materials flow and mixing of dissimilar joints.

#### 4.2 Properties of the Welding Base Materials

The as-received aluminum alloys were examined throughout the tensile testing and metallographic inspections to ensure the quality and compare the mechanical properties and chemical composition of the welding base materials. Efficiency of the welding joint is commonly measured related to the strength of the corresponding parent materials. In addition, the distribution of the weld hardness should also be compared to the actual level of the base materials hardness. It is then important to inspect the behavior of the selected materials before accessing the welding process. The results of tensile and hardness tests, as well as the microstructures of the welding materials are presented in the following sub-sections.

#### 4.2.1 Mechanical Properties

Six uniaxial tensile specimens (three along the rolling direction and three along the transverse directions) were tested for each of the base aluminum alloys. Results of the tests are presented in Table 4.1.

Table 4.1 Results of the tensile tests for the welding base materials

Property	WD	Test 1	Test 2	Test 3	Mean	Supplier	Standard
<b>AA6061-T6 aluminum alloy</b>							
Tensile strength (UTS), MPa	RD	301.32	298.55	300.94	300.27	308	310
	TD	306.20	307.91	306.44	306.85	308	310
Elongation (El), %	RD	13.26	12.15	13.77	13.06	12	12
	TD	12.74	10.33	13.25	12.11	12	12
<b>AA7075-T6 aluminum alloy</b>							
Tensile strength (UTS), MPa	RD	566.26	568.84	569.63	568.24	562	572
	TD	572.03	570.44	571.16	571.21	562	572
Elongation (El), %	RD	13.4	11.97	14.03	13.13	12.25	11
	TD	10.47	12.11	10.45	11.01	12.25	11
<b>AA2024-T351 aluminum alloy</b>							
Tensile strength (UTS), MPa	RD	449.26	448.31	446.89	448.15	444	469
	TD	450.38	449.04	448.71	449.38	444	469
Elongation (El), %	RD	17.63	19.05	20.11	18.93	18	19
	TD	18.31	16.14	17.58	17.34	18	19

(WD): welding direction; (RD): rolling direction; (TD): transverse direction; (SD): standard deviation; (SE): standard error

The ultimate tensile strength was slightly higher along the TD for all materials since they were not affected by the rolling deformation laterally (Koohbor et al., 2010). Accordingly, the welding experiments were conducted normal to the TD of the workpieces with a special study for the 3-mm-thick plates related to their rolling directions. On the other side, the tested materials have exhibited certain increase in the yield stress and tensile elongation along the RD. The average results were close to the corresponding standard and supplier values; hence the quality of the welding base materials was satisfactory.

#### 4.2.2 Metallographic Inspections

Micrographs of the welding base alloys are presented in Figure 4.1 through two different magnifications. The microstructure of all alloys consists of elongated grains with a random distribution of constituent precipitates or small black particles randomly

distributed across the aluminium grains (Zuo et al., 2017). This is in accordance with the standard structure of these advanced aluminium alloys.

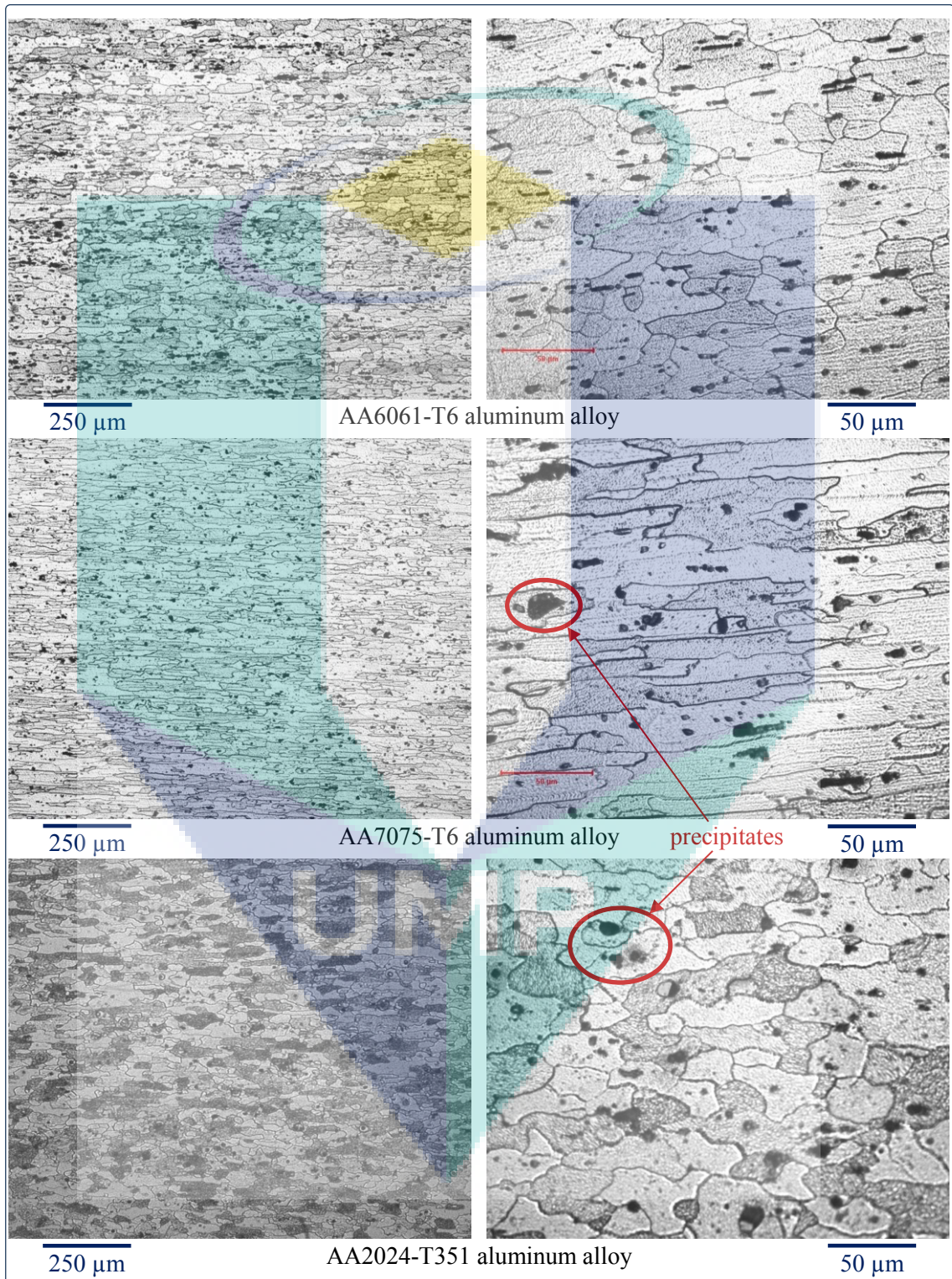


Figure 4.1 Microstructures of the welding base materials

The longest grains were observed during the inspection of the AA7075 alloy, while the shortest and smallest in size were seen in the AA2024 alloy. This is due to the difference in their chemical and mechanical properties. The microstructure of AA6061 alloy was lied in between these two materials related to the grain shape and size. Figure 4.2 presents the acquisition conditions and chemical composition of these materials as per the SEM/EDS identification. It is obvious that the results are similar to those presented previously in Table 3.2.

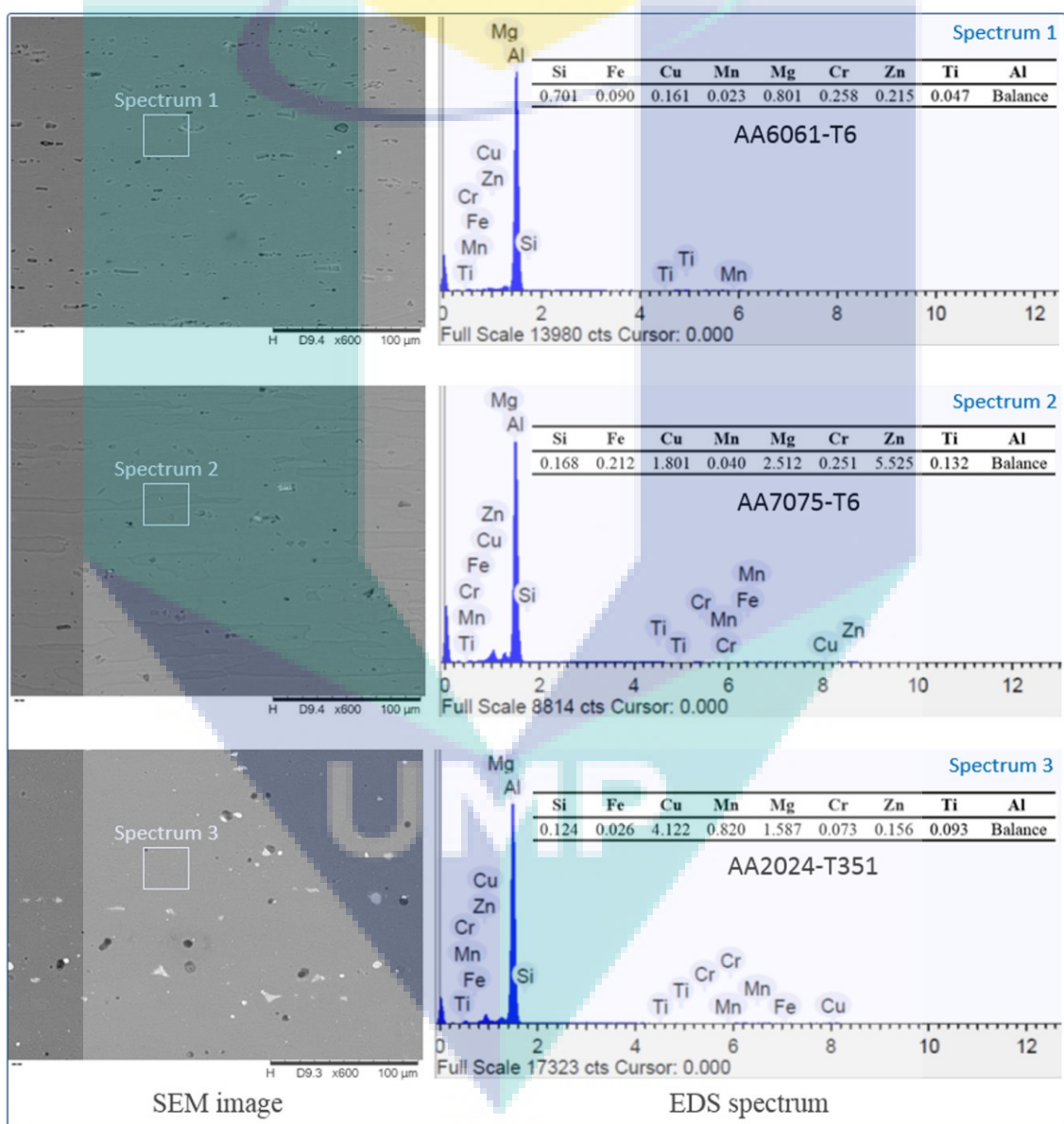


Figure 4.2 The SEM images and EDS spectrums with the acquired chemical compositions of base materials

Subsequently, the Vickers micro-hardness number was measured in five locations on the transverse centerline of the metallographic specimen of each welding base material, as shown in Figure 4.3. The evaluated mean VHN of the AA6061-T6 and AA7075-T6 aluminum alloys were 107 and 175, respectively while it was about 142 for the AA2024-T351 alloy. These results were also lied within the standard range of the Vickers hardness values.

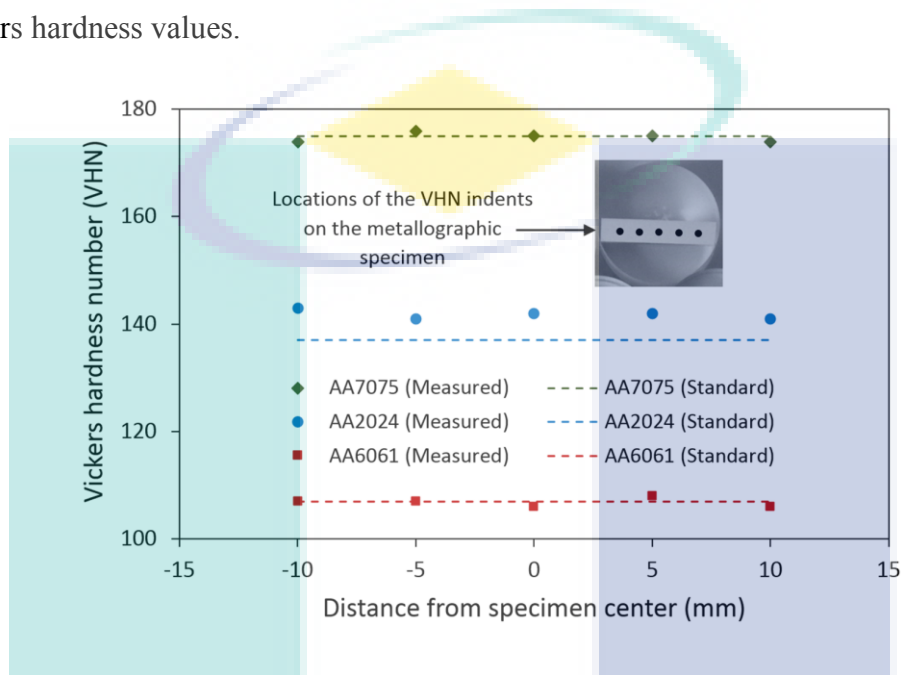


Figure 4.3 Micro-hardness of the base materials

### 4.3 Tool Design and Process Parameters

This section presents the design study of the welding pin tool in conjunction with machine variables and materials direction on the static strength of welding joint. The 3-mm-thick AA6061 and AA7075 aluminum alloys in the T6 temper condition were joined by the FSW using the simplified design of backing system and fixtures shown previously in Figure 3.6.

#### 4.3.1 Design of Experiments and Statistical Analysis

In addition to a number of pre-tests, 36 dissimilar AA6061-AA7075 friction stir welds were performed to identify the effect of pin tool profile and machine variables on the joint strength. The five welding tools explained previously in Section 3.5 and presented in Figure 3.4-(a) were tested under different spindle speeds, traverse rates and tilt angles. Sample group of the prepared joints is presented in Figure 4.4.

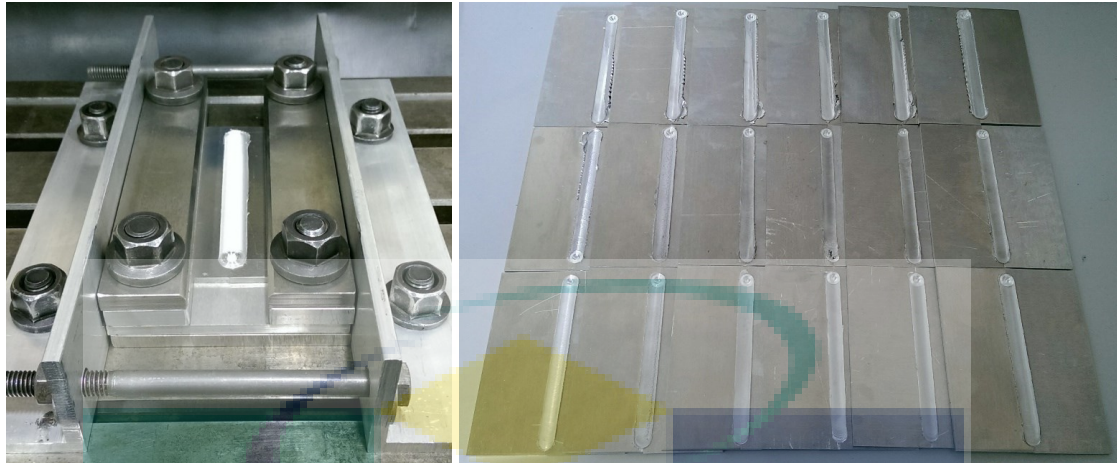


Figure 4.4 Dissimilar AA6061-AA7075 friction stir welds

According to the collected data of the complete CCD matrix, which were presented in Table 3.8, the response surface design was analyzed to estimate the coefficients of the model, as shown in Table 4.2.

Table 4.2 Estimated regression coefficients for UTS

Term	Coefficient	Standard error	<i>t</i> -ratio	<i>P</i> -value
Constant	252.086	1.0073	250.257	0.000
<i>T</i>	-2.887	0.5440	-5.308	0.000
<i>ω</i>	1.196	0.5440	2.198	0.043
<i>v</i>	-3.688	0.5440	-6.778	0.000
<i>θ</i>	-1.529	0.5440	-2.811	0.013
<i>Tω</i>	0.256	0.6663	0.385	0.706
<i>Tv</i>	-0.144	0.6663	-0.216	0.832
<i>Tθ</i>	-0.244	0.6663	-0.366	0.719
<i>ωv</i>	-0.656	0.6663	-0.985	0.339
<i>ωθ</i>	-0.031	0.6663	-0.047	0.963
<i>vθ</i>	-0.331	0.6663	-0.497	0.626
<i>T</i> <sup>2</sup>	-14.543	0.4984	-29.181	0.000
<i>ω</i> <sup>2</sup>	-6.006	0.4984	-12.051	0.000
<i>v</i> <sup>2</sup>	-7.331	0.4984	-14.709	0.000
<i>θ</i> <sup>2</sup>	-4.693	0.4984	-9.417	0.000

$$R^2 = 98.64\%; \text{ Adjusted } R^2 = 97.45\%; \text{ Standard error} = 2.66508$$

The regression coefficients were then re-evaluated by removing the insignificant terms ( $P > 0.05$ ) and considering the significant coefficients (linear and quadratic effect terms). Accordingly, Equation (3.3) was modified to construct the developed model for the ultimate tensile strength of dissimilar AA7075-AA6061 friction stir welds as follows:

$$\begin{aligned}
 UTS = & 252.086 - 2.8875(T) + 1.19583(\omega) - 3.6875(v) \\
 & -1.52917(\theta) - 14.5433(T^2) - 6.0058(\omega^2) \\
 & -7.3308(v^2) - 4.6933(\theta^2)
 \end{aligned}
 \tag{4.1}$$

Table 4.3 Regression coefficients of the developed model

Term	Coefficient	Standard error	t-ratio	P-value
Constant	252.086	0.8996	280.212	0.000
<i>T</i>	-2.887	0.4859	-5.943	0.000
$\omega$	1.196	0.4859	2.461	0.022
<i>v</i>	-3.688	0.4859	-7.590	0.000
$\theta$	-1.529	0.4859	-3.147	0.005
$T^2$	-14.543	0.4451	-32.674	0.000
$\omega^2$	-6.006	0.4451	-13.493	0.000
$v^2$	-7.331	0.4451	-16.470	0.000
$\theta^2$	-4.693	0.4451	-10.544	0.000

$R^2 = 98.51\%$ ; Adjusted  $R^2 = 97.96\%$ ; Standard error = 2.38019

As shown in Table 4.3, the presented coefficients of the reduced model showed higher significance with very small *P*-values and corresponding bigger numbers of *t*-ratio. Elevated regression coefficient ( $R^2 = 0.9851$ ) was recorded, which indicated that the developed model had a very high correlation, and then only 1.49% of the total variations would not be clarified by it. Simultaneously, the adjusted regression coefficient ( $R^2 = 0.9796$ ) gave another confirmation to the adequate fit of this developed response surface model.

Table 4.4 ANOVA of UTS for the developed model

Source	DF	Sum of squares	Mean squares	Adj. Mean squares	F-value	P-value
Model	8	8225.83	8225.83	1028.23	181.50	0.000
Linear	4	616.89	616.89	154.22	27.22	0.000
Square	4	7608.94	7608.94	1902.24	335.77	0.000
Residual error	22	124.64	124.64	5.67		
Lack-of-fit	16	112.01	112.01	7.00	3.33	0.072
Pure error	6	12.63	12.63	2.10		
Total	30	8350.47				

Furthermore, adequacy of the empirical model for predicting the ultimate strength as a function of tool profile, rotation speed, feed rate and tilt angle is also clear from the ANOVA output shown in Table 4.4. Consequently, the developed model was used to evaluate the ultimate tensile strength corresponding to the mean observed values shown

in the CCD matrix. The results showed a respectable fitness of the mathematical model with the experimental data within the range of the operating variables, as is obvious by the scatter plot shown in Figure 4.5.

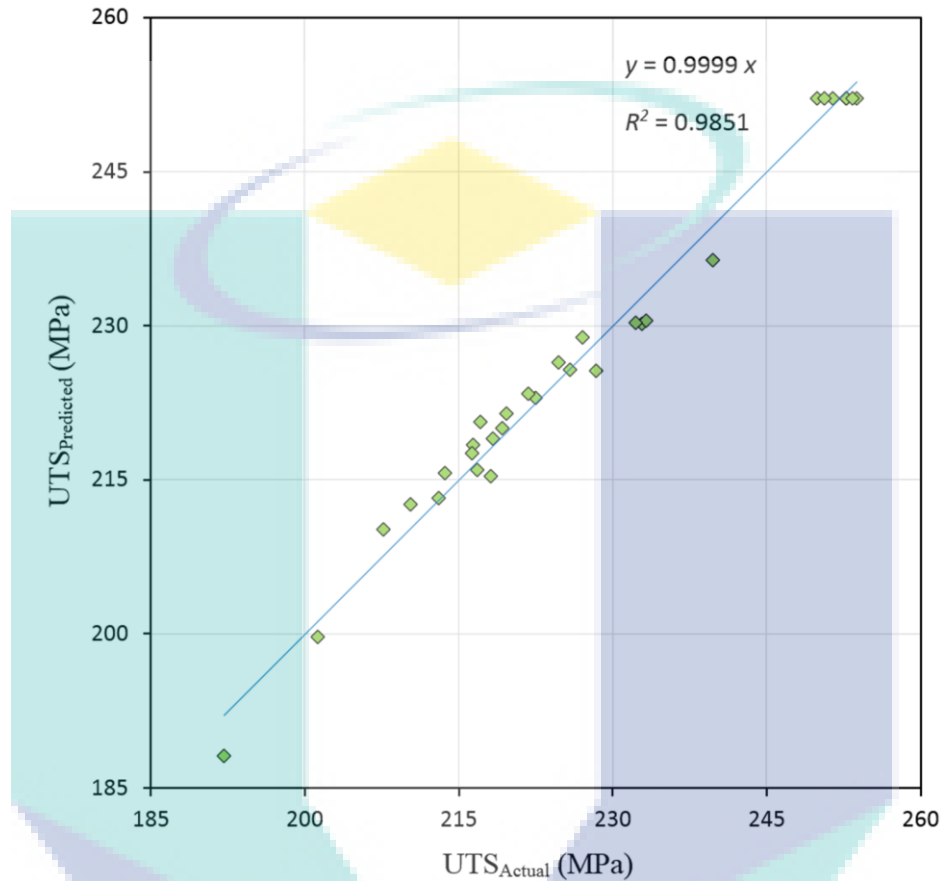


Figure 4.5 Scatter plot of the observed and predicted results of UTS

### 4.3.2 Validation Tests

To validate the accuracy of the developed model, extra workpieces were friction stir welded with selected levels of variables (other than those used in the design matrix). Tools (T<sub>2</sub> and T<sub>4</sub>) were tested at the central levels of the welding speeds and tilt angle to make a comparison between the five tools used in this study. For these additional welds, the values of ultimate tensile strength were measured after the same natural aging period and listed in Table 4.5. The developed model was used to predict the corresponding values. The verification tests showed well agreement between the observed and calculated values with low deviation, and within the acceptable  $\pm 10\%$  error (Steinberg & Kenett, 2014).

Table 4.5 The verification table

Run No.	Coded(actual) levels of parameters				Ultimate tensile strength, UTS (MPa)		
	$T$	$\omega$	$v$	$\theta$	Experimental*	Predicted	Err (%)**
1	-2(T <sub>1</sub> )	-1.5(950)	+0.5(325)	-1(2.5)	184.3 ± 3.1	177.5	+3.8
2	-1(T <sub>2</sub> )	0(1100)	0(300)	0(3.0)	237.6 ± 2.1	240.4	-1.2
3	0(T <sub>3</sub> )	-1(1000)	-1(250)	0(3.0)	234.6 ± 3.2	241.2	-2.8
4	+1(T <sub>4</sub> )	0(1100)	0(300)	0(3.0)	229.5 ± 2.2	234.7	-2.2
5	+2(T <sub>5</sub> )	+1.5(1250)	-0.5(275)	+1(3.5)	179.4 ± 2.2	170.2	+5.4

\* Mean of three tests ± Standard deviation

\*\* Percentage error (Err) = (Experimental – Predicted) × 100/ Experimental

### 4.3.3 Sensitivity Analysis

The ANOVA relating UTS was studied so far, which have concerned the variability propagation through the RSM model and resulting in a significant contribution to the overall output. The sensitivity analysis seeks, rather, to find out what process factors do produce larger variation in the responses whenever it is subjected to a small change in process parameters. First, relation between the ultimate tensile strength and independent variables was represented graphically by the developed response surface model in the 3D contour plots of Figure 4.6. Response surface methodology efficiently enables to detect the effect of selected variables on joint strength and to identify their optimal values that lead to gain the maximum response. In all plots, the predicted results of UTS were presented with two incessant variables, whereas the two other factors were fixed at their intermediate levels. The optimal values of independent variables could be detected from these graphs. It is clear that the ultimate strength of dissimilar joint is significantly affected by the rotation speed, feed rate and tilt angle regardless of the geometry of the welding tool. On the other side, the pin tool profile played an important role in the response of these variables.

To show which parameter has the major effect on the joint tensile strength, a brief sensitivity analysis on the developed model was attained. Sensitivity information should be interpreted using mathematical definition of derivatives. Mathematically, sensitivity of a design objective function with respect to a design variable is the partial derivative of that function with respect to its variables (Rajakumar et al., 2010). Therefore, the sensitivity coefficient of each variable on the tensile strength was calculated by partially differentiating Equation (4.1) with respect to the affected parameters, as in the following equations:

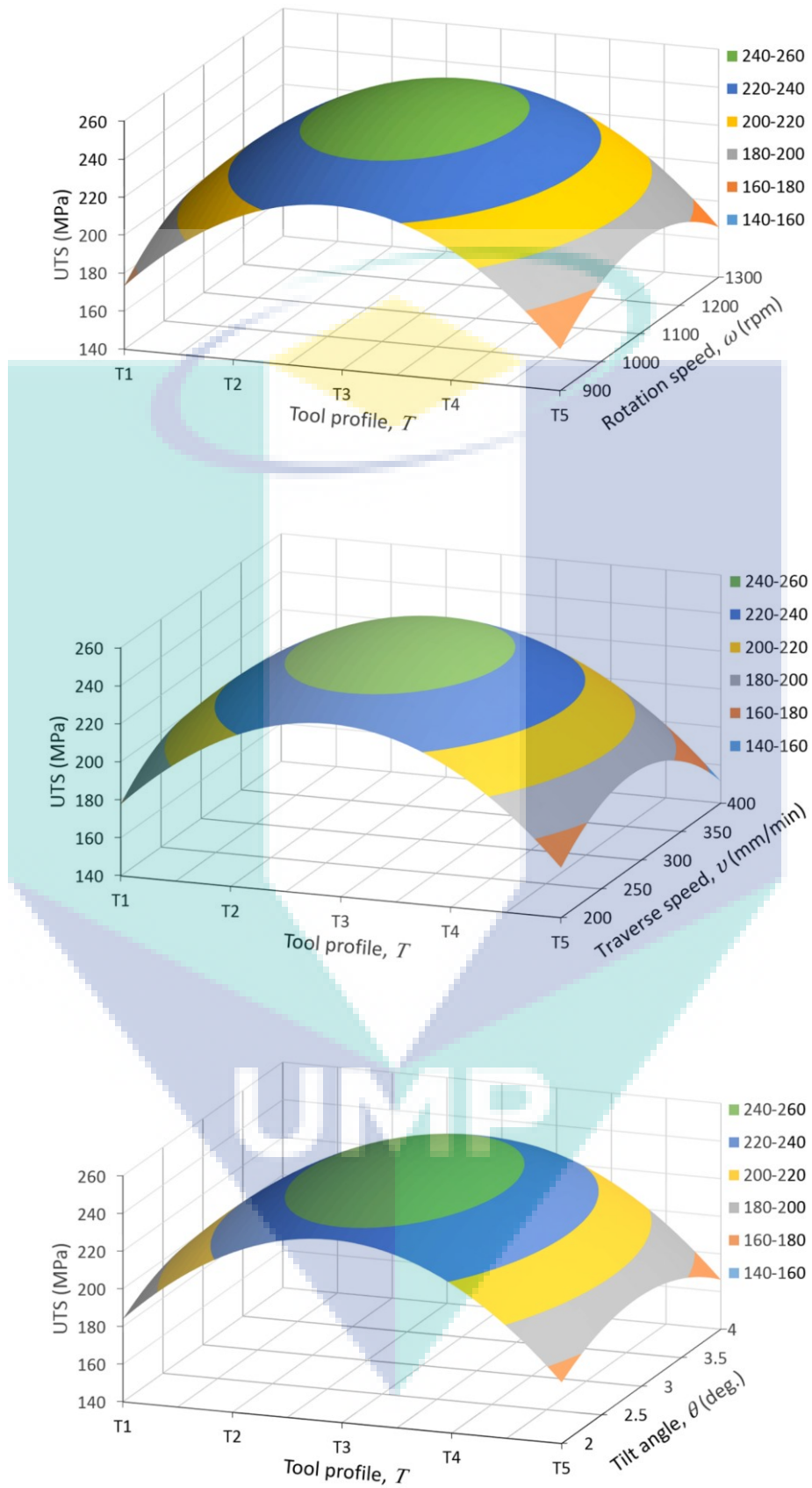


Figure 4.6 Response 3D contour plots. In each plot, the two other factors were fixed at their intermediate levels

$$\partial UTS / \partial T = -2.8875 - 29.0866T \quad (4.2)$$

$$\partial UTS / \partial \omega = 1.19583 - 12.0116\omega \quad (4.3)$$

$$\partial UTS / \partial v = -3.6875 - 14.6616v \quad (4.4)$$

$$\partial UTS / \partial \theta = -1.52917 - 9.3866\theta \quad (4.5)$$

The calculated results of sensitivity analysis of the process parameters on the weld tensile strength are presented in Figure 4.7. The histograms show the sensitivity of pin tool design, rotational speed, traverse speed and tool tilt angle on UTS. Geometry of the welding pin tool caused large changes in tensile strength, while the variation of tilt angle caused the least change in joint strength.

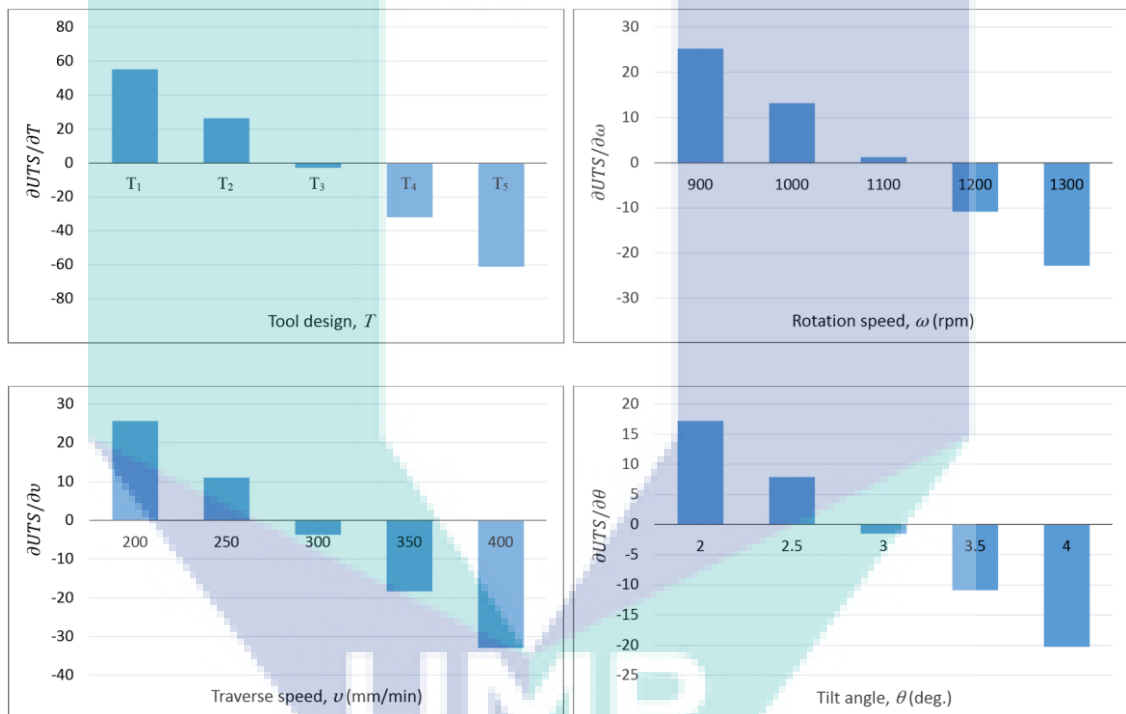


Figure 4.7 Results of the sensitivity analysis

The results revealed that the local maximum sensitivities of the variables are  $-61.1$ ,  $+25.2$ ,  $-33$  and  $-20.3$  for pin tool design, rotation speed, traverse speed and tilt angle, respectively. Accordingly, the tensile strength is more sensitive to the design of tool followed by traverse speed, rotation rate and tilt angle. Based on these results, the five welding tools were examined at the central levels of the other three variables. This is to establish a comparison between the weld strength and material flow related to the selected pin tool profiles, as will be discussed in the following section.

#### 4.3.4 Microstructure and Tensile Properties

The stress–strain curves and macrographs of the weld nuggets with the corresponding ultimate tensile strength of the welding joints produced by the five welding tools at the central levels of the other parameters are shown in Figure 4.8 and Figure 4.9, respectively.

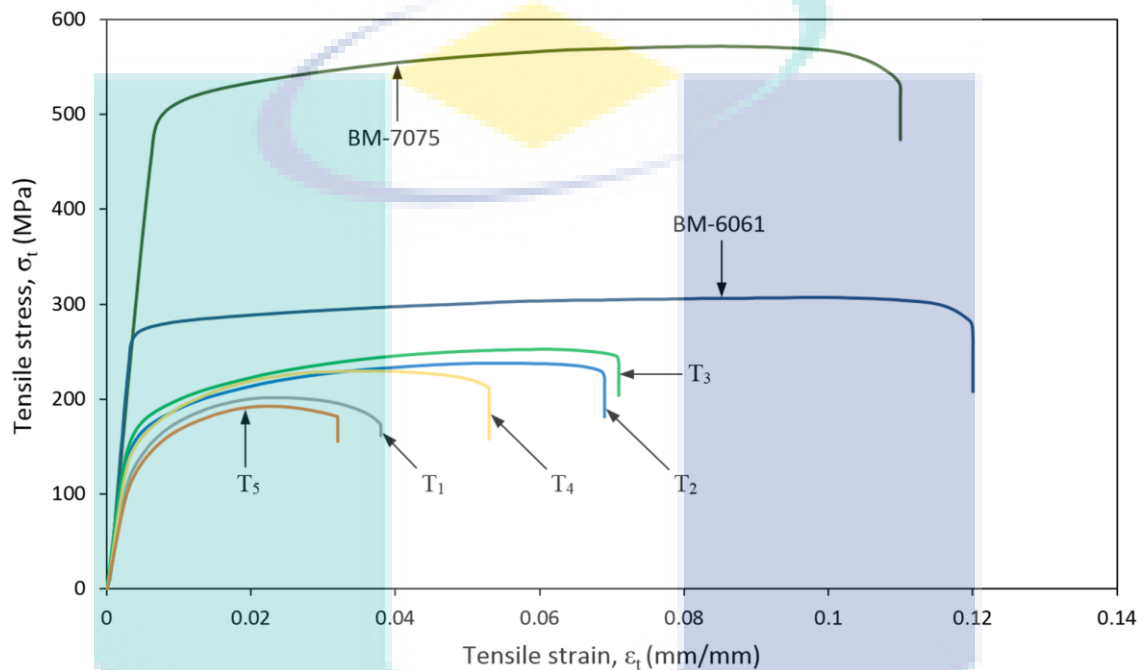


Figure 4.8 Stress–strain curves of the base materials and welding joints using the five tools at the central levels of the other three variables

Lower tensile strength and elongation at fracture with poor material mixing resulted from the first and last tools ( $T_1$  and  $T_5$ ) which consist of smooth tapered and cylindrical probes, respectively. This can be attributed to the improper material mixing, as will be explained later. However, the tensile strength and elongation were slightly higher with the tapered pin tool due to the reduction in welding force (Elangovan et al., 2008; Padmanaban & Balasubramanian, 2009; Zettler et al., 2004). By the fourth tool ( $T_4$ ), ultimate strength started to relatively increase, and the weld nugget became wider. This is due to the flat that has been added to the cone of the probe which improved the local deformation and material flow (Thomas et al., 2005). Nevertheless, the additional feature added to the cone of the smooth or non-threaded probe did not significantly improve the joint strength and material mixing. Consequently, left-hand threads were added to the tapered pin of tool ( $T_2$ ) to promote more effective material mixing.

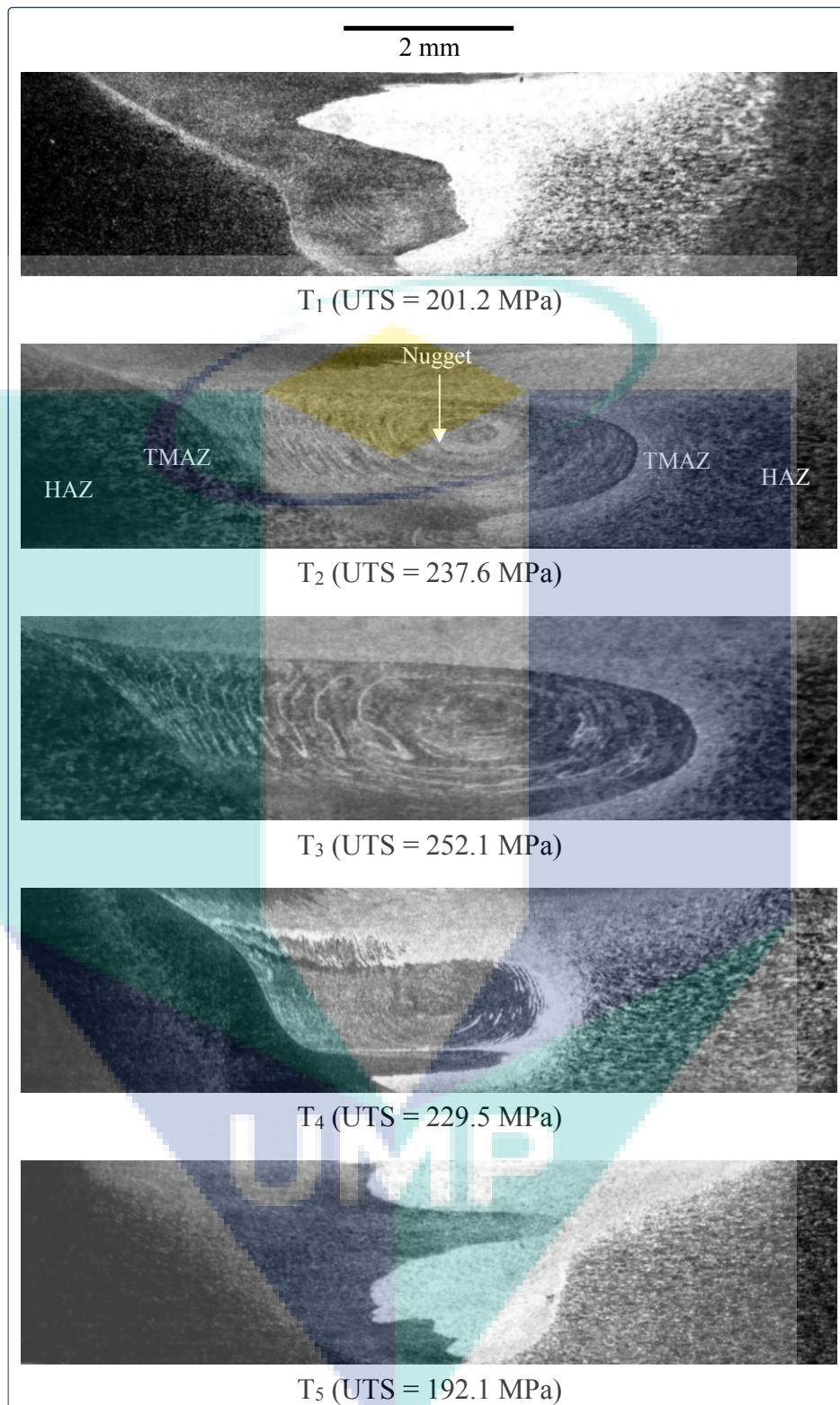


Figure 4.9 Macrographs of the weld nuggets related to the five welding tools with the observed ultimate tensile strength (UTS). The AA6061 alloy is placed on the left-hand side (AS) of each photo

Threads were fabricated in a direction opposite to that of the tool rotation in order to transport material from the shoulder down to the bottom of the pin to improve the

vertical material flow (Peel et al., 2003; Thomas & Dolby, 2003). With this tool, a noticeable growth in joint strength and an improved mixing of the base alloys at the weld zone were observed. The best outcomes were gained by stirring with tool (T<sub>3</sub>), which was similar to the previous one (T<sub>2</sub>) but with an additional tapered flat. By this tool, the base aluminum alloys were successfully friction stir welded with a very good surface finish, bigger nugget area, maximum elongation and high tensile strength (about 31% higher than T<sub>5</sub>). It is worth noting that the weld zone was free of internal voids in all joints, especially for those produced by the first and last tools. This is due to the proper and active design of clamping system and backing plates introduced in this work. The weld in the stir zone has exhibited the well-recognized onion rings, as shown in Figure 4.10.

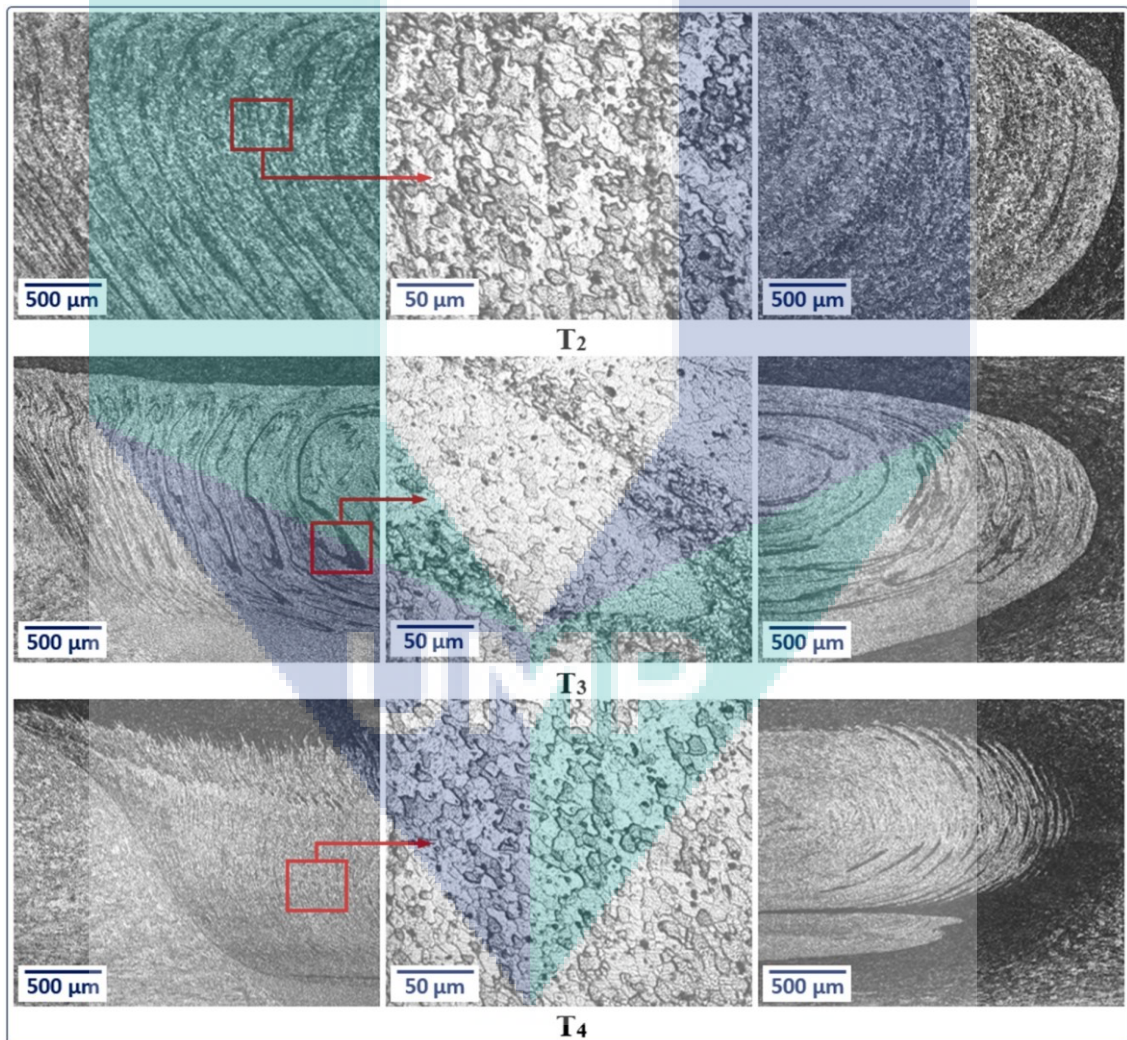


Figure 4.10 Macrographs of the weld nuggets related to the tools T<sub>2</sub>, T<sub>3</sub> and T<sub>4</sub> showing the onion rings. The AA6061 alloy is placed on the left-hand side (AS) of each photo

It would be rather difficult to understand the formation mechanism of onion rings. Some researchers explained the reasons of onion ring formation (Threadgill et al., 2009). They suggested that the onion ring was formed as a result of the extrusion of cylindrical sheets of material per each revolution of welding tool during its forward motion. The tool appears to wait for a very short time to produce frictional heat and extrude a cylindrical shaped material around the tool to the retreating side of the joint. They also found that the spacing between bands was equal to the pitch of forward motion of the tool in one rotation. Krishnan (Krishnan, 2002) stated that the formation of onion rings could be attributed to the process of frictional heating due to the rotation of tool and forward movement which extrudes the metal around to the retreating side of the tool. In addition to these explanations, the formation of onion ring could be attributed to the welding parameters such as rotation speed, welding speed and type of backing materials (Khodir & Shibayanagi, 2007). The clearer onion rings on the advancing side than retreating side could be attributed to the different rotating and travelling directions of the probe on both sides. The tangential component of the rotation has the same direction as the travelling direction on the advancing side, while the two directions are in opposite way on the retreating side. Thus, steeper gradient of plastic strain caused by the severer deformation mode eventually resulted in rather visible distinct between bands of onion ring on the advancing side (Yoon et al., 2016). The nugget zone resulted from the threaded tools T<sub>2</sub> (without flat) and T<sub>3</sub> (with single flat) were compared to the that produced by T<sub>4</sub>, which consisted of non-threaded probe with additional flat. The onion rings appeared more uniform when the threaded pin tool T<sub>2</sub> was used, while they were nearly vanished when the unthreaded tool T<sub>4</sub> was used. This is due to that when using a threaded probe in similar and dissimilar FSW, the material moves downward and a helical vertical rotational flow within the intermixed region generates beside the periphery of the rotating pin and hence forming the sub-layers or onion rings (Teimurnezhad et al., 2016). The shape of the rings was significantly changed when a flat was added to the cone of threaded pin tool T<sub>3</sub>. The flat pushed the abutting materials away from the probe and reduced the effect of threads. Nevertheless, the joint strength was not highly affected by the creation of such different layers.

The micro-hardness distribution along the transvers centerline of the weld related to the five welding tools at the central levels of the other three variables is presented in Figure 4.11. Overall, the welding joints have exhibited a noticeable decrease in the level

of Vickers hardness number compared to the base materials. This could be attributed to the grain refinement or recrystallization within the stir zone and the over-aging in the heat affected zone (Ahmed et al., 2017; Khan et al., 2017; Sun et al., 2016).

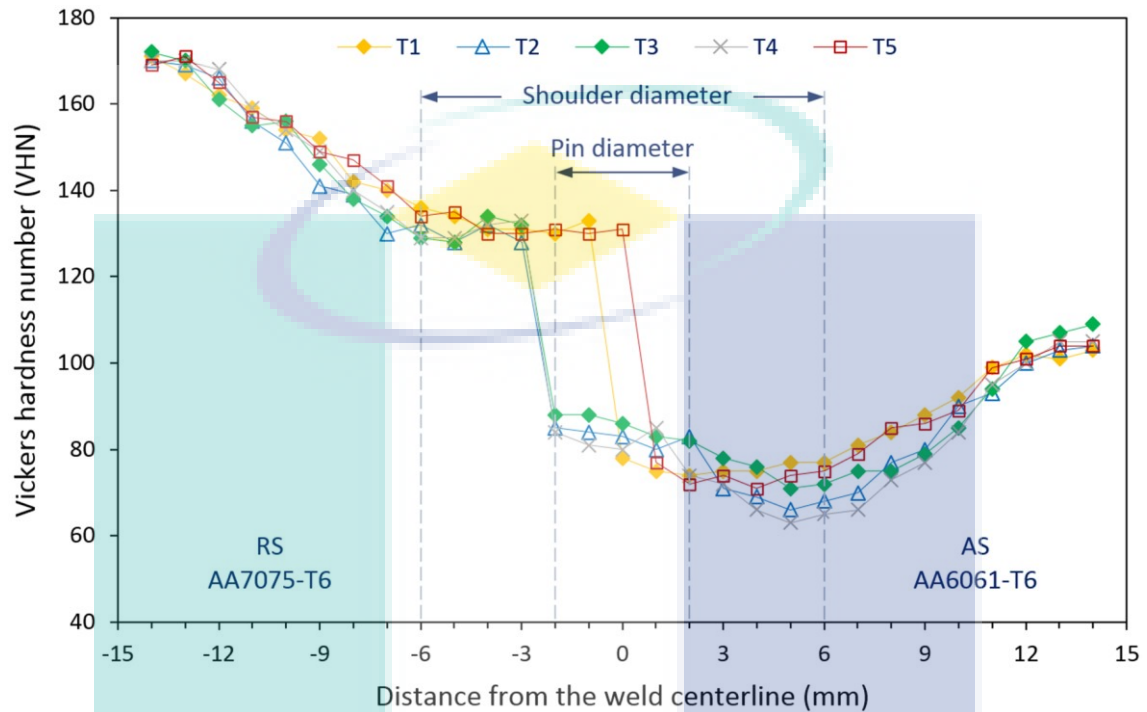


Figure 4.11 The weld micro-hardness distribution related to the five tools at the central levels of the other three variables

Maximum reduction of the weld hardness was observed in the HAZ of the AA6061-T6 alloy, which was fixed on the AS. The lowest hardness values of 63, 66 and 71 were measured in the welding joints produced by the welding tools T<sub>4</sub>, T<sub>2</sub> and T<sub>3</sub>, respectively. The fracture of the tension test specimens was initiated from the corresponding locations of these minimum hardness values at the HAZ. It was reported that the fracture takes place in the weakest region during the tensile test of the similar and dissimilar friction stir welds of aluminum alloys. In case of defect-free dissimilar friction stir welds, the HAZ of softer alloy represents the weakest region where the fracture commonly occurs (İpekoğlu & Çam, 2014; Rodriguez et al., 2015). On the other side, the fracture occurs within the stir zone if the weld nugget contains a certain weld defects and/or it has generated through insufficient material mixing (Pan & Lados, 2017; Sahu & Pal, 2017). This was happened during the tensile testing of the weld specimens made by using tools T<sub>1</sub> and T<sub>5</sub>. The VHN dropped at the nugget region of the corresponding

metallographic specimens due to the incomplete material mixing, as shown previously in the macrographs.

The results indicated that there is a clear relation between the material flow, tensile properties and hardness distribution of the friction stir welds. The complexity of the thermo-mechanical FSW process, especially in the case of dissimilar alloys, requires careful selection of the affecting parameters. The machine variables, tool design and clamping/backing system control the temperature generation and dissipation throughout the joining route (Colligan & Mishra, 2008; Yan et al., 2005). This in turn affects the material flow and tensile properties of welded coupons. Temperature in the workpiece must be high enough to adequately soften the abutting materials for the pin to stir but low enough to avoid access to the melting points (Tang et al., 1998). Too cold and too hot welding result in non-bonding and excessive material flow, respectively and hence degradation of the mechanical properties of the joint (Zettler, 2010; Zettler et al., 2010). The response surface and column graphs show that the highest weld strength of about 252 MPa could be achieved by applying 1100 rpm of rotation speed and 300 mm/min feed rate together with tool ( $T_3$ ), which tilted by  $3^\circ$  away from the vertical axes to the stirring direction. Since the joint efficiency for a dissimilar welding could be calculated based on the strength of softer material (Giraud et al., 2016), the achieved maximum joint strength represents an efficiency of about 82% with respect to the UTS of aluminum 6061-T6. This efficiency is 36% higher than the acceptable limit (60%) for the FSW of AA6061-T6 aluminum alloy as per the American Welding Society (AWS) standard (Dunn, 2016). The corresponding tensile elongation has increased from 3.2% for tool ( $T_5$ ) to about 7.1% for tool ( $T_3$ ). The tensile strength and elongation of the friction stir weldment started to decrease out of these conditions of the selected variables for all tool profiles.

#### **4.3.5 Effect of Materials Direction and Position**

The optimal pin tool profile and machine parameters were then used to investigate the effect of materials direction and relative location on the dissimilar friction stir weld. This study was conducted through eight case studies in two groups, as was explained previously in Section 3.8.2. The relative materials position and direction after the joining of specimen A3, in which the weld seam was parallel to the RD of AA7075 alloy and normal to the RD of AA6061 base material is presented in Figure 4.12.

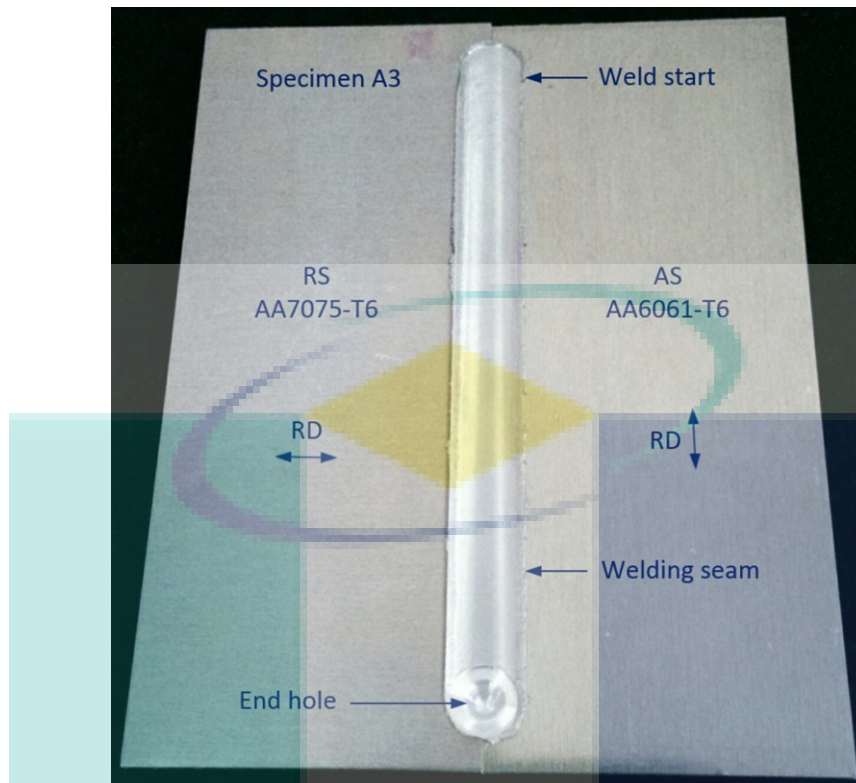


Figure 4.12 Photo of specimen A3 after welding showing the relative materials position and direction

#### 4.3.5.1 Microstructural Analysis

Micrographs of the weld nugget and the heat affected zones of specimen A3 are presented in Figure 4.13. This specimen has exhibited the best material mixing and tensile properties among the case studies of group A, when the softer AA6061-T6 was fixed on the advancing side of weld. The transportation of materials from the shoulder down to the bottom of the probe due to the pin tool threads which were fabricated in a direction opposite to that of the tool rotation generated the sub-layers or onion rings (Krishnan, 2002). The chemical composition of weld was analyzed in 14 different positions inside and beyond the nugget. The etching response of the dissimilar parent materials to the Keller's reagent are not the same due to the difference in their chemical composition (Firouzdor & Kou, 2010). For this reason, the micrographs revealed in dark and bright colors. Zone A shows an example of the different layers or onion rings, which is presented with a higher magnification through the SEM image in Figure 4.14. The corresponding EDS spectrums are also shown in this figure, and the complete chemical compositions of the analyzed regions are presented in Table 4.6.

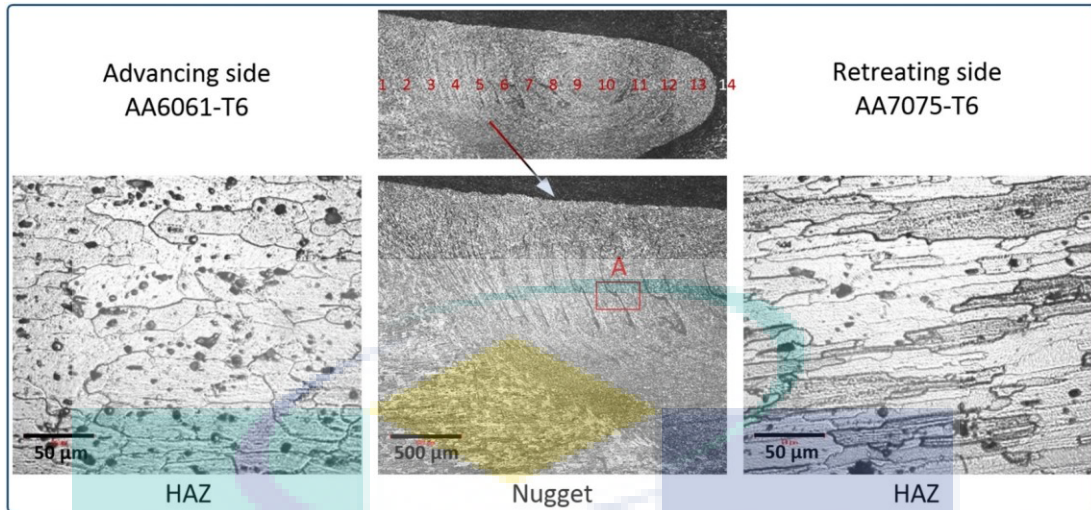


Figure 4.13 The weld microstructure of specimen A3

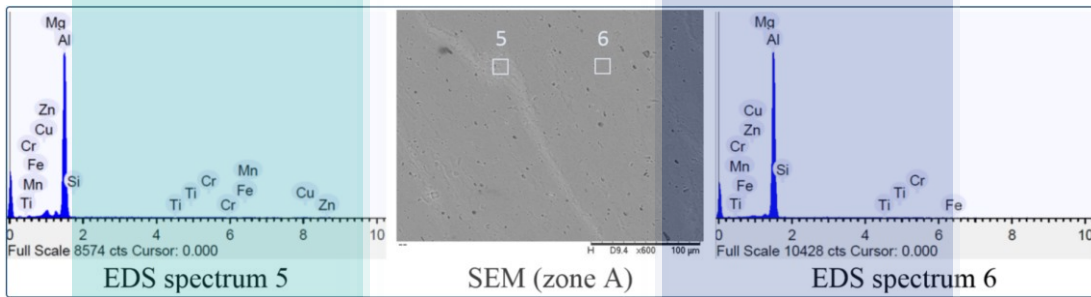


Figure 4.14 The SEM image of zone A shown in Figure 4.13 with the corresponding EDS spectrums

Table 4.6 The acquired chemical composition (wt.%) of the weld related to the spectrums shown in Figure 4.13

Spectrum	Si	Fe	Cu	Mn	Mg	Cr	Zn	Ti	Al
1	0.735	0.024	0.086	0.056	1.019	0.353	0.098	0.000	Balance
2	0.683	0.034	1.024	0.105	0.885	0.048	0.185	0.035	Balance
3	0.041	0.068	2.475	0.022	2.891	0.068	6.134	0.017	Balance
4	0.730	0.044	1.081	0.064	1.019	0.022	0.304	0.017	Balance
5	0.767	0.275	2.510	0.090	2.509	0.231	5.159	0.144	Balance
6	0.796	0.448	1.213	0.025	1.127	0.000	0.473	0.026	Balance
7	0.710	0.309	1.668	0.003	0.926	0.030	0.386	0.013	Balance
8	0.671	0.460	1.702	0.061	0.947	0.043	0.082	0.000	Balance
9	0.684	0.000	1.610	0.017	2.442	0.306	5.771	0.013	Balance
10	0.913	0.092	1.241	0.000	1.219	0.063	1.158	0.077	Balance
11	0.800	0.055	1.495	0.016	1.126	0.147	4.795	0.000	Balance
12	0.684	0.046	1.303	0.013	0.990	0.160	1.698	0.159	Balance
13	0.168	0.212	1.801	0.040	2.512	0.251	5.525	0.132	Balance
14	0.397	0.042	1.915	0.008	2.566	0.052	6.147	0.000	Balance
HAZ-6061	0.698	0.114	0.204	0.029	0.865	0.233	0.170	0.052	Balance
HAZ-7075	0.164	0.187	1.826	0.012	2.468	0.283	6.004	0.075	Balance
BM-6061	0.701	0.090	0.161	0.023	0.801	0.258	0.215	0.047	Balance
BM-7075	0.168	0.212	1.801	0.040	2.512	0.251	5.525	0.132	Balance

The results clarify that the bright rings are similar in composition to that of the AA7075-T6 alloy. The other wider regions are identical in composition to the softer AA6061-T6 base material. Spectrums 1 and 14 represent the TMAZ of the AA6061 alloy on the AS and TMAZ of the AA7075 on the RS, respectively. It was noticed that the chemical composition of these two regions are similar to their corresponding base materials. Same results were observed regarding the HAZ of both welding sides, which are close to their corresponding base alloys.

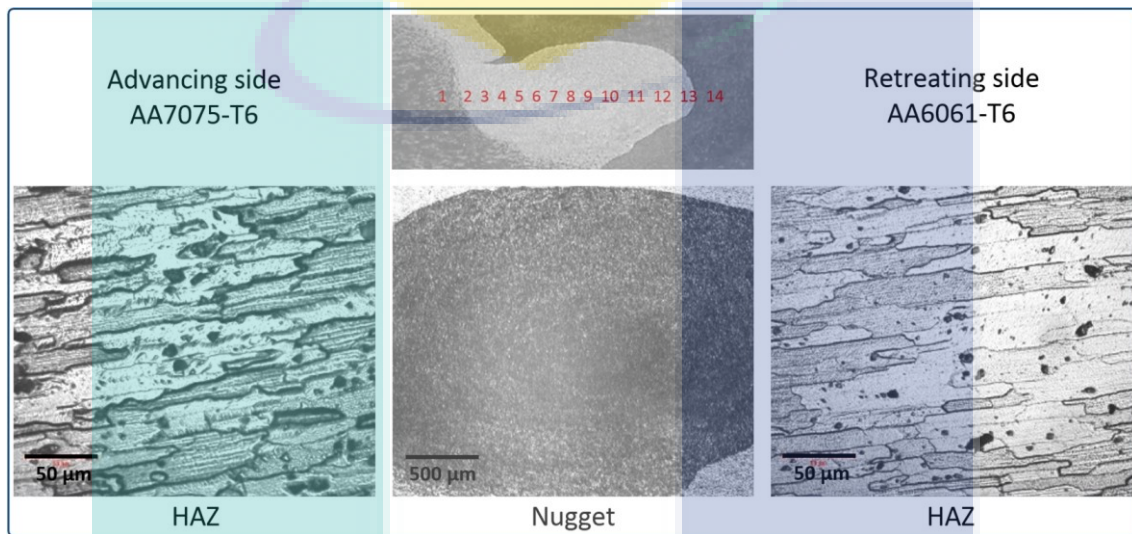


Figure 4.15 The weld microstructure of specimen A4

Table 4.7 The acquired chemical composition (wt.%) of the weld related to the spectrums shown in Figure 4.15

Spectrum	Si	Fe	Cu	Mn	Mg	Cr	Zn	Ti	Al
1	0.252	0.011	1.026	0.000	2.396	0.241	4.978	0.102	Balance
2	0.285	0.152	1.737	0.409	2.613	0.060	5.245	0.000	Balance
3	0.312	0.168	1.746	0.009	2.448	0.271	5.718	0.004	Balance
4	0.275	0.143	1.836	0.018	2.536	0.309	6.141	0.000	Balance
5	0.238	0.000	1.782	0.115	2.369	0.081	5.655	0.072	Balance
6	0.416	0.294	1.683	0.074	2.463	0.009	5.710	0.105	Balance
7	0.354	0.045	1.607	0.000	2.478	0.353	5.583	0.029	Balance
8	0.322	0.000	1.899	0.035	2.504	0.249	6.165	0.000	Balance
9	0.324	0.191	1.778	0.248	2.350	0.189	5.450	0.000	Balance
10	0.579	0.000	1.614	0.062	2.650	0.064	4.913	0.004	Balance
11	0.415	0.006	1.705	0.057	2.436	0.304	5.673	0.016	Balance
12	0.354	0.071	1.802	0.114	2.522	0.232	6.038	0.105	Balance
13	0.406	0.000	1.762	0.068	2.538	0.201	5.847	0.110	Balance
14	1.022	0.191	0.323	0.002	0.781	0.000	0.281	0.268	Balance
HAZ-6061	0.716	0.046	0.185	0.040	1.036	0.320	0.227	0.039	Balance
HAZ-7075	0.097	0.241	1.943	0.061	2.704	0.196	5.853	0.115	Balance
BM-6061	0.701	0.090	0.161	0.023	0.801	0.258	0.215	0.047	Balance
BM-7075	0.168	0.212	1.801	0.040	2.512	0.251	5.525	0.132	Balance

Figure 4.15 shows the micrographs of the weld nugget and heat affected zones of specimen B4, which exhibited the best material mixing and tensile properties among the case studies of group B in which the harder AA7075-T6 was fixed on the advancing side. The dynamic recrystallization caused in fine grains inside the nugget zone, and much more smaller grains are seen in this case compared to the previous one. The onion rings disappeared, and the nugget seemed uniform but smaller in size than that of specimen A3.

In a same way, the chemical composition was analyzed by an energy dispersive spectrometry in 14 different regions inside and close to the weld nugget. The corresponding results are presented in Table 4.7, which indicate that the chemical composition of weld nugget is more similar to the AA7075 aluminum alloy. As in the previous case study, the TMAZ and HAZ regions of each parent material contains a chemical composition similar to their corresponding base materials. It is worth noting herein that the grains of welding materials at the heat affected zones were highly stretched when the harder AA7075 alloy was placed on the AS. This extension results in a strain concentration at the HAZ and hence reduces the hardness level in this critical area (Li et al., 2015; Xu et al., 2013). In a word, better materials mixing was achieved through the A3 configuration, when the tool stirred in a direction parallel to the RD of AA7075 alloy and normal to that of AA6061 aluminum alloy when the softer alloy placed on the AS.

#### **4.3.5.2 Tensile Properties and Hardness Distribution**

Results of the tensile tests are presented in Figure 4.16. The mean value of the recorded results was considered for each case, and the indicated standard error which is calculated based on the standard deviation has not exceed 3%. It is obvious that the welding joints of group A, in which the AA6061 alloy was placed on the AS, have exhibited a certain joint strength increase compared to those of group B where the AA7075 alloy was located on the AS. This behavior is comparable to the observations outlined in some previous studies for placing the softer material on the AS (Guo et al., 2014; Jamshidi Aval et al., 2011; Lee et al., 2003; Park et al., 2010). Ultimate joint strength increased from 221.3 MPa for specimen B2, passing through 252 MPa for specimen A1 and reached the apex value of about 255.8 MPa for specimen A3. These results indicated that the weld strength can be improved when the welding tool is stirred in a direction parallel to the RD of the abutting plates (specimen A1) and could be further

raised when the weld seam is made in a direction parallel to the RD of AA7075-T6 and normal to that of AA6061-T6 (specimen A3). It is also clear that the joint strength has decreased when the weld line was normal to the RD of both welding sheets regardless of the relative materials position on the advancing and retreating sides. The highest elongation at break of about 7.16% was also recorded in specimens A3, which was about same of that resulted from specimen A1.

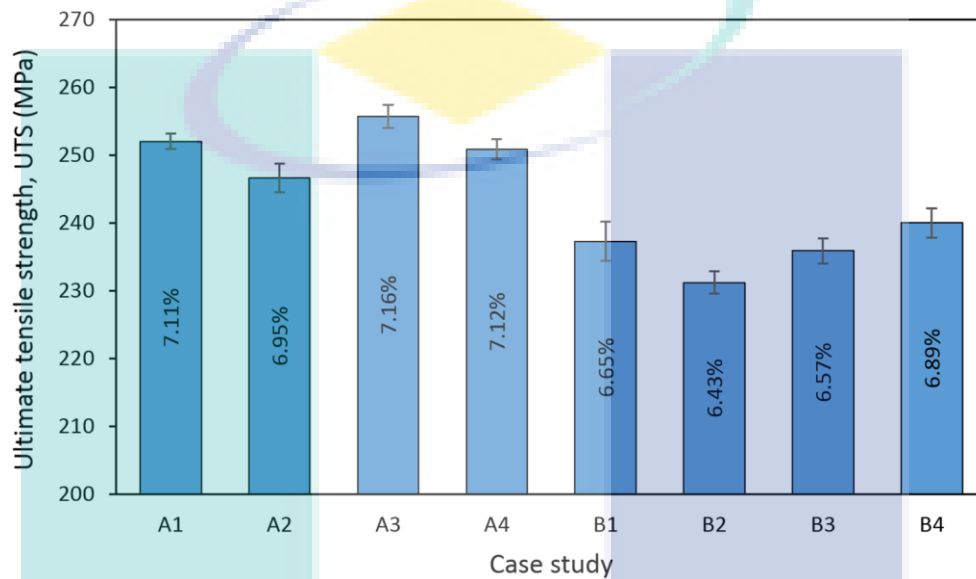


Figure 4.16 The weld tensile strength and percent elongation related to the materials position and rolling direction

Figure 4.17 presents the results of transverse weld micro-hardness of the eight specimens. The weld hardness was less than those of the base materials for all case studies. Slight difference in the VHN distribution was noticed within each group of specimens. The weld nugget has seen to be harder when the higher strength AA7075 alloy was placed on the advancing side. This is due to the chemical composition of weld in this case, which was close to that of the AA7075-T6 alloy (Khodir & Shibyanagi, 2008). On the other hand, the HAZ of AA6061 side showed the lowest hardness level. This drop of hardness could be attributed to the amount of heat generated during the welding process and the extension of grains in this region. It was reported that higher frictional heat is created when the harder alloy is positioned on the AS (Al-Badour et al., 2014; Cole et al., 2013).

In group A, the minimum hardness number of about 67 was recorded in specimen A2, while it was about 61 in specimen B2 which was the lowest value in group B and

whole case studies. In these two configurations, the welding seam was produced in a direction normal to the RD of the welding parent materials. On the other side, the minimum hardness numbers of about 73 and 66 were measured in specimens A3 and B4, respectively at the HAZ of the softer AA6061 alloy.

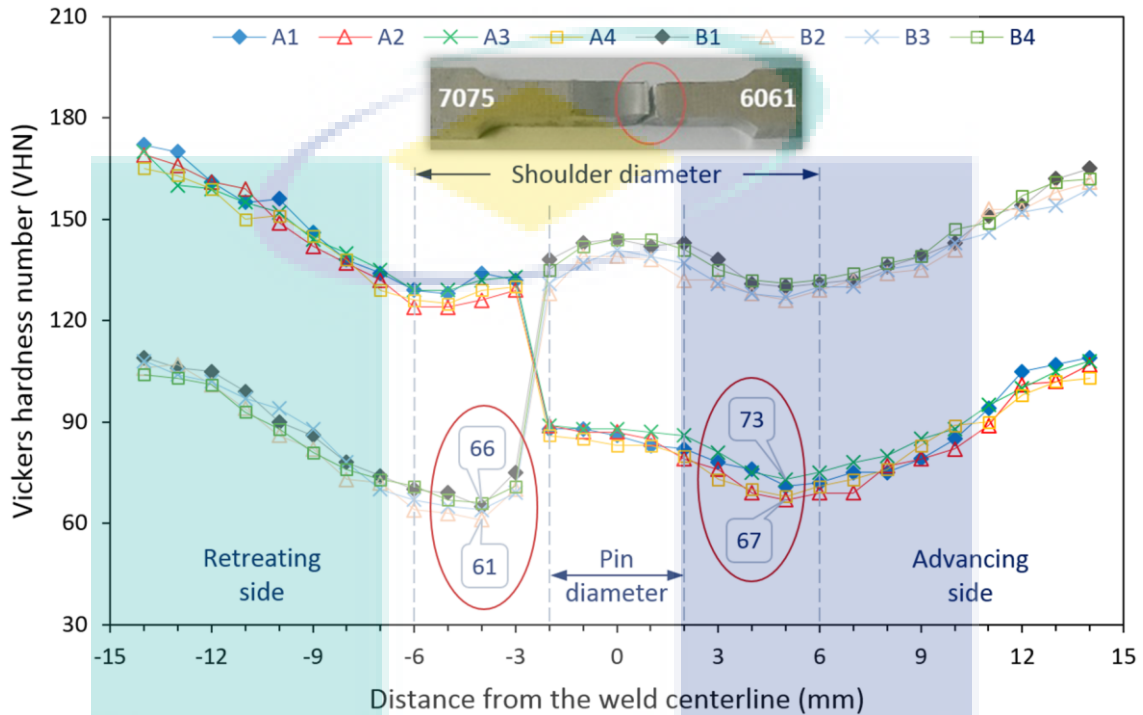


Figure 4.17 The weld micro-hardness distribution related to the materials position and rolling direction

Regardless of the relative materials position, all specimens were failed during the tensile tests in the HAZ of the AA6061 alloy where the maximum drop of hardness has occurred. The red ellipse shows the fracture zones of the tensile specimen and the corresponding VHN of the transverse weld centerline. This critical region represents the weakest zone of the defect-free friction stir welds.

In short, stronger joint could be achieved by placing the softer alloy on the advancing side of the weld and stirring the tool in a direction parallel to the RD of the abutting plates. The weld strength could be further improved when the weld seam is produced in a direction parallel to the RD of the softer material and normal to that of the harder one. Accordingly, the length of the welding coupons of the next joining tests will be parallel to the rolling direction of the as-received plates.

#### 4.4 FSW of Dissimilar AA7075-T6 and AA2024-T351 Aluminum Alloys

In this section the results of joining the 6-mm-thick AA7075-T6 and AA2024-T351 aluminum alloys by the FSW are presented. Several trials were made to join small workpieces of the dissimilar high-strength alloys using different process parameters. Single welding tool with the design presented in Figure 3.4-(b) was fabricated for these tests.

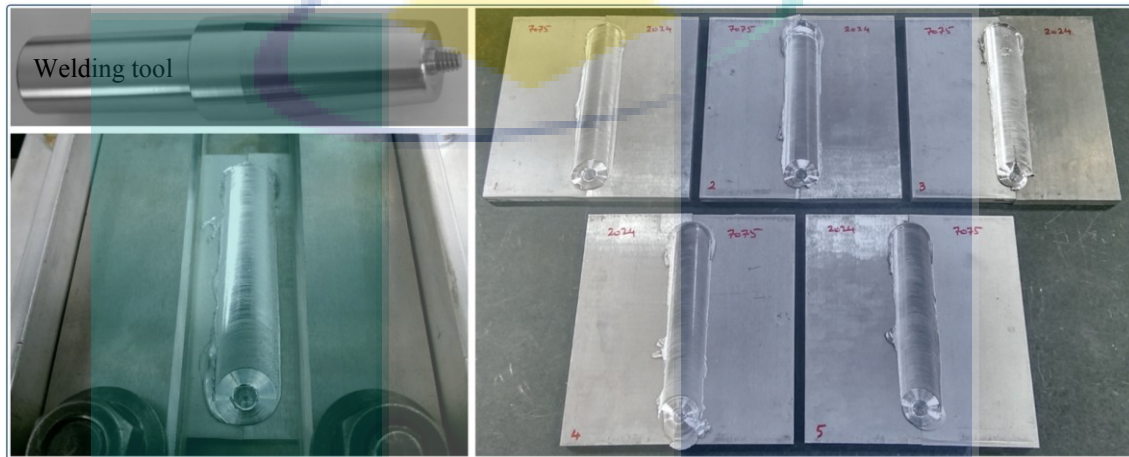


Figure 4.18 The initial welding trials of the 6-mm-thick AA7075-T6 and AA2024-T351 aluminum alloys

As shown in Figure 4.18, the welding trials were performed using the simplified design of backing system and fixtures shown previously in Figure 3.6, which was used during the joining of the 3-mm-thick AA6061 and AA7075 sheets. The objective of these initial welding trials is to test the fabricated tool and inspect the dissimilar joint under various welding speeds and relative materials position.

As per the literature findings presented in Table 2.1, three welding traverse speeds between 100 and 250 mm/min were tested using 1200 rpm of spindle speed and 3° of tilt angle. The AA2024 alloy was fixed on the AS in the first three welds, while it was placed on the RS in the other two joints. The workpieces were successfully joined within the range of selected parameters. Accordingly, a group of welding tools identical in design to the tested one were ordered to proceed with the research study. The developed backing/clamping system shown in Figure 3.7-(a) was then used to join the prepared welding coupons during the next stages of the current work.

Figure 4.19 presents a photograph captured during the joining of dissimilar AA7075-AA2024 aluminum alloys using the developed backing/clamping system, and selected group of the produced welding joints.

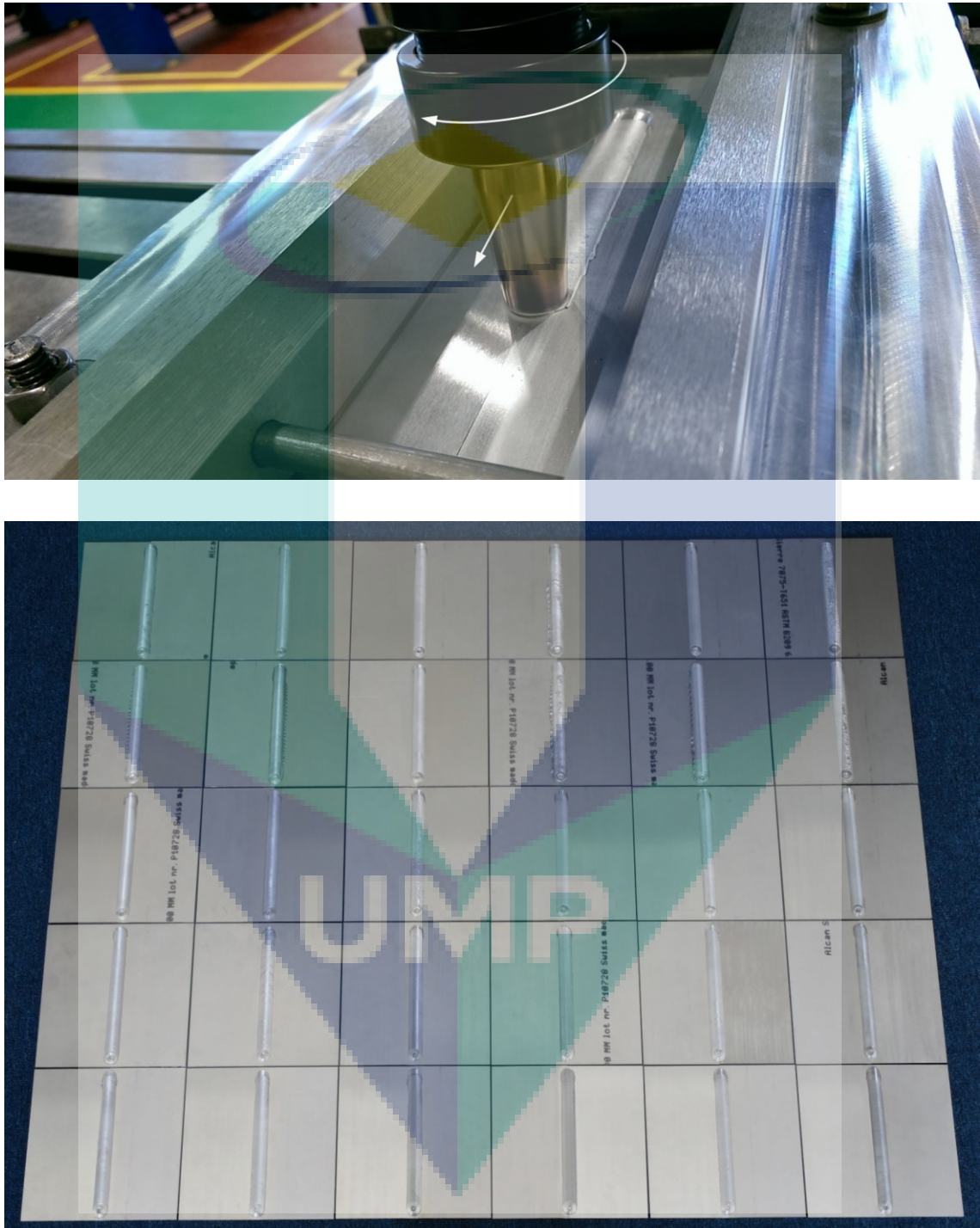


Figure 4.19 A photograph captured during the joining of dissimilar AA7075-AA2024 aluminum alloys using the developed backing/clamping system, and selected group of the produced welding joints

#### 4.4.1 Effect of Clamping Force

The influence of clamping pressure on the static strength of welding joint was investigated using equal vertical and lateral compressive forces. The aim of this part of the study is to identify the most suitable clamping force for the current welding conditions which could be then applied throughout the next stages of the work.

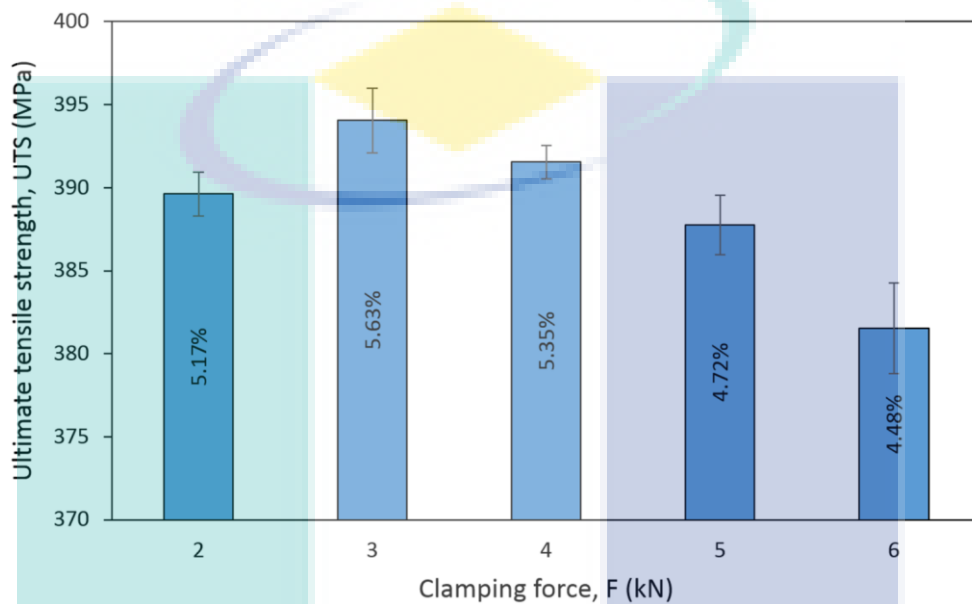


Figure 4.20 Joint tensile strength and percentage elongation related to the applied clamping forces

Six clamping forces were examined using the truncated threaded pin tool under 1200 rpm of spindle speed, 100 mm/min of traverse rate and 3° of tool tilt angle. The AA2024 aluminum alloy was always fixed on the AS. First, the workpieces were secured on the composite backing plate using 1 kN of vertical and lateral clamping forces. The weld under this clamping condition was cancelled since the applied compressive pressure was not enough to prevent the workpiece separation at the weld start. The clamping force was then successively increased from 2-6 kN in five welding trials.

Figure 4.20 presents the results of the weld tensile strength and percentage elongation related to the applied clamping force. It was noted that all joints were free of initial gap, and the most suitable clamping force for the current welding conditions is 3 kN. At this level of the compressive force, the welding joint has exhibited the highest mean tensile strength and elongation of about 394 MPa and 5.63%, respectively. Raising the clamping force to 6 kN resulted in a gradient reduction of the weld tensile strength

and percent elongation, which have reached the lowest mean values of about 381 MPa and 4.48%. At this relatively high compressive clamping force, the welding seam appeared nonuniform as shown in Figure 4.21. The weld at the end quarter of the joining route exhibited excessive material flow at the surface of the welding seam, as illustrated by the red dash borderline. This could be attributed to the high lateral compressive stresses and the elevation of the process temperature. The backing plate and tool shoulder restrict the plasticized abutting materials from flowing out, but the compressed materials escaped from the shoulder edge during the joining sequence. Consequently, the lateral clamping force applied by the long bolt close to the end of the weld (see Figure 3.7-(a) and Table 3.6) was lower than its initial value. This was clear during the release of the dissimilar welded plates from the backing/clamping system after the end of the joining process.

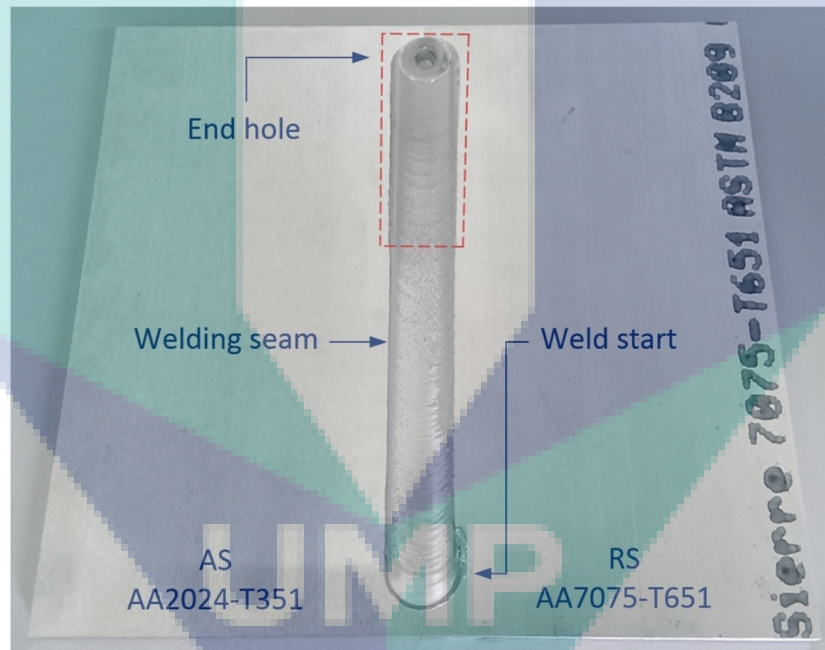


Figure 4.21 The weld profile under 6 kN of clamping force

Decreasing the lateral clamping force at the end of weld is in accordance with the results obtained by Richter-Trummer et al. (Richter-Trummer et al., 2012) during the FSW of 3.18-mm-thick AA2198-T8 aluminum alloy. They found that at high clamping force, the final horizontal clamping force was significantly reduced, and they attributed this behavior to the shape distortion of the welding coupons since no cover plate was used. The optimal clamping force was then fixed all over the next welding tests.

#### **4.4.2 Effect of Tool Rotation Speed**

This part presents the results of the investigation that has been conducted to inspect the optimal spindle speed for maximum joint strength. The reason behind this study is the difference found in the literature regarding the previously applied welding parameters during the FSW of dissimilar AA7075-AA2024 aluminum alloys, as has been discussed in Section 2.3.2. In addition, there has no open access article could be found in the literature concerning the friction stir welding of the developed aircraft AA2024 aluminum alloy in the T351 temper condition to the highest strength aluminum 7075-T6. Accordingly, ten pairs of welding coupons were joined by the friction stir welding using five tool rotation rates between 600 and 1800 rpm considering the materials position on the advancing and retreating sides of the weld. The travers speed was fixed at 100 mm/min, and the welding tool was tilted with 3°. The welded joints were examined through visual inspection, metallographic analysis and tensile testing. The following sections introduce the obtained results with their detailed discussion.

##### **4.4.2.1 Visual Inspection of the Weld Surface**

The visual monitoring was adopted to examine the surface finish of the resulting welds. Figure 4.22 shows the surface finish of the welding seam according to the tool rotation rate and placement of the aluminum alloys on the advancing and retreating sides of the weld. Regardless of the relative materials position, surface defects were significantly grown when the spindle speed was increased. This can be attributed to the increase of heat generated during the welding process, which is proportional to the tool rotation rate (Zettler, 2010; Zettler et al., 2010). Too hot welding condition results in an excessive material flow and leads to material expulsion. The excessive flash and surface galling or scaling shown at 1500 and 1800 rpm are clear results of this materials overflow. The most excessive flash was formed at the AA7075 side when the AA2024 was placed on the AS. On the other hand, better surface finish was observed at 900 rpm when the AA7075 was located on the AS. This gives an indication that the relative position of the base materials is also affects the heat generation and material flow in dissimilar FSW, since the amount of heat generated during the welding process is sensitive to the material location and spindle speed (Al-Badour et al., 2014; Mironov et al., 2015).

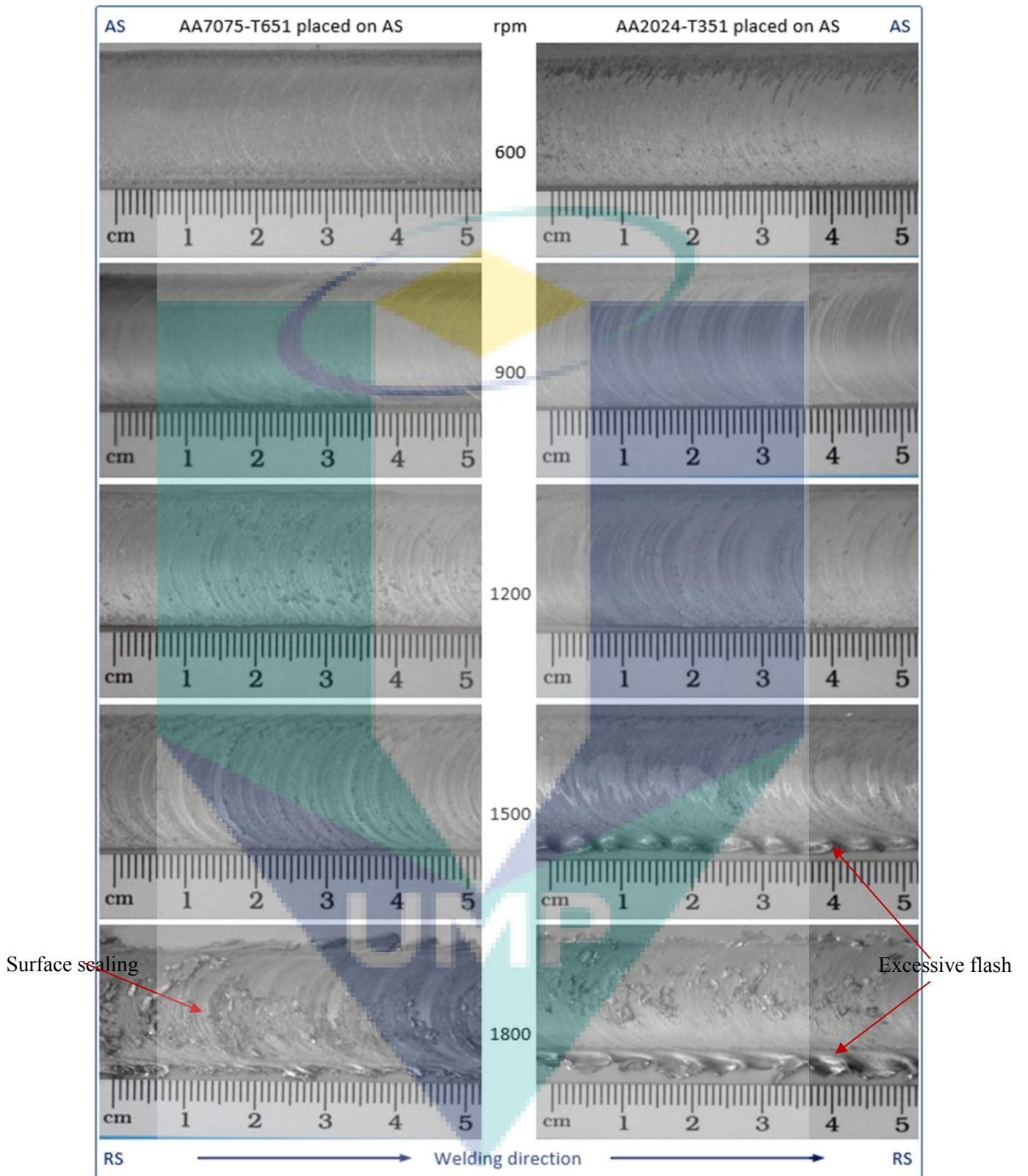


Figure 4.22 Surface finish of the resulting welds at different tool rotation speeds and materials position

#### 4.4.2.2 Metallographic Analysis

Weld macrographs related to the tool rotation rate and materials location are presented in Figure 4.23. The metallographic specimens were prepared along the weld cross section, and the right-hand side of each photo represents the advancing side of welding tool. The high strain rate due to the tool rotation and translation resulted in a severe deformation and dynamic recrystallization of the grains at the mixing stir zone (Mishra et al., 2015).

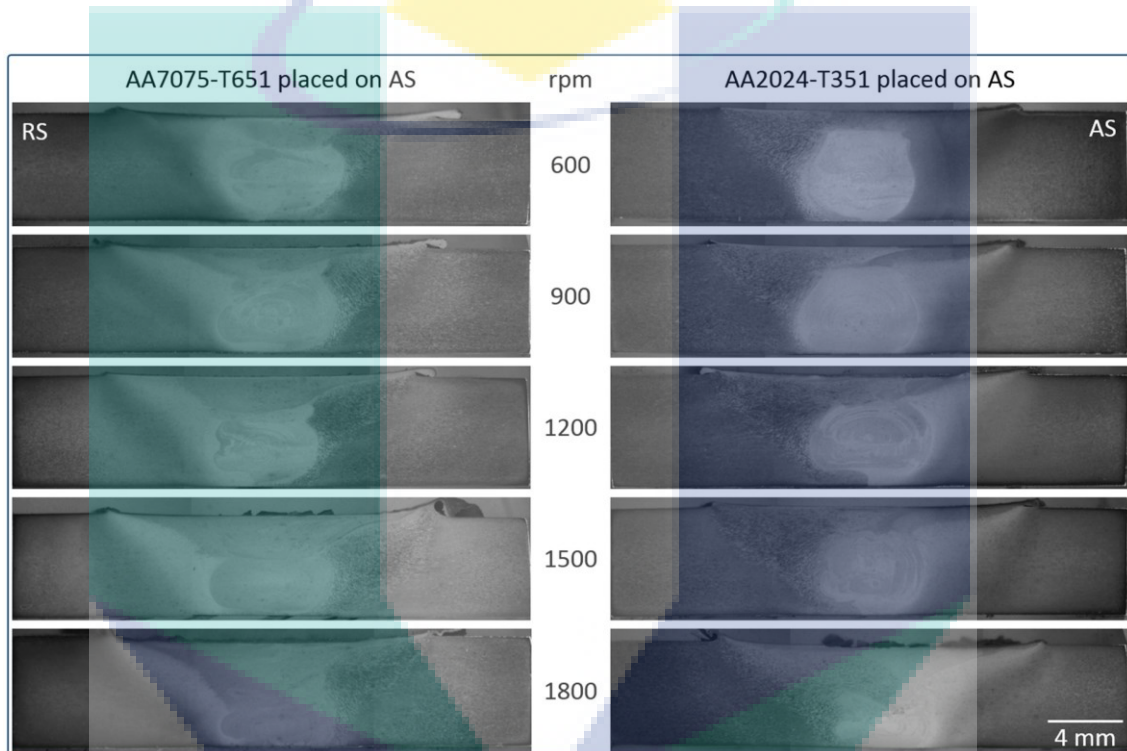


Figure 4.23 Macrographs of the weld at different tool rotation speeds

It is well established that vertical and circular plastic flows of the coupled materials occur during the FSW process (Luo et al., 2016). The left-hand threads of the pin tool push the material down away from the shoulder in conjunction with the circular motion of the tool. The heat generated and materials movement lead the grains of the base alloys to enter into each other and form the weld nugget (Trimble et al., 2015). Fine grains are seen in Figure 4.24 in the weld nugget when the spindle speed was fixed at 600 rpm. The nugget seemed inhomogeneous when the harder AA7075 alloy was placed on the AS. The materials flow and mixing were improved, and the nugget became more uniform when the tool was rotated with 900 rpm.

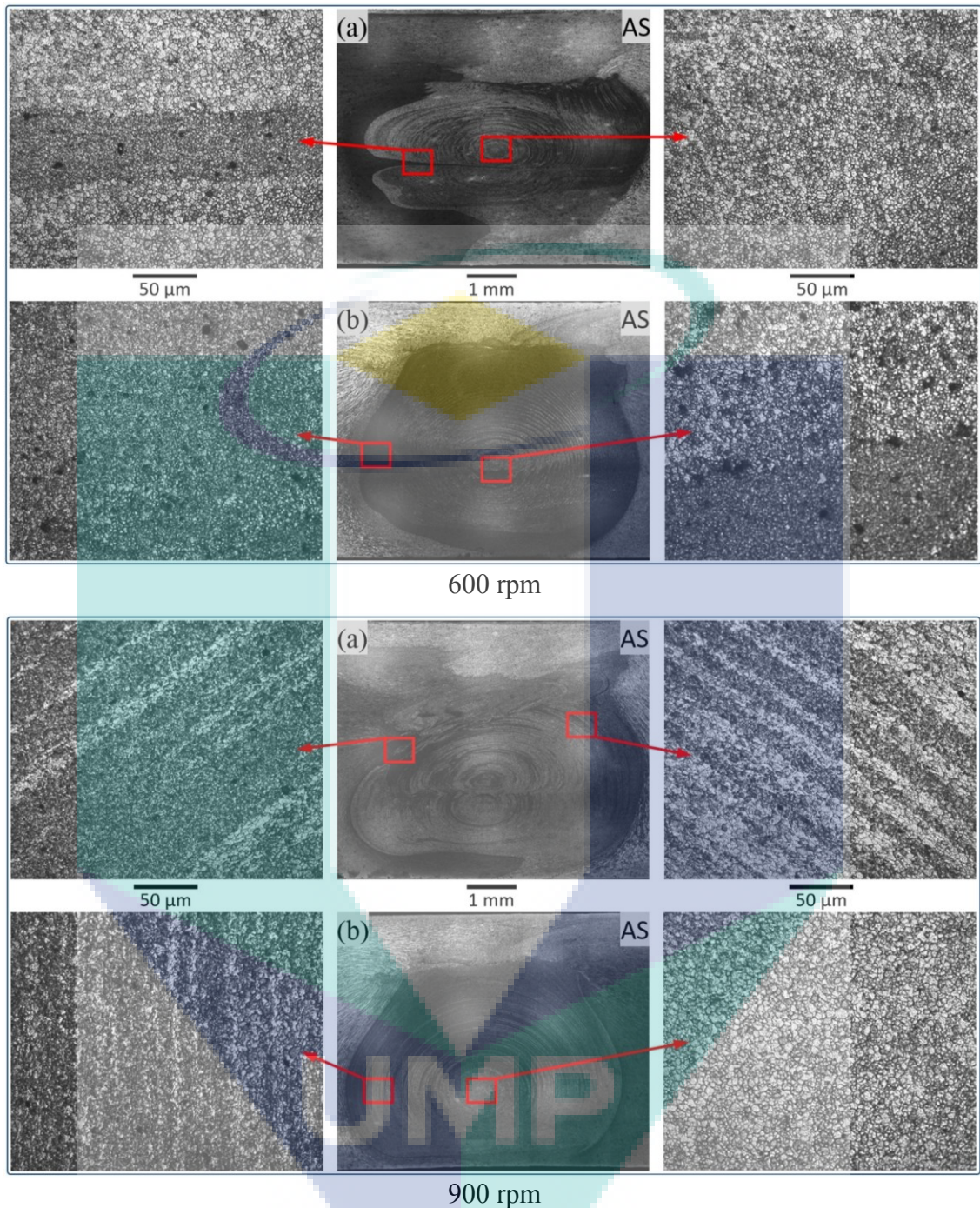


Figure 4.24 Micrographs of the weld nugget at 600- and 900 rpm of spindle speed. (a) AA7075-T6 placed on AS and (b) AA2024-T351 placed on AS

The penetration of the softened materials into each other seemed to be incomplete when the AA7075 was placed on the AS, and discontinued onion rings were seen at the advancing and retreating sides of the weld. Much more uniform mixing and concentric rings were observed when the AA2024 was fixed at the advancing side. This is because the materials on the advancing and retreating sides have different flow patterns and the two alloys have very different flow stress (Guo et al., 2014). The higher flow stress of

harder AA7075 alloy, when located on the advancing side, makes it very difficult for softer alloy to penetrate into the nugget (Khodir & Shibayanagi, 2007). Because of the materials mixing in the welding stir zone, the grains at TMAZ are stretched and rotated, as seen in the micrographs of Figure 4.25.

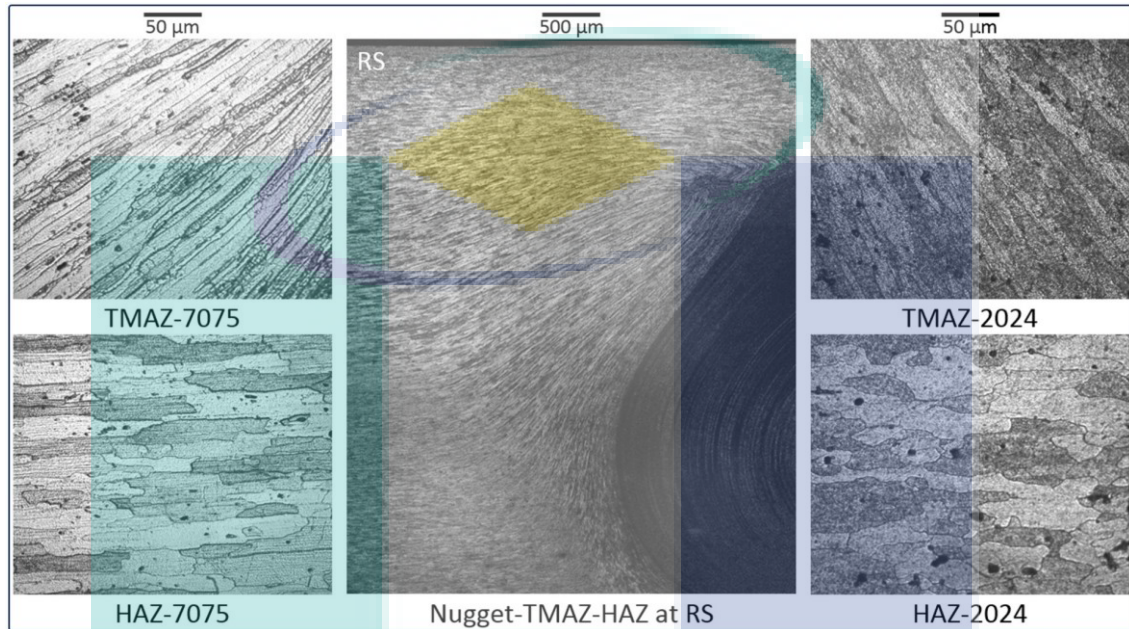


Figure 4.25 Micrographs of the weld nugget-TMAZ-HAZ at 900 rpm. AA7075-T6 placed on RS

This could be attributed to the vertical and circular materials flow due to the tool rotation and stirring, in addition to the threads of the pin (Peel et al., 2003; Thomas & Dolby, 2003). The grains were severely bent from deformation without recrystallization, while they were slightly stretched in the HAZ but without bending (Cavaliere et al., 2005). It was reported that the stretching of the grains at the HAZ-TMAZ increases the concentration of the strain at these welding zones where the fracture arises during the tensile testing (Mahoney et al., 1998).

The weld nugget looks like the onion in which the concentric rings appeared thinner at the edges and become thicker towards the nugget center (NC), as seen in Figure 4.26. Thickness of the onion rings increased from less than 10  $\mu\text{m}$  close to the TMAZ to more than 130  $\mu\text{m}$  near the NC. The weld layers in the nugget appeared in different colors due to the variation of materials response to the Keller's reagent (Firouzidor & Kou, 2010). For this reason, the micrographs revealed in dark and bright colors. The chemical composition of materials at these different layers and at the HAZ/TMAZ were analyzed

and compared with those of the base welding alloys. Table 4.8 presents the acquired records of the energy dispersive spectrometry.

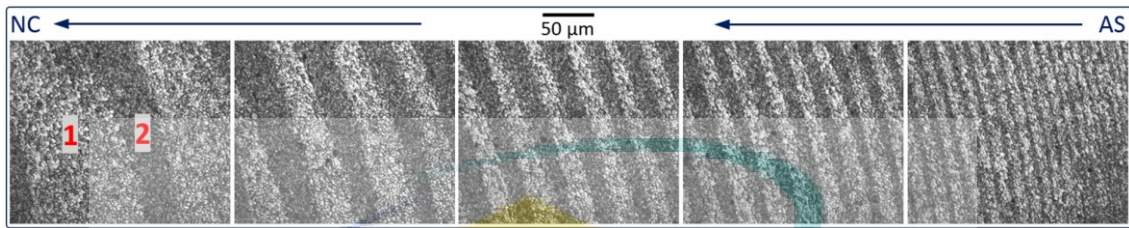


Figure 4.26 Variation of the onion rings from the edge of weld nugget close to the AS towards the nugget center (NC) at 900 rpm. AA2024-T351 placed on AS

Table 4.8 The chemical composition (wt.%) of the weld HAZ, TMAZ and the regions shown in Figure 4.26 at 900 rpm

Spectrum	Si	Fe	Cu	Mn	Mg	Cr	Zn	Ti	Al
1	0.035	0.224	2.626	0.295	2.159	0.098	4.233	0.026	Balance
2	0.173	0.122	4.793	0.243	1.620	0.041	1.614	0.053	Balance
HAZ-7075	0.032	0.009	1.655	0.067	2.428	0.044	5.815	0.092	Balance
HAZ-2024	0.185	0.087	4.069	0.439	1.444	0.046	0.223	0.054	Balance
TMAZ-7075	0.066	0.073	1.750	0.101	2.501	0.020	5.794	0.089	Balance
TMAZ-2024	0.169	0.019	4.058	0.739	1.447	0.086	0.114	0.075	Balance
BM-7075	0.013	0.056	1.516	0.118	2.553	0.017	5.968	0.067	Balance
BM-2024	0.124	0.026	4.122	0.820	1.587	0.073	0.156	0.093	Balance

The results clarified that the bright layer (spectrum 1) has contained more of the aluminum 7075 composition such as Zn and Mg. On the other side, the dark region (spectrum 2) consisted of higher copper ratio and hence it was more comparable to the AA2024 base alloy. It is also obvious that the non-recrystallized HAZ and TMAZ in both welding advancing and retreating sides are similar to their corresponding parent materials. This behavior was also outlined in several previous articles regarding the FSW of similar and dissimilar materials (Kumar et al., 2015; Mishra et al., 2015; Tan et al., 2017). It was reported that the grains in these welding zones are stretched without any change in their chemical composition.

At 1200 rpm, the grains seemed to be bigger and the weld nugget seemed different, as shown in Figure 4.27. The non-recrystallized and recrystallized TMAZ of the AA7075 alloy are clear in this figure when this harder base material was placed on the AS. Variation of the nugget structure can be observed when the softer AA2024 alloy

was fixed on the AS. The edge of the nugget was surrounded with a dark thin layer, and the onion rings were distorted.

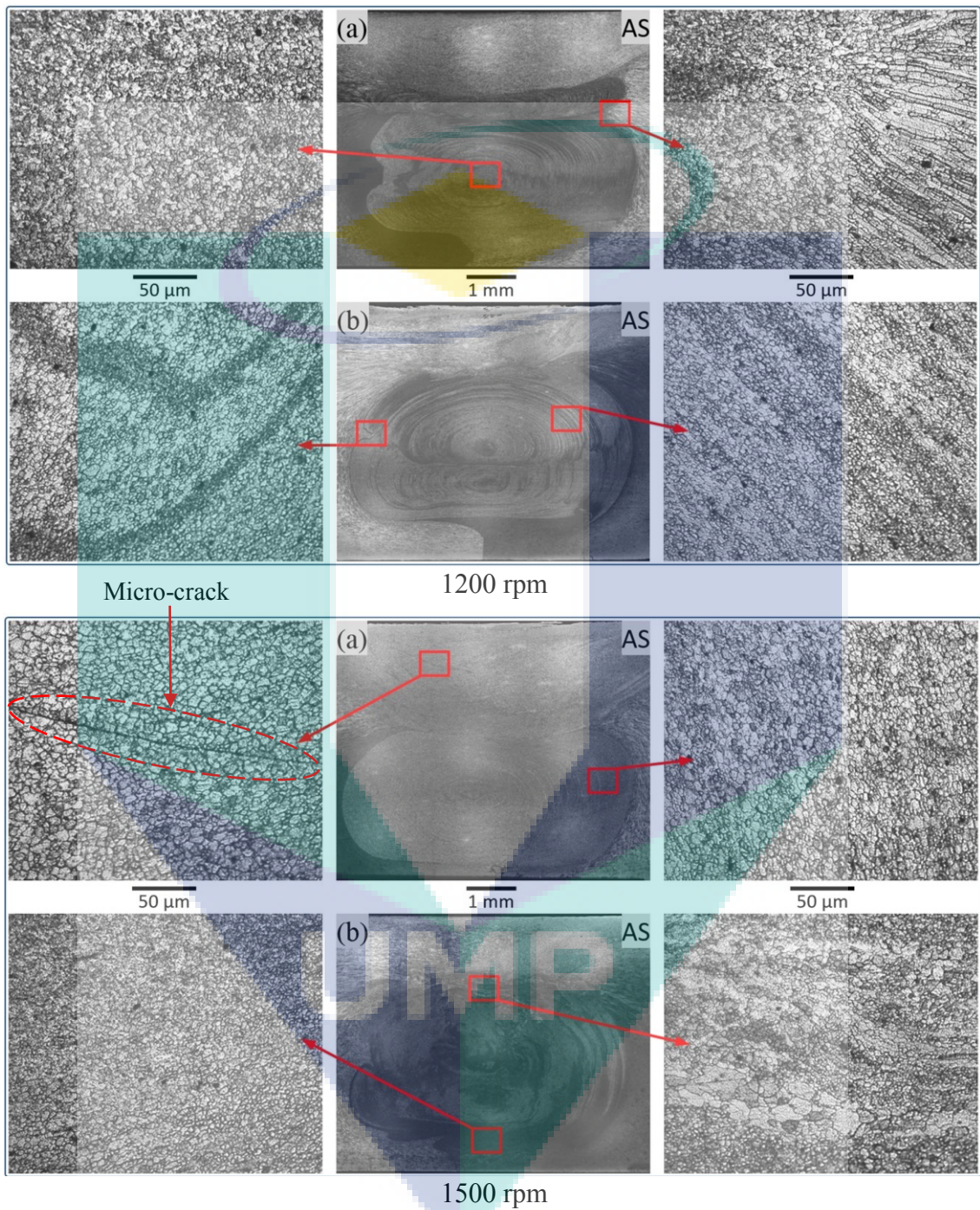


Figure 4.27 Micrographs of the weld nugget at 1200- and 1500 rpm of spindle speed. (a) AA7075-T6 placed on AS and (b) AA2024-T351 placed on AS

Long micro-cracks are created in the crown of the nugget when the spindle speed was increased to 1500 rpm and the harder AA7075 aluminum alloy was fixed on the AS. The weld nugget started to degrade due to the relatively high rotation rate when the softer

AA2024 alloy was positioned on the AS. At this material placement, non-equiaxed grains are generated within the weld nugget. The difference in material flow and mixing related to the material fixed position could be attributed to the resistant of the welding base alloys to deformation (Fujii et al., 2006). The hard-to-deform AA7075 alloy is forced to inter into the other material with a high rotation rate when it placed on the AS. This in turn resulted in a considerable change in the onion ring pattern and generate the internal cracks.

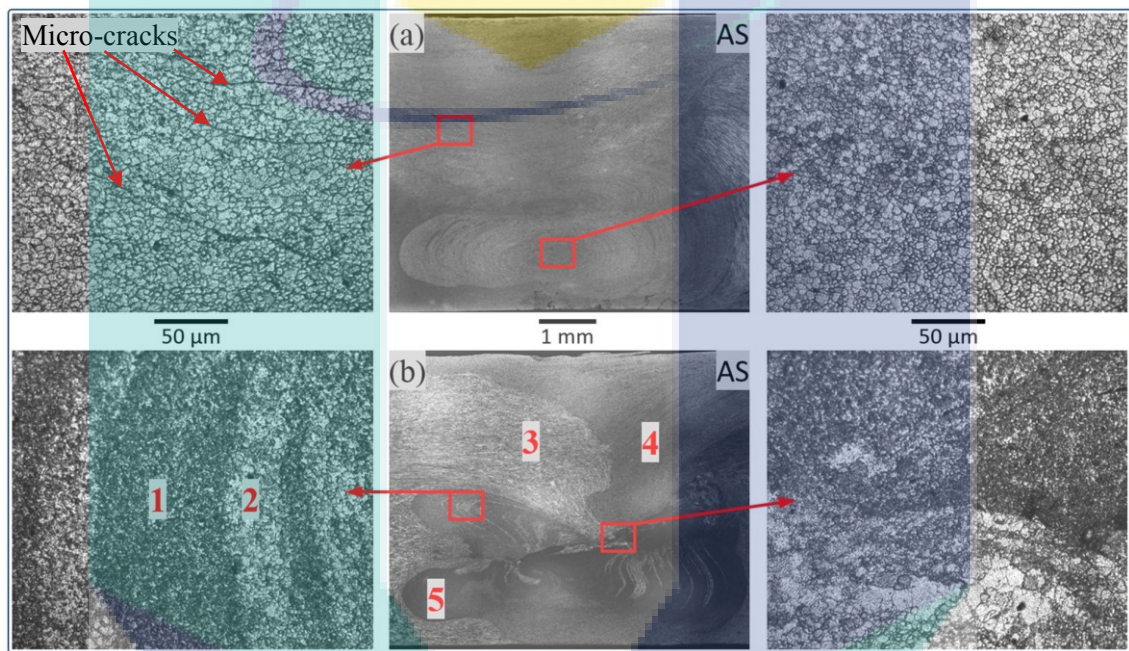


Figure 4.28 Micrographs of the weld nugget at 1800 rpm. (a) AA7075-T6 placed on AS and (b) AA2024-T351 placed on AS

Table 4.9 The chemical composition (wt.%) of the weld related to the regions shown in Figure 4.28 at 1800 rpm

Spectrum	Si	Fe	Cu	Mn	Mg	Cr	Zn	Ti	Al
1	0.165	0.023	4.921	0.000	0.428	0.066	0.653	0.004	Balance
2	0.104	0.094	1.863	0.409	0.002	0.126	5.591	0.043	Balance
3	0.357	0.194	1.697	0.003	2.433	0.275	6.075	0.000	Balance
4	0.152	0.000	5.466	0.497	1.440	0.000	0.439	0.017	Balance
5	0.188	0.083	4.971	0.115	0.423	0.023	1.217	0.053	Balance
BM-7075	0.013	0.056	1.516	0.118	2.553	0.017	5.968	0.067	Balance
BM-2024	0.124	0.026	4.122	0.820	1.587	0.073	0.156	0.093	Balance

Figure 4.28 shows clearly that the weld nugget has collapsed when the rotation speed was raised to 1800 rpm. This can be attributed to the excessive material flow and high power input (Zettler, 2010). This in turn resulted in a relatively bigger grain size and

non-uniform material mixing. Long micro cracks were created when the AA7075 was placed on the AS. On the other side, inhomogeneous grains were appeared when the AA2024 was located on the AS. These non-equiaxed grains were formed in the stir zone due to the relatively high circular material flow. The weld zone consisted of different regions, which revealed in various colors after the chemical etching. The EDS evaluation presented in Table 4.9 shows that the dark regions comprise of higher copper ratio, which is varied from 4.921% to 5.466%. This made these zones similar in composition to that of the AA2024 base material. On the other side, higher Zn-ratio (5.591-6.075%) were estimated in the bright nugget zones which were comparable to the AA7075 base alloy. It was noticed that the average grain size of the weld stir zone increased from 4.3  $\mu\text{m}$  at 600 rpm to about 8.2  $\mu\text{m}$  at 1800 rpm when the AA7075 was located on the AS. Similarly, the average grain size increased from 4.7  $\mu\text{m}$  at 600 rpm to 7.8  $\mu\text{m}$  at 1800 rpm when the AA2024 was located on the AS. This growth in grain size could be attributed to the increase of weld temperature at higher rotation rate (Mironov et al., 2015; Upadhyay & Reynolds, 2012), since it is well acknowledged that the average grain size of the mixing SZ increases with increasing FSW process heat (Hirata et al., 2007; Khodir et al., 2006; Rahimzadeh Ilkhichi et al., 2014; Upadhyay & Reynolds, 2014).

#### **4.4.2.3 Hardness Distribution and Tensile Properties**

Distributions of the Vickers hardness number along the transverse nugget centerline are presented in Figure 4.29 for three different joints. The three samples were selected to compare the results at the highest, lowest, and best rotation rates when the AA2024 was fixed on the AS. The welding joints have exhibited a noticeable micro-hardness decrease compared to the base materials. This could be attributed to the grain refinement or recrystallization within the stir zone and the over-aging in the heat affected zone (Sun et al., 2016). In comparison between the higher and lower tool rotation rates, the lowest hardness level in the nugget was observed at 1800 rpm. Hardness level of the weld nugget was higher at 600 rpm, in which the grain size was smaller. These results indicate that the nugget hardness is affected by the tool rotation rate and inversely proportion to the grain size. Several researchers reported that the micro-hardness decreases with increasing grain size (Fratini et al., 2010; Imam et al., 2014). However, the maximum hardness level in the weld nugget was obtained at 900 rpm. At this rate of spindle speed, more effective material mixing was produced by the welding tool. The

weld hardness at the mixing stir zone increased with the increase of tool rotation speed until it reached the maximum level and decreased again when the spindle speed was further raised. This could be attributed to the change in frictional heat related to the spindle speed. Increasing the spindle speed results in higher process heat which affect, not only the material flow, but the HAZ in both welding sides (Colligan & Mishra, 2008). This in turn affects the hardness distribution of the welding joint.

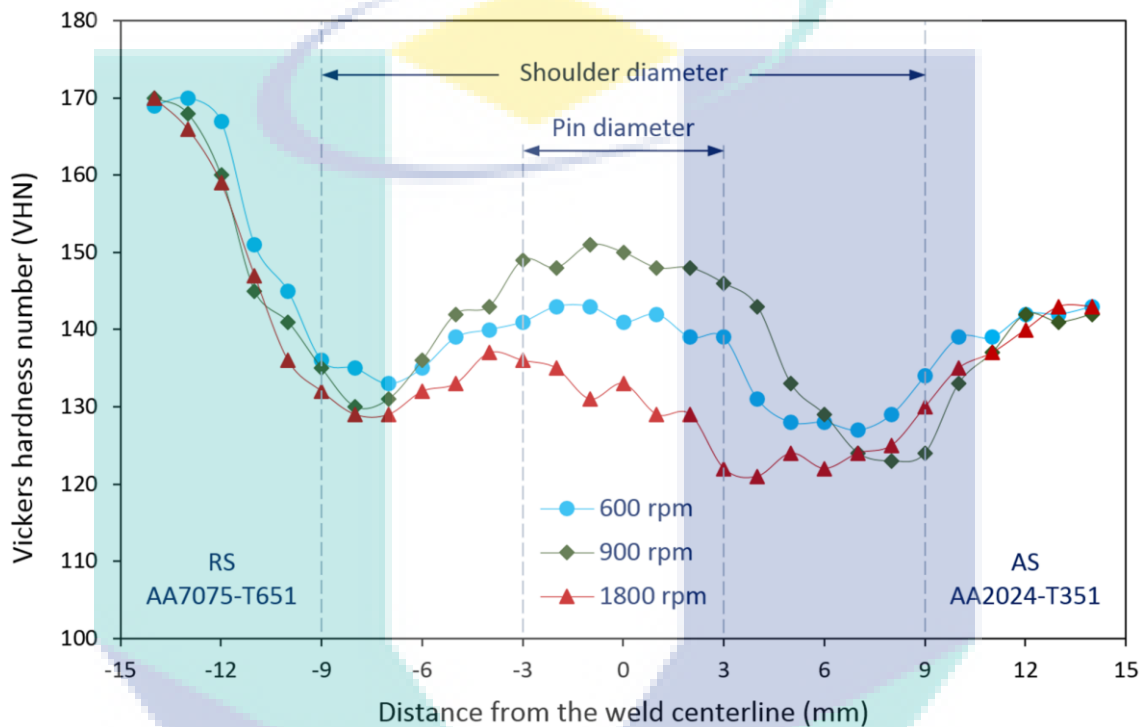


Figure 4.29 The weld micro-hardness distribution related to the tool rotation rate

Accordingly, materials mixing plays an important role in the resulting level of nugget hardness. Along the whole welding joint, the minimum VHN was recorded on the AA2024 side in the heat-affected zone and thermo-mechanical affected zone. This drop of hardness could be attributed to the amount of heat generated during the welding process and the extension of the grains in this region (Guo et al., 2014).

The fracture locations of the tension test specimens were observed at the HAS/TMAZ of the softer alloy the defect-free welds for the joints produced at 600-1200 rpm, as shown clearly in Figure 4.30. Due to the microcracks and insufficient material mixing resulted at 1500- and 1800 rpm, the fracture was initiated from the weld nugget. Detailed discussion of the fracture location will be explained later in Section 4.4.4.2.

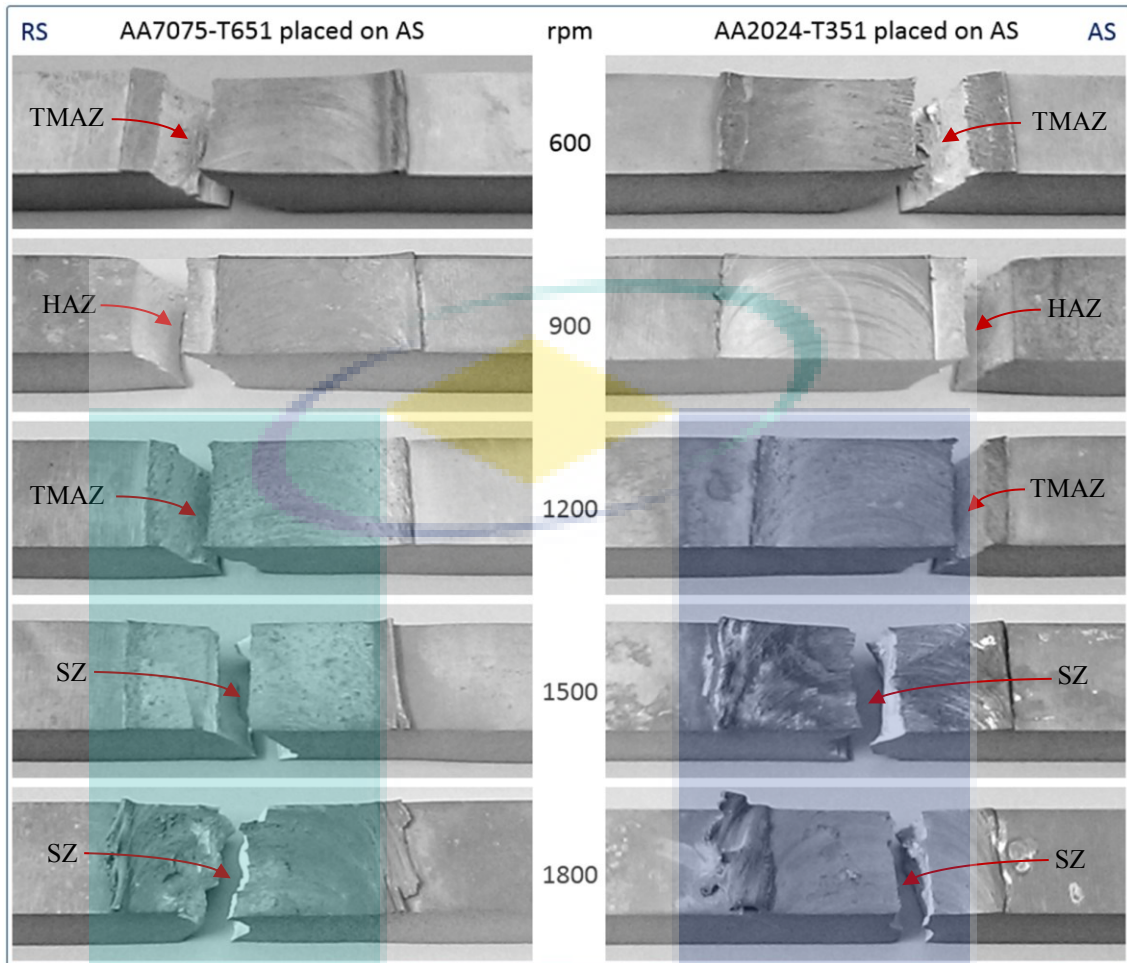


Figure 4.30 Fracture locations of the tension test specimens at different tool rotation rates

The ultimate tensile strength of the weld and the corresponding percentage elongation at fracture are presented in Figure 4.31 related to the applied spindle speeds. It was noted that the joint strength has improved at 900 rpm regardless of the relative materials position. The maximum joint strength and tensile elongation of about 400 MPa and 6%, respectively, were observed when the AA2024 was fixed on the AS, where the most uniform nugget with the best hardness level was produced. Since the joint efficiency for a dissimilar welding could be calculated based on the softer material (Giraud et al., 2016), this value of UTS represents an efficiency of about 89% with respect to the strength of the AA2024 alloy. The lowest UTS value of about 359 MPa, which represents an efficiency of about 80%, was recorded at 1800 rpm when the AA7075 was placed on the AS. In this case, the lowest tensile elongation of about 3.5% was recorded. This means that the tensile elongation is proportional to the joint strength.

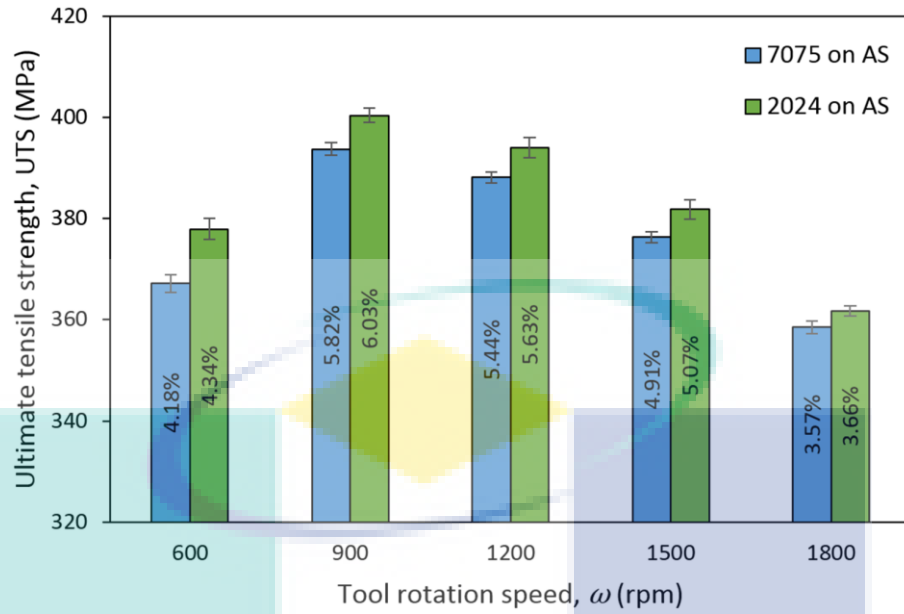


Figure 4.31 The weld ultimate tensile strength and percentage elongation at different spindle speeds and materials position

It is also obvious that the difference in tensile strength ( $\Delta$ UTS) related to the materials location decreased with the increase of tool rotation rate, as seen in Figure 4.32. This behavior implies that the effect of materials position on the joint strength reduced at high rotation rate and vice versa.

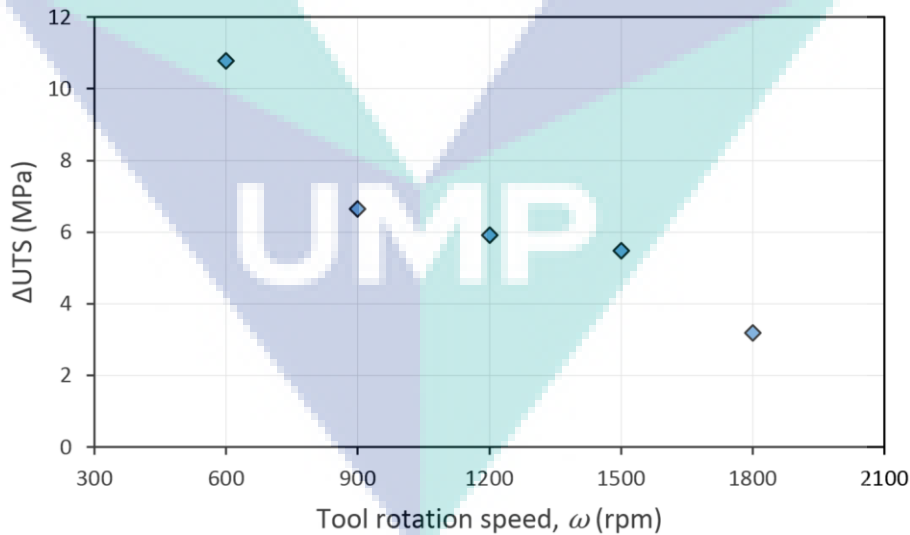


Figure 4.32 Difference in the weld ultimate tensile strength ( $\Delta$ UTS) related to the materials position under various spindle speeds

Variation of the joint strength as per the materials location could be attributed to the rate of material mixing and process thermal energy (Guo et al., 2014). At lower

spindle speed, placing of the higher strength AA7075 aluminum alloy on the advancing side makes it very difficult for the AA6061 alloy to penetrate into the nugget. This difficulty reduced when the process power is increased at the higher rotation rate. Furthermore, the nugget degradation and formation of the internal microcracks weakened the welding joint and reduced the effect of the relative materials position on the resulting strength.

#### **4.4.3 Initial Plunge Phase and Dwell Sequence**

This section presents the results obtained using the active methodology for welding without applying the initial plunge cycle, which was conducted to avoid the primary deformation of the pin tool. An initial pilot hole was drilled at the weld start point, and the dwell sequence was studied. As discussed previously in Section 3.8.2, four stationary dwell periods between 3 and 24 seconds were examined, and the results was compared to those of the new TSW methods. The revealed microstructure and measured ultimate strength of the welding joints were considered. Four transverse tensile specimens normal to the welding seam were tested to inspect the efficiency of each weldment. The following sub-sections presents the observed results with their detailed discussion.

##### **4.4.3.1 Visual Inspection and Metallographic Analysis**

First, surface finish of the weld seam was examined throughout the visual monitoring. Figure 4.33 shows the weld surface finish at the first welding quarter related to each stationary dwell sequence. Deep surface-breaking void or lack of fill was generated when the welding tool was driven laterally along the workpieces after 3 seconds of dwell time, as seen in Figure 4.33-(a). This type of defect reduced when the dwell sequence was increased to 6 seconds as seen in Figure 4.33-(b), and vanished when the dwell periods were set to 12 and 24 seconds as seen in Figure 4.33-(c and d).

Macrographs of the weld section and the microstructures of their corresponding nugget zones under various dwell sequences are presented in Figure 4.34. It has been noted that the dwell time affects the size and location of the generated voids. The largest groove was formed during the shortest dwell period and its size reduced by more than half when the time was doubled. As the welding tool rotated inside the pilot hole, the generated frictional heat transferred to the workpieces and conducted to the backing/cover and tool materials.

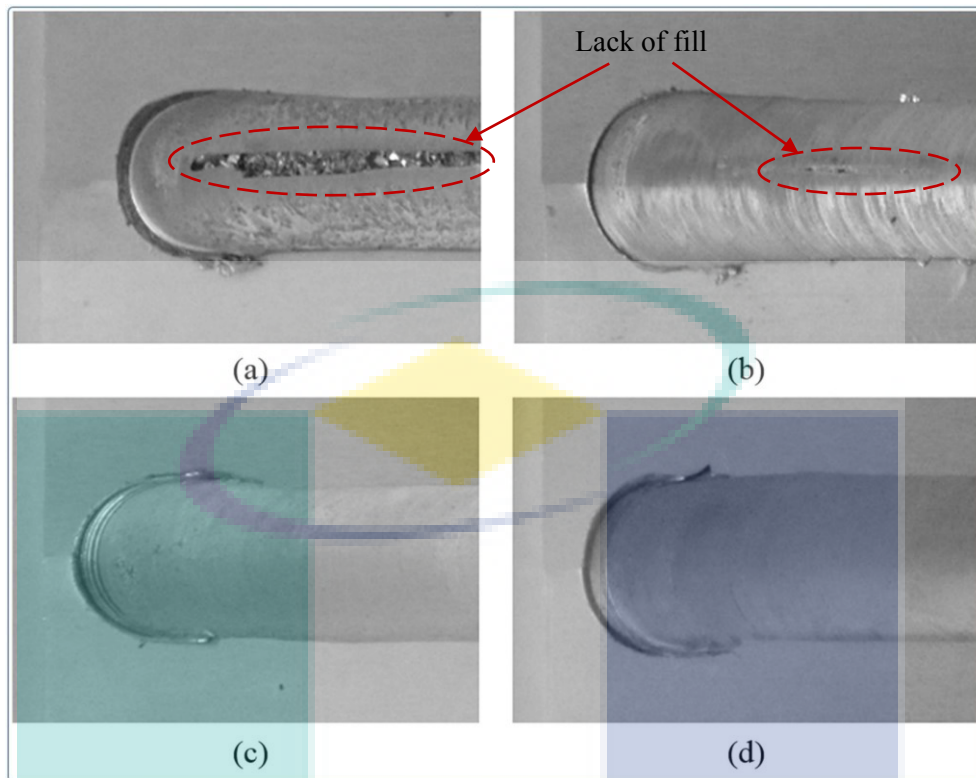


Figure 4.33 The weld surface finish at at the first welding quarter under different stationary dwell sequences. (a) 3 sec, (b) 6 sec, (c) 12 sec and (d) 24 sec

Vertical and circular plastic flows of the coupled materials occur during the process (Luo et al., 2016). The left-hand threads of the probe pushed the material down and away from the shoulder in conjunction with the circular motion of the tool. The high strain rate and temperature generated due to the tool rotation and material flow resulted in severe deformation and dynamic recrystallization of the base materials' grains, which entered into each other and form the weld nugget (Trimble et al., 2015). The main phase, where the weld is produced through the FSW, normally starts directly after the plunge sequence or, in some materials, after a short stationary dwell (Colligan, 2010). In this method, the plunge stage was omitted, and the micrographs showed that 3 and 6 seconds were not enough periods to produce sufficient heat required to soften the joined materials before welding. This in turn resulted in relatively cooler plasticized materials and unstable temperature distribution within the workpieces and the welding tool. Under such inadequate forging condition, the tool pin crushed the surrounding materials of the workpieces below the top of weld along the first quarter of the entire length of the welding seam. This chaotic stirring resulted in tool lifting and the workpieces moving apart; therefore, the location of the generated grooves tended to the advancing side of the

welding tool. This is clear from the print of the threaded profile of the probe shown on the right-hand side of the nugget for the 3-seconds-dwell.

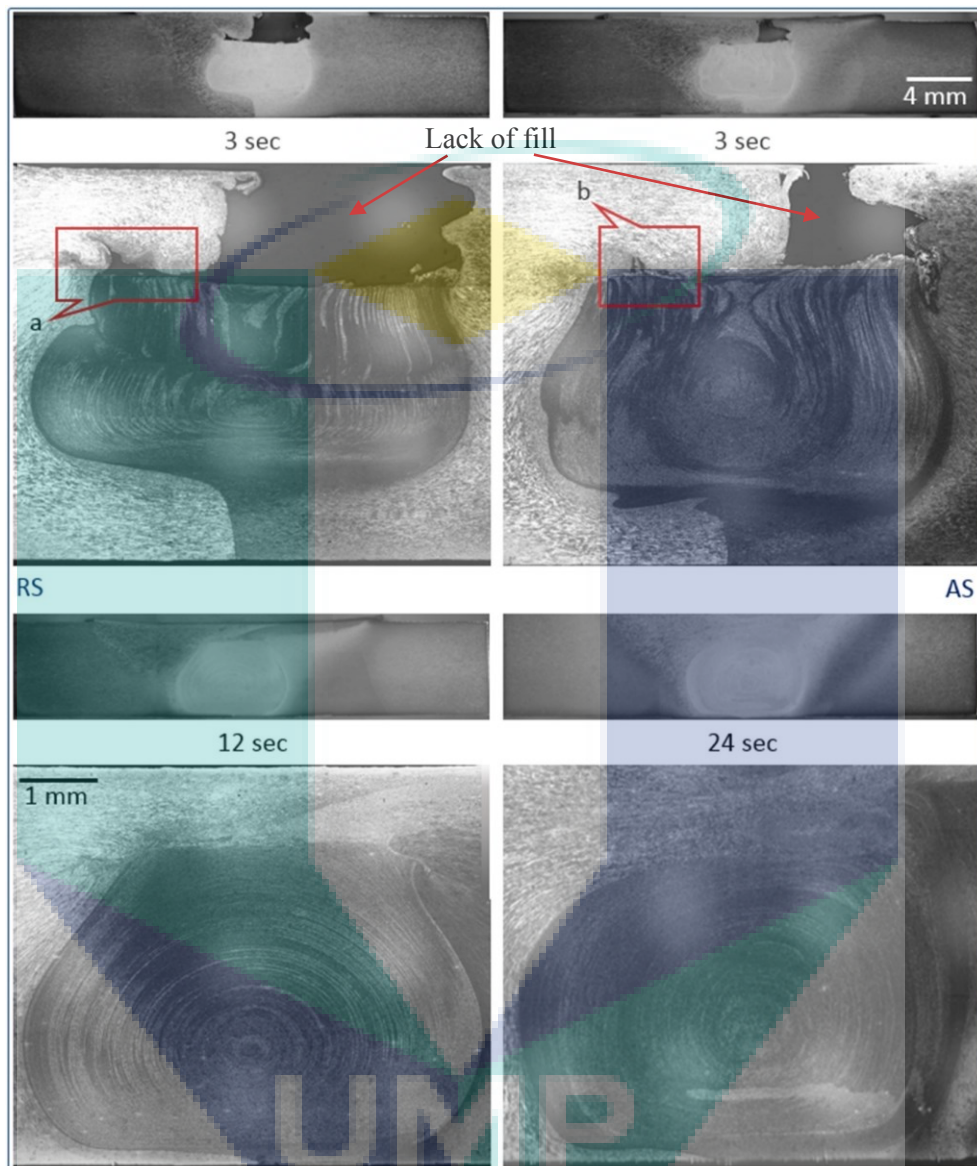


Figure 4.34 Macrographs of the weld and their corresponding nugget micrographs related to the applied dwell sequences

Fixing the AA7075 harder alloy on the retreating side of the weld was the reason behind the tool shifting towards the AA2024 softer alloy (Beygi et al., 2017). This movement of the welding tool resulted in further cavities on the upper left-hand side of the weld nugget (zones a and b in Figure 4.34), which are presented with higher magnification in Figure 4.35. Same behavior and such resulted surface-breaking voids were also observed by Leonard and Lockyer (Leonard & Lockyer, 2003) in a weld produced from 6-mm-thick AA2014 aluminum plate at high traverse speeds.

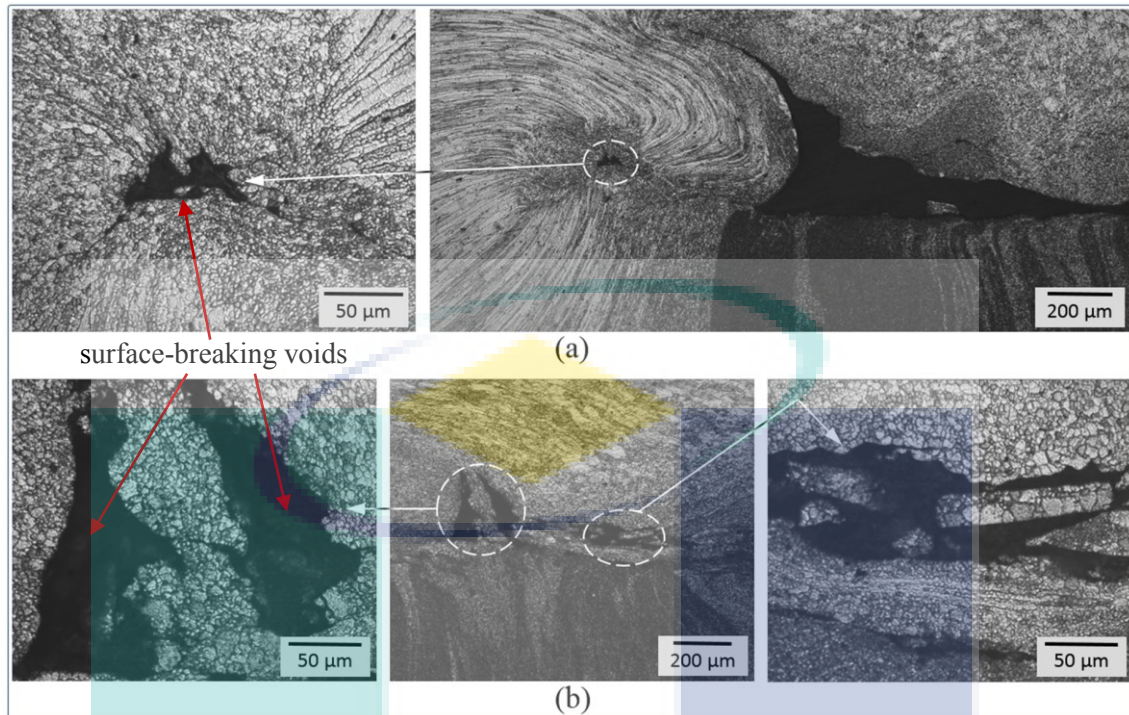


Figure 4.35 Higher magnification of the upper left-hand side of the weld nugget after (a) 3 sec and (b) 6 sec of stationary dwell time

It is well-known that the generated heat in the FSW reduces with increasing welding traverse speed (Chao et al., 2003). The formation of the unconsolidated voids was attributed to the difficulty of forging improperly softened materials. The lack of fill could then be avoided by a proper selection of the initial dwell sequence. Defect-free welds were produced when the stationary delay was raised, and the most uniform material mixing was observed after 12 seconds from the start of tool rotation.

Shoulder wear that may results from the stationary dwell could be reduced if the welding process is conducted without applying the delay time. The idea is represented by the ability of producing the initial softening heat by moving the workpieces with a slow speed at a certain length of the weld seam before the start of the main welding phase. This means that the welding seam is produced through two-stage welding (TSW). The workpieces in this TSW method were slowly moved through a feed rate of 30 mm/min along a distance of 6 mm before starting with the existing welding speed (100 mm/min), as illustrated in Figure 4.36. Therefore, the duration of the TSW was 12 seconds related to the initial slow travel rate of the welding tool at the start of the process.

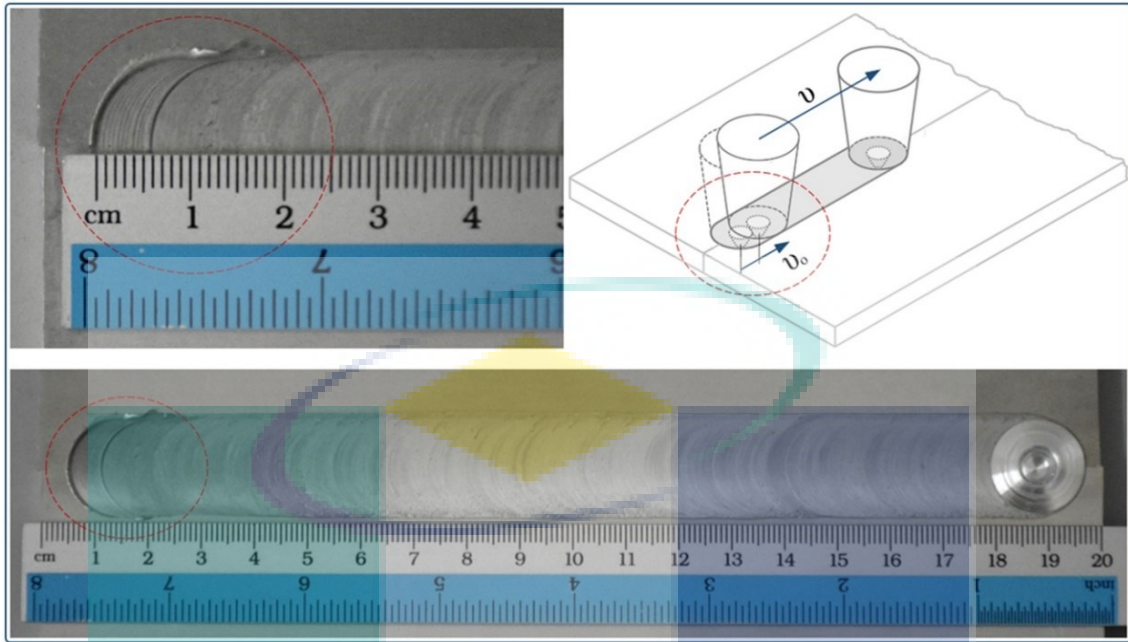


Figure 4.36 An illustration of the TSW.  $v_0 = 30$  mm/min along 6 mm of the welding line and  $v = 100$  mm/min (welding traverse speed)

As shown in Figure 4.37, sound weld with uniform nugget and good surface finish was obtained by applying the TSW method. The weld nugget presented in this figure is free of voids and other internal defects. The surface finish at the weld start region was also free of tool crushing and other imperfection.

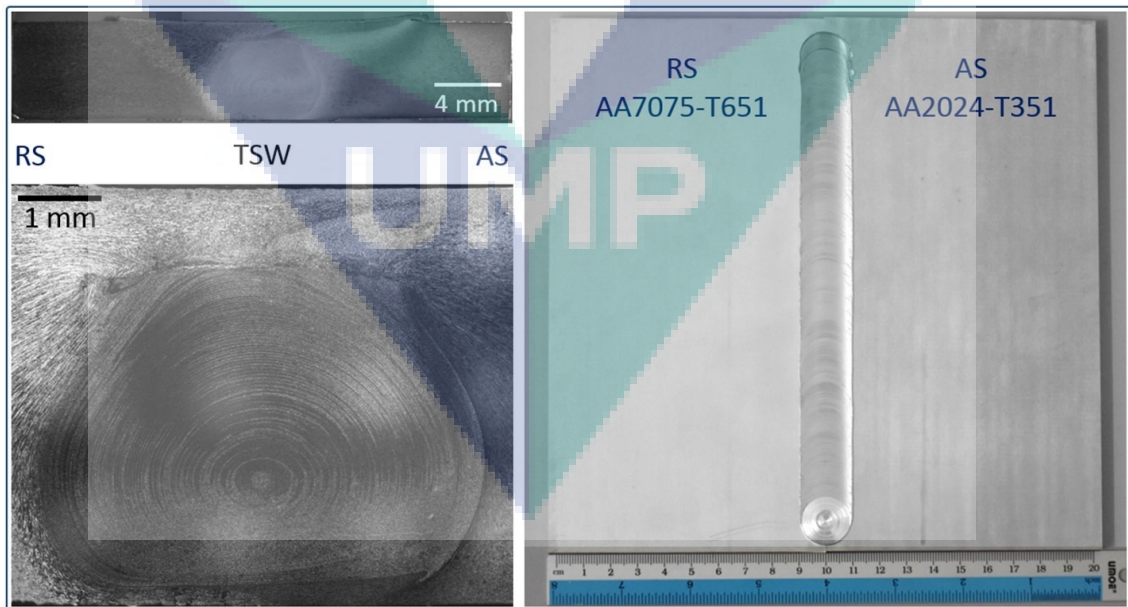


Figure 4.37 Macrograph of the weld and the corresponding nugget microstructure with a photo of the welding joint resulted from using the TSW method

#### 4.4.3.2 Tensile Properties and Hardness Distribution

The tensile tests revealed that the use of the TSW method resulted in the most stable weld with the highest average tensile strength (396.1 MPa) and minimum standard deviation, as seen in Figure 4.38-(a). On the other hand, high non-conformity in joint strength was observed when the first two short stationary dwell periods were applied, as presented in Figure 4.38-(b). This could be attributed to the improper material mixing at the weld start when the short dwell periods were applied.

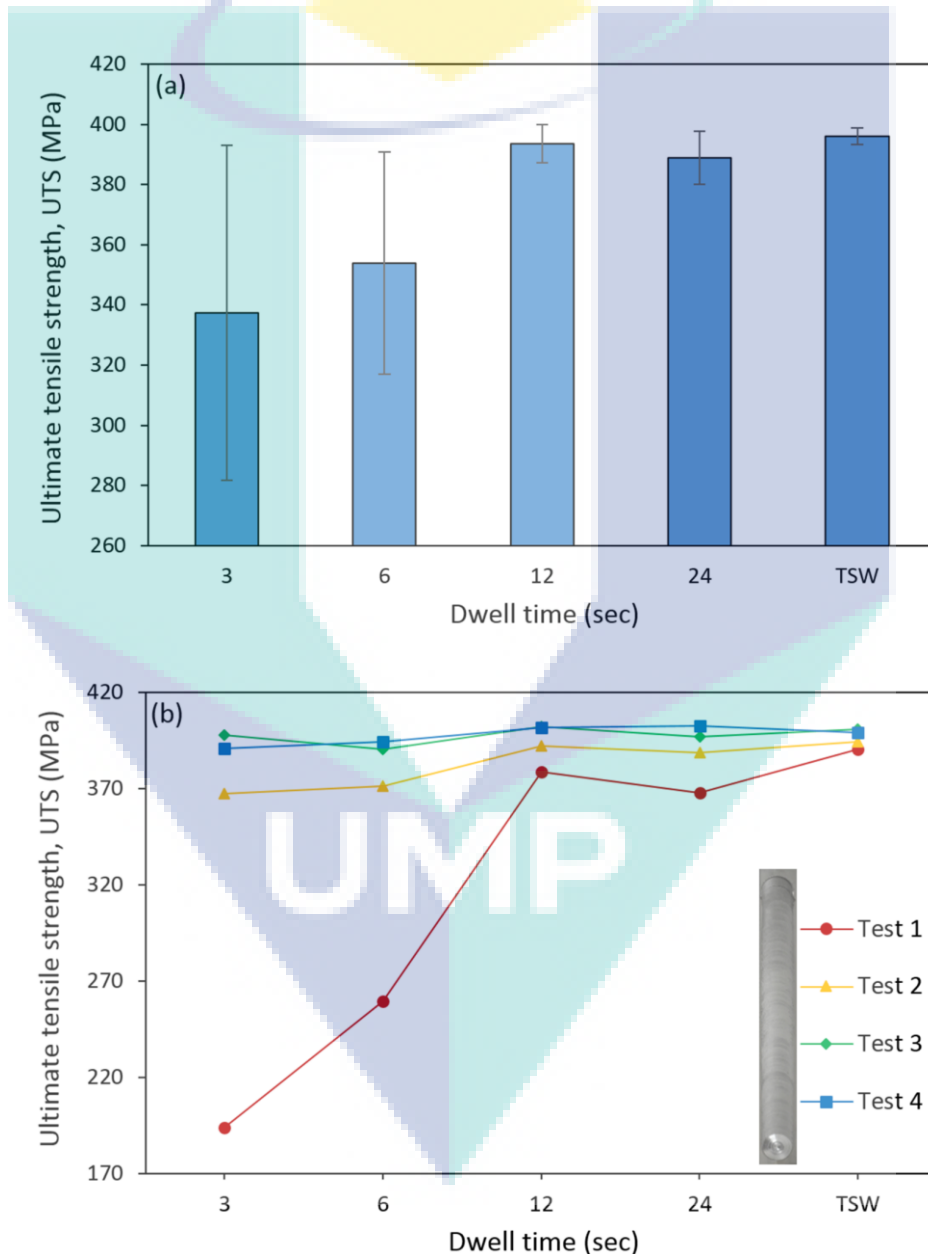


Figure 4.38 The weld tensile strength and its variation along the welding seam related to the stationary dwell sequences and TSW method

As shown in Figure 4.39, the lowest joint strengths (193.9 and 259.5) were recorded related to the 3 and 6 seconds' dwell times, respectively in the first tensile test whose specimen was close to the starting region of the welding seam. The fracture occurred in the mixing SZ for these two specimens, while it occurred in the heat affected zone of AA2024 alloy during the other tests for all dwell sequences. Typically, fracture of the tension test specimen starts from the HAZ of the softer alloy in sound dissimilar friction stir welds, while the incidence of defects make the failure arises in the mixing SZ (İpekoğlu & Çam, 2014). Hardness drops in the HAZ due to the elevated temperature and the mechanical extension of the grains (Emami & Saeid, 2015; Guo et al., 2014).

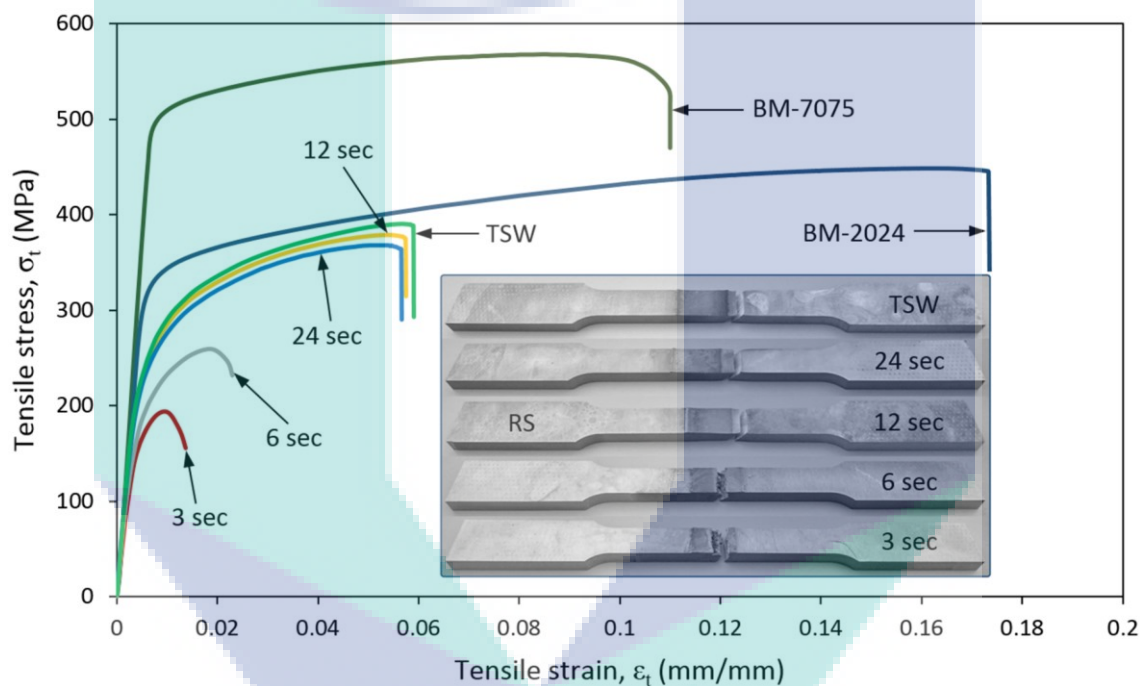


Figure 4.39 Variation of the tensile strength along the welding seam related to the stationary dwell sequences and TSW method

The hardness distribution at the weld start quarter for all dwell sequences are presented in Figure 4.40. The highest level of Vickers micro-hardness number in the weld nugget was observed when 24 seconds of stationary dwell was applied. In contrast, the lowest hardness level was recorded in the heat affected zone of AA2024 base material for the same dwell period. This trend indicates that the apex temperature was reached by this delay time. The hardness distribution showed a noticeable drop in the VHN at the weld nugget for the lowest dwell sequences, and the minimum level was noted at 3 seconds. These results are expected outputs for incomplete material mixing in the mixing SZ.

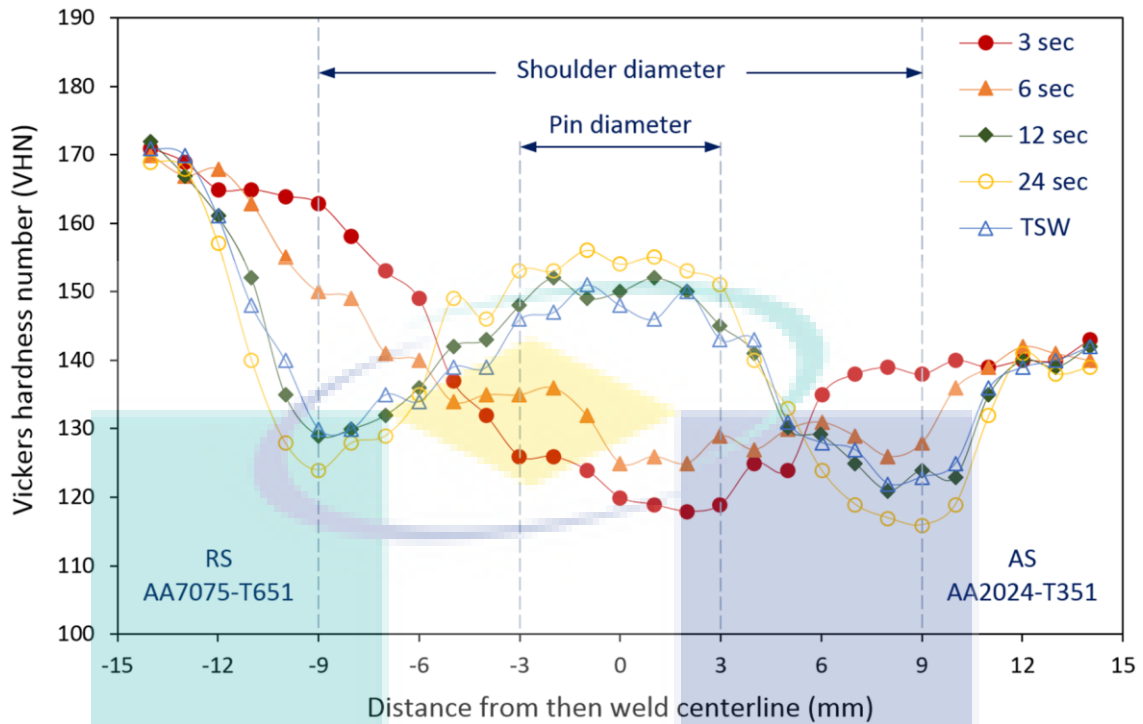


Figure 4.40 Hardness distribution at the start quarter of welding seam related to the dwell sequences and TSW method

By using the TSW and the 12 seconds of stationary dwell, the distribution of weld hardness has been significantly improved. Consequently, weld strength and ductility were enhanced compared to other dwell sequences. In the final stage of this study, a number of tests were conducted to show the ability of the present method of TSW and pilot hole of reducing the tool wear compared to the ordinary plunge phase. Two welding tools were fabricated with the same design and material as previously used. The first one was used to produce fourteen normal plunge cycles and one complete weld without using a pilot hole. The second tool was driven to prepare fifteen weldments by applying the current methodology.

Figure 4.41 presents the pin tool profile before and after the friction stir welding phases. Cyclic insertion of the driven tool inside the base materials without using a preliminary hole resulted in a permanent deformation in the geometry of the probe, as seen in Figure 4.41-(b). The length of pin has been significantly decreased by about 28% with respect to the original size. On the contrary, insensible change in the pin tool dimensions were detected when the plunge cycle was omitted in the second group of weldments, as shown in Figure 4.41-(c). Tensile strength of the weld made by tool (b) after the plunge cycles was decreased about 23% of the average strength of the weld produced using the

TSW method, while the decrease of weld strength did not exceed 5% using tool (c) and pilot hole. These observations imply that the present procedure can be effectively used to prevent the early mechanical wear of the probe in the initial plunge phase, and hence increase the useful lifetime of the welding tool and produce stable welds. Consequently, the TSW method is used in the next welding tests.

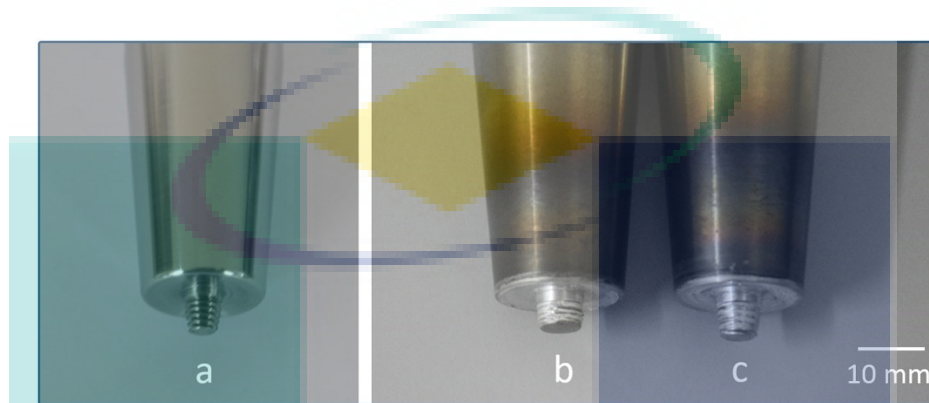


Figure 4.41 Profile of the pin tool (a) before welding, (b) after 14 plunge cycles and one complete weld (without pilot hole) and (c) after 15 weldments (with pilot hole)

#### 4.4.4 Effect of Backing and Clamping Material

Reducing the heat input during the FSW process by decreasing the tool rotation rate and/or increasing the workpiece travel speed is one of the methods used for increasing the joint strength. However, there is a limited range of tool rotation rate and travel speeds that could be controlled. The backing and clamping materials may change the amount and distribution of the welding heat, but this factor has received limited attention compared to other process variables. It is hence though necessary to understand the influence of backing material and clamping system on the joint strength in conjunction with varying levels of the welding speeds during the dissimilar FSW. In this case, materials position on the advancing and retreating sides of the weld is another factor that should be considered. With the objective of creating very high strength welds, the following sections present the results of current investigation regarding the dissimilar FSW of high-strength AA7075-T6 and AA2024-T351 aluminum alloys using the modified design of backing/clamping system. The primary three systems that presented in Figure 3.7-(b) and discussed in Section 3.6.2 were examined through various welding travers speeds and materials placement. The welding travers speeds ranged between 50-250 mm/min and the optimal 900 rpm spindle speed was used. All joints were produced using the truncated threaded pin tool, which was tilted with 3°. Temperature distribution

throughout the welding route was considered in this stage of the study. The fourth asymmetric backing/clamping system was then tested as per the results of the weld tensile strength.

#### 4.4.4.1 Visual Inspection of the Resulting Welds

First, the three-primary backing/clamping systems were examined at 100 mm/min of traverse speed. The visual monitoring of the finish welds showed a slight surface galling when the workpieces were only clamped on the central steel anvil (System 3), as seen in Figure 4.42.

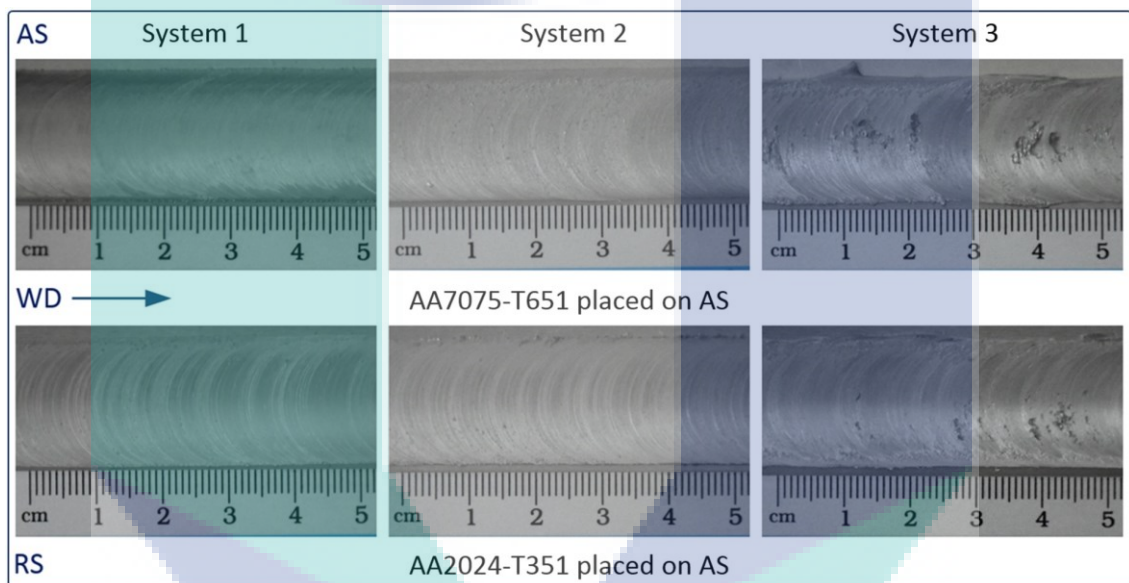


Figure 4.42 Surface finish of the resulting welds related to the backing/clamping systems at 900 rpm spindle speed and 100 mm/min traverse rate

For all backing/clamping systems, significant amounts of flash were generated when the traverse speed was reduced to 50 mm/min regardless of the relative materials position, as shown in Figure 4.43. This could be attributed to the increase of heat input, since the FSW process temperature increases with the decrease of the welding traverse speed (Chao et al., 2003). The maximum and minimum amounts of flash were generated under System 3 and System 1, respectively. This is due to the difference in thermal conductivity of the backing and cover materials. Through using System 3, the workpieces were insulated and the heat dissipation was minimized. On the other hand, the aluminum backing and cover plates (System 1) worked as an active heat sink and increased the extraction of the process heat from the weld zone.

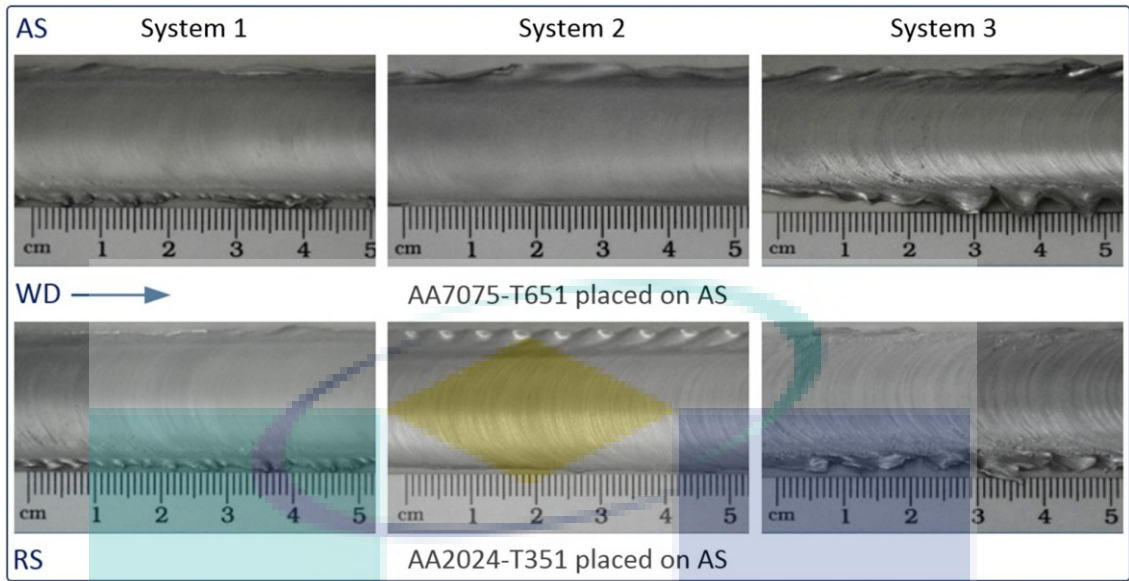


Figure 4.43 Surface finish of the resulting welds related to the backing/clamping systems at 900 rpm spindle speed and 50 mm/min traverse rate

As shown in Figure 4.44, the surface finish of the resulting welds has become free of defects when the traverse speed was raised to 150 mm/min. Some surface defects started to appear on the weld surface beyond this level of travers speed.

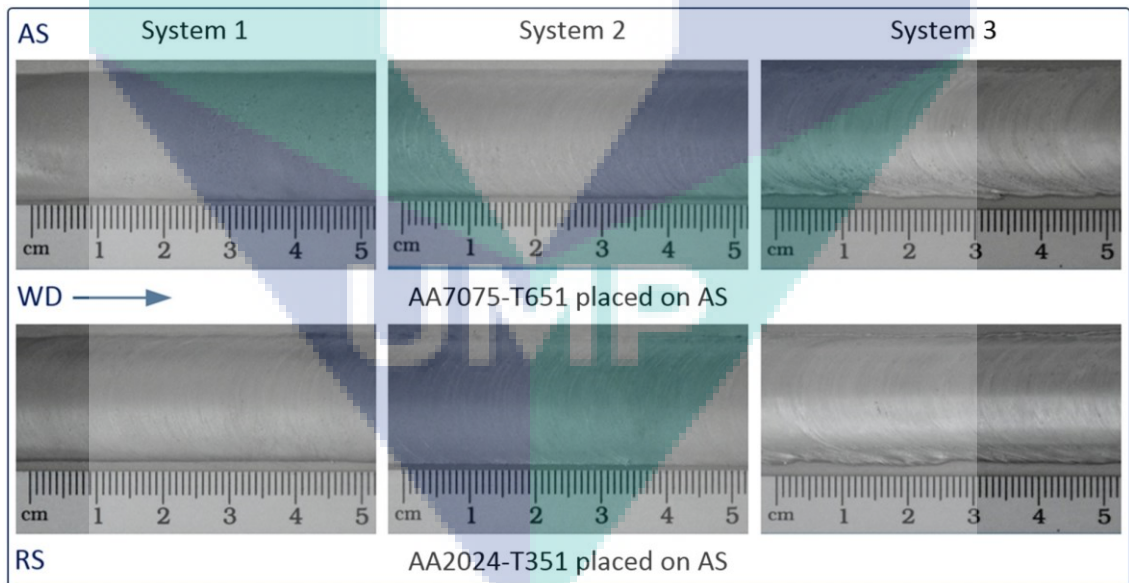


Figure 4.44 Surface finish of the resulting welds related to the backing/clamping systems at 900 rpm spindle speed and 150 mm/min traverse rate

Surface scaling and galling are seen on the surface of the weld produced using System 1 at 200 mm/min, especially when the AA7075 aluminum alloy was placed on the advancing side of the weld, as shown in Figure 4.45.

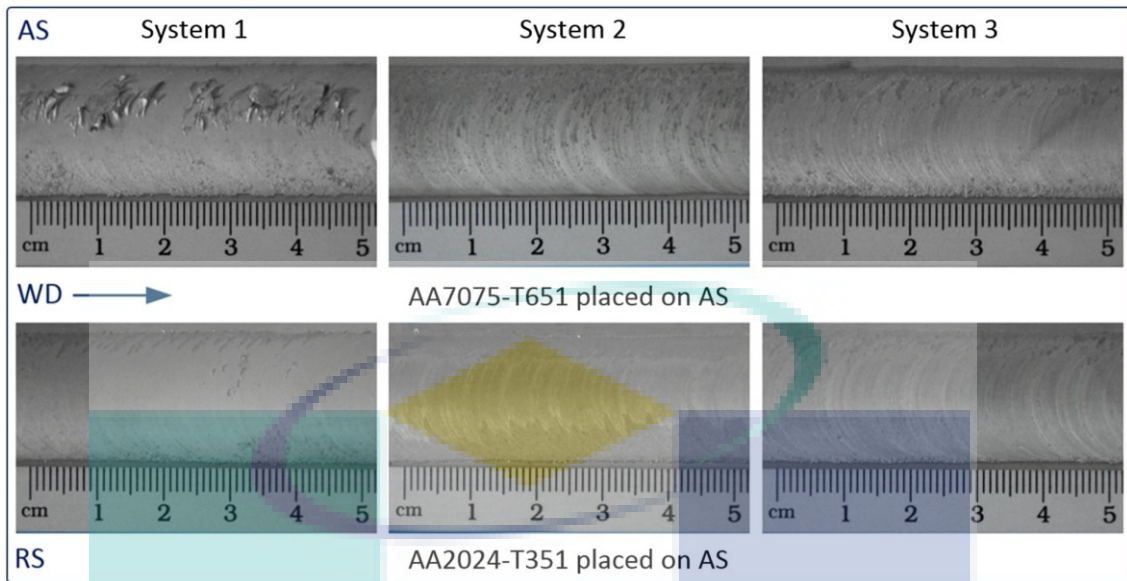


Figure 4.45 Surface finish of the resulting welds related to the backing/clamping systems at 900 rpm spindle speed and 200 mm/min traverse rate

Regardless of the fixed position of the base materials on the advancing and retreating sides of the weld, surface defects were seen at 250 mm/min on the surface of the welds produced using System 1 and slightly with System 2, as shown in Figure 4.46.

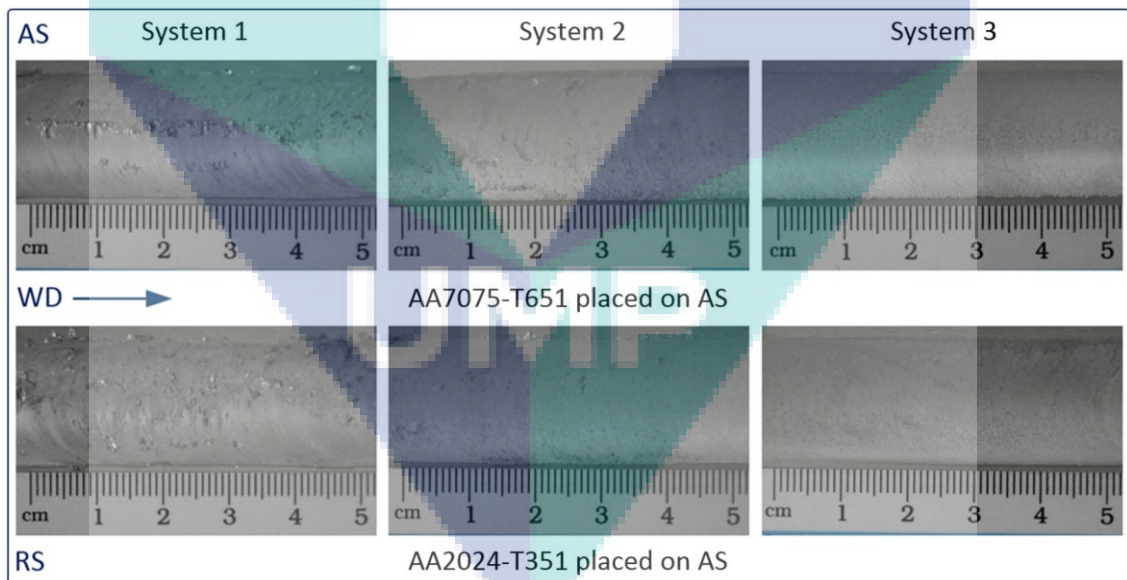


Figure 4.46 Surface finish of the resulting welds related to the backing/clamping systems at 900 rpm spindle speed and 250 mm/min traverse rate

These results give an indication that the dissipation of process heat is not preferred at higher welding travers rates, and the generated temperature was not enough to properly soften the materials around the pin tool. This is due to the fact that the friction stir process

heat decrease with increasing the traverse rate (Chao et al., 2003). It is worth noting herein that unsuccessful welding trial was resulted when the welding speed was raised to 300 mm/min. In this case, the abutting materials have crushed at the weld start, as shown in Figure 4.47, and the test was hence canceled.



Figure 4.47 Surface finish of the unsuccessful welding trial at 900 rpm spindle speed and 300 mm/min traverse rate

#### 4.4.4.2 Tensile Properties

The obtained results of the ultimate tensile strength and percentage elongation of the welding joints produced using the three backing/clamping systems at different traverse speeds and materials position are presented in Figure 4.48.

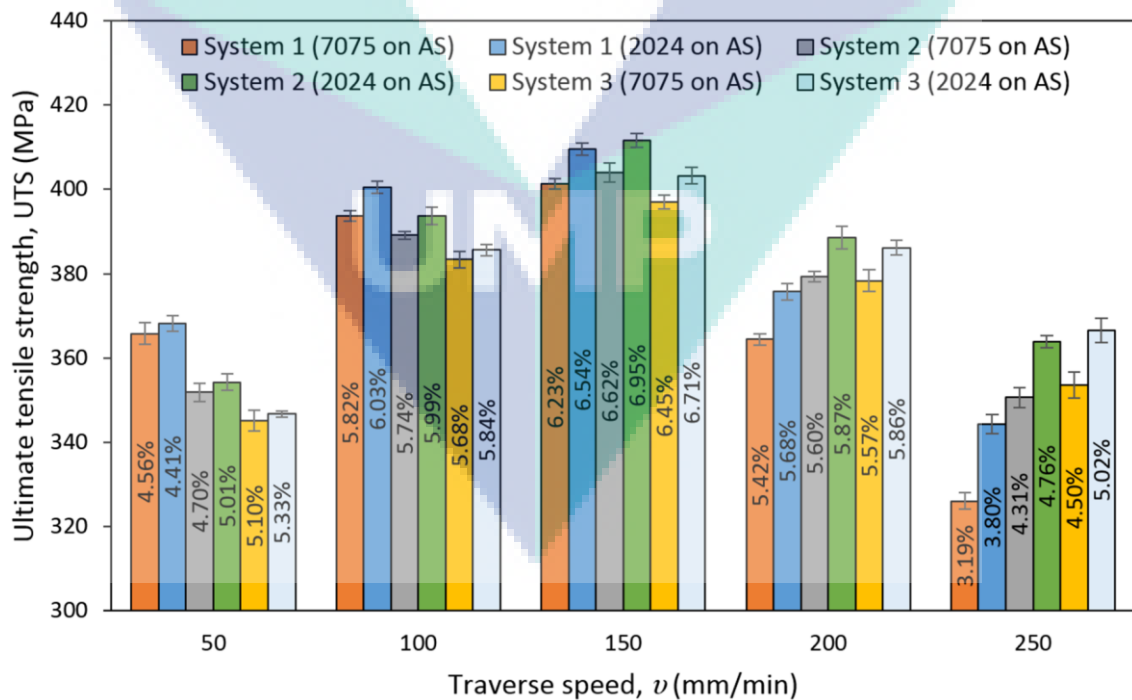


Figure 4.48 Joint strength and percentage elongation related to the three backing/clamping systems at different traverse speeds and materials position

The error bars correspond to standard deviation of three tests for each case. It is obvious that the effect of backing material and clamping systems on the weld tensile strength and elongation is changed with the variation of the applied welding traverse speeds. This behavior clarifies some of the differences found in the previously published data of Khodir et al. (2006), Zhang et al. (2013), Upadhyay & Reynolds (2014) and Imam et al. (2014) regarding the effect of backing plate material on the mechanical properties of friction stir welds.

Regardless of the materials placement on the advancing and retreating sides of the weld, the use of System 1 resulted in the maximum joint strength at 100 mm/min followed by System 2 and System 3. At this level of welding travers speed, the tension test specimens fractured at the HAZ of the softer AA2024 aluminum alloy wherever it located (i.e. on the advancing or retreating sides of the weld) for all backing/clamping systems as shown in Figure 4.49.

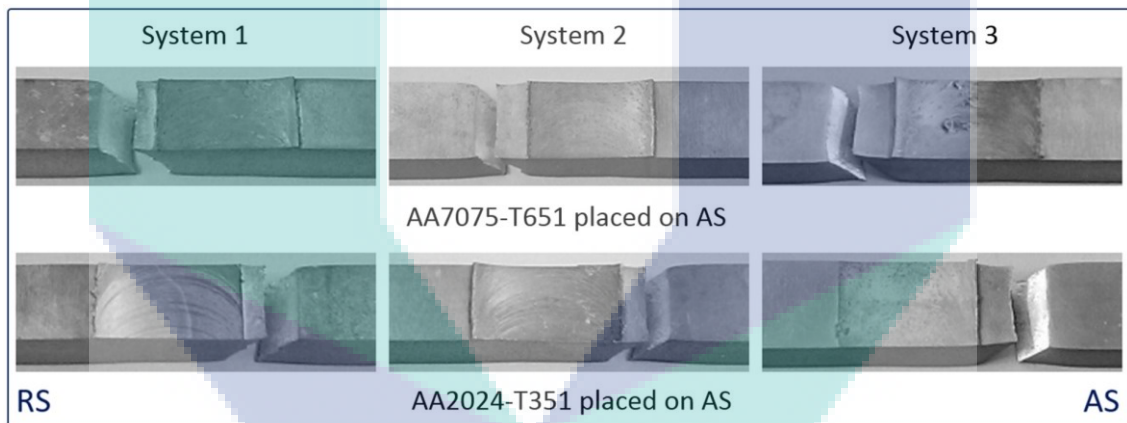


Figure 4.49 The fracture locations related to the backing/clamping systems at 900 rpm spindle speed and 100 mm/min traverse rate

When the traverse speed was reduced to 50 mm/min, the weld strength decreased with the same effect of the backing/clamping systems at 100 mm/min. This drop in joint strength could be attributed to the increase of the heat input, as discussed previously. Among the three backing/clamping systems, minimum joint strength was recorded when the workpieces were clamped using System 3 and the AA7075-T6 placed on the AS. The measured mean UTS was about 345 MPa, which represents an efficiency of 76.8%. The excessive flash formation generated at this relatively low traverse speed reduced the amount of materials at the mixing stir zone. The difference of weld flash or the equivalent amount of material lost made the tensile elongation non-proportional to the joint strength.

In addition, the various regions produced in the FSW make the elongation inappropriate measure of the weld ductility (Upadhyay & Reynolds, 2014). As shown in Figure 4.50, the fracture occurred at the TMAZ and HAZ of the AA2024 alloy regardless of the materials locations on the advancing and retreating sides of the weld.

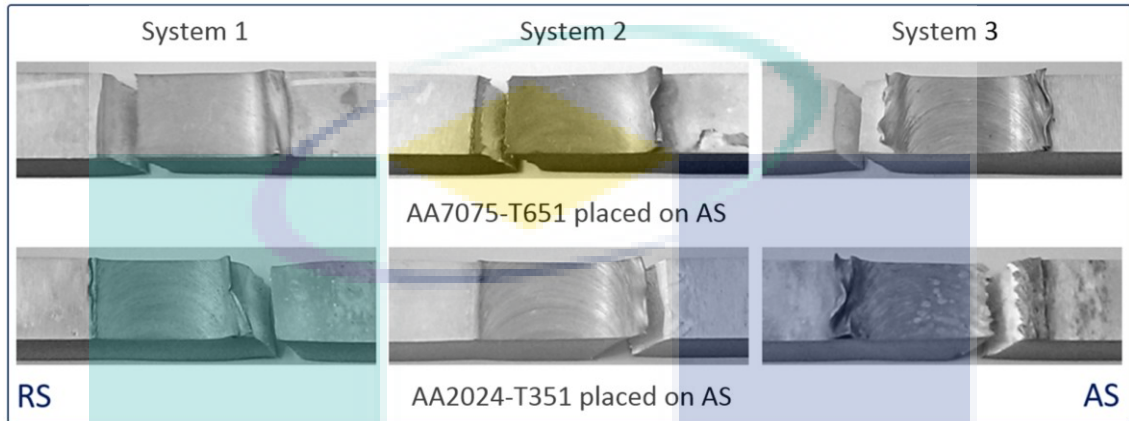


Figure 4.50 The fracture locations related to the backing/clamping systems at 900 rpm spindle speed and 50 mm/min traverse rate

Joint strength was improved when the traverse speed was raised to 150 mm/min. The maximum UTS value of about 411.6 MPa, which represents an efficiency of 91.6%, was recorded when the AA2024 alloy was placed on the AS using System 2. The weld efficiency slightly decreased when System 1 and System 3 were used. The tension test specimens failed at the TMAZ of the AA2024 alloy for System 1 and at the HAZ of the same material for System 2 and System 3, as presented in Figure 4.51.

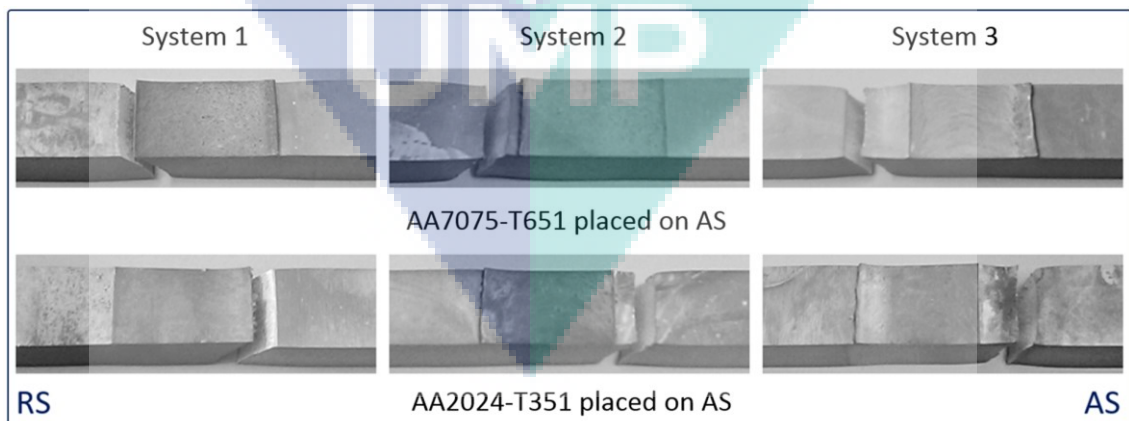


Figure 4.51 The fracture locations related to the backing/clamping systems at 900 rpm spindle speed and 150 mm/min traverse rate

Increasing the traverse speed beyond this level resulted in a degradation of the joint strength with an inverse effect of the backing/clamping systems. The maximum reduction in joint strength was recorded at 250 mm/min for the weld produced using System 1, when the harder AA7075-T6 was placed on the AS. At this highest traverse speed, the evaluated mean UTS was equal to 326 MPa, which represents an efficiency of about 72%.

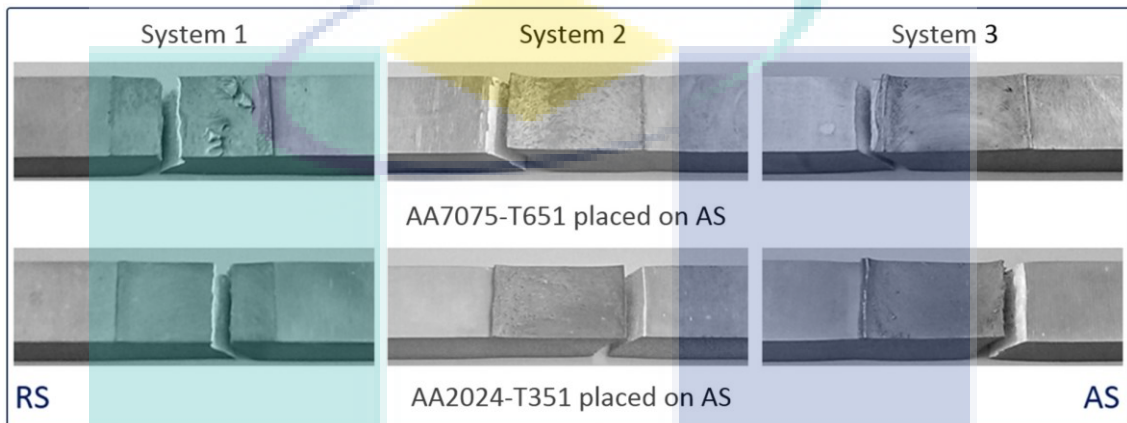


Figure 4.52 The fracture locations related to the backing/clamping systems at 900 rpm spindle speed and 200 mm/min traverse rate

As seen in Figure 4.52 the fracture of the tension test specimens was initiated from the TMAZ of the AA2024 alloy for System 2 and System 3 while it occurred in the mixing SZ for System 1 regardless of the relative materials location.



Figure 4.53 The fracture locations related to the backing/clamping systems at 900 rpm spindle speed and 250 mm/min traverse rate

The fracture locations moved toward the weld nugget at 250 mm/min regardless the materials position and backing/clamping systems, as shown in Figure 4.53. This also

implies that the generated temperature was not enough to properly soften the materials around the pin tool.

In the FSW, fracture of the tension test specimens normally arises from the weakest region. The HAZ of the softer alloy represents the weakest region of the sound dissimilar friction stir welds regardless of the relative materials location (İpekoğlu & Çam, 2014; Rodriguez et al., 2015). The drop of micro-hardness could be attributed to the elevated temperature and mechanical extension of the grains. The failure takes place at the stir zone if there is an over material mixing resulted from high rotation speed or poor mixing if the traverse rate is so high (Serio et al., 2016; Zhou et al., 2016). It is worth noting herein that the influence of materials position on the tensile strength has grown with the increase of traverse speed. This behavior is similar to that appeared when the effect of tool rotation rate on the weld strength was investigated. The difference in joint strength related to the materials placement hence increases when the generated temperature decreases. This could be clarified by the fact that higher process energy is required when the harder material is placed on the AS in dissimilar FSW (Cole et al., 2013; Kumar et al., 2015). Variation of the effect of backing/clamping materials on joint strength could be attributed to the difference in thermal conductivity of these materials and the amount of heat generated during the welding process. At lower traverse speed, the aluminum backing and cover material used in System 1, which has a relatively high thermal conductivity, worked as an adequate heat sink to extract some of the welding heat. This heat dissipation minimized the overheating effect which resulted from the low-speed or hot welding. On the other side, the insulation of the workpieces at higher traverse speeds by the air gaps in System 3 reduced the drop in joint strength which resulted from the high-speed or cold welding. It is true then to say that the generation and dissipation of the FSW process heat could be controlled by using a proper design of backing/clamping system in conjunction with appropriate selection of the welding speeds and other process parameters.

#### **4.4.4.3 Metallographic Analysis and Temperature Distribution**

Macrographs of the weld and their corresponding nugget microstructures for the three backing/clamping systems at 100 mm/min are presented in Figure 4.54. The effect of backing and clamping systems on material mixing depends on the applied traverse speed. Producing defect-free weld with efficient material mixing is essential to attain

strong joints. In addition, controlling the temperature distribution during the welding process could further improve the joint strength through enhancing the weld hardness (Khodir et al., 2006).

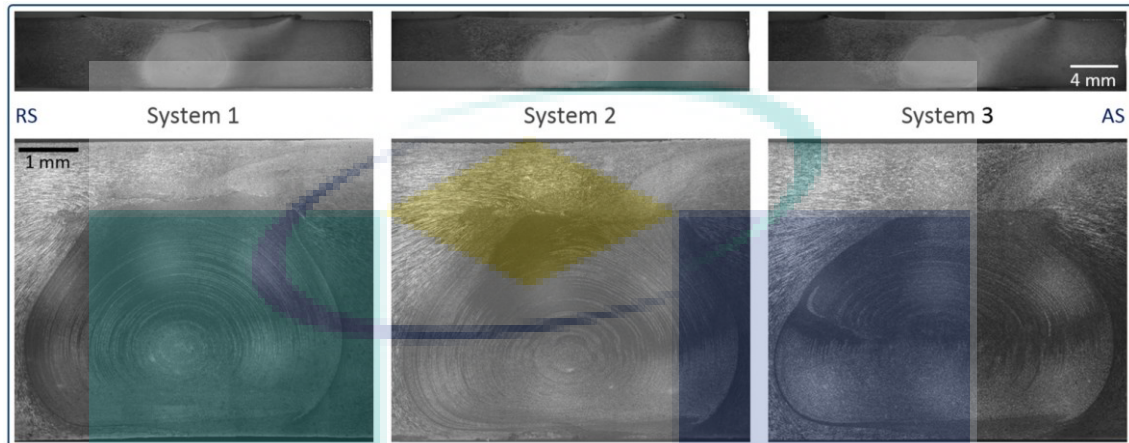


Figure 4.54 Macrographs of the weld and their corresponding nugget microstructures related to the backing/clamping systems at 900 rpm and 100 mm/min. AA2024-T351 placed on AS

The transient temperatures along the transverse centerline of the advancing side of the weld are presented in Figure 4.55 for the three backing/clamping systems. The typical temperature-time data were recorded using four thermocouple wires in different locations related to the weld centerline, as discussed previously in Section 3.7 and presented in Figure 3.8-(a). In comparison between the three backing/clamping systems, the graphs show that the amount of heat transferred toward the backing and covering materials increased throughout the use of System 1. This extraction of the welding heat reduced the peak temperature compared to System 3. For all systems, the temperature decreased as the distance from the welding seam increased due to the heat dissipation to the workpieces and backing/clamping materials. The peak temperature was recorded by the thermocouple TC-A1, which was secured close to the welding seam at the HAZ of the softer AA2024-T351 aluminum alloy where the fracture occurred in the tensile tests of the stronger joints. The apex temperatures were measured after about 82 seconds from the weld start, and this time was gradually increased with the increase of the distance from the welding seam. The first 12 seconds of this period represent the initial heating stage, since the TSW method was applied. Same behavior was noticed in the RS, where the AA7075 alloy was positioned, as shown in Figure 4.56 but the temperatures were lower compared to those measured on the advancing side, as illustrated in Figure 4.57.

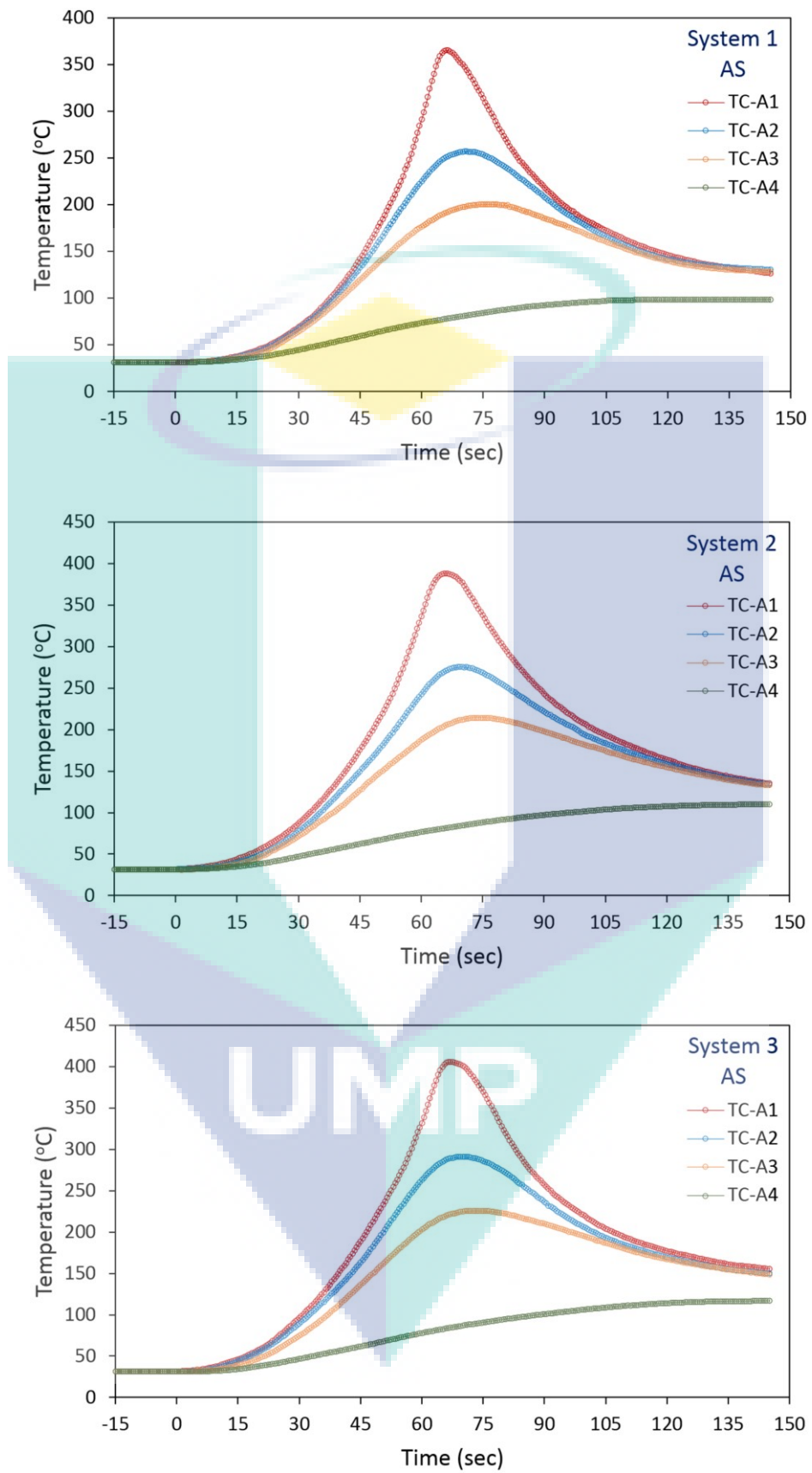


Figure 4.55 Temperature distributions in the AS at 900 rpm and 100 mm/min related to the materials position and backing/clamping systems. AA2024-T351 placed on AS

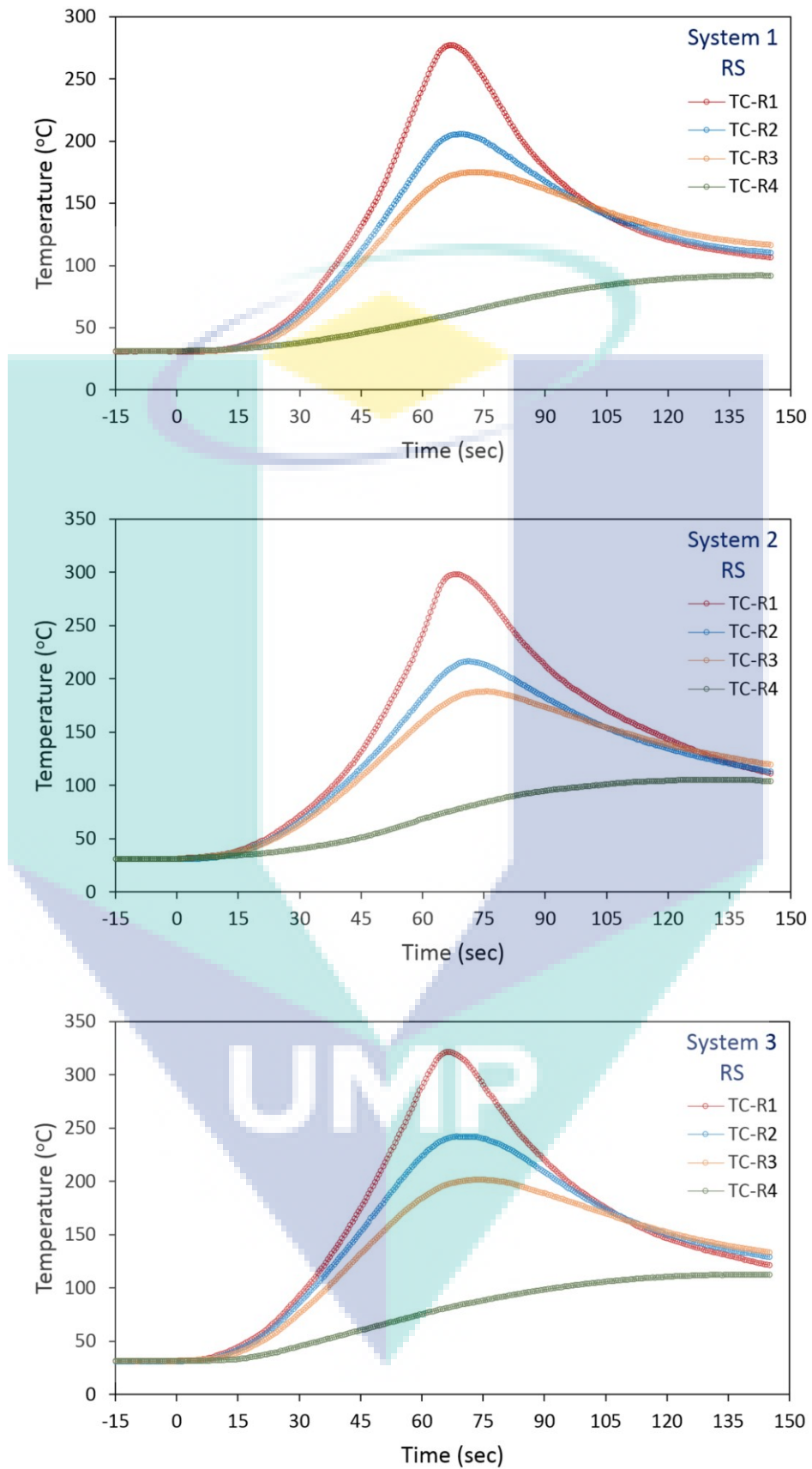


Figure 4.56 Temperature distributions in the RS at 900 rpm and 100 mm/min related to the materials position and backing/clamping systems. AA7075-T6 placed on RS

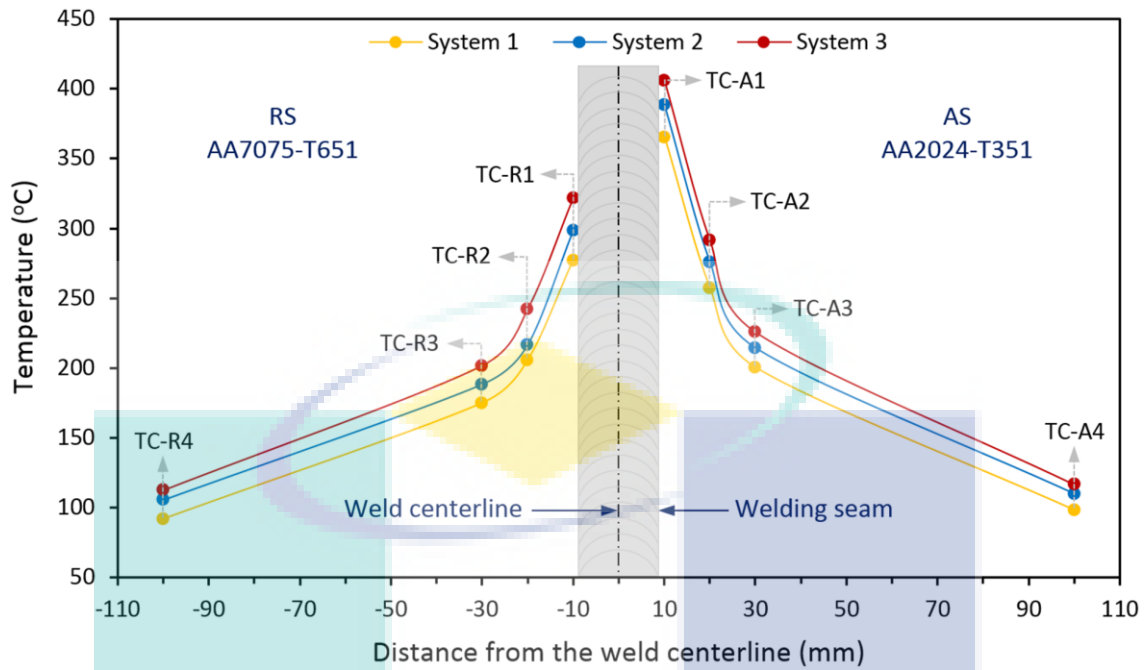


Figure 4.57 Peak temperatures from the eight thermocouples at 900 rpm and 100 mm/min related to the backing/clamping systems

For System 1, the peak temperature in the RS was 277.25 °C, while it raised to reach 365.48 °C in the AS. For System 2, it increased from 298.47 °C in the RS to about 388 °C in the AS. The joint produced using System 3 has exhibited the highest weld temperatures, which increased from 321.51 °C in the RS to about 406 °C in the AS. The change in peak temperatures as per the backing/clamping systems could be attributed to the difference in heating and cooling rates resulting from the variation of thermal conductivity of their corresponding materials (Khodir et al., 2006; Zhang et al., 2013). In addition, the observed results clearly confirmed that the weld temperatures are asymmetric between the two sides of the welding seam.

The calculated difference in peak temperatures between the advancing and retreating sides of the weld was 88.63 °C for System 1, 89.83 °C for System 2 and 84.21 °C for System 3. This asymmetry may affect the mechanical properties of the welding joint (Guo et al., 2014), and in case of dissimilar friction stir welding, the alloy with the lower resistance to deformation always produces the higher processing temperature regardless of the relative materials location on the advancing and retreating sides of the weld (Zettler et al., 2006). The reasons for higher process temperatures in what can be termed the softer low solute content alloys can be seen to be related to an increasing deformation volume, i.e. stir zone. Hence an increased stir zone gives rise to an increased

potential for adiabatic shear and heat generation to occur. Subsequently it can be assumed for such alloys that viscous heat dissipation dominates over friction induced heating. The microstructure evolution depends not only on the tool design, but on the temperature history during the FSW process, which in turn depends on the welding speeds (Colligan & Mishra, 2008; Mironov et al., 2015).

To examine the difference in materials mixing within the SZ for the backing/clamping systems at different welding speeds, Figure 4.58 shows the macrographs of the weld and their corresponding nugget microstructures at 150 mm/min. Variation in the materials mixing and nugget microstructure related to the backing/clamping systems is clear.

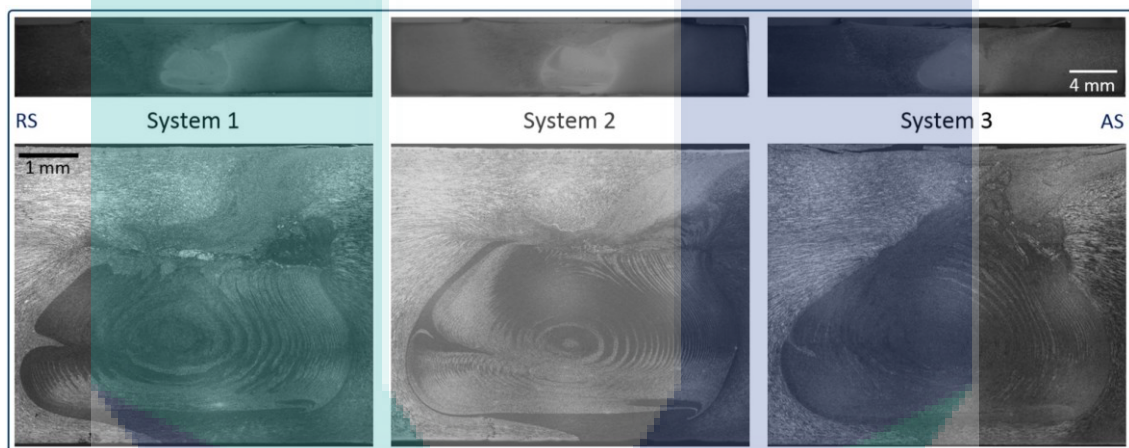


Figure 4.58 Macrographs of the weld and their corresponding nugget microstructures related to the backing/clamping systems at 900 rpm and 150 mm/min. AA2024-T351 placed on AS

The temperature-time history was also considered at this level of the welding traverse speed. Similar behavior to that noticed at 100 mm/min was observed throughout the graphs presented in Figure 4.59 and Figure 4.60. The maximum temperatures were recorded in the weld produced using System 3 followed by System 2 and then System 1. The peak temperatures were measured after about 63 seconds from the weld start, and this time was slightly increased with the increase of the distance from the welding seam. The process temperatures were also higher at the advancing side than those measured at the retreating side for all backing/clamping systems, as will be discussed in the next section.

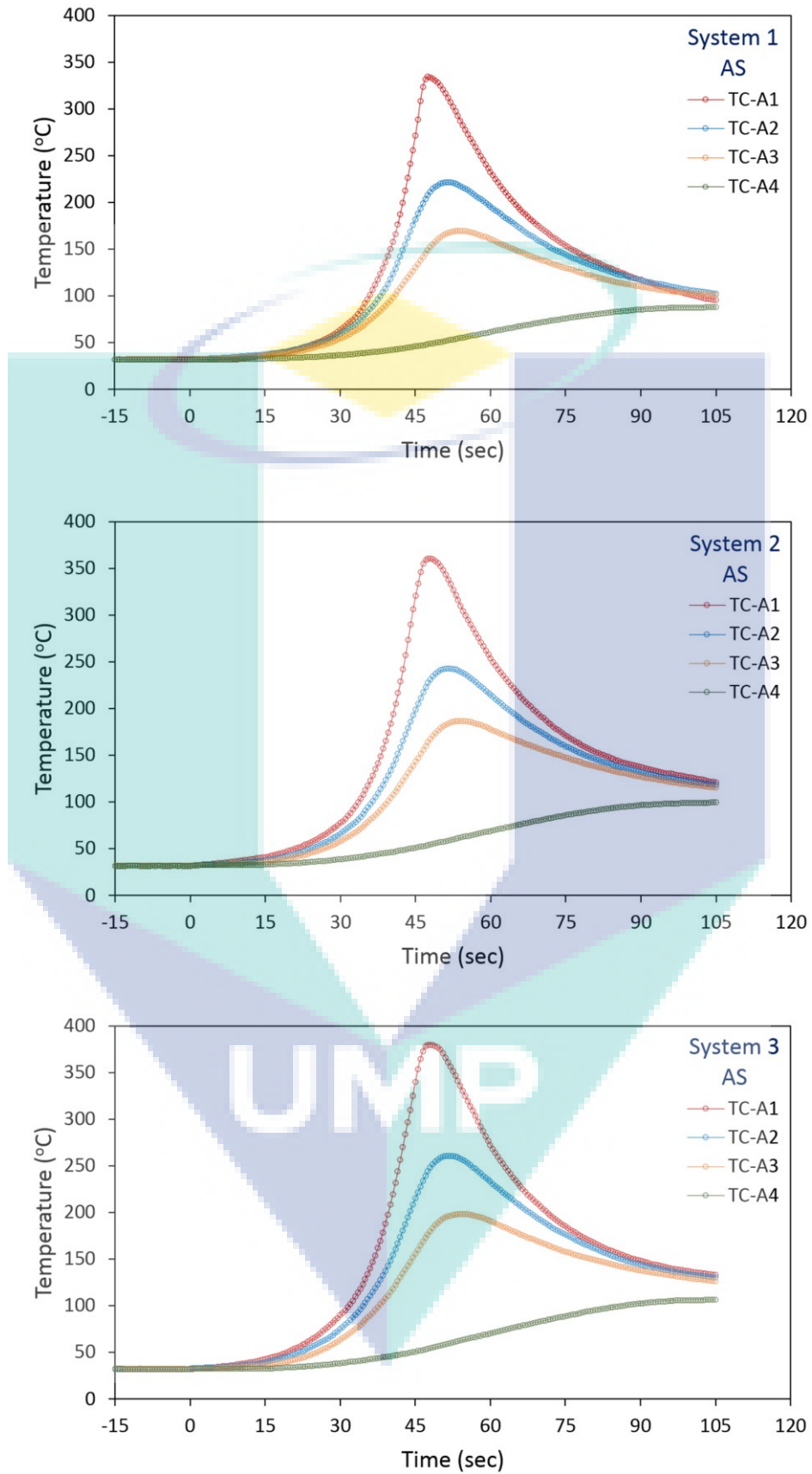


Figure 4.59 Temperature distributions in the AS at 900 rpm and 150 mm/min related to the materials position and backing/clamping systems. AA2024-T351 placed on AS

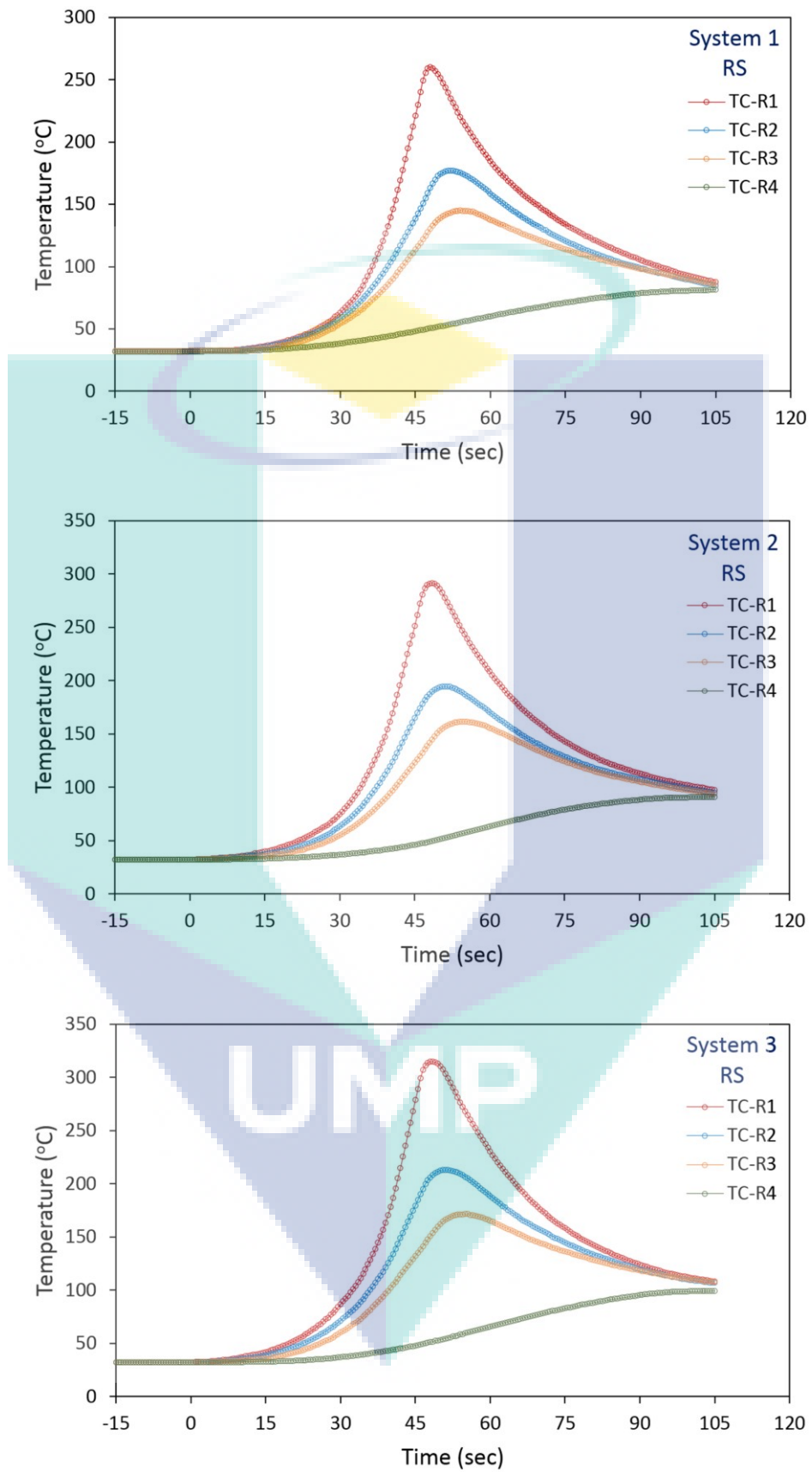


Figure 4.60 Temperature distributions in the RS at 900 rpm and 150 mm/min related to the materials position and backing/clamping systems. AA7075-T6 placed on RS

#### 4.4.4.4 The Asymmetric Backing and Clamping System

Based on the observed results discussed in the previous section, an idea was inspired to use asymmetric backing and clamping design (System 4). The composite backing plate in this system was assembled from SS-SS-Al, as seen in Figure 3.7-b-(4). The softer AA2024-T351 base material was placed on the advancing side above the Al sheet and covered by the same high thermal conductivity material, while the low thermal conductivity steel sheets were used below and above the AA7075-T6 base alloy on the retreating side. This arrangement was used to extract more amount of welding heat from the advancing side and keep the temperature high enough in the stir zone. This may assist to reduce the temperature asymmetry between the advancing and retreating sides of the weld and enhance the joint strength. The weld was produced at 900 rpm and 150 mm/min following the same procedures used with the other backing/clamping systems. Figure 4.61 shows photographs of the surface finish and bottom profile of the weld produced using this novel asymmetric backing/clamping system. The initial visual inspection showed excellent finished weld with smooth surface and clean bottom-face.



Figure 4.61 Photographs of the surface finish (on the left) and bottom profile (on the right) of the weld produced using the novel asymmetric backing/clamping system (System 4) at 900 rpm and 150 mm/min

Defect-free weld with uniform grains was obtained, as shown in Figure 4.62 which presents the macrograph of the joint and the corresponding nugget microstructure. Equiaxed grains were noticed at the crown and center of the mixing SZ with eccentric

onion rings. The welding joint appeared more homogeneous compared to those generated using the other three backing/clamping systems.

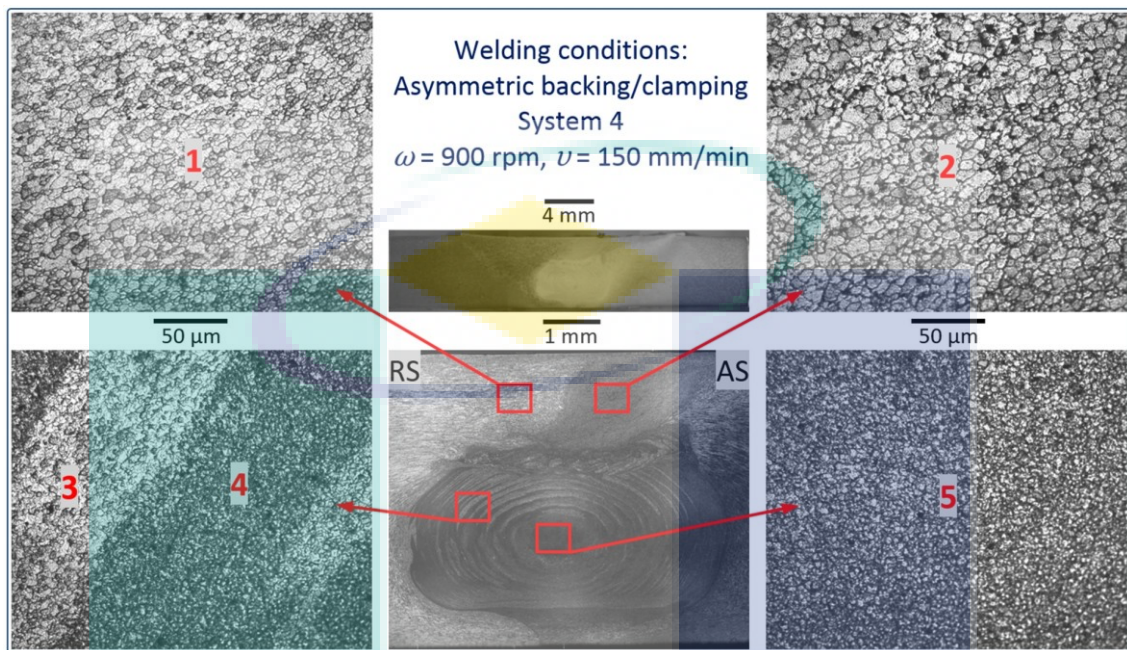


Figure 4.62 Macrograph of the weld and the corresponding nugget microstructure resulted from using the asymmetric backing/clamping system (System 4) at 900 rpm and 150 mm/min. AA2024-T351 placed on AS

The EDS evaluation presented in Table 4.10 shows that the bright region of the crown (spectrum 1) comprises of higher Zn-ratio. This made these zones similar in composition to that of the AA7075 base material. On the other side, higher Cu-ratio was estimated in the dark region of the crown (spectrum 2) which was comparable to the AA2024 base alloy. Same behavior was found in spectrums 3 and 4, which represent the layers of the onion rings. The chemical composition at the center of the weld nugget (spectrum 5) was also close to the AA2024 aluminum alloy.

Table 4.10 The chemical composition (wt.%) of the weld related to the regions shown in Figure 4.62

Spectrum	Si	Fe	Cu	Mn	Mg	Cr	Zn	Ti	Al
1	0.024	0.029	1.731	0.135	2.634	0.009	5.304	0.045	Balance
2	0.130	0.046	4.207	0.247	1.614	0.016	0.622	0.033	Balance
3	0.040	0.063	1.704	0.085	2.609	0.026	6.005	0.048	Balance
4	0.160	0.011	4.270	0.583	1.396	0.041	0.743	0.005	Balance
5	0.122	0.038	3.920	0.310	1.450	0.008	0.704	0.167	Balance
BM-7075	0.013	0.056	1.516	0.118	2.553	0.017	5.968	0.067	Balance
BM-2024	0.124	0.026	4.122	0.820	1.587	0.073	0.156	0.093	Balance

The temperature distributions at the advancing and retreating sides are presented in Figure 4.63. The temperatures on the AS were slightly higher than those of System 1, whereas the temperatures on the RS were slightly lower than those of System 2.

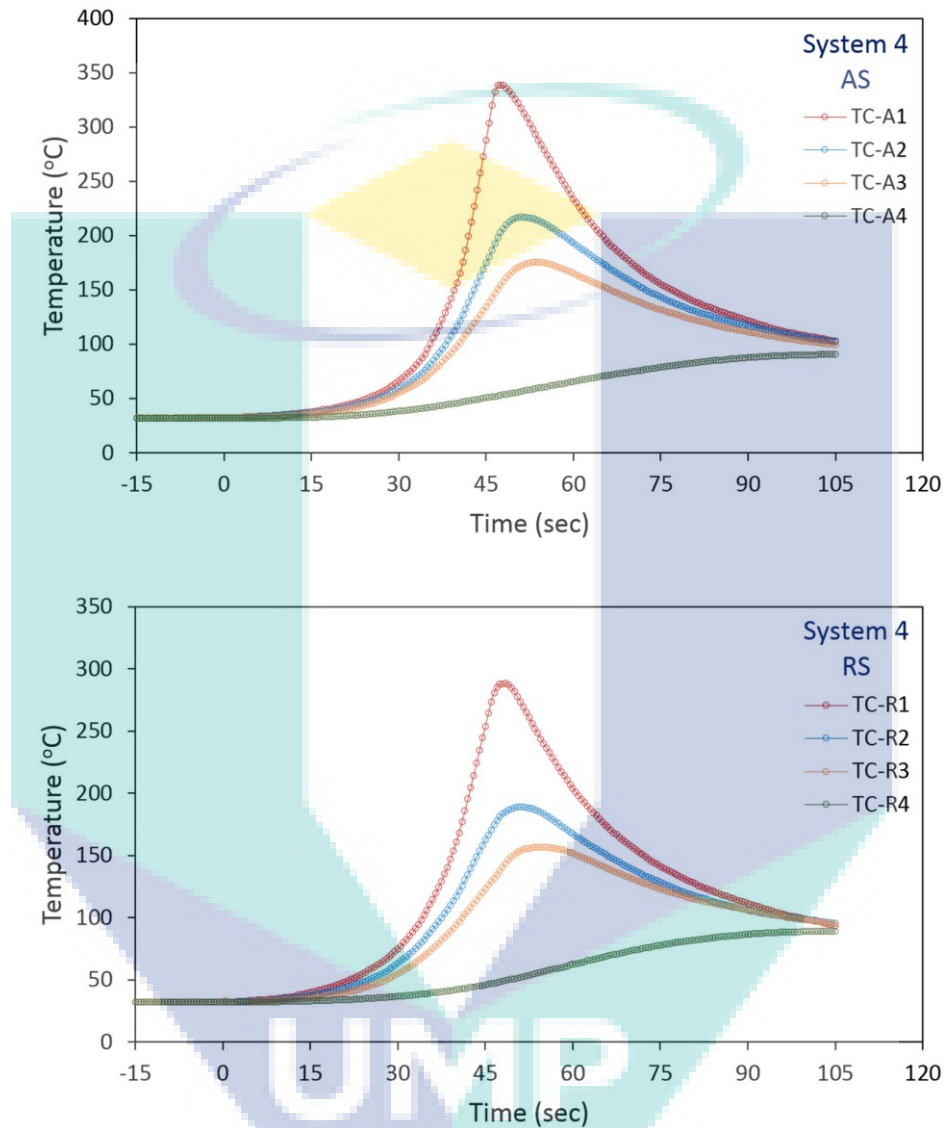


Figure 4.63 Temperature distributions in the advancing and retreating sides of the weld produced using the asymmetric backing/clamping system (System 4) at 900 rpm and 150 mm/min. AA2024-T351 placed on AS

The recorded peak temperatures for this system and the other three systems (Systems 1-3) are drawn in Figure 4.64. The graph shows that the difference in temperatures between the advancing and retreating sides of the weld resulting from using System 4 was reduced compared to the other backing/clamping systems. For System 1, the peak temperature in the RS was 260.05 °C, while it raised to reach 334.3 °C in the AS. For System 2, it increased from 291.62 °C in the RS to about 361 °C in the AS. The

joint produced using System 3 has exhibited the highest weld temperatures, which increased from 314.95 °C in the RS to about 379.58 °C in the AS. The peak weld temperature related to System 4 was increased from 288.57 °C in the RS to 338.75 °C in the AS. Hence, the difference in peak temperatures between the advancing and retreating sides of the weld was 74.25 °C for System 1, 68.95 °C for System 2 and 64.63 °C for System 3, while it was equal to 50.18 °C in System 4.

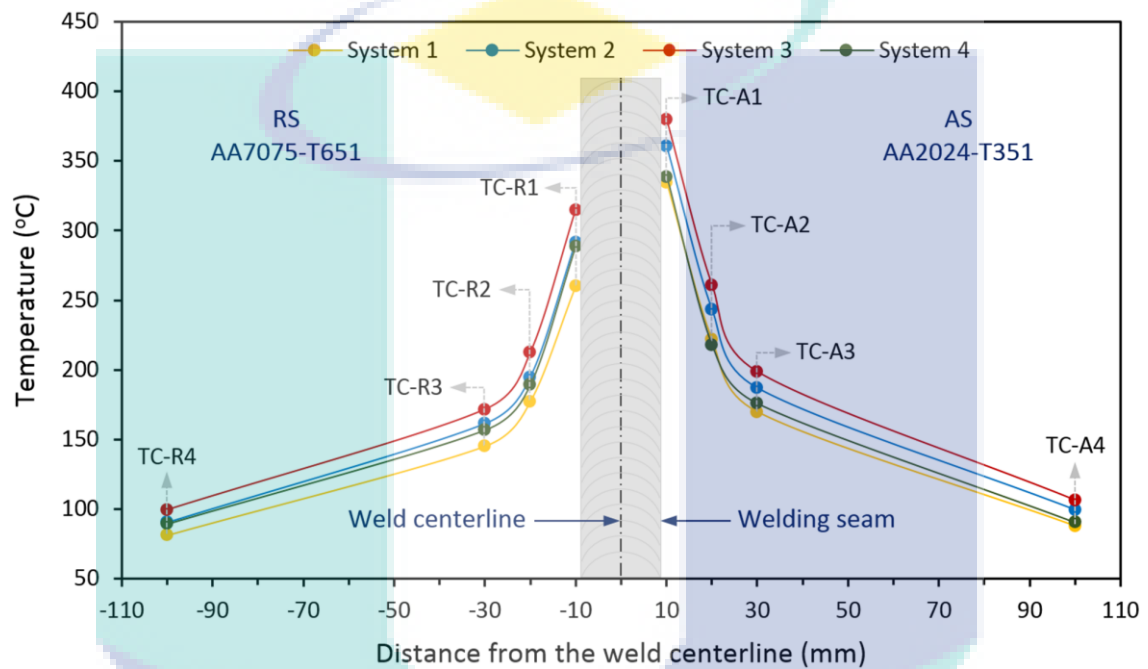


Figure 4.64 Peak temperatures from the eight thermocouples at 900 rpm and 150 mm/min for all backing/clamping systems

Reducing the temperature asymmetry contributed to improve the materials mixing and enhance the hardness distribution of the weld, as shown in Figure 4.65 which presents the weld micro-hardness for all backing/clamping systems at 900 rpm and 150 mm/min. The hardness level of weld nugget related to System 4 was slightly higher than that of System 1. This can be attributed to the modification in heat sinking made in System 4 on the RS. The low thermal conductivity SS sheet inserted below and above the AA7075 alloy instead of the high thermal conductivity Al plate reduced the heat loss in the retreating side of the weld and hence improved the nugget hardness. In addition, the hardness of the HAZ was increased in the advancing side compared to System 2. This is due to the replacement of the low thermal conductivity SS sheet with the high thermal conductivity Al plate below and above the AA2024 alloy to extract more amount of welding heat from the advancing side.

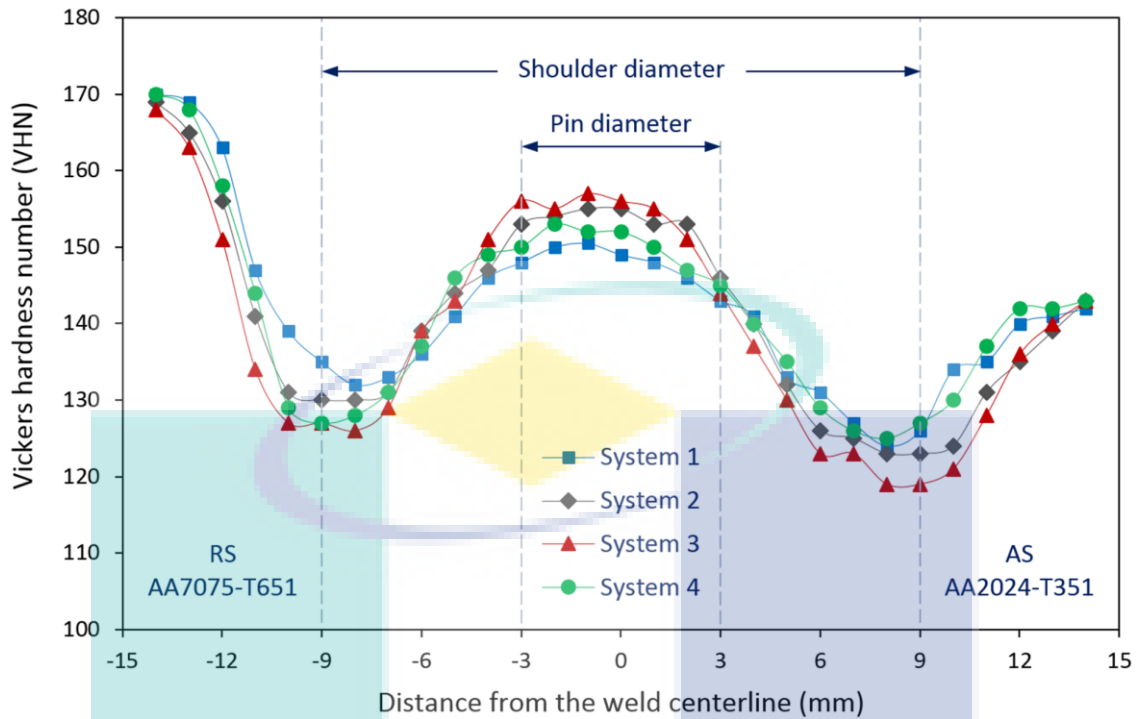


Figure 4.65 The weld micro-hardness distribution at 900 rpm and 150 mm/min for all backing/clamping systems

The ultimate strength and tensile elongation of the weld was hence considerably increased, as revealed by the stress-strain curves presented in Figure 4.66.

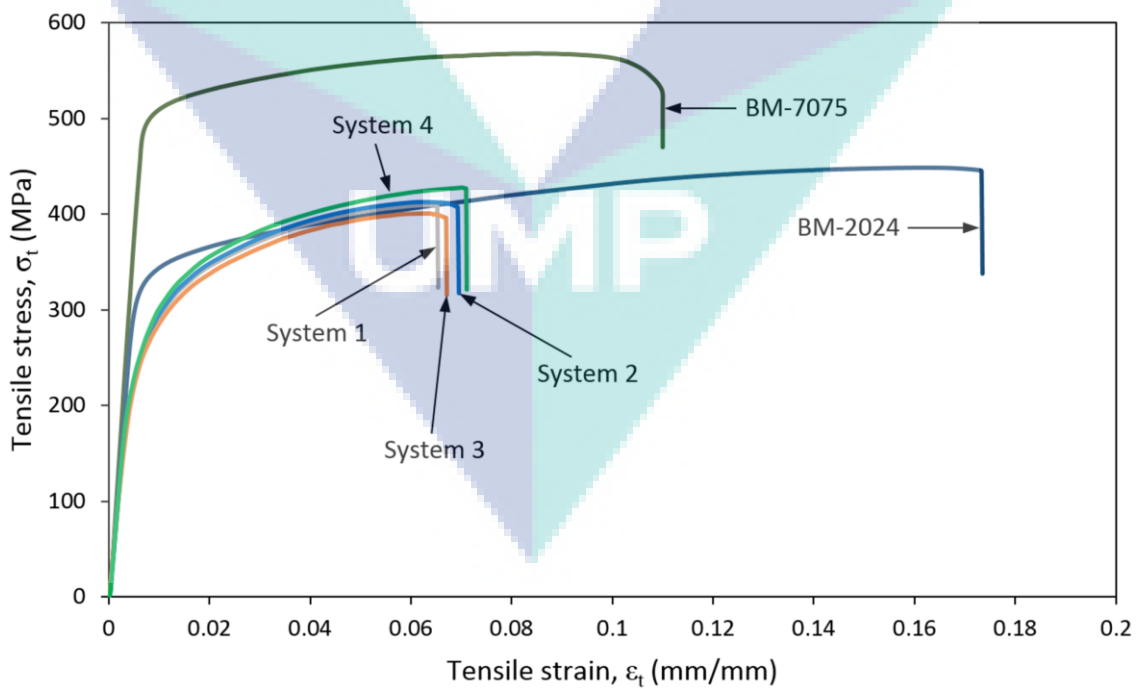


Figure 4.66 Stress-strain curves of the base materials and welding joints for all backing/clamping systems at 900 rpm and 150 mm/min. AA2024-T351 placed on AS

The graphs indicate that the highest joint strength of about 426 MPa were obtained through using System 4. This value represents an efficiency of 94.8% with respect to the strength of the softer base material. At this case, the maximum tensile elongation of about 7.1% was observed, which represents the apex record compared to the other backing/clamping systems.

#### 4.4.5 Characterization of the Pin Tool Design

This section presents a further design study of the welding pin tool through investigating the effect of flute radius on the tensile strength of dissimilar AA7075-T6 and AA2024-T351 friction stir welds. As illustrated in Figure 3.4-(c) and described in Table 3.3, five welding pin tools with different flute radius were examined. Based on the results outlined in the previous sections, the welding trials were performed under 900 rpm and 150 mm/min using the composite Al-SS backing and clamping system (System 2). The relative position of materials on the advancing and retreating sides of weld was also considered. The metallographic analysis of the resulting welds and their corresponding tensile properties are presented and discussed in the following sections.

##### 4.4.5.1 Metallographic Analysis

The macrographs of dissimilar welding joints produced using different pin tool profile related to the base materials position are presented in Figure 4.67.

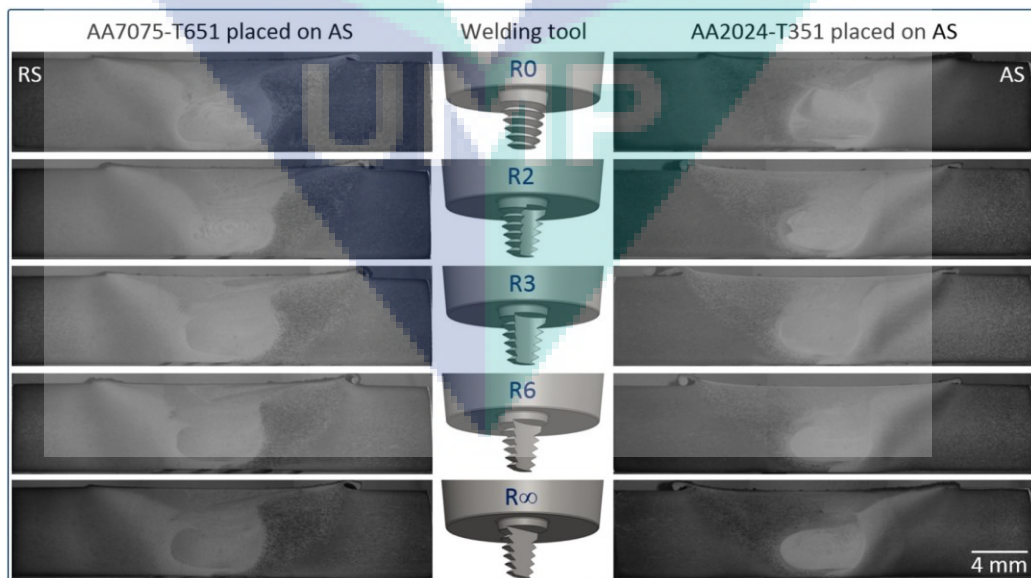


Figure 4.67 Macrographs of the dissimilar welding joints related to the pin tool profile and materials position

The metallographic specimens were prepared along the weld cross section, and the right-hand side of each photo represents the advancing side of welding tool. The graphs show clearly the difference in material flow and mixing related to the probe design. The high strain rate due to the tool rotation and translation resulted in a severe deformation and dynamic recrystallization of the grains at the mixing stir zone (Kumar & Kailas, 2008). That vertical and circular plastic flows of the coupled materials occur during the FSW process (Luo et al., 2016). The left-hand threads of the pin tool push the material down away from the shoulder in conjunction with the circular motion of the tool. The heat generated and materials movement lead the grains of the base alloys to enter into each other and form the weld nugget (Trimble et al., 2015). Variation of the flow pattern within the mixing SZ due to the flute radius is introduced through the micrographs of the weld nugget. Figure 4.68 shows the microstructure of the weld nugget produced by the base threaded pin tool R0. Non-homogeneous onion rings were generated when the harder AA7075 aluminum alloy was placed on the AS. The rings were more clear and concentric when the softer AA2024 alloy was fixed on the AS.

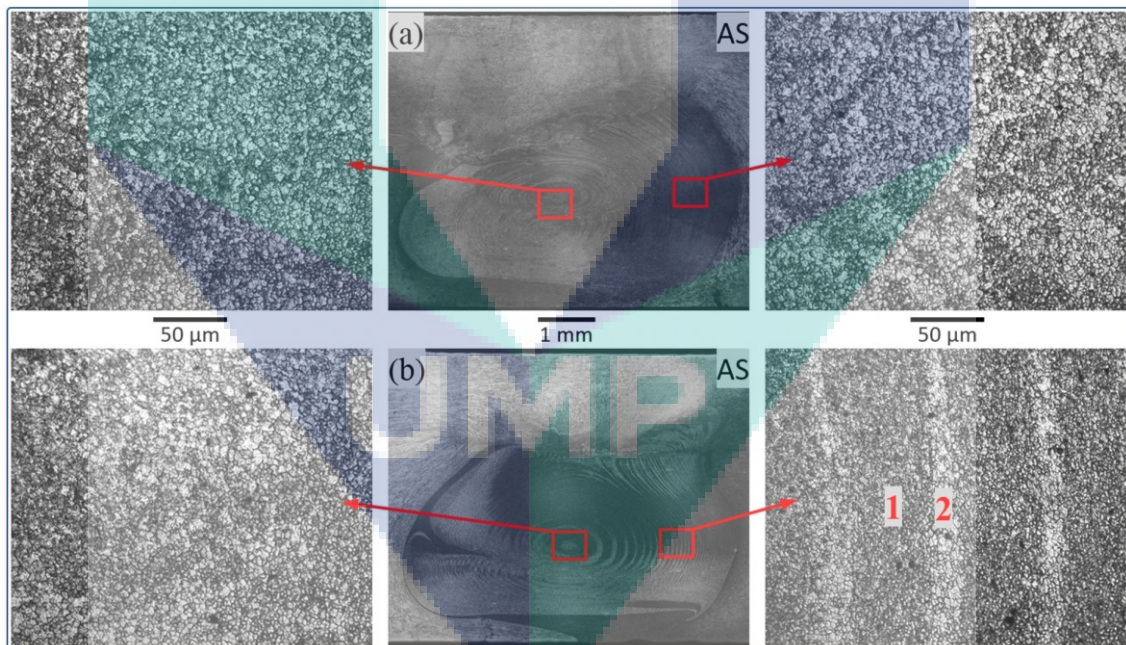


Figure 4.68 Micrographs of the weld nugget produced by the pin tool R0. (a) AA7075-T6 placed on AS and (b) AA2024-T351 placed on AS

As mentioned before, the etching response of the dissimilar parent materials to the Keller's reagent are not the same due to the difference in their chemical composition (Firouzdor & Kou, 2010). For this reason, the micrographs were revealed in dark and

bright colors. In the advancing part of the weld, thickness of the bright rings increased from the edge of the nugget towards its center due to the tool rotational mixing of materials (Tongne et al., 2017). The grains were slightly bigger when the AA7075 alloy was positioned on the AS. Forming a flute with 2 mm radius on the cone of the pin tool R2 significantly affects the nugget shape regardless of the relative materials position, as presented in Figure 4.69. The onion rings started to decrease when the AA2024 alloy was located on the advancing side.

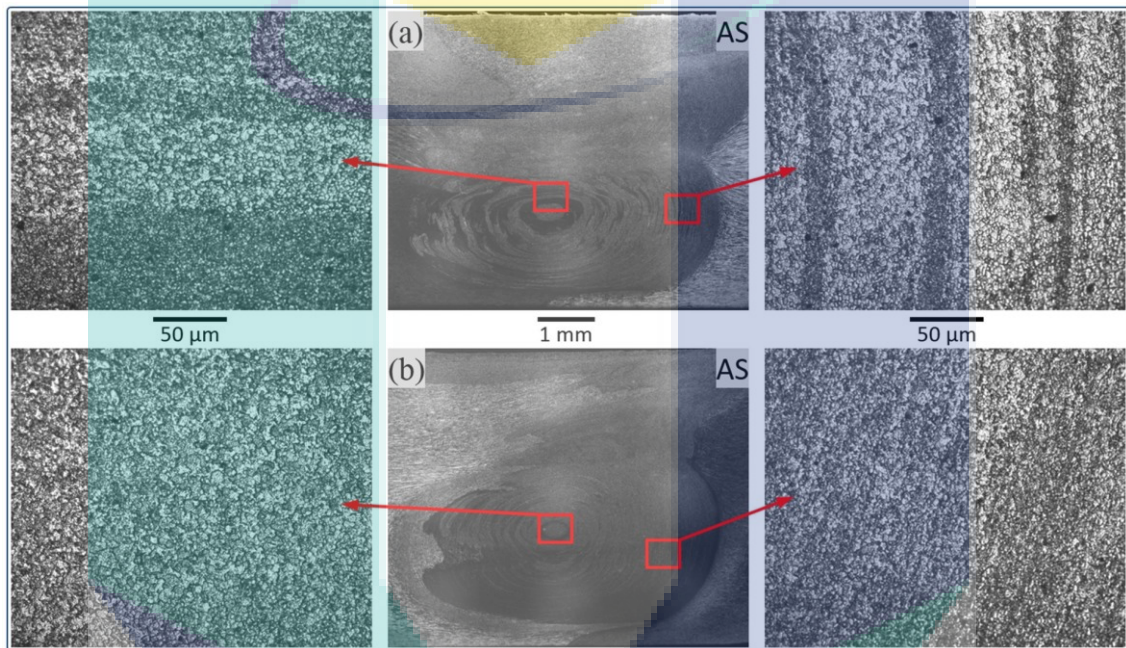


Figure 4.69 Micrographs of the weld nugget produced by the pin tool R2. (a) AA7075-T6 placed on AS and (b) AA2024-T351 placed on AS

When the flute radius was enlarged to 3 mm in pin tool R3, the weld nugget has exhibited very soft onion rings, as seen in Figure 4.70. The grains were clearly bigger when the AA7075 alloy was positioned on the AS than those of the weld produced by placing the softer AA2024 alloy on the AS. Hence, it can be indicated that the weld temperature became higher when the harder base material was positioned on the advancing side of the welding tool. This is because the average grain size of the mixing SZ increases with increasing the process temperature (Rahimzadeh Ilkhichi et al., 2014). However, the weld nuggets seemed more homogeneous and alike through using this welding pin tool design.

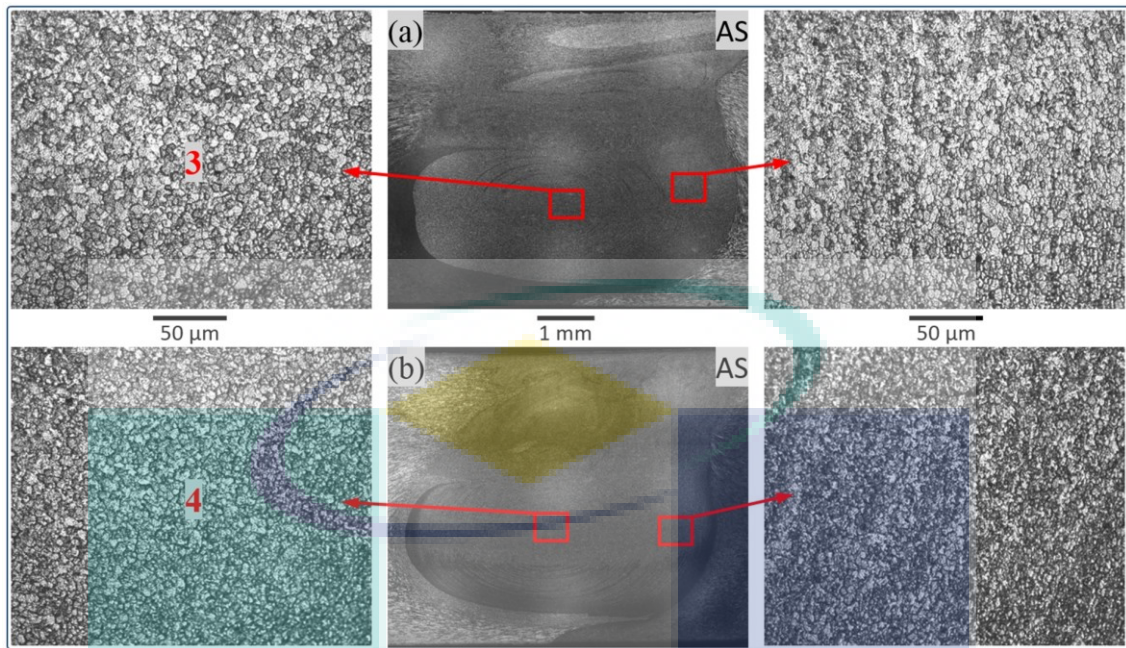


Figure 4.70 Micrographs of the weld nugget produced by the pin tool R3. (a) AA7075-T6 placed on AS and (b) AA2024-T351 placed on AS

Increasing the flute radius to 6 mm in pin tool R6 made the weld nugget darker when the AA2024 alloy was fixed on the AS with fine grains at the center and some non-equiaxed particles at the crown, as presented in Figure 4.71.

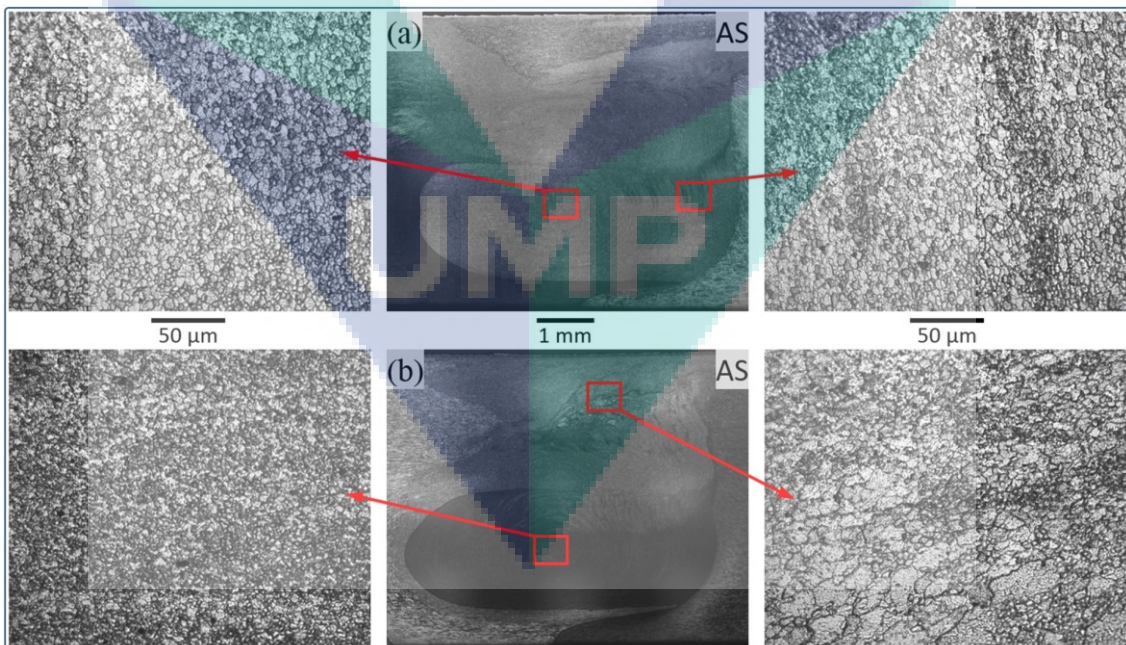


Figure 4.71 Micrographs of the weld nugget produced by the pin tool R6. (a) AA7075-T6 placed on AS and (b) AA2024-T351 placed on AS

Slight dark layers were generated at the right-hand side of the nugget and the grains were also bigger when the AA7075 alloy was placed on the AS. Same behavior was noticed when the flute was further enlarged in tool  $R_{\infty}$ , which can be considered as a truncated threaded pin tool with a single flat. In this case, the onion ring pattern became more clear but still inhomogeneous and irregular, as seen in Figure 4.72. The taper and threads affect the local flow around the pin, affecting the layered deposition of material related to the onion ring structure and move material downward toward the root surface (Schneider et al., 2016). In addition, the flat acts as a paddle in moving material to plasticize additional material near the tool surface (Thomas & Dolby, 2003).

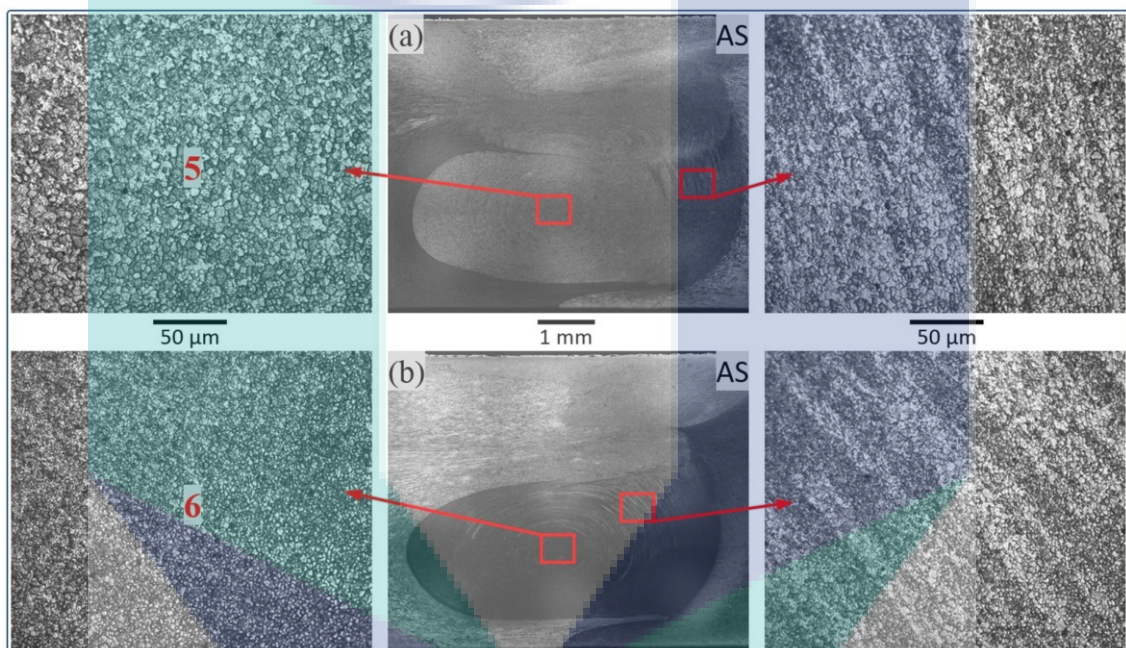


Figure 4.72 Micrographs of the weld nugget produced by the pin tool  $R_{\infty}$ . (a) AA7075-T6 placed on AS and (b) AA2024-T351 placed on AS

The chemical composition was analyzed by an energy dispersive spectrometry in six different regions inside the weld nugget and compared with those of the base welding alloys. As shown in Figure 4.73, two sections of the onion rings generated by using tool  $R_0$  was primarily examined when the AA2024 alloy was placed on the advancing side. As was previously observed and clarified in Section 4.4.2.2, the dark region (spectrum 1) consisted of higher copper ratio and was more similar to the AA2024 base alloy, as presented in Table 4.11. On the other side, the bright layer (spectrum 2) contained more of the aluminum 7075 composition such as Zn and Mg.

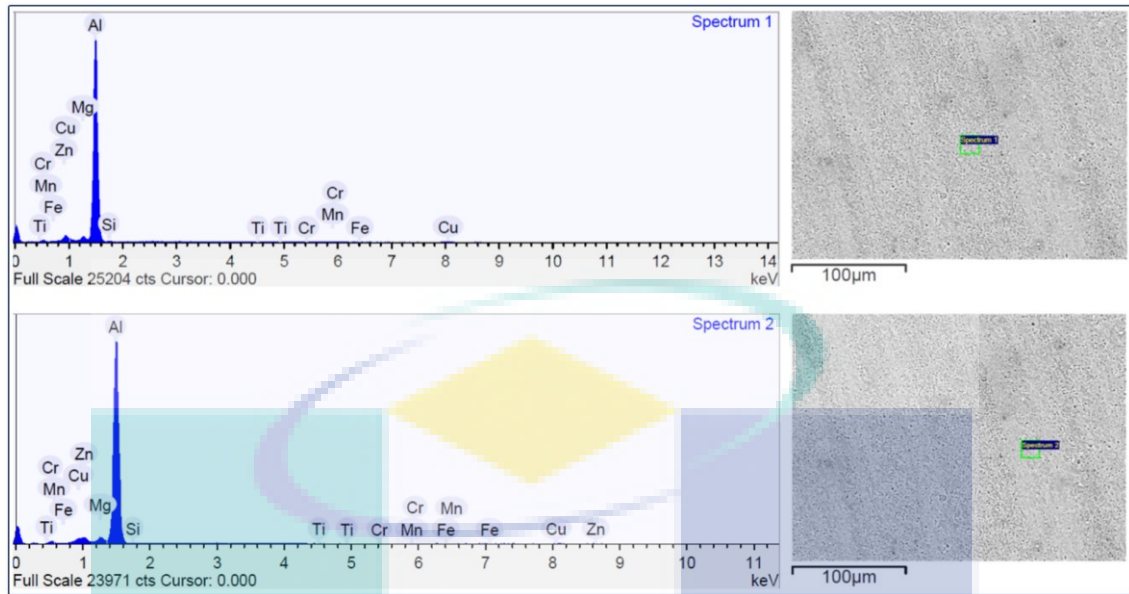


Figure 4.73 The EDS spectra as per the regions numbered in Figure 4.68

Spectrums 3 and 4 represent the center regions of the welds produced by pin tool R3 when the AA7075 alloy was positioned on the advancing and retreating sides, respectively. The acquired chemical composition of the weld nugget at these sections implies that better material mixing was achieved using this probe design. Nevertheless, the material contents of AA7075 alloy such as the Zn-ratio were higher when this base material was fixed on the AS, while the composition of AA2024 parent alloy such as Cu-ratio was higher when it was located on the AS. Similar results were recorded in spectrum 5 when the AA7075 alloy was placed on the AS during the use of tool R $\infty$ , but the chemical composition of spectrum 6 was close to the AA2024 aluminum alloy when this welding material was located on the advancing side of the weld. Analyzing of the non-recrystallized HAZ/TMAZ regions was not included here, since it was previously shown that these zones are similar to their corresponding base materials.

Table 4.11 The chemical composition (wt.%) of the weld related to the regions shown in Figure 4.68, Figure 4.70 and Figure 4.72

Spectrum	Si	Fe	Cu	Mn	Mg	Cr	Zn	Ti	Al
1	0.019	0.031	1.683	0.141	2.604	0.014	5.836	0.091	Balance
2	0.127	0.027	4.173	0.652	1.703	0.065	0.582	0.041	Balance
3	0.079	0.054	2.633	0.207	3.107	0.047	5.114	0.015	Balance
4	0.093	0.035	3.066	0.419	2.675	0.050	3.743	0.031	Balance
5	0.073	0.037	3.181	0.330	2.957	0.008	4.962	0.071	Balance
6	0.096	0.044	4.416	0.380	1.853	0.053	1.016	0.084	Balance
BM-7075	0.013	0.056	1.516	0.118	2.553	0.017	5.968	0.067	Balance
BM-2024	0.124	0.026	4.122	0.820	1.587	0.073	0.156	0.093	Balance

#### 4.4.5.2 Tensile Properties and Hardness Distribution

Figure 4.74 presents the tensile strength and percentage elongation of the joints produced by the five welding tools related to the materials position. Generally, placing the softer AA2024 alloy on the AS resulted in a slight increase of the tensile properties of the welding joints. The introduction of pin tool flute/flat improved the ultimate tensile strength and elongation. This could be attributed to the improvement in material flow, as was presented in previous section. The strongest joint was produced using tool R3, which contains a flute of 3-mm-radius. In this case, the observed UTS and percentage elongation were 424 MPa and 7.18%, respectively. This joint strength represents an efficiency of about 94.3% with respect to the AA2024 base material. All tension test specimens were fractured at the HAZ of the softer base material regardless of the fixed position of the welding parent materials.

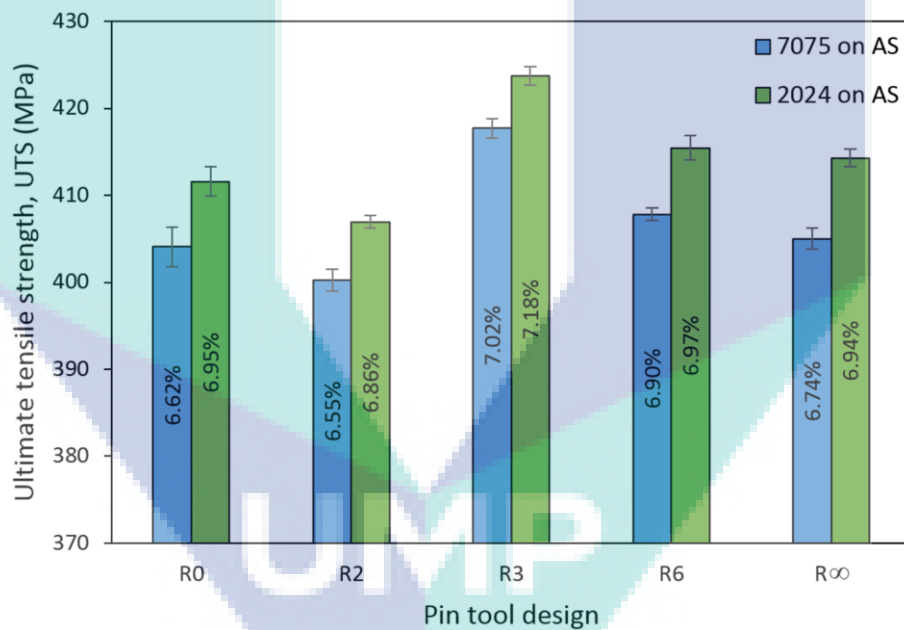


Figure 4.74 Joint strength and percentage elongation related to the pin tool design

The transverse Vickers micro-hardness distribution is drawn in Figure 4.75 for the weld produced by the pin tool that is free of the additional flat/flute (R0), pin tool with optimal flute radius (R3) and tool containing the single flat (R∞). This is to make a comparison between the tools produced with and without flat/flute features on their probes. For the three case studies, the softer AA2024-T351 was located on the AS. Another case was considered for the pin tool with flute radius R3 when the harder AA7075-T6 was placed on the AS (the blue-color curve). This is to show the difference

in hardness distribution related to the position of the welding base materials. Overall, the weld joint has exhibited a noticeable micro-hardness decrease compared to the base materials. This could be attributed to the grain refinement or recrystallization within the stir zone and over-aging in the heat affected zone (Ahmed et al., 2017; Khan et al., 2017; Sun et al., 2016). Maximum reduction of the weld hardness was observed in the heat affected zone of both welding sides regardless of the relative materials position. Modification of the welding tool by forming a flute on the cone of the probe improved the weld hardness regardless of the flute radius. In the mixing SZ, the apex hardness level was noticed when the harder AA7075 alloy was placed on the AS but the VHN was dropped to the minimum value at the HAZ of the AA2024 alloy. The HAZ of the softer alloy represents the weakest region of the sound dissimilar friction stir welds regardless of the relative materials location (İpekoğlu & Çam, 2014; Rodriguez et al., 2015). The micro-hardness dropped in this region due to the elevated temperature and mechanical extension of the grains (Sun et al., 2016). Minimum reduction of VHN at the HAZ was recorded when the weld was produced by tool R3 and the AA2024 alloy was placed on the AS. This clarifies the reason behind the improvement of the efficiency of joint produced using this pin tool.

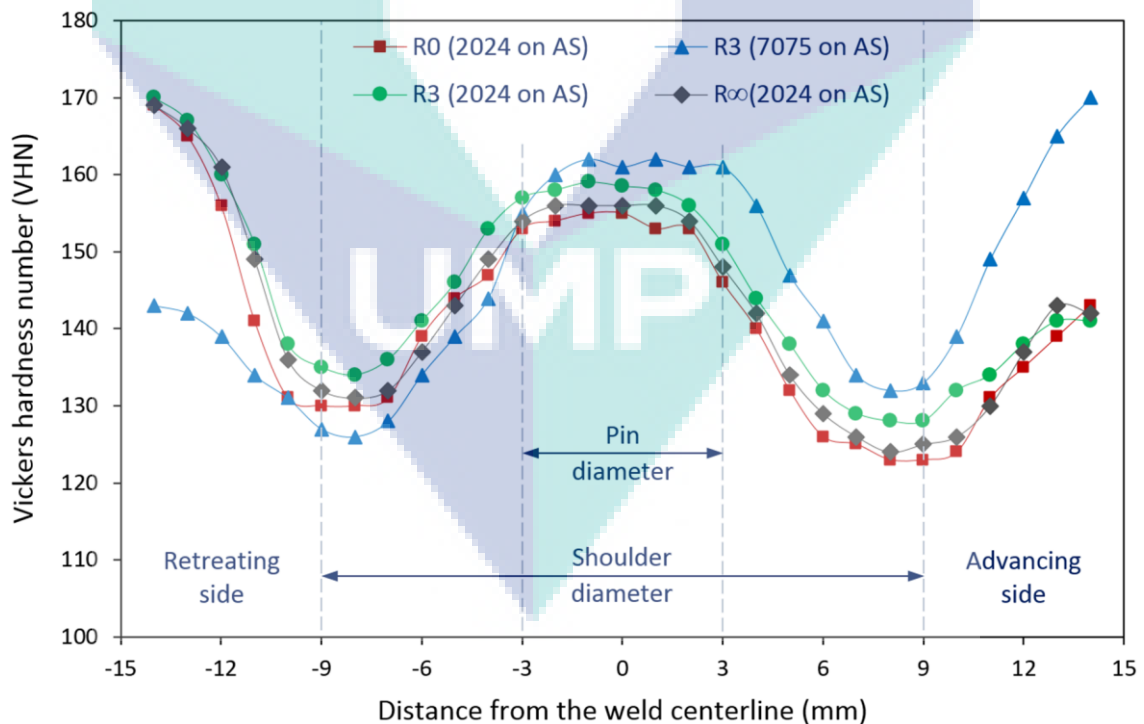
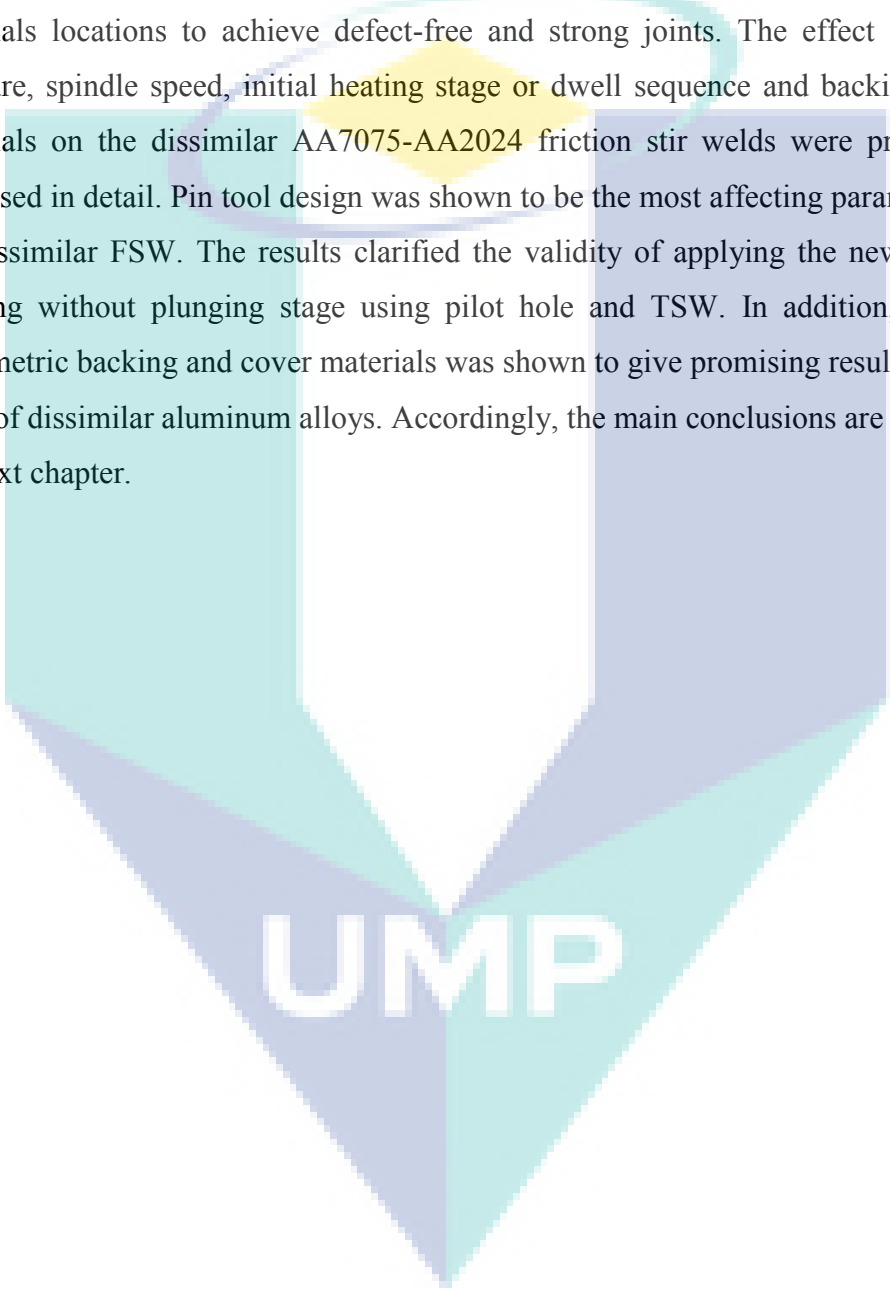


Figure 4.75 The weld micro-hardness distribution related to the pin tool design and materials position

## 4.5 Summary

In this chapter, the acquired results of current research study regarding the design of welding tool and backing/clamping system with optimized process parameters for the friction stir welding of dissimilar aluminum alloys are presented and discussed. Different pin tool profiles were tested in conjunction with varied levels of welding speeds and materials locations to achieve defect-free and strong joints. The effect of clamping pressure, spindle speed, initial heating stage or dwell sequence and backing/clamping materials on the dissimilar AA7075-AA2024 friction stir welds were presented and discussed in detail. Pin tool design was shown to be the most affecting parameter during the dissimilar FSW. The results clarified the validity of applying the new method of welding without plunging stage using pilot hole and TSW. In addition, the use of asymmetric backing and cover materials was shown to give promising results during the FSW of dissimilar aluminum alloys. Accordingly, the main conclusions are addressed in the next chapter.

The logo for UMP (University of Miskatonic) is a large, stylized shield shape. It is divided into four quadrants by a white 'V' shape pointing downwards. The top-left and bottom-right quadrants are light blue, while the top-right and bottom-left quadrants are light purple. The letters 'UMP' are written in a bold, white, sans-serif font across the center of the shield.

UMP

## CHAPTER 5

### CONCLUSIONS AND RECOMMENDATIONS

#### 5.1 Introduction

Joining dissimilar high-strength and lightweight AA7075-T6 and AA2024-T351 aluminum alloys by the FSW was investigated in this dissertation. Tool design, process parameters and thermal boundary condition were optimized to produce quality weld. The experiments were accomplished using specially designed backing/clamping systems. Several aspects were presented and discussed related to the broad scope to provide advanced knowledge in the field of study. Summary of the findings obtained from the work carried out in the present scientific research is presented in this chapter. In addition, the future recommendations that may be followed to extend the study of the friction stir welding of dissimilar materials are outlined.

#### 5.2 Summary of the Findings

The following sections present the main concluding remarks that can be drawn as per the observed results of the current research work.

##### 5.2.1 Tool Design

Five welding tools with concave shoulders and different probe profiles (cylindrical and tapered, smooth and threaded, flatted and non-flatted) were examined through the FSW of dissimilar 3-mm-thick AA7075-T6 and AA6061-T6 aluminum alloys under a range of machine variables planned by the central composite design. The obtained results showed that tool design is the most influential aspect in dissimilar friction stir welding. The welding tools with tapered probe and additional features (threads and flat) can be effectively used to produce sound welds with smooth surface finish, good material mixing and high tensile strength. On the other side, tools with smooth straight

cylindrical or even tapered probes are not preferable, since they result in poor material mixing and hence lower joint strength.

Tool design was further investigated through analyzing the effect of flute radius of the probe on the material flow and joint strength of dissimilar 6-mm-thick AA7077-T651 and AA2024-T351 aluminum alloys. Different sizes of cutting tools were used to add a single flute or flat to the cone of the base truncated threaded pin tool. The observed results showed that the strongest welding joint can be produced by using featured pin tool with a flute of radius equal to the base radius of the probe.

### 5.2.2 Mathematical Modeling

The welding tool rotation and traverse speeds were optimized in this work for different joint thicknesses. These principal variables were optimized in conjunction with the tool design and tilt angle during the FSW of the thinner aluminum alloys 7075 and 6061. A reduced second order polynomial equation was successfully developed and validated to adequately fit the observed results of the weld ultimate tensile strength. This model seemed to be an active tool for the prediction of joint strength as a function of the selected variables. A respectable fitness of the developed model with the experimental data within the range of the operating variables was indicated with an elevated regression coefficient ( $R^2 = 0.9851$ ). Well agreement between the observed and calculated values with low deviation (error within  $\pm 10\%$ ) was also recorded through the validation tests. It was concluded that the weld strength increases with the increasing of process parameters until it reached the apex level and decrease again when these parameters are further raised. The stronger joint with maximum joint strength of about 252 MPa, which represents an efficiency of 82 % was reached at 1100 rpm of tool rotation speed, 300 mm/min of traverse speed and  $3^\circ$  of tool tilt angle.

The optimal welding speed were different when the joint thickness of the dissimilar AA7075-AA2024 friction stir welds was 6 mm. The maximum joint strength of about 400 MPa, which represents an efficiency of 89% was recorded at 900 rpm when the tool rotation speed was preliminarily investigated at 100 mm/min of traverse speed and  $3^\circ$  of tilting angle. Raising this rotation rate resulted in a stretching of the nugget grains due to the fast cycling of materials mixing and elevation of the welding temperature, which in turn led to decrease the hardness at the HAZ and hence, affected

the weld ultimate strength. This means that the spindle speed should be reduced for the thicker welding joints. Same behavior was noticed regarding the tool traverse speed. The maximum weld efficiency of 91.6% was calculated at 150 mm/min, which is equal to half of the optimal traverse speed used to join the thinner plates.

### **5.2.3 Materials Direction and Position**

Four different configurations related to the rolling direction of welding plates were examined in two groups related to the materials position on the advancing and retreating sides of the weld. The eight case studies were conducted through the FSW of the 3-mm-thick AA7075 and AA6061 aluminum alloys. It was noticed that stronger joint could be achieved by placing the softer alloy on the advancing side of the weld and stirring the tool in a direction parallel to the RD of the abutting plates. The weld strength can be further improved when the welding seam is produced in a direction parallel to the RD of the softer material and normal to that of the harder one. Through this welding configuration and materials location, the joint tensile strength reached the maximum value of 255.8 MPa, which represents an efficiency of about 84.3%. On the other side, the strength of joint was slightly decreased when the welding seam generated in a direction normal to the RD of both welding sheets, regardless of the relative materials position on the advancing and retreating sides. Minimum joint strength of about 221.3 was recorded when the RD of both sheets was normal to the welding line, and the softer material placed on the AS.

The influence of the fixed location of the welding base materials on the joint strength was also studied during the FSW of the 6-mm-thick aluminum 7075 and 2024. It was concluded that the effect of materials position has increased with decreasing tool rotation rate and increasing traverse speed. In other words, the weld strength decreased when the harder material was placed on the AS. This drop of strength has enlarged at cold welding (welding at low rotation rate or raised traverse speed) due to the higher power required to drive the welding tool when the harder material is fixed on the advancing side.

### **5.2.4 Clamping Force**

The optimal clamping pressure was detected through joining several pairs of AA7075 and AA2024 aluminum coupons secured on the machine table by equal vertical and lateral forces ranged from 1-6 kN using the developed backing/clamping system. It

was exposed that 1 kN is not enough force to prevent the separation of the workpieces during the initial plunging stage of the welding process. Beyond this level of clamping force, the produced joints were free of the undesirable initial gap. The weld strength was reached the maximum value of 394 MPa when the clamping force was fixed at 3 kN. Further increase in the clamping force resulted in a gradient reduction in the weld tensile strength, which have reached the lowest value of about 381 MPa when the clamping force was fixed at 6 kN. Accordingly, the abutting plates should be subjected to moderate clamping pressure to produce efficient and stable weld.

### **5.2.5 Initial Heating Stage or Dwell Sequence**

The ordinary plunge phase of the friction stir processing is the main cause of the early wear in the welding pin tool due to the high compressive stress and temperature endured by the probe. Omitting this plunge cycle assists to extend the lifetime of the pin tool, which is essential for producing stable weldments with minimum manufacturing cost. A pilot hole slightly smaller than the probe can be created at the weld start point to achieve this objective. An estimation of the appropriate stationary dwell time is then indispensable to generate the sufficient heat required to soften the abutting materials before the main welding phase. Consequently, the stationary delay time was examined and a new method of using two-stage welding was introduced in this work. The latter way was attained to minimize the shoulder wear that may result from the stationary dwell period. The test-coupons were prepared through dissimilar joining of the high-strength AA7075 and AA2024 aluminum alloys. It was noticed that surface-breaking voids generate during the shorter dwell sequences, while the defect-free weld is produced after 12 seconds of stationary delay time. Raising this period to 24 seconds reduces the joint strength due to the hardness drop at the HAZ of the softer alloy, which indicates that the amount of the generated frictional heat is higher than the required level. The most stable weldment with the highest tensile strength and minimum deviation was achieved by using the two-stage welding method, which significantly reduced the longitudinal deformation of the pin tool compared to the ordinary plunging cycle. It is also able to minimize the shoulder wear that may result from the stationary dwell sequence.

### 5.2.6 Backing and Clamping Materials

An attempt was made to improve the joint strength by controlling the temperature distribution during the FSW of dissimilar AA7075-T6 and AA2024-T351 aluminum alloys. Three composite backing plates and clamping systems were tested in conjunction with varying levels of the tool traverse speeds and materials position. The developed backing/clamping system was modified to insert high and low thermal conductivity aluminum and stainless steel sheets below and above the workpieces. Moreover, the dissimilar base material was insulated in the third system by an air-gap to minimize the process heat lost. The transient temperatures were experimentally measured at different distances from the welding line. The welding temperature must be kept high enough in the mixing stir zone and reduced at the heat affected zone to improve the joint strength. Consequently, the use of material with high thermal conductivity in the modified backing/clamping system at hot welding (welding at low traverse speed) was favorable. At this case, the system worked as an adequate heat sink to dissipate some of the welding heat and minimize the drop of the joint strength caused by the overheating effect. On the other side, the welding traverse speed could be raised by minimizing the dissipated heat through insulating the workpieces or inserting low thermal conductivity material in the composite backing/clamping system.

High-temperature difference was noticed between the advancing and retreating sides of the weld. The temperatures were higher on the advancing side compared to those measured on the retreating side. The peak temperature was observed close to the welding seam where the fracture occurred during the tensile testing of the stronger joints. Accordingly, a novel asymmetric backing/clamping system was used to extract more amount of the welding heat from the advancing side and keep the temperature high enough in the mixing stir zone. This was attained by inserting high-thermal conductivity material below and above the workpiece in the AS and low-thermal conductivity material below and above the workpiece in the RS. Accordingly, the temperature asymmetry between the welding sides was reduced and the joint micro-hardness was enhanced. The produced weld has exhibited a considerable increase in the tensile strength of 426 MPa, which represents a superior joint efficiency of about 95%.

### **5.3 Contributions of the Study**

The contributions of this dissertation are summarized as follows:

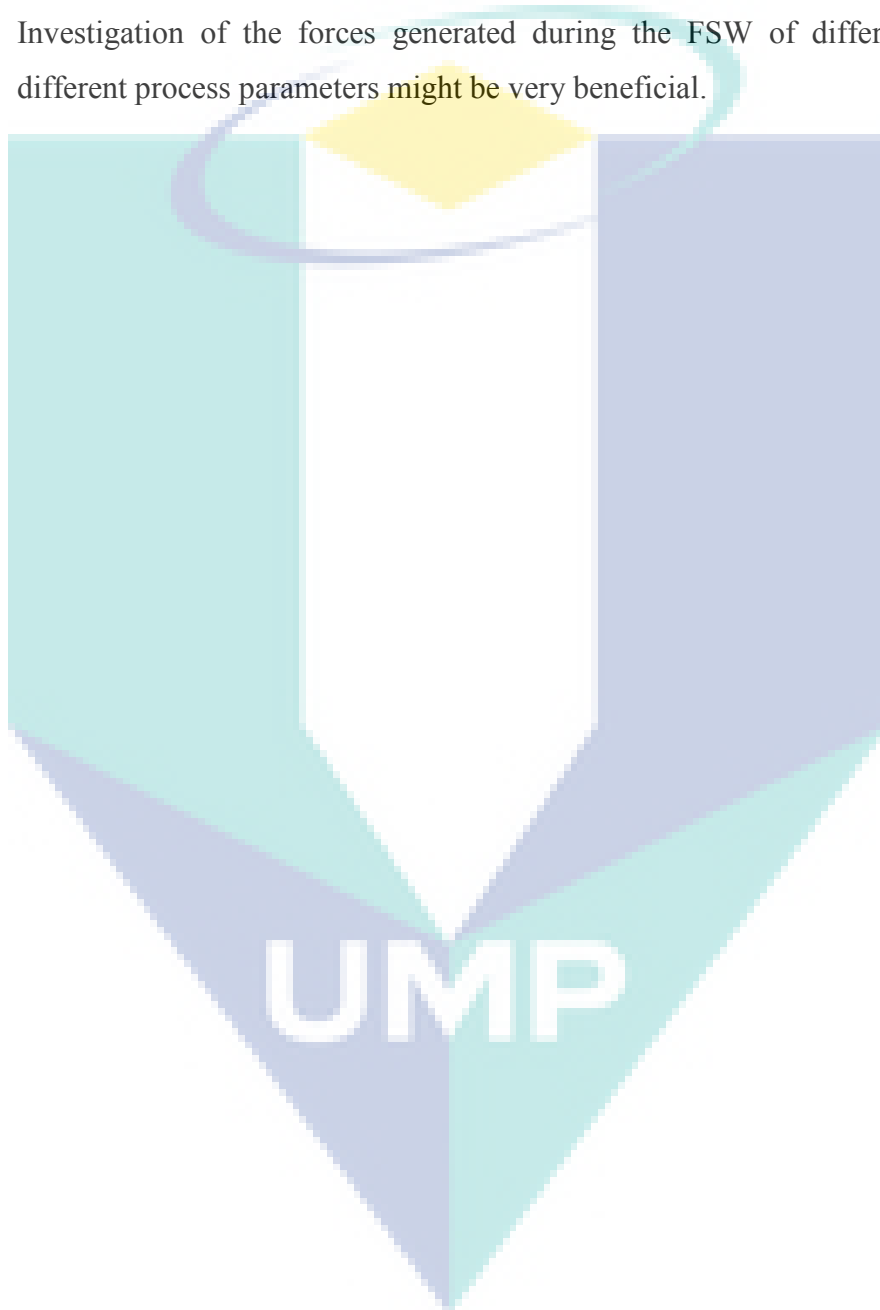
- i. Introducing a design of FSW tool permits to produce quality weld of dissimilar high-strength aluminum alloys.
- ii. Optimizing the initial heating stage or dwell sequence to extend the welding tool life by verifying a new method of friction stir welding without applying the ordinary plunge stage to avoid the initial longitudinal wear of the probe.
- iii. Constructing a design of backing and clamping system enables controlling the clamping force and temperature distribution during the FSW of dissimilar aluminum alloys to accomplish high-efficient joints.
- iv. Improving the material flow and mixing of dissimilar FSW weld by optimizing the radius of a single flute that can be formed on a truncated threaded pin tool for maximum weld strength.

### **5.4 Recommendations**

Future research will continue to advance the knowledge of dissimilar FSW, extending the understanding of the complex physical interactions which motivate a process that developed first as a technology. Areas of much interest recently are tool design and thermal management, which is being attempted with both thermal boundary condition modification and closed-loop temperature control. With the objective of producing high efficient dissimilar welds, these important topics were considered in the current dissertation. However, the research should be extended to cover the following headlines, which are recommended for future work:

- i. Higher thickness aluminum plates can be welded by employing double sided FSW. One can try to use tools made of different materials to improve the quality of the joints.
- ii. Using new tool designs which have frustum shapes, surface coating of the probe and surface heat treatment techniques could be viable solutions to improve both tool life and joint efficiency.

- iii. Inspecting the FSW of dissimilar aluminum alloys in lap and T-joint configurations through introducing asymmetric backing and clamping system.
- iv. Studying the influence of backing materials and clamping system on the FSW of dissimilar materials from different families, such as aluminum and steel.
- v. Investigation of the forces generated during the FSW of different alloys at different process parameters might be very beneficial.



## REFERENCES

- Abbasi, M., Bagheri, B., & Keivani, R. (2015). Thermal analysis of friction stir welding process and investigation into affective parameters using simulation. *Journal of Mechanical Science and Technology* 29(2), 861-866. doi:<http://dx.doi.org/10.1007/s12206-015-0149-3>
- Abdullah, K., Wild, P., Jeswiet, J., & Ghasempoor, A. (2001). Tensile testing for weld deformation properties in similar gage tailor welded blanks using the rule of mixtures. *Journal of Materials Processing Technology*, 112(1), 91-97. doi:[http://dx.doi.org/10.1016/S0924-0136\(01\)00555-6](http://dx.doi.org/10.1016/S0924-0136(01)00555-6)
- Ahmed, M., Ataya, S., Seleman, M. E.-S., Ammar, H., & Ahmed, E. (2017). Friction stir welding of similar and dissimilar AA7075 and AA5083. *Journal of Materials Processing Technology*, 242, 77-91. doi:<http://dx.doi.org/10.1016/j.jmatprotec.2016.11.024>
- Al-Badour, F., Merah, N., Shuaib, A., & Bazoune, A. (2014). Thermo-mechanical finite element model of friction stir welding of dissimilar alloys. *The International Journal of Advanced Manufacturing Technology*, 72(5-8), 607-617. doi:<http://dx.doi.org/10.1007/s00170-014-5680-3>
- Aliha, M. R. M., Shahheidari, M., Bisadi, M., Akbari, M., & Hossain, S. (2016). Mechanical and metallurgical properties of dissimilar AA6061-T6 and AA7277-T6 joint made by FSW technique. *International Journal of Advanced Manufacturing Technology* 86(9-12), 2551-2565. doi:<http://dx.doi.org/10.1007/s00170-016-8341-x>
- ASTM:E3-11. (2011). Standard Guide for Preparation of Metallographic Specimens, ASTM International, West Conshohocken, PA, United States. Available from: [www.astm.org/Standards/E3.htm](http://www.astm.org/Standards/E3.htm).
- ASTM:E8/E8M-11. (2011). Standard Test Methods for Tension Testing of Metallic Materials. ASTM international, West Conshohocken, PA, United States. Available from: <http://www.astm.org/Standards/E8.htm>.
- Aval, H. J., & Serajzadeh, S. (2014). A study on natural aging behavior and mechanical properties of friction stir-welded AA6061-T6 plates. *The International Journal of Advanced Manufacturing Technology*, 71(5-8), 933-941. doi:<http://dx.doi.org/10.1007/s00170-013-5531-7>
- Avinash, P., Manikandan, M., Arivazhagan, N., Ramkumar, K. D., & Narayanan, S. (2014). Friction Stir Welded Butt Joints of AA2024 T3 and AA7075 T6 Aluminum Alloys. *Procedia Engineering*, 75, 98-102. doi:<http://dx.doi.org/10.1016/j.proeng.2013.11.020>
- Bahrami, A., Anijdan, S. H. M., Golozar, M. A., Shamanian, M., & Varahram, N. (2005). Effects of conventional heat treatment on wear resistance of AISI H13 tool steel. *Wear*, 258(5-6), 846-851. doi:<http://dx.doi.org/10.1016/j.wear.2004.09.008>
- Bahrami, M., Besharati Givi, M. K., Dehghani, K., & Parvin, N. (2014). On the role of pin geometry in microstructure and mechanical properties of AA7075/SiC nano-composite fabricated by friction stir welding technique. *Materials & Design*, 53, 519-527. doi:<http://dx.doi.org/10.1016/j.matdes.2013.07.049>
- Bang, H., Bang, H., Hong, J. H., Jeon, G. H., Kim, G. S., & Kaplan, A. F. H. (2016). Effect of Tungsten-Inert-Gas Preheating on Mechanical and Microstructural Properties of Friction

- Stir Welded Dissimilar Al Alloy and Mild Steel. *Strength of Materials* 48(1), 152-159. doi:<http://dx.doi.org/10.1007/s11223-016-9750-7>
- Banjare, P. N., Sahlot, P., & Arora, A. (2017). An assisted heating tool design for FSW of thermoplastics. *Journal of Materials Processing Technology*, 239, 83-91. doi:<http://dx.doi.org/10.1016/j.jmatprotec.2016.07.035>
- Bayazid, S. M., Farhangi, H., & Ghahramani, A. (2015). Investigation of Friction Stir Welding Parameters of 6063-7075 Aluminum Alloys by Taguchi Method. *Procedia Materials Science*, 11, 6-11. doi:<http://dx.doi.org/10.1016/j.mspro.2015.11.007>
- Bertoncello, J. C. B., Manhabosco, S. M., & Dick, L. F. P. (2015). Corrosion study of the friction stir lap joint of AA7050-T76511 on AA2024-T3 using the scanning vibrating electrode technique. *Corrosion Science*, 94, 359-367. doi:<http://dx.doi.org/10.1016/j.corsci.2015.02.029>
- Beygi, R., Kazeminezhad, M., Mehrizi, M. Z., Eisaabadi, B. G., & Loureiro, A. (2017). Friction stir butt welding of Al-Cu bilayer laminated composites: analysis of force, torque, and temperature. *International Journal of Advanced Manufacturing Technology* 88(1-4), 393-400. doi:<http://dx.doi.org/10.1007/s00170-016-8778-y>
- Blignault, C., Hattingh, D. G., & James, M. N. (2011). Optimizing Friction Stir Welding via Statistical Design of Tool Geometry and Process Parameters. *Journal of Materials Engineering and Performance*. doi:<http://dx.doi.org/10.1007/s11665-011-9984-2>
- Buffa, G., Campanile, G., Fratini, L., & Prisco, A. (2009). Friction stir welding of lap joints: Influence of process parameters on the metallurgical and mechanical properties. *Materials Science and Engineering: A*, 519(1-2), 19-26. doi:<http://dx.doi.org/10.1016/j.msea.2009.04.046>
- Buffa, G., Hua, J., Shivpuri, R., & Fratini, L. (2006). Design of the friction stir welding tool using the continuum based FEM model. *Materials Science and Engineering: A*, 419(1-2), 381-388. doi:<http://dx.doi.org/10.1016/j.msea.2005.09.041>
- Çam, G. (2011). Friction stir welded structural materials: beyond Al-alloys. *International Materials Reviews*, 56(1), 1-48. doi:<http://dx.doi.org/10.1179/095066010X12777205875750>
- Cao, X., & Jahazi, M. (2011). Effect of tool rotational speed and probe length on lap joint quality of a friction stir welded magnesium alloy. *Materials & Design*, 32(1), 1-11. doi:<http://dx.doi.org/10.1016/j.matdes.2010.06.048>
- Casavola, C., Cazzato, A., Moramarco, V., & Pappalettere, C. (2015). Temperature field in FSW process: Experimental measurement and numerical simulation. In N. Sottos, R. Rowlands, & K. Dannemann (Eds.), *Experimental and Applied Mechanics, Volume 6* (pp. 177-186): Springer International Publishing.
- Caseiro, J. F., Valente, R. A. F., Andrade-Campos, A., & Yoon, J. W. (2013). On the elasto-plastic buckling of Integrally Stiffened Panels (ISP) joined by Friction Stir Welding (FSW): Numerical simulation and optimization algorithms. *International Journal of Mechanical Sciences* 76, 49-59. doi:<http://dx.doi.org/10.1016/j.ijmecsci.2013.09.002>
- Cavaliere, P., Cerri, E., & Squillace, A. (2005). Mechanical response of 2024-7075 aluminium alloys joined by Friction Stir Welding. *Journal of Materials Science*, 40(14), 3669-3676. doi:<http://dx.doi.org/10.1007/s10853-005-0474-5>

- Cavaliere, P., Nobile, R., Panella, F. W., & Squillace, A. (2006). Mechanical and microstructural behaviour of 2024–7075 aluminium alloy sheets joined by friction stir welding. *International Journal of Machine Tools and Manufacture* 46(6), 588-594. doi:<http://dx.doi.org/10.1016/j.ijmachtools.2005.07.010>
- Cavaliere, P., & Panella, F. (2008). Effect of tool position on the fatigue properties of dissimilar 2024-7075 sheets joined by friction stir welding. *Journal of Materials Processing Technology*, 206(1–3), 249-255. doi:<http://dx.doi.org/10.1016/j.jmatprotec.2007.12.036>
- Chao, Y. J., Qi, X., & Tang, W. (2003). Heat transfer in friction stir welding—experimental and numerical studies. *Journal of Manufacturing Science and Engineering* 125(1), 138-145. doi:<http://dx.doi.org/10.1115/1.1537741>
- Christner, B., & Sylva, G. (1996). *Friction stir welding development for aerospace applications*. Paper presented at the ICAWT, Columbus, OH, USA.
- Cole, E. G., Fehrenbacher, A., Duffie, N. A., Zinn, M. R., Pfefferkorn, F. E., & Ferrier, N. J. (2013). Weld temperature effects during friction stir welding of dissimilar aluminum alloys 6061-t6 and 7075-t6. *The International Journal of Advanced Manufacturing Technology*, 71(1-4), 643-652. doi:<http://dx.doi.org/10.1007/s00170-013-5485-9>
- Colligan, K. J. (2010). 2 - The friction stir welding process: an overview. In D. Lohwasser & Z. Chen (Eds.), *Friction Stir Welding* (pp. 15-41): Woodhead Publishing.
- Colligan, K. J., & Mishra, R. S. (2008). A conceptual model for the process variables related to heat generation in friction stir welding of aluminum. *Scripta Materialia*, 58(5), 327-331. doi:<http://dx.doi.org/10.1016/j.scriptamat.2007.10.015>
- Costa, M., Verdera, D., Costa, J., Leitao, C., & Rodrigues, D. (2015). Influence of pin geometry and process parameters on friction stir lap welding of AA5754-H22 thin sheets. *Journal of Materials Processing Technology*, 225, 385-392. doi:<http://dx.doi.org/10.1016/j.jmatprotec.2015.06.020>
- da Silva, A. A. M., Arruti, E., Janeiro, G., Aldanondo, E., Alvarez, P., & Echeverria, A. (2011). Material flow and mechanical behaviour of dissimilar AA2024-T3 and AA7075-T6 aluminium alloys friction stir welds. *Materials & Design*, 32(4), 2021-2027. doi:<http://dx.doi.org/10.1016/j.matdes.2010.11.059>
- Daniolos, N. M., & Pantelis, D. I. (2016). Microstructural and mechanical properties of dissimilar friction stir welds between AA6082-T6 and AA7075-T651. *The International Journal of Advanced Manufacturing Technology*. doi:<http://dx.doi.org/10.1007/s00170-016-8965-x>
- Davis, J. R. (2004). *Tensile testing* (2nd ed.). Materials Park, OH, United States: ASM international.
- Doley, J. K., & Kore, S. D. (2016). A Study on Friction Stir Welding of Dissimilar Thin Sheets of Aluminum Alloys AA 5052–AA 6061. *Journal of Manufacturing Science and Engineering* 138(11), 114502. doi:<http://dx.doi.org/10.1115/1.4033691>
- Dubourg, L., Merati, A., & Jahazi, M. (2010). Process optimisation and mechanical properties of friction stir lap welds of 7075-T6 stringers on 2024-T3 skin. *Materials & Design*, 31(7), 3324-3330. doi:<http://dx.doi.org/10.1016/j.matdes.2010.02.002>

- Dunn, B. D. (2016). Requirements for Spacecraft Materials *Materials and Processes: for Spacecraft and High Reliability Applications* (pp. 7-53). Cham: Springer International Publishing.
- Durđević, A., Živojinović, D., Grbović, A., Sedmak, A., Rakin, M., Dascau, H., & Kirin, S. (2015). Numerical simulation of fatigue crack propagation in friction stir welded joint made of Al 2024-T351 alloy. *Engineering Failure Analysis* 58, Part 2, 477-484. doi:<http://dx.doi.org/10.1016/j.engfailanal.2015.08.028>
- Dursun, T., & Soutis, C. (2014). Recent developments in advanced aircraft aluminium alloys. *Materials & Design*, 56, 862-871. doi:<http://dx.doi.org/10.1016/j.matdes.2013.12.002>
- Dutka, M., Ditaranto, M., & Løvås, T. (2015). Application of a central composite design for the study of NOx emission performance of a low NOx burner. *Energies*, 8(5), 3606-3627. doi:<http://dx.doi.org/10.3390/en8053606>
- El-Batahgy, A.-M., Miura, T., Ueji, R., & Fujii, H. (2016). Investigation into feasibility of FSW process for welding 1600MPa quenched and tempered steel. *Materials Science and Engineering: A*, 651, 904-913. doi:<http://dx.doi.org/10.1016/j.msea.2015.11.054>
- Elangovan, K., & Balasubramanian, V. (2007). Influences of pin profile and rotational speed of the tool on the formation of friction stir processing zone in AA2219 aluminium alloy. *Materials Science and Engineering: A*, 459(1-2), 7-18. doi:<http://dx.doi.org/10.1016/j.msea.2006.12.124>
- Elangovan, K., & Balasubramanian, V. (2008). Influences of tool pin profile and welding speed on the formation of friction stir processing zone in AA2219 aluminium alloy. *Journal of Materials Processing Technology*, 200(1-3), 163-175. doi:<http://dx.doi.org/10.1016/j.jmatprotec.2007.09.019>
- Elangovan, K., Balasubramanian, V., & Valliappan, M. (2008). Influences of tool pin profile and axial force on the formation of friction stir processing zone in AA6061 aluminium alloy. *The International Journal of Advanced Manufacturing Technology*, 38(3-4), 285-295. doi:<http://dx.doi.org/10.1007/s00170-007-1100-2>
- Emami, S., & Saeid, T. (2015). Effects of Welding and rotational speeds on the Microstructure and Hardness of Friction Stir Welded Single-Phase Brass. *Acta Metallurgica Sinica (English Letters)*, 28(6), 766-771. doi:<http://dx.doi.org/10.1007/s40195-015-0259-z>
- Eslami, S., Tavares, P. J., & Moreira, P. M. G. P. (2016). Friction stir welding tooling for polymers: review and prospects. *The International Journal of Advanced Manufacturing Technology*. doi:<http://dx.doi.org/10.1007/s00170-016-9205-0>
- Farajkhah, V., & Liu, Y. (2016). Effect of clamping area and welding speed on the friction stir welding-induced residual stresses. *The International Journal of Advanced Manufacturing Technology*, 1-10. doi:<http://dx.doi.org/10.1007/s00170-016-9393-7>
- Farias, A., Batalha, G. F., Prados, E. F., Magnabosco, R., & Delijaicov, S. (2013). Tool wear evaluations in friction stir processing of commercial titanium Ti-6Al-4V. *Wear*, 302(1), 1327-1333. doi:<http://dx.doi.org/10.1016/j.wear.2012.10.025>
- Firouzidor, V., & Kou, S. (2010). Formation of liquid and intermetallics in Al-to-Mg friction stir welding. *Metallurgical and Materials Transactions A*, 41(12), 3238-3251. doi:<http://dx.doi.org/10.1007/s11661-010-0366-4>

- Forcellese, A., Gabrielli, F., & Simoncini, M. (2012). Mechanical properties and microstructure of joints in AZ31 thin sheets obtained by friction stir welding using “pin” and “pinless” tool configurations. *Materials & Design*, 34, 219-229. doi:<http://dx.doi.org/10.1016/j.matdes.2011.08.001>
- Fratini, L., Micari, F., Buffa, G., & Ruisi, V. F. (2010). A new fixture for FSW processes of titanium alloys. *CIRP Annals - Manufacturing Technology*, 59(1), 271-274. doi:<http://dx.doi.org/10.1016/j.cirp.2010.03.003>
- Fu, M. J., Li, X. H., Han, X. Q., & Xu, H. Y. (2016). *Research on Work Hardening Type Superplastic Deformation Behavior of FSW Titanium Alloy*. Paper presented at the Materials Science Forum.
- Fuchs, R., Heuser, H., & Hahn, B. (2010). Welding of dissimilar materials. *Materials at High Temperatures* 27(3), 183-190. doi:<http://dx.doi.org/10.3184/096034010X12813771363483>
- Fujii, H., Cui, L., Maeda, M., & Nogi, K. (2006). Effect of tool shape on mechanical properties and microstructure of friction stir welded aluminum alloys. *Materials Science and Engineering: A*, 419(1–2), 25-31. doi:<http://dx.doi.org/10.1016/j.msea.2005.11.045>
- García-Bernal, M. A., Mishra, R. S., Verma, R., & Hernández-Silva, D. (2016). Influence of friction stir processing tool design on microstructure and superplastic behavior of Al-Mg alloys. *Materials Science and Engineering: A*, 670, 9-16. doi:<http://dx.doi.org/10.1016/j.msea.2016.05.115>
- Gibson, B. T., Lammlein, D. H., Prater, T. J., Longhurst, W. R., Cox, C. D., Ballun, M. C., . . . Strauss, A. M. (2014). Friction stir welding: Process, automation, and control. *Journal of Manufacturing Processes*, 16(1), 56-73. doi:<http://dx.doi.org/10.1016/j.jmapro.2013.04.002>
- Giraud, L., Robe, H., Claudin, C., Desrayaud, C., Bocher, P., & Feulvarch, E. (2016). Investigation into the dissimilar friction stir welding of AA7020-T651 and AA6060-T6. *Journal of Materials Processing Technology*, 235, 220-230. doi:<http://dx.doi.org/10.1016/j.jmatprotec.2016.04.020>
- Guillo, M., & Dubourg, L. (2016). Impact & improvement of tool deviation in friction stir welding: Weld quality & real-time compensation on an industrial robot. *Robotics and Computer-Integrated Manufacturing*, 39, 22-31. doi:<http://dx.doi.org/10.1016/j.rcim.2015.11.001>
- Guo, J. F., Chen, H. C., Sun, C. N., Bi, G., Sun, Z., & Wei, J. (2014). Friction stir welding of dissimilar materials between AA6061 and AA7075 Al alloys effects of process parameters. *Materials & Design*, 56, 185-192. doi:<http://dx.doi.org/10.1016/j.matdes.2013.10.082>
- Hattingh, D. G., Blignault, C., van Niekerk, T. I., & James, M. N. (2008). Characterization of the influences of FSW tool geometry on welding forces and weld tensile strength using an instrumented tool. *Journal of Materials Processing Technology*, 203(1–3), 46-57. doi:<http://dx.doi.org/10.1016/j.jmatprotec.2007.10.028>
- Heidarzadeh, A., & Saeid, T. (2013). Prediction of mechanical properties in friction stir welds of pure copper. *Materials & Design*, 52, 1077-1087. doi:<http://dx.doi.org/10.1016/j.matdes.2013.06.068>

- Hirata, T., Oguri, T., Hagino, H., Tanaka, T., Chung, S. W., Takigawa, Y., & Higashi, K. (2007). Influence of friction stir welding parameters on grain size and formability in 5083 aluminum alloy. *Materials Science and Engineering: A*, 456(1-2), 344-349. doi:<http://dx.doi.org/10.1016/j.msea.2006.12.079>
- Ilangovan, M., Rajendra Boopathy, S., & Balasubramanian, V. (2015). Effect of tool pin profile on microstructure and tensile properties of friction stir welded dissimilar AA 6061–AA 5086 aluminium alloy joints. *Defence Technology*, 11(2), 174-184. doi:<http://dx.doi.org/10.1016/j.dt.2015.01.004>
- Iliopoulos, A., Michopoulos, J. G., & Lambrakos, S. (2015). *Towards inverse estimation of properties, process parameters and residual effects for friction stir welding*. Paper presented at the ASME 2015 International Design Engineering Technical Conferences and Computers and Information in Engineering Conference.
- Imam, M., Racherla, V., & Biswas, K. (2014). Effect of backing plate material in friction stir butt and lap welding of 6063-T4 aluminium alloy. *The International Journal of Advanced Manufacturing Technology*. doi:<http://dx.doi.org/10.1007/s00170-014-6617-6>
- İpekoğlu, G., & Çam, G. (2014). Effects of initial temper condition and postweld heat treatment on the properties of dissimilar friction-stir-welded joints between AA7075 and AA6061 aluminum alloys. *Metallurgical and Materials Transactions A*, 45(7), 3074-3087. doi:<http://dx.doi.org/10.1007/s11661-014-2248-7>
- Ishak, M., Noordin, N., Razali, A., Shah, L., & Romlay, F. (2015). Effect of filler on weld metal structure of AA6061 aluminum alloy by tungsten inert gas welding. *International Journal of Automotive & Mechanical Engineering*, 11. doi:<http://dx.doi.org/10.15282/ijame.11.2015.24.0205>
- Islam, M. R., Ishak, M., Shah, L. H., Idris, S. R. A., & Meriç, C. (2016). Dissimilar welding of A7075-T651 and AZ31B alloys by gas metal arc plug welding method. *The International Journal of Advanced Manufacturing Technology*, 88(9-12), 2773-2783. doi:<http://dx.doi.org/10.1007/s00170-016-8993-6>
- Jain, R., Pal, S. K., & Singh, S. B. (2016). A study on the variation of forces and temperature in a friction stir welding process: A finite element approach. *Journal of Manufacturing Processes*, 23, 278-286. doi:<http://dx.doi.org/10.1016/j.jmapro.2016.04.008>
- Jamshidi Aval, H. (2015). Influences of pin profile on the mechanical and microstructural behaviors in dissimilar friction stir welded AA6082–AA7075 butt Joint. *Materials & Design*, 67, 413-421. doi:<http://dx.doi.org/10.1016/j.matdes.2014.11.055>
- Jamshidi Aval, H., Serajzadeh, S., & Kokabi, A. H. (2011). Evolution of microstructures and mechanical properties in similar and dissimilar friction stir welding of AA5086 and AA6061. *Materials Science and Engineering: A*, 528(28), 8071-8083. doi:<http://dx.doi.org/10.1016/j.msea.2011.07.056>
- Ji, S. D., Meng, X. C., Ma, L., & Gao, S. S. (2016). Effect of groove distribution in shoulder on formation, macrostructures, and mechanical properties of pinless friction stir welding of 6061-O aluminum alloy. *The International Journal of Advanced Manufacturing Technology*. doi:<http://dx.doi.org/10.1007/s00170-016-8734-x>
- Kallee, S., Lohwasser, D., & Chen, Z. (2010). *Friction Stir Welding—from basics to application*: Woodhead Publishing, Cambridge.

- Karthikeyan, R., & Balasubramanian, V. (2013). Statistical optimization and sensitivity analysis of friction stir spot welding process parameters for joining AA 7075 aluminum alloy. *Experimental Techniques*, 37(2), 6-15. doi:<http://dx.doi.org/10.1111/j.1747-1567.2011.00746.x>
- Kass, R. E., Eden, U. T., & Brown, E. N. (2014). Analysis of variance *Analysis of Neural Data* (pp. 361-389): Springer.
- Khan, N. Z., Siddiquee, A. N., Khan, Z. A., & Mukhopadhyay, A. K. (2017). Mechanical and microstructural behavior of friction stir welded similar and dissimilar sheets of AA2219 and AA7475 aluminium alloys. *Journal of Alloys and Compounds*, 695, 2902-2908. doi:<http://dx.doi.org/10.1016/j.jallcom.2016.11.389>
- Khodabakhshi, F., Haghshenas, M., Chen, J., Shalchi Amirkhiz, B., Li, J., & Gerlich, A. (2016). Bonding mechanism and interface characterisation during dissimilar friction stir welding of an aluminium/polymer bi-material joint. *Science and Technology of Welding and Joining* 1-9. doi:<http://dx.doi.org/10.1080/13621718.2016.1211583>
- Khodir, S. A., & Shibayanagi, T. (2007). Microstructure and mechanical properties of friction stir welded dissimilar aluminum joints of AA2024-T3 and AA7075-T6. *Materials Transactions*, 48(7), 1928-1937. doi:<http://dx.doi.org/10.2320/matertrans.MRA2007042>
- Khodir, S. A., & Shibayanagi, T. (2008). Friction stir welding of dissimilar AA2024 and AA7075 aluminum alloys. *Materials Science and Engineering: B*, 148(1-3), 82-87. doi:<http://dx.doi.org/10.1016/j.mseb.2007.09.024>
- Khodir, S. A., Shibayanagi, T., & Naka, M. (2006). Control of hardness distribution in friction stir welded AA2024-T3 aluminum alloy. *Materials Transactions*, 47(6), 1560-1567. doi:<http://dx.doi.org/10.2320/matertrans.47.1560>
- Koohbor, B., Ohadi, D., Serajzadeh, S., & Akhgar, J. (2010). Effect of rolling speed on the occurrence of strain aging during and after warm rolling of a low-carbon steel. *Journal of Materials Science*, 45(13), 3405-3412. doi:<http://dx.doi.org/10.1007/s10853-010-4365-z>
- Krasnowski, K., Hamilton, C., & Dymek, S. (2015). Influence of the tool shape and weld configuration on microstructure and mechanical properties of the Al 6082 alloy FSW joints. *Archives of Civil and Mechanical Engineering*, 15(1), 133-141. doi:<http://dx.doi.org/10.1016/j.acme.2014.02.001>
- Krishnan, K. (2002). On the formation of onion rings in friction stir welds. *Materials Science and Engineering: A*, 327(2), 246-251. doi:[http://dx.doi.org/10.1016/S0921-5093\(01\)01474-5](http://dx.doi.org/10.1016/S0921-5093(01)01474-5)
- Kumar, K., & Kailas, S. V. (2008). The role of friction stir welding tool on material flow and weld formation. *Materials Science and Engineering: A*, 485(1), 367-374.
- Kumar, N., Mishra, R. S., & Yuan, W. (2015). *Friction stir welding of dissimilar alloys and materials: A volume in the friction stir welding and processing book series*: Butterworth-Heinemann.
- Lammlein, D. H., DeLapp, D. R., Fleming, P. A., Strauss, A. M., & Cook, G. E. (2009). The application of shoulderless conical tools in friction stir welding: An experimental and theoretical study. *Materials & Design*, 30(10), 4012-4022. doi:<http://dx.doi.org/10.1016/j.matdes.2009.05.023>

- Lee, W., Yeon, Y., & Jung, S. (2003). The mechanical properties related to the dominant microstructure in the weld zone of dissimilar formed Al alloy joints by friction stir welding. *Journal of Materials Science*, 38(20), 4183-4191. doi:<http://dx.doi.org/10.1023/A:1026337807920>
- Leonard, A., & Lockyer, S. (2003). *Flaws in friction stir welds*. Paper presented at the 4th International Symposium on Friction Stir Welding, Park City, Utah, USA.
- Li, H., Dai, Q.-L., & Shi, Q.-Y. (2015). Experimental Study on the Heterogeneity of Mechanical Properties of Friction Stir Welded Joints with the Digital Image Correlation Method. *Strength of Materials* 47(1), 80-86. doi:<http://dx.doi.org/10.1007/s11223-015-9631-5>
- Li, W., Li, J., Zhang, Z., Gao, D., Wang, W., & Luan, G. (2014). Pinless friction stir welding of AA2024-T3 joint and its failure modes. *Transactions of Tianjin University*, 20(6), 439-443. doi:<http://dx.doi.org/10.1007/s12209-014-2157-2>
- Liu, C., & Zhang, J. X. (2009). Numerical simulation of transient welding angular distortion with external restraints. *Science and Technology of Welding and Joining* 14(1), 26-31. doi:<http://dx.doi.org/10.1179/136217108X341175>
- Liu, Q. S., Mahdavian, S. M., Aswin, D., & Ding, S. (2009). Experimental study of temperature and clamping force during Nd:YAG laser butt welding. *Optics & Laser Technology* 41(6), 794-799. doi:<http://dx.doi.org/10.1016/j.optlastec.2008.12.002>
- Liu, Z., Cui, H., Ji, S., Xu, M., & Meng, X. (2016). Improving Joint Features and Mechanical Properties of Pinless Fiction Stir Welding of Alcaid 2A12-T4 Aluminum Alloy. *Journal of Materials Science & Technology*. doi:<http://dx.doi.org/10.1016/j.jmst.2016.07.003>
- Lohwasser, D., & Chen, Z. (2009). *Friction stir welding: From basics to applications*: Elsevier.
- Lohwasser, D., & Chen, Z. (2010). 1 - Introduction. In D. Lohwasser & Z. Chen (Eds.), *Friction Stir Welding* (pp. 1-12): Woodhead Publishing.
- Luo, C., Li, X., Song, D., Zhou, N., Li, Y., & Qi, W. (2016). Microstructure evolution and mechanical properties of friction stir welded dissimilar joints of Mg–Zn–Gd and Mg–Al–Zn alloys. *Materials Science and Engineering: A*, 664, 103-113.
- Ma, Z. Y., Mishra, R. S., & Mahoney, M. W. (2002). Superplastic deformation behaviour of friction stir processed 7075Al alloy. *Acta Materialia*, 50(17), 4419-4430. doi:[http://dx.doi.org/10.1016/S1359-6454\(02\)00278-1](http://dx.doi.org/10.1016/S1359-6454(02)00278-1)
- Mahoney, M., Rhodes, C., Flintoff, J., Bingel, W., & Spurling, R. (1998). Properties of friction-stir-welded 7075 T651 aluminum. *Metallurgical and Materials Transactions A*, 29(7), 1955-1964. doi:<http://dx.doi.org/10.1007/s11661-998-0021-5>
- Maisonnette, D., Suery, M., Nelias, D., Chaudet, P., & Epicier, T. (2011). Effects of heat treatments on the microstructure and mechanical properties of a 6061 aluminium alloy. *Materials Science and Engineering: A*, 528(6), 2718-2724. doi:<http://dx.doi.org/10.1016/j.msea.2010.12.011>
- Malarvizhi, S., & Balasubramanian, V. (2012). Influences of tool shoulder diameter to plate thickness ratio (D/T) on stir zone formation and tensile properties of friction stir welded dissimilar joints of AA6061 aluminum–AZ31B magnesium alloys. *Materials & Design*, 40, 453-460. doi:<http://dx.doi.org/10.1016/j.matdes.2012.04.008>

- Mason, R. L., Gunst, R. F., & Hess, J. L. (2003). *Statistical design and analysis of experiments: with applications to engineering and science* (Vol. 474): John Wiley & Sons.
- Mathews, P. G. (2010). *Design of Experiments with MINITAB*: ASQ Quality Press.
- McClure, J. C., Tang, W., Murr, L., Guo, X., Feng, Z., & Gould, J. E. (1998). A thermal model of friction stir welding. *Trends in Welding Research*, 1(999), 62.
- Mehta, M., Arora, A., De, A., & DebRoy, T. (2011). Tool geometry for friction stir welding—optimum shoulder diameter. *Metallurgical and Materials Transactions A*, 42(9), 2716-2722. doi:<http://dx.doi.org/10.1007/s11661-011-0672-5>
- Mendes, N., Neto, P., Loureiro, A., & Moreira, A. P. (2016). Machines and control systems for friction stir welding: A review. *Materials & Design*, 90, 256-265. doi:<http://dx.doi.org/10.1016/j.matdes.2015.10.124>
- Miles, M. P., Ridges, C. S., Hovanski, Y., Peterson, J., Santella, M. L., & Steel, R. (2013). Impact of tool wear on joint strength in friction stir spot welding of DP 980 steel. *Science and Technology of Welding and Joining* 16(7), 642-647. doi:<http://dx.doi.org/10.1179/1362171811y.0000000047>
- Mironov, S., Inagaki, K., Sato, Y. S., & Kokawa, H. (2015). Effect of welding temperature on microstructure of friction-stir welded aluminum alloy 1050. *Metallurgical and Materials Transactions A*, 46(2), 783-790. doi:<http://dx.doi.org/10.1007/s11661-014-2651-0>
- Mishra, R. S., De, P. S., & Kumar, N. (2014). FSW of Aluminum Alloys *Friction Stir Welding and Processing* (pp. 109-148): Springer.
- Mishra, R. S., & Ma, Z. Y. (2005). Friction stir welding and processing. *Materials Science and Engineering: R: Reports*, 50(1-2), 1-78. doi:<http://dx.doi.org/10.1016/j.mser.2005.07.001>
- Mishra, R. S., & Mahoney, M. W. (2007). *Friction stir welding and processing*: ASM International.
- Mishra, R. S., Mahoney, M. W., Sato, Y., & Hovanski, Y. (2015). *Friction Stir Welding and Processing VIII*: Wiley.
- Moghadam, D. G., Farhangdoost, K., & Nejad, R. M. (2016). Microstructure and Residual Stress Distributions Under the Influence of Welding Speed in Friction Stir Welded 2024 Aluminum Alloy. *Metallurgical and Materials Transactions B-Process Metallurgy and Materials Processing Science*, 47(3), 2048-2062. doi:<http://dx.doi.org/10.1007/s11663-016-0611-3>
- Mondolfo, L. F. (2013). *Aluminum alloys: structure and properties*: Elsevier.
- Montgomery, D. C. (2013). *Design and Analysis of Experiments* (Eighth Edition ed.): John Wiley & Sons Singapore Pte. Ltd.
- Murphy, A., Ekmekyapar, T., Özakça, M., Poston, K., Moore, G., & Elliott, M. (2014). Buckling/post-buckling strength of friction stir welded aircraft stiffened panels. *Proceedings of the Institution of Mechanical Engineers, Part G: Journal of Aerospace Engineering* 228(2), 178-192. doi:<http://dx.doi.org/10.1177/0954410012468537>

- Murphy, A., Ekmekyapar, T., Quinn, D., Özakça, M., Poston, K., Moore, G., & Niblock, J. (2014). The influence of assembly friction stir weld location on wing panel static strength. *Thin-Walled Structures*, 76(0), 56-64. doi:<http://dx.doi.org/10.1016/j.tws.2013.11.004>
- Mustafa, F. F., Kadhym, A. H., & Yahya, H. H. (2015). Tool Geometries Optimization for Friction Stir Welding of AA6061-T6 Aluminum Alloy T-Joint Using Taguchi Method to Improve the Mechanical Behavior. *Journal of Manufacturing Science and Engineering* 137(3), 031018. doi:<http://dx.doi.org/10.1115/1.4029921>
- Nandan, R., Debroy, T., & Bhadeshia, H. (2008). Recent advances in friction-stir welding – Process, weldment structure and properties. *Progress in Materials Science* 53(6), 980-1023. doi:<http://dx.doi.org/10.1016/j.pmatsci.2008.05.001>
- Padmanaban, G., & Balasubramanian, V. (2009). Selection of FSW tool pin profile, shoulder diameter and material for joining AZ31B magnesium alloy – An experimental approach. *Materials & Design*, 30(7), 2647-2656. doi:<http://dx.doi.org/10.1016/j.matdes.2008.10.021>
- Palanivel, R., Koshy Mathews, P., Murugan, N., & Dinaharan, I. (2012). Effect of tool rotational speed and pin profile on microstructure and tensile strength of dissimilar friction stir welded AA5083-H111 and AA6351-T6 aluminum alloys. *Materials & Design*, 40, 7-16. doi:<http://dx.doi.org/10.1016/j.matdes.2012.03.027>
- Pan, Y., & Lados, D. A. (2017). Friction Stir Welding in Wrought and Cast Aluminum Alloys: Weld Quality Evaluation and Effects of Processing Parameters on Microstructure and Mechanical Properties. *Metallurgical and Materials Transactions a-Physical Metallurgy and Materials Science*, 48a(4), 1708-1726. doi:<http://dx.doi.org/10.1007/s11661-016-3943-3>
- Papahn, H., Haghpanahi, M., & Bahemmat, P. (2015). Using a novel fixture to study of temperature and applied forces during friction stir welding. *Journal of the Brazilian Society of Mechanical Sciences and Engineering*, 1-11. doi:<http://dx.doi.org/10.1007/s40430-015-0408-3>
- Parida, B., Vishwakarma, S. D., & Pal, S. (2015). Design and development of fixture and force measuring system for friction stir welding process using strain gauges. *Journal of Mechanical Science and Technology* 29(2), 739-749. doi:<http://dx.doi.org/10.1007/s12206-015-0134-x>
- Park, S.-K., Hong, S.-T., Park, J.-H., Park, K.-Y., Kwon, Y.-J., & Son, H.-J. (2010). Effect of material locations on properties of friction stir welding joints of dissimilar aluminium alloys. *Science and Technology of Welding & Joining*, 15(4), 331-336. doi:<http://dx.doi.org/10.1179/136217110X12714217309696>
- Park, S. H. C., Sato, Y. S., Kokawa, H., Okamoto, K., Hirano, S., & Inagaki, M. (2009). Boride Formation Induced by pcBN Tool Wear in Friction-Stir-Welded Stainless Steels. *Metallurgical and Materials Transactions A*, 40(3), 625-636. doi:<http://dx.doi.org/10.1007/s11661-008-9709-9>
- Pasha, M. A., Reddy, P. R., Laxminarayana, P., & Khan, I. A. (2016). The Effects of SiC Particle Addition as Reinforcement in the weld Zone during Friction Stir Welding of Magnesium Alloy AZ31B. *IRA-International Journal of Technology & Engineering (ISSN 2455-4480)*, 3(3).

- Peel, M., Steuwer, A., Preuss, M., & Withers, P. J. (2003). Microstructure, mechanical properties and residual stresses as a function of welding speed in aluminium AA5083 friction stir welds. *Acta Materialia*, 51(16), 4791-4801. doi:[http://dx.doi.org/10.1016/S1359-6454\(03\)00319-7](http://dx.doi.org/10.1016/S1359-6454(03)00319-7)
- Prakash, D. G. L., & Regener, D. (2008). Quantitative characterization of Mg17Al12 phase and grain size in HPDC AZ91 magnesium alloy. *Journal of Alloys and Compounds*, 461(1–2), 139-146. doi:<http://dx.doi.org/10.1016/j.jallcom.2007.07.017>
- Prime, M., Gnaupelherold, T., Baumann, J., Lederich, R., Bowden, D., & Sebring, R. (2006). Residual stress measurements in a thick, dissimilar aluminum alloy friction stir weld. *Acta Materialia*, 54(15), 4013-4021. doi:<http://dx.doi.org/10.1016/j.actamat.2006.04.034>
- Querin, J., Rubisoff, H., & Schneider, J. (2009). Effect of weld tool geometry on friction stir welded Ti-6Al-4V. *Trends in Welding Research (ASM International, Materials Park, 2009)*, 108-112. doi:<http://dx.doi.org/10.1361/cp2008twr108>
- Rahimzadeh Ilkhichi, A., Soufi, R., Hussain, G., Vatankhah Barenji, R., & Heidarzadeh, A. (2014). Establishing Mathematical Models to Predict Grain Size and Hardness of the Friction Stir-Welded AA 7020 Aluminum Alloy Joints. *Metallurgical and Materials Transactions B*, 46(1), 357-365. doi:<http://dx.doi.org/10.1007/s11663-014-0205-x>
- Rai, R., De, A., Bhadeshia, H. K. D. H., & DebRoy, T. (2011). Review: friction stir welding tools. *Science and Technology of Welding and Joining* 16(4), 325-342. doi:<http://dx.doi.org/10.1179/1362171811y.0000000023>
- Rajakumar, S., Muralidharan, C., & Balasubramanian, V. (2010). Optimization of the friction-stir-welding process and tool parameters to attain a maximum tensile strength of AA7075–T6 aluminium alloy. *Proceedings of the Institution of Mechanical Engineers, Part B: Journal of Engineering Manufacture* 224(8), 1175-1191.
- Reza-E-Rabby, M., Tang, W., & Reynolds, A. P. (2015). Effect of tool pin features on process response variables during friction stir welding of dissimilar aluminum alloys. *Science and Technology of Welding and Joining* 20(5), 425-432. doi:<http://dx.doi.org/10.1179/1362171815y.0000000036>
- Richter-Trummer, V., Suzano, E., Beltrão, M., Roos, A., dos Santos, J. F., & de Castro, P. M. S. T. (2012). Influence of the FSW clamping force on the final distortion and residual stress field. *Materials Science and Engineering: A*, 538(0), 81-88. doi:<http://dx.doi.org/10.1016/j.msea.2012.01.016>
- Rodriguez, R. I., Jordon, J. B., Allison, P. G., Rushing, T., & Garcia, L. (2015). Microstructure and mechanical properties of dissimilar friction stir welding of 6061-to-7050 aluminum alloys. *Materials & Design*, 83, 60-65. doi:<http://dx.doi.org/10.1016/j.matdes.2015.05.074>
- Sahu, P. K., & Pal, S. (2017). Mechanical properties of dissimilar thickness aluminium alloy weld by single/double pass FSW. *Journal of Materials Processing Technology*, 243, 442-455. doi:<http://dx.doi.org/10.1016/j.jmatprotec.2017.01.009>
- Salih, O. S., Ou, H., Sun, W., & McCartney, D. G. (2015). A review of friction stir welding of aluminium matrix composites. *Materials & Design*, 86, 61-71. doi:<http://dx.doi.org/10.1016/j.matdes.2015.07.071>

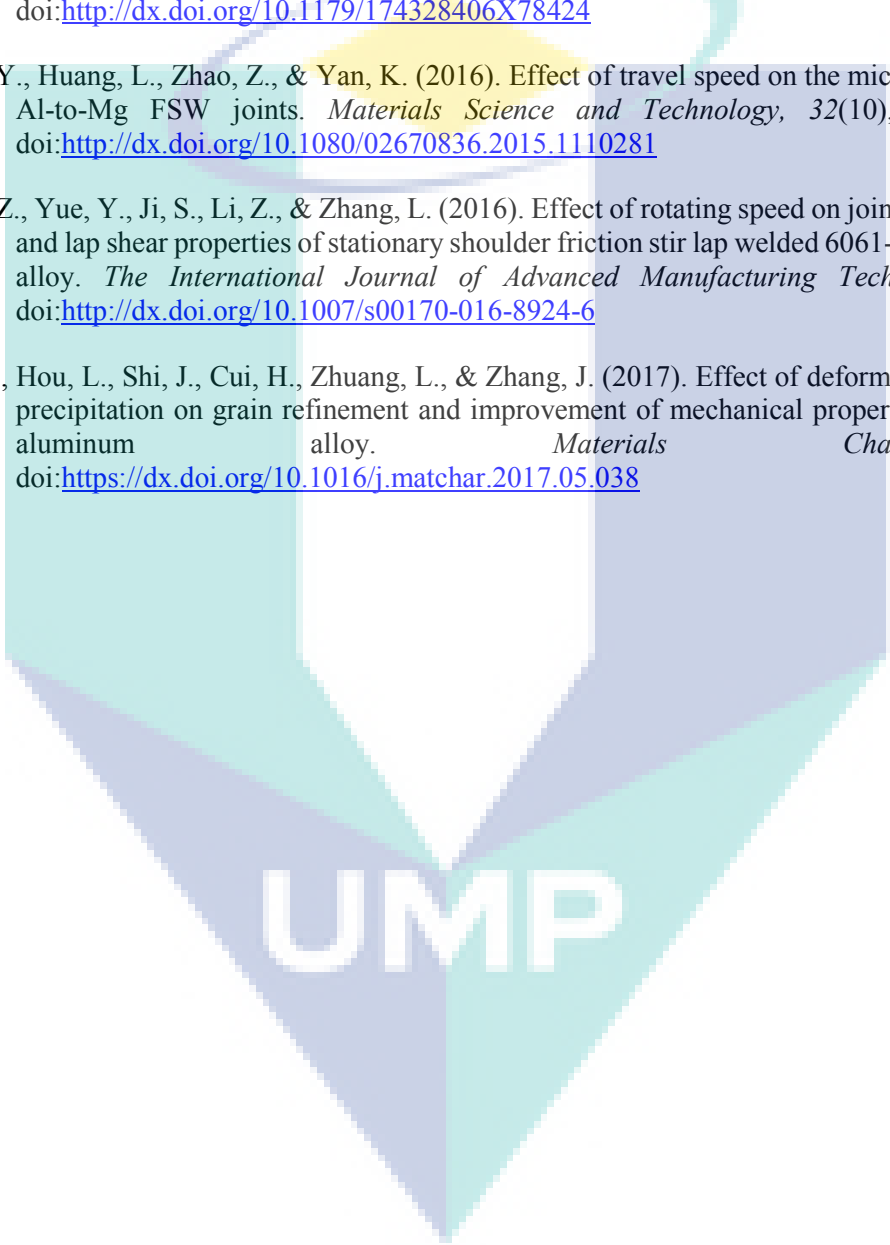
- Saravanan, V., Rajakumar, S., Banerjee, N., & Amuthakkannan, R. (2016). Effect of shoulder diameter to pin diameter ratio on microstructure and mechanical properties of dissimilar friction stir welded AA2024-T6 and AA7075-T6 aluminum alloy joints. *International Journal of Advanced Manufacturing Technology* 87(9-12), 3637-3645. doi:<http://dx.doi.org/10.1007/s00170-016-8695-0>
- Saravanan, V., Rajakumar, S., & Muruganandam, A. (2016). Effect of Friction Stir Welding Process Parameters on Microstructure and Mechanical Properties of Dissimilar AA6061-T6 and AA7075-T6 Aluminum Alloy Joints. *Metallography, Microstructure, and Analysis*, 1-10. doi:<http://dx.doi.org/10.1007/s13632-016-0315-8>
- Sathari, N., Razali, A., Ishak, M., & Shah, L. (2015). Mechanical strength of dissimilar AA7075 and AA6061 aluminum alloys using friction stir welding. *International Journal of Automotive & Mechanical Engineering*, 11, 2713-2721. doi:<http://dx.doi.org/10.15282/ijame.11.2015.47.0228>
- Schmidt, H. N. B. (2010). 10 - Modelling thermal properties in friction stir welding. In D. Lohwasser & Z. Chen (Eds.), *Friction Stir Welding* (pp. 277-313): Woodhead Publishing.
- Schneider, J., Brooke, S., & Nunes Jr, A. C. (2016). Material flow modification in a FSW through introduction of flats. *Metallurgical and Materials Transactions B*, 47(1), 720-730. doi:<http://dx.doi.org/10.1007/s11663-015-0523-7>
- Scialpi, A., De Filippis, L. A. C., & Cavaliere, P. (2007). Influence of shoulder geometry on microstructure and mechanical properties of friction stir welded 6082 aluminium alloy. *Materials & Design*, 28(4), 1124-1129. doi:<http://dx.doi.org/10.1016/j.matdes.2006.01.031>
- Scialpi, A., Troughton, M., Andrews, S., & De Filippis, L. (2009). Viblade™: friction stir welding for plastics. *Welding International* 23(11), 846-855. doi:<http://dx.doi.org/10.1080/09507110902843271>
- Serio, L., Palumbo, D., De Filippis, L., Galietti, U., & Ludovico, A. (2016). Effect of Friction Stir Process Parameters on the Mechanical and Thermal Behavior of 5754-H111 Aluminum Plates. *Materials*, 9(3), 122. doi:<http://dx.doi.org/10.3390/ma9030122>
- Sevvel, P., & Jaiganesh, V. (2015). Effect of Tool Shoulder Diameter to Plate Thickness Ratio on Mechanical Properties and Nugget Zone Characteristics During FSW of Dissimilar Mg Alloys. *Transactions of the Indian Institute of Metals*, 68(1), 41-46. doi:<http://dx.doi.org/10.1007/s12666-015-0602-0>
- Shah, L. H., Zainal Ariffin, N. F., & Razali, A. R. (2014). Parameter Optimization of AA6061-AA7075 Dissimilar Friction Stir Welding Using the Taguchi Method. *Applied Mechanics and Materials*, 695, 20-23.
- Shanmuga Sundaram, N., & Murugan, N. (2010). Tensile behavior of dissimilar friction stir welded joints of aluminium alloys. *Materials & Design*, 31(9), 4184-4193. doi:<http://dx.doi.org/10.1016/j.matdes.2010.04.035>
- Shao, Q., He, Y., Zhang, T., & Wu, L. (2014). Numerical analysis of static performance comparison of friction stir welded versus riveted 2024-T3 aluminum alloy stiffened panels. *Chinese Journal of Mechanical Engineering*, 27(4), 761-767. doi:<http://dx.doi.org/10.3901/CJME.2014.0507.087>

- Shrivastava, A., Overcash, M., & Pfefferkorn, F. E. (2015). Prediction of unit process life cycle inventory (UPLCI) energy consumption in a friction stir weld. *Journal of Manufacturing Processes*, 18, 46-54. doi:<http://dx.doi.org/10.1016/j.jmapro.2014.10.006>
- Smith, C. B., Hinrichs, J. F., Crusan, W. A., & Leverett, J. (2003). FSW Stirs Up Welding Process Competition. *Forming and Fabricating*(2), 25–31.
- Song, Y., Yang, X., Cui, L., Hou, X., Shen, Z., & Xu, Y. (2014). Defect features and mechanical properties of friction stir lap welded dissimilar AA2024–AA7075 aluminum alloy sheets. *Materials & Design*, 55(0), 9-18. doi:<http://dx.doi.org/10.1016/j.matdes.2013.09.062>
- Steinberg, D. M., & Kenett, R. S. (2014). Response surface methodology. *Encyclopedia of Statistics in Quality and Reliability*. doi:<http://dx.doi.org/10.1002/9780470061572.eqr033>
- Sun, Y., Tsuji, N., & Fujii, H. (2016). Microstructure and mechanical properties of dissimilar friction stir welding between ultrafine grained 1050 and 6061-t6 aluminum alloys. *Metals*, 6(10), 249. doi:<http://dx.doi.org/10.3390/met6100249>
- Tan, Y., Wang, X., Ma, M., Zhang, J., Liu, W., Fu, R., & Xiang, S. (2017). A study on microstructure and mechanical properties of AA 3003 aluminum alloy joints by underwater friction stir welding. *Materials Characterization*, 127, 41-52. doi:<http://dx.doi.org/10.1016/j.matchar.2017.01.039>
- Tang, W., Guo, X., McClure, J., Murr, L., & Nunes, A. (1998). Heat input and temperature distribution in friction stir welding. *Journal of Materials Processing and Manufacturing Science* 7, 163-172.
- Teimurnezhad, J., Pashazadeh, H., & Masumi, A. (2016). Effect of shoulder plunge depth on the weld morphology, macrograph and microstructure of copper FSW joints. *Journal of Manufacturing Processes*, 22, 254-259. doi:<http://dx.doi.org/10.1016/j.jmapro.2016.04.001>
- Thelning, K.-E. (2013). *Steel and its heat treatment*. Butterworth-Heinemann.
- Thomas, W., & Dolby, R. (2003). Friction stir welding developments. *Proceedings of the sixth international trends in welding research*, 203-211.
- Thomas, W., Johnson, K. I., & Wiesner, C. S. (2003). Friction stir welding—recent developments in tool and process technologies. *Advanced Engineering Materials* 5(7), 485-490. doi:<http://dx.doi.org/10.1002/adem.200300355>
- Thomas, W., & Nicholas, E. (1997). Friction stir welding for the transportation industries. *Materials & Design*, 18(4), 269-273. doi:[http://dx.doi.org/10.1016/S0261-3069\(97\)00062-9](http://dx.doi.org/10.1016/S0261-3069(97)00062-9)
- Thomas, W., Nicholas, E., Needham, J. C., Murch, M., Templesmith, P., & Dawes, C. (1991). Friction stir welding. *International patent application No. PCT/GB92102203 and Great Britain Patent Application No. 9125978.8*.
- Thomas, W., Norris, I., Staines, D., & Watts, E. (2005). Friction stir welding—process developments and variant techniques. *The SME Summit*, 1, 1-21.

- Thomas, W., Siores, E., Rowe, C., & Moon, D. (2010). FRICTION STIR WELDING DEVELOPMENTS IN STEEL. *Annals of "Dunarea de Jos" University of Galati. Fascicle XII: Welding Equipment and Technology*, 21.
- Thomas, W., Staines, D., Norris, I., & De Frias, R. (2003). Friction stir welding tools and developments. *Welding in the World*, 47(11-12), 10-17.
- Threadgill, P., Leonard, A., Shercliff, H., & Withers, P. (2009). Friction stir welding of aluminium alloys. *International Materials Reviews*, 54(2), 49-93. doi:<http://dx.doi.org/10.1179/174328009X411136>
- Threadgill, P. L. (2007). Terminology in friction stir welding. *Science and Technology of Welding and Joining* 12(4), 357-360. doi:<http://dx.doi.org/10.1179/174329307X197629>
- Threadgill, P. L. (2010). 6 - The future of friction stir welding. In D. Lohwasser & Z. Chen (Eds.), *Friction Stir Welding* (pp. 164-182): Woodhead Publishing.
- Tongne, A., Desrayaud, C., Jahazi, M., & Feulvarch, E. (2017). On material flow in Friction Stir Welded Al alloys. *Journal of Materials Processing Technology*, 239, 284-296. doi:<http://dx.doi.org/10.1016/j.jmatprotec.2016.08.030>
- Tozaki, Y., Uematsu, Y., & Tokaji, K. (2010). A newly developed tool without probe for friction stir spot welding and its performance. *Journal of Materials Processing Technology*, 210(6-7), 844-851. doi:<http://dx.doi.org/10.1016/j.jmatprotec.2010.01.015>
- Trimble, D., O'Donnell, G. E., & Monaghan, J. (2015). Characterisation of tool shape and rotational speed for increased speed during friction stir welding of AA2024-T3. *Journal of Manufacturing Processes*, 17(0), 141-150. doi:<http://dx.doi.org/10.1016/j.jmapro.2014.08.007>
- Trueba Jr, L., Heredia, G., Rybicki, D., & Johannes, L. B. (2015). Effect of tool shoulder features on defects and tensile properties of friction stir welded aluminum 6061-T6. *Journal of Materials Processing Technology*, 219(0), 271-277. doi:<http://dx.doi.org/10.1016/j.jmatprotec.2014.12.027>
- Upadhyay, P., & Reynolds, A. (2014). Effect of backing plate thermal property on friction stir welding of 25-mm-thick AA6061. *Metallurgical and Materials Transactions A*, 45(4), 2091-2100. doi:<http://dx.doi.org/10.1007/s11661-013-2121-0>
- Upadhyay, P., & Reynolds, A. P. (2012). Effects of forge axis force and backing plate thermal diffusivity on FSW of AA6056. *Materials Science and Engineering: A*, 558(0), 394-402. doi:<http://dx.doi.org/10.1016/j.msea.2012.08.018>
- Wang, W., Li, T. Q., Wang, K. S., Cai, J., & Qiao, K. (2016). Effect of Travel Speed on the Stress Corrosion Behavior of Friction Stir Welded 2024-T4 Aluminum Alloy. *Journal of Materials Engineering and Performance*, 25(5), 1820-1828. doi:<http://dx.doi.org/10.1007/s11665-016-1979-6>
- Williams, S. W., & Steuwer, A. (2010). 8 - Residual stresses in friction stir welding. In D. Lohwasser & Z. Chen (Eds.), *Friction Stir Welding* (pp. 215-244): Woodhead Publishing.
- Xu, R. Z., Ni, D. R., Yang, Q., Liu, C. Z., & Ma, Z. Y. (2016). Pinless Friction Stir Spot Welding of Mg-3Al-1Zn Alloy with Zn Interlayer. *Journal of Materials Science & Technology*, 32(1), 76-88. doi:<http://dx.doi.org/10.1016/j.jmst.2015.08.012>

- Xu, W., Liu, J., Zhu, H., & Fu, L. (2013). Influence of welding parameters and tool pin profile on microstructure and mechanical properties along the thickness in a friction stir welded aluminum alloy. *Materials & Design*, 47, 599-606. doi:<http://dx.doi.org/10.1016/j.matdes.2012.12.065>
- Yan, J., Sutton, M. A., & Reynolds, A. P. (2005). Process–structure–property relationships for nugget and heat affected zone regions of AA2524–T351 friction stir welds. *Science and Technology of Welding & Joining*, 10(6), 725-736. doi:<http://dx.doi.org/10.1179/174329305X68778>
- Yoon, T.-J., Yun, J.-G., & Kang, C.-Y. (2016). Formation mechanism of typical onion ring structures and void defects in friction stir lap welded dissimilar aluminum alloys. *Materials & Design*, 90, 568-578. doi:<http://dx.doi.org/10.1016/j.matdes.2015.11.014>
- Zain-ul-abdein, M., Nélias, D., Jullien, J.-F., & Deloison, D. (2010). Experimental investigation and finite element simulation of laser beam welding induced residual stresses and distortions in thin sheets of AA 6056-T4. *Materials Science and Engineering: A*, 527(12), 3025-3039. doi:<http://dx.doi.org/10.1016/j.msea.2010.01.054>
- Zain-Ul-Abdein, M., Nélias, D., Jullien, J. F., & Deloison, D. (2008). Thermo-mechanical analysis of laser beam welding of thin plate with complex boundary conditions. *International Journal of Material Forming* 1(1), 1063-1066. doi:<http://dx.doi.org/10.1007/s12289-008-0202-1>
- Zappia, T. (2010). 7 - Inspection and quality control in friction stir welding. In D. Lohwasser & Z. Chen (Eds.), *Friction Stir Welding* (pp. 183-212): Woodhead Publishing.
- Zappia, T., Smith, C., Colligan, K., Ostersehltte, H., & Kallee, S. W. (2010). 4 - Friction stir welding equipment. In D. Lohwasser & Z. Chen (Eds.), *Friction Stir Welding* (pp. 73-117): Woodhead Publishing.
- Zettler, R. (2010). 3 - Material deformation and joint formation in friction stir welding. In D. Lohwasser & Z. Chen (Eds.), *Friction Stir Welding* (pp. 42-72): Woodhead Publishing.
- Zettler, R., Lomolino, S., Dos Santos, J., Donath, T., Beckmann, F., Lippman, T., & Lohwasser, D. (2004). *A study on material flow in FSW of AA 2024-T351 and AA 6056-T4 alloys*. Paper presented at the 5th International FSW Symposium-Metz, France.
- Zettler, R., Potomati, F., dos Santos, J. F., & de Alcantara, N. G. (2006). Temperature Evolution and Mechanical Properties of Dissimilar Friction Stir Weldments when Joining AA2024 and AA7075 with an AA6056 Alloy. *Welding in the World*, 50(11-12), 107-116. doi:<http://dx.doi.org/10.1007/BF03263467>
- Zettler, R., Vugrin, T., & schmÜcker, M. (2010). 9 - Effects and defects of friction stir welds. In D. Lohwasser & Z. Chen (Eds.), *Friction Stir Welding* (pp. 245-276): Woodhead Publishing.
- Zhang, H., Wang, M., Zhang, X., & Yang, G. (2015). Microstructural characteristics and mechanical properties of bobbin tool friction stir welded 2A14-T6 aluminum alloy. *Materials & Design*, 65, 559-566. doi:<http://dx.doi.org/10.1016/j.matdes.2014.09.068>
- Zhang, L., Ji, S., Luan, G., Dong, C., & Fu, L. (2011). Friction Stir Welding of Al Alloy Thin Plate by Rotational Tool without Pin. *Journal of Materials Science & Technology*, 27(7), 647-652. doi:[http://dx.doi.org/10.1016/s1005-0302\(11\)60120-5](http://dx.doi.org/10.1016/s1005-0302(11)60120-5)

- Zhang, Y. N., Cao, X., Larose, S., & Wanjara, P. (2012). Review of tools for friction stir welding and processing. *Canadian Metallurgical Quarterly*, 51(3), 250-261. doi:<http://dx.doi.org/10.1179/1879139512y.0000000015>
- Zhang, Z., Li, W., Shen, J., Chao, Y. J., Li, J., & Ma, Y.-E. (2013). Effect of backplate diffusivity on microstructure and mechanical properties of friction stir welded joints. *Materials & Design*, 50, 551-557. doi:<http://dx.doi.org/10.1016/j.matdes.2013.03.034>
- Zhao, Y.-H., Lin, S.-B., Qu, F.-X., & Wu, L. (2006). Influence of pin geometry on material flow in friction stir welding process. *Materials Science and Technology*, 22(1), 45-50. doi:<http://dx.doi.org/10.1179/174328406X78424>
- Zhao, Y., Huang, L., Zhao, Z., & Yan, K. (2016). Effect of travel speed on the microstructure of Al-to-Mg FSW joints. *Materials Science and Technology*, 32(10), 1025-1034. doi:<http://dx.doi.org/10.1080/02670836.2015.1110281>
- Zhou, Z., Yue, Y., Ji, S., Li, Z., & Zhang, L. (2016). Effect of rotating speed on joint morphology and lap shear properties of stationary shoulder friction stir lap welded 6061-T6 aluminum alloy. *The International Journal of Advanced Manufacturing Technology*, 1-7. doi:<http://dx.doi.org/10.1007/s00170-016-8924-6>
- Zuo, J., Hou, L., Shi, J., Cui, H., Zhuang, L., & Zhang, J. (2017). Effect of deformation induced precipitation on grain refinement and improvement of mechanical properties AA 7055 aluminum alloy. *Materials Characterization*. doi:<https://dx.doi.org/10.1016/j.matchar.2017.05.038>

The logo for UMP (Université de Moncton) is a large, stylized letter 'U' composed of several overlapping triangles in shades of teal, light blue, and white. The letters 'UMP' are printed in a bold, white, sans-serif font across the center of the 'U' shape.

UMP

## LIST OF PUBLICATIONS

### *Journal papers*

Hasan, M. M., Ishak, M., & Rejab, M. (2017). Effect of backing material and clamping system on the tensile strength of dissimilar AA7075-AA2024 friction stir welds. *The International Journal of Advanced Manufacturing Technology*, 91(9-12), 3991-4007. doi: <http://dx.doi.org/10.1007/s00170-017-0033-7> ISI (IF = 2.209)

Hasan, M. M., Ishak, M., & Rejab, M. R. M. (2016). Influence of machine variables and tool profile on the tensile strength of dissimilar AA7075-AA6061 friction stir welds. *The International Journal of Advanced Manufacturing Technology*, 90(9), 2605-2615. doi: <http://dx.doi.org/10.1007/s00170-016-9583-3> ISI (IF = 2.209)

Hasan, M. M., Ishak, M., & Rejab, M. R. M. (2015). A simplified design of clamping system and fixtures for friction stir welding of aluminum alloys. *Journal of Mechanical Engineering and Sciences*, 9, 1628-1639. doi: <http://dx.doi.org/10.15282/jmes.9.2015.10.0158> (Scopus Index)

Hasan, M. M., Ishak, M., & Rejab, M. R. M. (2017). Effect of pin tool design on the material flow of dissimilar AA7075-AA6061 friction stir welds. *IOP Conf. Series: Materials Science and Engineering*, 257 (2017) 012022. doi: <http://dx.doi.org/10.1088/1757-899X/257/1/012022>. (Scopus Index)

Hasan, M. M., Ishak, M., & Rejab, M. R. M. (2017). Effect of tool rotation rate on the tensile strength of friction stir weldments of AA7075-T651 and AA2024-T351 aluminum alloys. *Journal of Mechanical Engineering and Sciences*. (Scopus Index). Revised

Hasan, M. M., Ishak, M., & Rejab, M. R. M. (2017). Effect of pin tool flute radius on the material flow and microstructure of dissimilar AA7075-AA2024 friction stir welds. *International Journal of Mechanical Sciences*. ISI (IF = 2.884). Under review

Hasan, M. M., Ishak, M., & Rejab, M. R. M. (2017). A methodology for reducing the longitudinal wear of the pin tool in friction stir welding of dissimilar aluminum alloys. *Journal of Material Processing Technology*. ISI (IF = 2.236). Under review

Hasan, M. M., Ishak, M., & Rejab, M. R. M. (2017). Effect of material direction and location on the friction stir welding of dissimilar aluminum alloys. *Journal of Materials Science and Technology*. ISI (IF = 1.909). Under review

### ***Conferences***

3rd International Conference on Mechanical Engineering Research (ICMER2015)/ Kuantan, Pahang, Malaysia. 18-19 August 2015.

2nd International Conference on Automotive Innovation and Green Energy Vehicle (AiGEV2016)/ Malaysia Automotive Institute (MAI), Cyberjaya, Selangor, Malaysia. 2-3 August 2016.

4th International Conference on Mechanical Engineering Research (ICMER2017)/ Kuantan, Pahang, Malaysia. 1-2 August 2017.

### ***Patent***

Clamping jig for dissimilar friction stir welding. *Patent Application No. PI2017700587.*

### ***Awards***

*Best presenter award* in the 2nd International Conference on Automotive Innovation and Green Energy Vehicle (AiGEV2016)/ Malaysia Automotive Institute (MAI), Cyberjaya, Selangor, Malaysia. 2-3 August 2016.

*Best achievement award* for excellent achievement in Preparatory Intensive English (PIE) Programme, UMP, 2014.

*Bronze Medal* in the Citrex 2017 Exhibition. UMP, Gambang, Malaysia.

The logo of Universiti Malaysia Pahang (UMP) is a large, stylized 'U' shape. The top part of the 'U' is a yellow diamond. The left and right sides of the 'U' are teal and light blue respectively. The bottom part of the 'U' is a dark blue triangle. The letters 'UMP' are written in white, bold, sans-serif font across the bottom of the 'U' shape.

**UMP**